NICKEL AND IRON COMPLEXES FOR ELECTROCHEMICAL REDUCTION OF PROTONS AND CARBON DIOXIDE

Navid Jameei Moghaddam

UNIVERSITAT ROVIRA i VIRGILI

Nickel and Iron complexes for electrochemical reduction of protons and Carbon dioxide

Navid Jameei Moghaddam

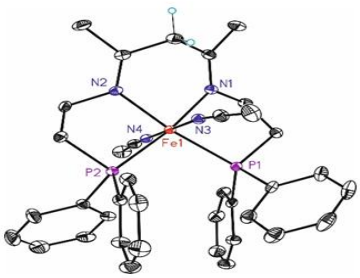

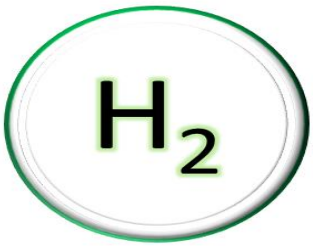

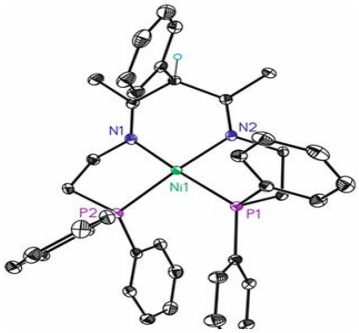

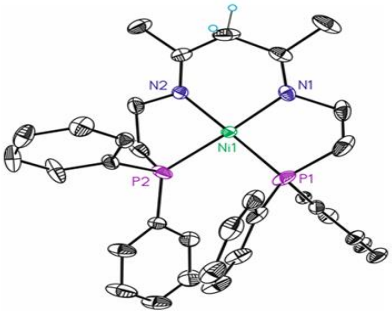

DOCTORAL THESIS

2022

UNIVERSITAT ROVIRA I VIRGILI
NICKEL AND IRON COMPLEXES FOR ELECTROCHEMICAL REDUCTION OF PROTONS AND CARBON DIOXIDE
Navid Jameei Moghaddam

Navid Jameei Moghaddam

Nickel and Iron complexes for electrochemical reduction of protons and Carbon dioxide

DOCTORAL THESIS

Supervised by:

Prof. Dr. Antoni Llobet and Dr. Carolina Gimbert Suriñach

Institute of Chemical Research of Catalonia

UNIVERSITAT ROVIRA I VIRGILI

ICIQ Institut Català d'Investigació Química

Tarragona

2022

ICIQ - Institut Català d'Investigació Química

Avgda, Països Catalans 16,

43007 Tarragona (Spain)

Prof. Dr. Antoni Llobet, Group Leader at the Institute of Chemical Research of Catalonia and Dr. Carolina Gimbert Suriñach *Ramón y Cajal* Fellow at the Universitat Autònoma de Barcelona,

We STATE that the present study, entitled "**Nickel and Iron complexes for electrochemical reduction of protons and Carbon dioxide**" presented by Navid Jameei Moghaddam for the award of the degree of doctor, has been carried out under our supervision in our group at the Institute of Chemical Research of Catalonia

Tarragona, June 5th, 2022

Doctoral thesis supervisors	
Prof. Dr. Antoni Llobet	Dr. Carolina Gimbert Suriñach
	

UNIVERSITAT ROVIRA I VIRGILI
NICKEL AND IRON COMPLEXES FOR ELECTROCHEMICAL REDUCTION OF PROTONS AND CARBON DIOXIDE
Navid Jameei Moghaddam

Acknowledgements

In the memory of my beloved mother who I lost her during this period

First, my sincere gratitude goes to Prof. Dr. Antoni Llobet for giving me this valuable opportunity to do my PhD studies in his research group and under his supervision. It was great period in my scientific life since I learned a lot about coordination chemistry, organic synthesis, and catalysis.

Second, I must thank Dr. Carolina Gimbert Suriñach for her kind helps during my PhD studies, honestly, finishing the thesis was not possible without her kind favours. She translated me the meaning of humanity at the same time she thought me how I can be a great Scientist. ***Gràcies per tot.***

Third, I dedicate the thesis to my family and all my friends **Mohsen**, **Mojtaba** , **Koroosh**, **Mengfei** for being true and loyal friends, also my group mates **Pablo**, **Chuanjun**, **Abi**, **Sergi**, **Jan Holub**, **Jia-Wei Wang**, **Laura**, **Andrew Howe**, **Andrew Bagnall**, **Yuanyuan**, **Tingting**, **Dr.Marcus**, **Marta**, **Natalia, Asmaul, Primavera,** for being friendly and creating friendly atmosphere inside the lab which made doing research more pleasant.

Abstract

Chapter 1. General introduction

This chapter includes a brief introduction about the natural photosynthesis process as a one of the most important processes taking place in nature and a blueprint for renewable energy conversion and storage. Moreover, inspiring from this fundamental process, the concept of artificial photosynthesis which tries to mimic natural photosynthesis is discussed. Finally, recent developments, requirements, and challenges for the development of efficient synthetic catalyst for the CO_2 and proton reduction reactions, inspired by enzymatic active sites are presented.

Chapter 2. Objectives

Following the progress in the field of artificial photosynthesis discussed in the General Introduction, the main objectives are exposed. The Objectives try to address some of the current challenges in designing robust and effective molecular catalysts for the reduction side of an artificial photosynthesis system.

Chapter 3. β-Diimine compounds as precursors to κ^2-N_2, κ^3-PN_2 and κ^4-P_2N_2 β-diketiminato ligands

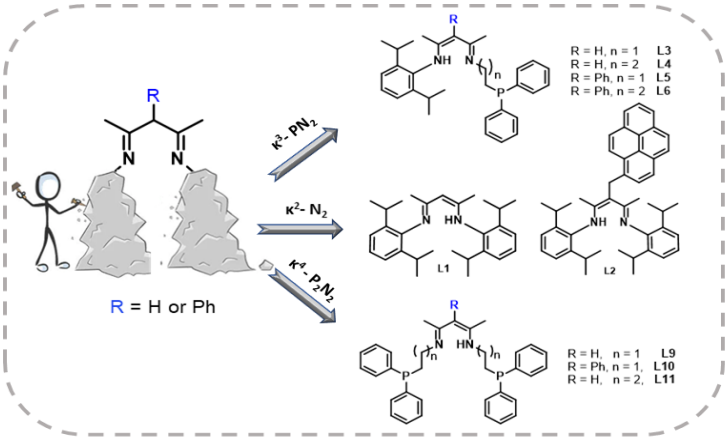

In this chapter, synthesis and characterization of three different groups of β-diimino (BDI) compounds as precursors to β-diketiminato (BDK) ligands with different denticity have been described. The first derivative **L1** belongs to the κ^2-N_2 type of ligands and was synthesized via direct double condensation reaction of 2,4-pentanedione with two equivalents of 2,6-diisopropyl aniline in the presence of catalytic amounts of acid. It was further modified with a dangling pyrene group in the α-carbon intradiimine position enabling the resulting compound to be anchored on graphitic substrates via π-π stacking interactions (**L2**). The second group of ligands are asymmetric κ^3-PN_2 type of ligands (**L3**-**L6**), whose synthesis is based on a two-step reaction process starting with 2,4-pentanedione, which reacts first with 2,6-diisopropyl aniline and then with the corresponding amino derivative substituted with a phosphine group. The last group of BDK compounds presented in this chapter are symmetrical κ^4-P_2N_2 ligands (**L9**-**L11**).

Chapter 4. Interplay between β-diimino and β-diketiminato ligands in Nickel complexes active in the proton reduction reaction

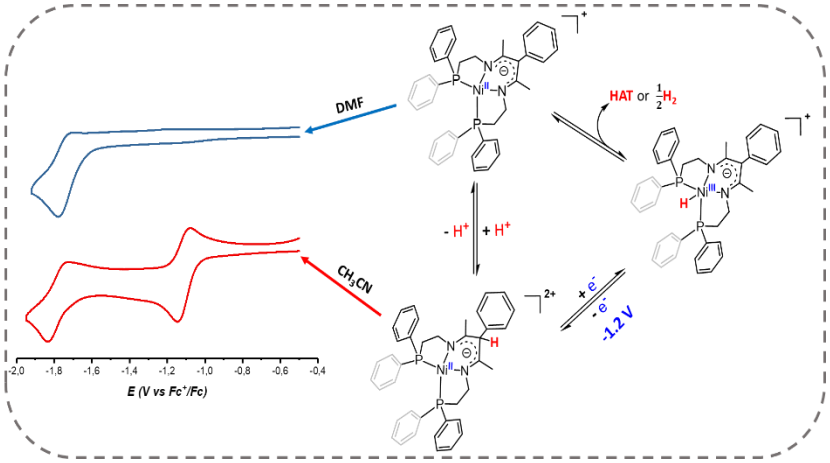

Two Ni complexes with κ^4-P_2N_2 β-diimino (BDI) ligands with general formula [Ni(XBDI)]$(BF_4)_2$, where BDI is *N*-(2-(diphenylphosphaneyl)ethyl)-4-((2-(diphenylphosphaneyl)ethyl)imino)pent-2-en-2-amine and X indicates the substituent in the α-carbon position, X = H for **1**$(BF_4)_2$ and X = Ph for **2**$(BF_4)_2$, are reported. Electrochemical analysis together with UV-vis and NMR spectroscopy in acetonitrile and dimethylformamide (DMF) indicate the conversion of the β-diimino complexes $\mathbf{1}^{2+}$ and $\mathbf{2}^{2+}$ to the negatively charged β-diketiminato (BDK) analogues $(\mathbf{1\text{-}H})^+$ and $(\mathbf{2\text{-}H})^+$ via deprotonation in DMF. Moreover, further electrochemical and spectroscopy evidence indicate that the one-electron reduced derivatives $\mathbf{1}^+$ and $\mathbf{2}^+$ can also rapidly evolve to the BDK $(\mathbf{1\text{-}H})^+$ and $(\mathbf{2\text{-}H})^+$ respectively, either via hydrogen atom transfer to the solvent or via hydrogen gas evolution through a bimolecular homolytic pathway. Finally, both complexes are demonstrated to be active for the proton reduction reaction in DMF at E_{app} = -1.8 V vs $Fc^{+/0}$, being the active species the one-electron reduced derivative of **1-H** and **2-H**.

Chapter 5. β-diimino and β-diketiminato Iron complexes and their interaction with CO_2

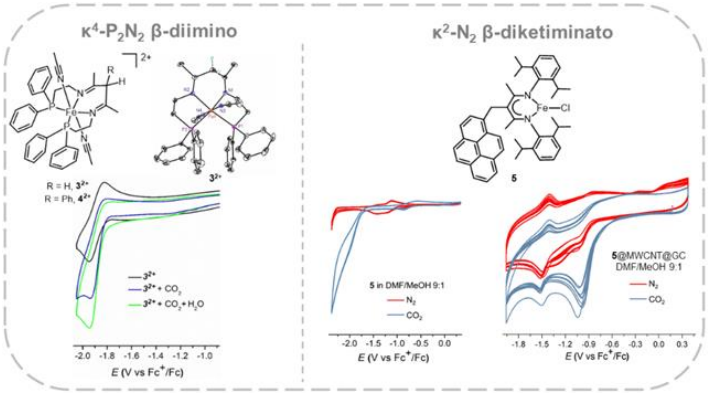

In this chapter, the synthesis and characterization of three novel iron complexes containing κ^4-P_2N_2 β-diimino (κ^4-BDI) or κ^2-N_2 β-diketiminato (κ^2-BDK) ligands are described. The first family of complexes $\mathbf{3}^{2+}$ and $\mathbf{4}^{2+}$ are isolated after the reaction of iron(II) triflate and the corresponding diimino compound; (2, 4)-*N*-(2-(diphenylphosphaneyl) ethyl (diphenylphosphaneyl) ethyl) imino) pent-2-en-2-amine (HBDI, **L9**) or (2, 4)-*N*-(2-(diphenylphosphaneyl) ethyl)-4-((2-(diphenylphosphaneyl) ethyl) imino)-3-phenylpent-2-en-2-amine (PhBDI, **L10**), respectively, affording two pseudo-octahedral compounds with the BDI ligand coordinating in a tetradentate fashion and two acetonitrilo ligands occupying the axial positions. Compounds $\mathbf{3}^{2+}$ and $\mathbf{4}^{2+}$ are Fe(II) diamagnetic compounds and have been characterized by NMR and cyclic voltammetry. They both react with carbon dioxide after a first reduction event, but the outcome of this reaction has not been elucidated and preliminary results point to decomposition processes. On the other hand, a third iron complex has been synthesized starting with the κ^2-N_2 BDI ligand precursor N-((2Z,4E)-4-((2,6-diisopropylphenyl)imino)-3-(pyren-1-ylmethyl)pent-2-en-2-yl)-2,6-diisopropylaniline (**L2**), containing a dangling pyrene group in the α-carbon intradiimine position. After reaction with n-BuLi and transmetalation with $FeCl_2(THF)_{1.5}$, a putative three coordinated iron(II) chlorido complex (**Fe-Cl**, **5**) is isolated. Compound **5** readily reacts with carbon dioxide or protons affording clean conversions towards **Fe-CO_2** or **Fe-H** products, respectively. Although the structures of **5** and its derivatives **Fe-CO_2** and **Fe-H** have not been confirmed, they all show very characteristic redox features that have been analyzed in detail. In particular, **5** shows a clear catalytic process in DMF in the presence of CO_2 and MeOH, suggesting a CO_2 reduction process. In addition, **5** was used to prepare a hybrid electrode by grafting it to multiwalled carbon nanotubes (MWCNT), followed by drop-casting onto glassy carbon (GC). Electrochemical analyses of the resulting modified electrode **5**@MWCNT@GC support the successful attachment of the complex and represents the first example of a β-diketiminato complex that has been heterogenized with potential application to electrocatalytic carbon dioxide reduction.

Chapter 6. Nickel complexes containing κ^4-N_4-dipicolinamido ligands for the CO_2 reduction reaction

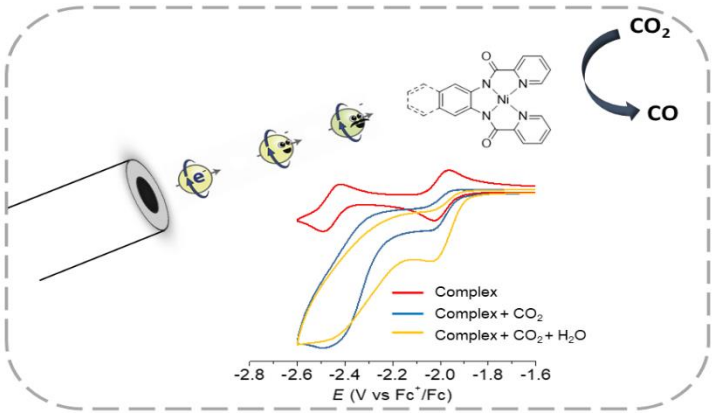

Two Nickel(II) complexes with the formula PDPANi (**6**) and NDPANi (**7**) have been prepared, where $PDPAH_2$ is *N*,*N*'-(1,2-phenylene)dipicolinamide and $NDPAH_2$ is *N*,*N*'-(naphthalene-2,3-diyl)dipicolinamide. They have been characterized by cyclic voltammetry in dimethylformamide, showing a first reversible reduction wave at $E_{1/2}$ = -1.99 V (**6**) and $E_{1/2}$ = -1.95 V (**7**) vs $Fc/Fc^{+/0}$. The 40 mV anodic shift observed for **7** compared to **6**, suggests a ligand based reduction facilitated by the higher conjugation of the naphthyl group compared to the phenyl ring, but a metal-based reduction is not ruled out at such low potentials. A second reduction wave appears at $E_{1/2}$ = -2.45 V and $E_{1/2}$ = -2.41 V vs $Fc/Fc^{+/0}$ for **6** and **7**, respectively. In the presence of carbon dioxide, both reductions events become irreversible, and a significant increase of the current is also observed at $E_{p,c}$ = -2.46 vs $Fc^{+/0}$ (**6**) and $E_{p,c}$ = -2.36 vs $Fc^{+/0}$ (**7**), close to the second reduction waves. Further addition of water induces an increase of the current at lower potentials; $E_{p,c}$ = -2.03 vs $Fc^{+/0}$ for **6** and $E_{p,c}$ = -1.95 vs $Fc^{+/0}$ for **7**, suggesting a CO_2 reduction process. A bulk electrolysis experiment of a DMF solution of **6** at E_{app} = -2.00 vs $Fc^{+/0}$ in the presence of CO_2 and H_2O, confirms the formation of CO as the unique gas product with no traces of H_2. This is tentatively attributed to the ligand-based nature of the first reduction of the complexes, which avoids the formation of a low valent Ni complex that would favour the formation of a Ni-hydride and further proton reduction to produce H_2.

Chapter 7. General conclusions

1- Table of content

UNIVERSITAT ROVIRA I VIRGILI
NICKEL AND IRON COMPLEXES FOR ELECTROCHEMICAL REDUCTION OF PROTONS AND CARBON DIOXIDE
Navid Jameei Moghaddam

Glossary of terms and abbreviations

AP	Artificial photosynthesis
TFE	Trifluoroethanol
WO	Water oxidation
CV	Cyclic Voltammetry
DCM	Dichloromethane
DFT	Density Functional Theory
DPV	Differential Pulse Voltammetry
E	Potential
E°	Standard potential
$E_{½}$	Half-wave potential
ESI-MS	Electrospray Ionization Mass Spectrometry
i	Current
HER	Hydrogen evolution reaction
i_p	Current intensity
j	Current density
m/z	Mass-to-Charge ratio
NHE	Normal Hydrogen Electrode
NMR	Nuclear Magnetic Resonance
OEC	Oxygen Evolving Center
PCET	Proton Coupled Electron Transfer
PSI	Photosystem I
PSII	Photosystem II
CO_2RR	Carbon dioxide reduction reaction
WOC	Water oxididation catalyst
GC-TCD	Gas chromatography coupled to thermal conductivity detector
p-TsOH	Para toluene sulfonic acid
TOF	Turnover Frequency
TON	Turnover Numbers
ACN	Acetonitrile
MHAT	Metal hydrogen atom transfer
UV-Vis	Ultraviolet-visible Spectroscopy
XAS	X-ray absorption spectroscopy
XRD	X-ray diffraction
ε	Extinction coefficient
SHE	Standard hydrogen electrode

UNIVERSITAT ROVIRA I VIRGILI
NICKEL AND IRON COMPLEXES FOR ELECTROCHEMICAL REDUCTION OF PROTONS AND CARBON DIOXIDE
Navid Jameei Moghaddam

Chapter 1

General Introduction

Chapter 1. General Introduction

1- Global warming and energy crisis

Increasing population of the world has increased the demand for energy. Since the main energy resource currently used are finite and contaminant fossil fuels there is an urgent need to find alternative, clean and sustainable energy resources. Using fossil fuels as the main energy resource have had adverse environmental impact associated with increasing greenhouse gas emissions to the atmosphere such as carbon dioxide (**Figure 1**).[2,3] Global warming is one of the severe impacts caused by atmospheric composition change from anthropogenic emissions of greenhouse gases, such as carbon dioxide, methane or nitrous oxide. These gases have long atmospheric lifetimes (decades to centuries), the result is an accumulation in the atmosphere and consequently trapping outgoing radiation from the Earth to space. One of the important consequences of the global warming is climate change which can cause rising level of the sea or ocean, droughts, animal extinctions, etc. A recent report by the International Energy Agency (IEA) in 2021 indicates that the world CO_2 annual concentration in the atmosphere has reached 421.5 ppm, which is 50% higher than that since the industrial revolution began.[10] This increase is directly proportional to the utilisation and burning of fossil fuels like coal, gas, oil used by economies around the world. (**Figure 1 bottom**). Noteworthy mentioning that the world CO_2 annual concentration in atmosphere has decreased due to COVID in recent year. Transition from this situation necessitates that the world economies decrease their dependency to fossil fuels as the main energy source and instead developing technologies to produce and utilise carbon free fuels and energy carriers like hydrogen or using renewable energy resources such as wind, Sun, tidal wave, etc. One of the downfalls of renewable energies is that they are intermittent, and they should be captured and stored to be able to use them later. For this purpose, nature uses photosynthesis, a process in which the solar energy photons are captured and their energy stored in the form of chemical bonds of high energy molecules (cellular energy carriers). The process provides an excellent blueprint for renewable energy storage and conversions, so understanding details of the process will help to design systems and develop a technology for alternative, clean and sustainable energy resource to replace the fossil fuels.[1–10] In the next sections, details and requirements for developing different strategies and systems which try to mimic natural photosynthesis under the concept of artificial photosynthesis will be presented and discussed. In this context, catalytic materials able to facilitate chemical

reactions will play an important role to make the process economically viable.

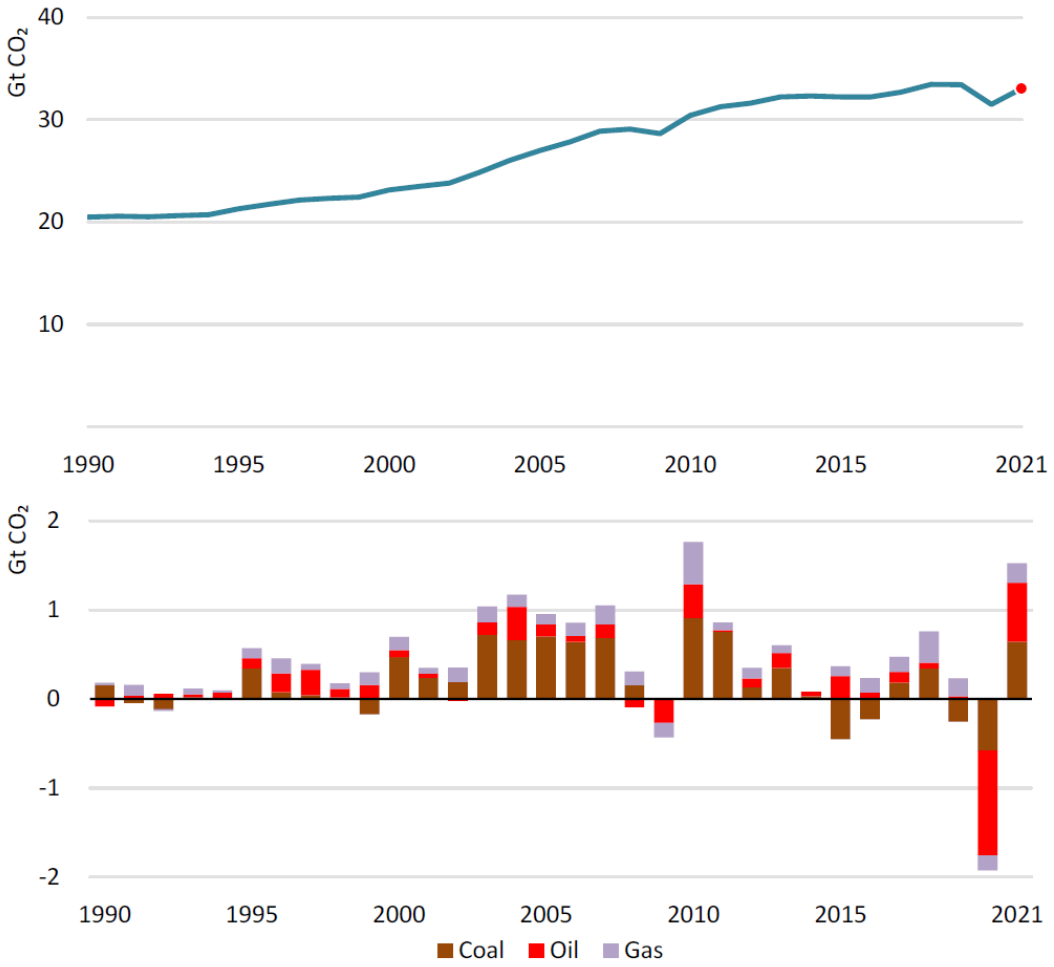

Figure 1- Global energy-related CO_2 emissions, 1990-2021 (**top**), and change in CO_2 emissions by fuel, 1990-2021(**bottom**). [10]

2- Natural and artificial photosynthesis

2.1- Natural photosynthesis

Photosynthesis is a process in which sun's energy is captured and stored as chemical bonds in the form of carbohydrates by some organisms. The process is not only key for providing food and oxygen for most living organisms on earth but also it is necessary for maintaining the level of the oxygen gas on earth. Photosynthetic organisms were among the first organisms to perform energy transformations on the Earth, emerging 3.8 billion years ago. There are two

different types of photosynthesis that have been evolved in organisms; *oxygenic* and *anoxygenic* photosynthesis. This classification has been derived from the utilisation of water as electron donor on each process. In oxygenic photosynthesis water used as electron donor and oxygen is produced as by-product. Plants, algae, and cyanobacteria are doing oxygenic photosynthesis while phototropic green bacteria, phototropic purple bacteria and heliobacteria use anoxygenic photosynthesis.[12,13] In oxygenic photosynthesis organisms, photosynthesis takes place in subcellular structures know as chloroplast. Inside the chloroplast membrane, there are stacks of grana. Each stack of grana structure is called thylakoid which is surrounded by a membrane. The site where photosynthesis takes place is the thylakoid membrane, which contains integral and peripheral membrane protein complexes, including the pigments that absorb light energy, and form the photosystems. Oxygenic photosynthesis is a complicated process that can be divided into five simple steps:

1) Light harvesting
2) Charge separation
3) Electron transfer
4) Energy career production
5) Catalytic water oxidation

The first step of oxygenic photosynthesis is the harvesting of sunlight by the pigments (antenna). Two types of photosystems (PS) exist on the thylakoid membrane; PSI (P700) and PSII (P680), which later transfers excitation energy to reaction centres (RC) through charge separation.[14,15] This step produces the ion-radical pair $P680^+/Phe^-$ where Phe^- is$^-$ (pheophytin) is a chemical compound that serves as the first electron carrier intermediate in the electron transfer pathway of Photosystem II. The electrons are then transferred to PSI via complex electron transfer chains (*vide infra*), while $P680^+$ recovers its electron deficiency by oxidation of tyrosine Yz, which is later recovered by the electron transfer from a Mn_4Ca cluster (see Figure 4). The role of the Mn_4Ca cluster in PSII is to catalyse the conversion of water into molecular oxygen, that is, water oxidation (WO). Electrons derived from WO in PSII are transferred across the photosynthetic electron-transport chain which includes plastoquinone (PQ), Cytochromeb_6f (Cytb_6f), plastocyanin (PC), and PSI to ferodoxine (Fd). Then, $Fd^–$ $NADP^+$ oxidoreductase (FNR) transfers the electrons to $NADP^+$ with the final production of nicotinamide adenine dinucleotide phosphate (NADPH) (**Figure 2**). On the other hand, protons

are released into the thylakoid lumen when water is oxidized. The proton gradient across the thylakoid membrane is used by adenosine triphosphate (ATP) synthase to produce ATP. The ATP and nicotinamide adenine dinucleotide phosphate (NADPH) generated during the primary photosynthetic processes are consumed for CO_2 fixation in the Calvin–Benson cycle, which produces sugars and ultimately starch. Or under anaerobic conditions, hydrogenase can accept electrons from the reduced Fd molecules and use them to reduce protons to molecular hydrogen. Anaerobic conditions also allow starch to be used as a source of protons and electrons for H_2 production (via NADPH, PQ, $Cytb_6/f$, PC, and PSI) using a hydrogenase enzyme.[16,17]

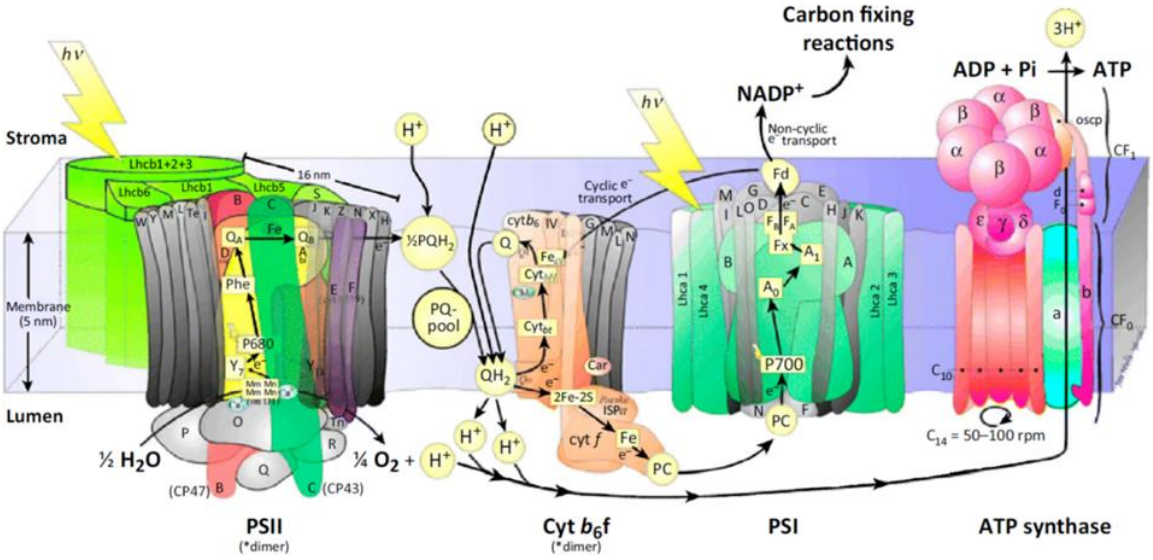

Figure 2- Schematic representation of the thylakoid membrane where transmembrane protein cofactors necessary for the photosynthesis process are embedded.[18]

In 2011, The high-resolution structure of PSII at 1.9Å resolution from the thermophilic cyanobacterium T. vulcanus clearly revealed the structure of the WO catalyst. The results indicated that the catalyst responsible for water oxidation is the arrangement of three Mn atoms and a Ca atom in a cubane structure with one manganese located at the outside of the cube giving the cluster Mn_4CaO_5 stoichiometric formula (**Figure 3**). All the Manganese and Calcium atoms are bridged by five Oxygen atoms in a μ-oxo bridge fashion, and four water molecules are coordinated to the cluster in which some of them can act as substrate for

dioxygen formation.[18–22]

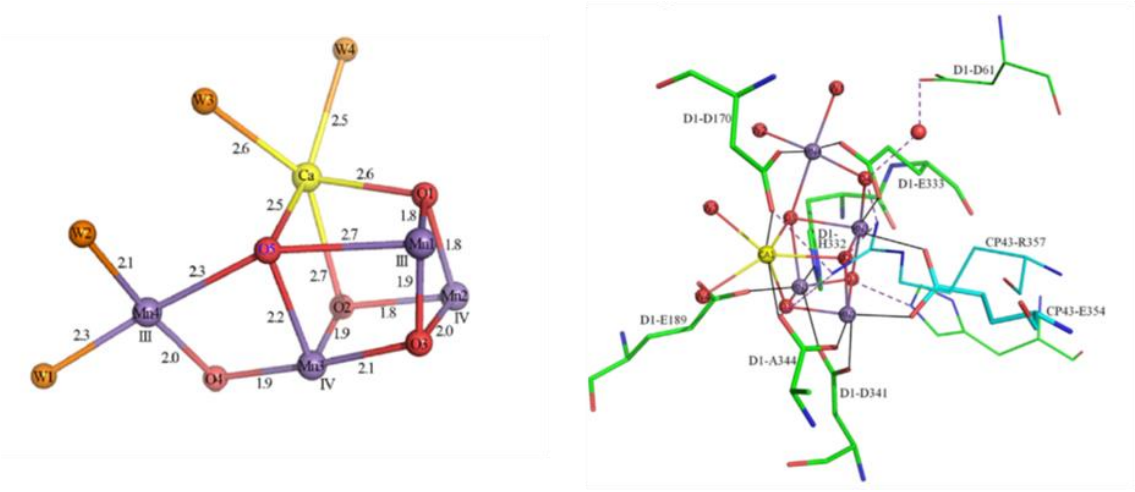

Figure 3- Crystal structure of $Mn_4CaO_5.4H_2O$ cluster at the resolution of 1.195Å (**left**) and the amino acid arrangement around Mn_4CaO_4 cluster in PSII (**right**).

2.2- Artificial photosynthesis

Since natural photosynthesis is a complicated process with complex components' structures, a full mimicking of the process is not possible, and the concept of artificial photosynthesis (AP) has been developed. The main goal of AP, like natural photosynthesis, is capturing sunlight and storing its energy in chemical bonds. For this purpose, AP uses the electrons generated by the water oxidation reaction to reduce CO_2 and protons and convert them to simple organic such as methane, methanol, ethanol, etc, and also hydrogen gas. All these energetic compounds (fuels) would be key energy carriers for a new energetic paradigm. For developing technologies base on AP, the following components are required:

1) A compound/material for sunlight's photons absorption and formation of charge-separation states.
2) A catalytic molecule/material active in the water oxidation reaction to generate oxygen, mimicking the $Mn_4CaO_5.4H_2O$ cluster.
3) A catalytic molecule/material active in the fuel generation reaction, either CO_2

reduction (CO_2RR) or hydrogen evolution reaction (HER).

All the above components should be combined to build devices, which can be divided in two general configurations, although hybrid systems combining features of both have also been described and are currently under investigation.

1) **Photovoltaic electrolyser (PVE)**

   A photovoltaic solar cell absorbs the photons from sunlight and converts them to electrical current which can be used to perform electrocatalysis with an appropriate catalytic system on the anode and cathode to mediate water oxidation and fuel production, respectively (**Figure 4**, left).[14]

2) **Photoelectrochemical cell (PEC)**

   In this kind of devices, semiconductors (alone or in combination with molecular photosensitizers) are responsible for light absorption and charge separation. The chemical reactions (water oxidation and fuel production) are taking place at catalytic centres at the surface of the same photoelectrodes (**Figure 4**, right).[23–25]

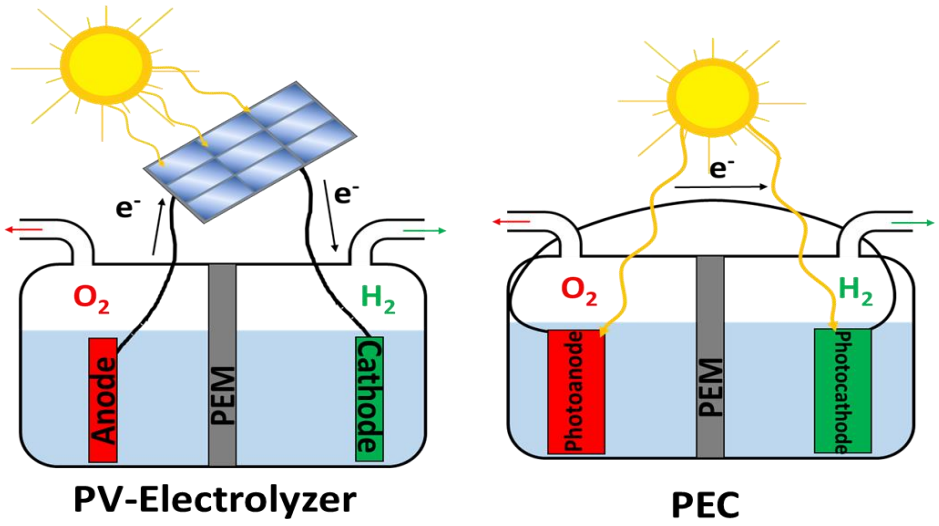

Figure 4- Schematic representation of two configurations of artificial photosynthesis devices; PVE (**Left**) and PEC (**Right**).

This thesis is focused on the development of molecular catalytic centres to perform the chemical reaction that produce fuel from CO_2 and/or protons. Thus, in the next sections, details

on the chemistry of CO_2 and hydrogen, as well as a revision of reported molecular catalysts that are active in the catalytic conversion of CO_2RR and HER will be given.

3- Chemistry of Carbon dioxide

Carbon dioxide is a linear and symmetrical molecule with $D_{\infty}h$ symmetry. Its symmetry gives this molecule nonpolar character but at the same time it has dipole momentum because of the difference in electronegativity between C and O and it can be viewed as "$O^{\delta-}$-$C^{2\delta+}$-O^{δ}". This structure shows that this molecule is susceptible to interact with electrophiles via its oxygen atoms and nucleophiles via its carbon atom (**Figure 5**, right). Moreover, qualitative MO diagram of the CO_2 molecule shows that the LUMO orbitals energy is near to that of carbon atom and is another evidence for the ability of this molecule to interact with nucleophiles via its carbon atom. In addition nonbonding orbitals have oxygen atom characteristic and make these molecule susceptible to interact with electrophiles through O (**Figure 5**, left).[26–28]

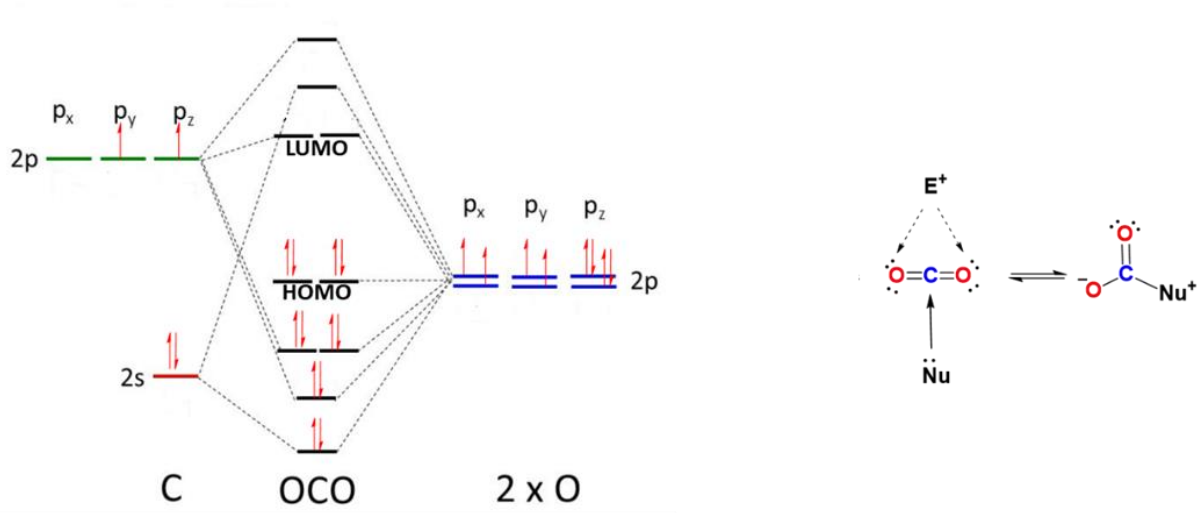

Figure 5- qualitative MO diagram of CO_2 (**left**) and potential reactivity positions on CO_2 molecule (**right**). $\mathbf{E^+}$ = Electrophile, **Nu** = Nucleophiles.

4- Hydrogen

Hydrogen atom is the most abundant element in the universe, it is found in our planet mainly in water and organic compounds. It is the lightest and simplest element, which consists of one electron and one proton. This element has three isotopes in nature ^{1}H (99, 98%), ^{2}D, ^{3}T and can be found in combination with other elements like carbon and oxygen. Molecular hydrogen

(H_2) is nontoxic, odorless, colorless, highly flammable, lighter than air and nowadays can be stored in different states of the matter such as liquid and gas. Being lighter than air, it dissipates in the air and lacks odor making it hard to be detected upon leakage. Its low ignition point causes that additional protection to be considered while usage and transportation.

Hydrogen has gained attention in recent years as a second energy carrier besides fossil fuels. Hydrogen can be used as fuel in almost any application, where fossil fuels can be used. This energy carrier has many advantages over fossil fuels. First, hydrogen has higher heating value than common liquid hydrocarbons like gasoline as well as better energy density by weight in gas form than normal hydrocarbons.[22,23] However, it has poor volumetric energy density in both gas and liquid forms and needs bigger tanks to be stored. Second, if hydrogen is produced from renewable energies, it is considered as zero-carbon-emission energy at the production and use points (Green hydrogen) and thus considered an environmentally friendly energy carrier. Third, hydrogen has a high energy capacity (120 MJ/L) which is about three times more than prevalent fossil fuels like natural gas.[25] These properties along with others, make hydrogen one of the potential candidates for the partial replacement of fossil fuels in the future in the so-called post-fossil fuel age.

Nowadays hydrogen is used in different industrial production such as ammonia and other nitrogenized fertilizers, as well as in the preparation of alternative fuels for instance by the Fischer–Tropsch (FT) process. It can be used in fuel cells to produce electricity upon reaction with oxygen producing water as by product.

There are a lot of pathways and technologies for hydrogen production varying in feedstock materials, energy sources and catalyst materials. Today industrially, 96 % of hydrogen is produced by *steam reforming*, a well-established technology to extract hydrogen from fossil fuel stocks, and another 4 % of hydrogen is produced from water *electrolysis*.[22-26] In this technology, water is split into oxygen and hydrogen using electric current. Pathways and technologies employed for hydrogen production are highly dependent on the scale of the hydrogen production, degree of the clean hydrogen produced (low carbon emission or purity of the hydrogen), availability of the feedstock materials and energy sources that can be used. Moreover feasibility, cost-effective and efficiency of the technologies used are important parameters for reaching future possible hydrogen economy. For reaching this goal, catalytic

materials used in different technologies play an important role because they increase hydrogen production efficiency and cost effectiveness. Hence, finding efficient, low cost, robust catalysts for new emerging technologies such as artificial photosynthesis for producing hydrogen are necessary.

5- CO_2 reduction reaction

Carbon dioxide is a thermodynamically and kinetically stable molecule, thus the activation of the molecule requires overcoming high activation energy barriers, mainly for C=O dissociation which requires 230 J/mol .[27] **Table 1** indicates the electrochemical energy required for direct CO_2 activation at pH=7 vs SHE. The data clearly indicates that this energy depends on the number of electrons and protons associated with the process as well as in the formation or not of new C-C bonds. Using catalytic systems to facilitate these reactions, not only allow to overcome activation barriers and make the activation of this molecule feasible and the process economically viable but also to avoid the formation of high energetic intermediate species like radical anions that lead to side-reactions.[27] Another clear feature arising from **Table 1** is the selectivity problematic for the CO_2 reduction reaction taking into account the large variety of products that can be formed. In this context, catalysts also play a key role in allowing to favour

Table 1-Standard redox potentials for CO_2 reduction in aqueous solution.

Reduction process	E^0(vs SHE V Ph=7)
$CO_{2(g)} + 2H^+_{(aq)} + 2e^- = HCOOH_{(aq)}$	**-0.25**
$CO_{2(g)} + H_2O_{(l)} + 2e^- = HCOO^-_{(aq)} + OH^-_{(aq)}$	**-1.08**
$CO_{2(g)} + 2H^+_{(aq)} + 2e^- = CO_{(g)} + H_2O_{(l)}$	**-0.11**
$CO_{2(g)} + H_2O_{(l)} + 2e^- = CO_{(g)} + 2OH^-_{(aq)}$	**-0.93**
$CO_{2(g)} + 4H^+_{(aq)} + 4e^- = CH_2O_{(l)} + H_2O_{(l)}$	**-0.07**
$CO_{2(g)} + 3H_2O_{(l)} + 4e = CH_2O_{(l)} + 4OH^-_{(aq)}$	**-0.90**
$CO_{2(g)} + 6H^+_{(aq)} + 6e^- = CH_3OH_{(l)} + H_2O_{(l)}$	**+0.02**
$CO_{2(g)} + 5H_2O_{(l)} + 6e^- = CH_3OH_{(l)} + 6OH^-_{(aq)}$	**-0.81**
$CO_{2(g)} + 8H^+_{(aq)} + 8e^- = CH_{4(g)} + 2H_2O_{(l)}$	**+0.17**
$CO_{2(g)} + 6H_2O_{(l)} + 8e^- = CH_{4(g)} + 8OH^-_{(aq)}$	**-0.66**
$2CO_{2(g)} + 2H^+_{(aq)} + 2e^- = H_2C_2O_{4\,(aq)}$	**-0.50**
$2CO_{2(g)} + 2e^- = C_2O_4{}^{2-}_{(aq)}$	**-0.59**
$2CO_{2(g)} + 12H^+_{(aq)} + 12e^- = CH_2CH_{2(g)} + 4H_2O_{(l)}$	**+0.06**
$2CO_{2(g)} + 12H^+_{(aq)} + 12e^- = CH_3CH_2OH_{(l)} + 3H_2O_{(l)}$	**+0.08**

Chapter 1. General Introduction

In nature, there are two types of metalloenzymes that can catalyse CO_2 to CO reversibly:

1) NiFe-CO dehydrogenase [NiFe] CODH
2) MoCu-CO dehydrogenase [MoCu] CODH

The first class of metalloenzymes [NiFe] CODH are air sensitive and can be found in organisms like *Moorella thermotactic*, *Carboxythermus hydrogenoformas* and *Methanosarcina bakerii*. These organisms are using the [NiFe]CODH active site for reversible conversion of CO_2 to CO. The enzyme is highly active with turnover frequency (TOF) of 4000 $0s^{-1}$ for CO oxidation at 70 °C and 45 s^{-1} for CO_2 reduction and operates close to the thermodynamic potential of the CO_2/CO reduction couple (-0.11 V vs. SHE at pH =7) with almost zero over-potential. The second class of CODHs active sites are air stable [Mo-S-Cu] containing enzymes found in aerobes such as *Oligotrophs carboxidovorans*. These enzymes show lower CO oxidation activity (TOF 100 s^{-1}) compared to NiFe analogues and do not show any CO_2 reduction activity.

The crystal structure of [NiFe] CODHs indicates that the structure of the active site is composed of one Ni and one Fe atom (**Figure 6**, right). The two metal centres are bridged by a Fe_3S_4 cluster which binds these two atoms rigidly and near to each other. The proximity of the two atoms enables them most likely to cooperative interact during catalysis. The Ni centre binds to two S atoms in planar T-shaped geometry, and the first coordination of the Fe centre consists of a histidine ligand, a cysteine, a μ_3-sulfido ligand and the fourth ligand which is most likely is water or hydroxide.

The crystal structure of [MoCu] CODH shows a Mo atom in a square pyramidal geometry in the first coordination sphere. Moreover, a Cu atom is connected to Mo through a sulphido bridge. In addition to the bridging S atom, two sulphur atoms of cytosine dinucleotide cofactor coordinate to the Mo ion and the hydroxide ion complete the metal coordination sphere (**Figure 6**, left). [29–33]

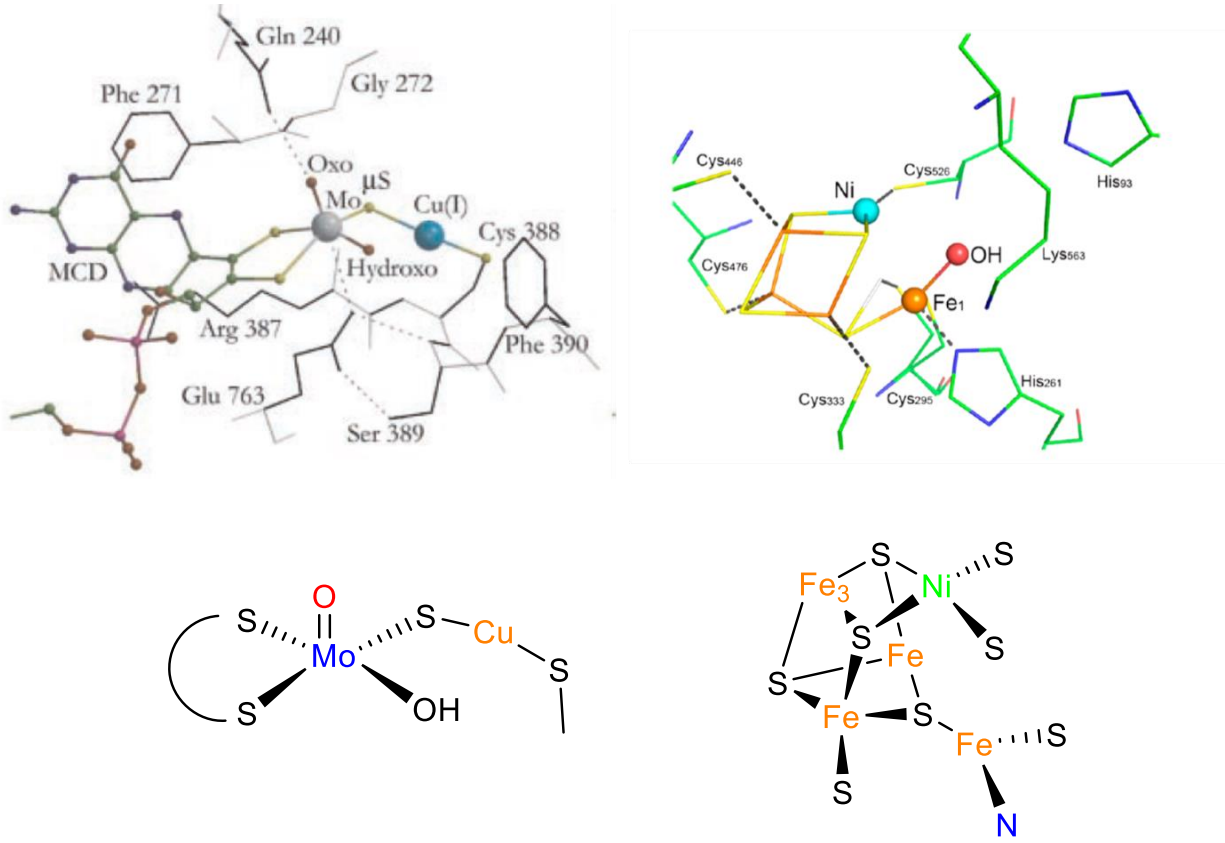

Figure 6- Active site of [Mo Cu]CODH (**left**) and [NiFe] CODH) (**right**) with amino acid arrangement around them.[32,33]

5.1- Molecular catalysts for the CO_2 reduction reaction (CO_2RR)

Inspiring from enzymatic active sites, lots of efforts have been devoted to the synthesis of homogenous and heterogeneous catalysts with non-noble metals for the CO_2 reduction reaction. For this purpose, first-row transition metals, in particular Fe, Co and Ni, have been in the focus recently. These catalysts have been applied for CO_2 reduction via different methodologies such as photochemical, electrochemical, and sacrificial chemical approaches. Regardless of the methodology employed, the role of the catalyst has been key to increase the kinetics and product selectivity of the process. In the case of electrochemical CO_2RR the catalyst avoids the formation of the CO_2 radical anion intermediate caused by direct reduction of CO_2 on the surface of the electrode, in addition to minimize the over potential for the overall process. In the next sections, a selection of state-of-the-art non-noble metal complexes for electrochemical CO_2 reduction is discussed divided according to the metal active centre.[17,34–37]

5.1.1- Cobalt based catalysts

One of the pioneering investigations for electrochemical CO_2 reduction by Cobalt coordination compounds was performed by Toshima et.al in 1977 using tetra sulfonated phthalocyanine Cobalt complex **Co-5** (**Figure 7**). The group successfully decreased the over potential of CO_2 reduction about 0.2V to 0.4 V at 1 mA/cm^2 by addition of the catalyst to a CO_2 saturated solution in aqueous media. The group postulated that the reduction process consists of two steps; first the formation of a coordinated CO_2 complex and second an electron Cobalt quatropyridine complex **Co-2** in **Figure 7** was studied by Robert *et.al.* in acetonitrile solution, in the presence of phenol as proton source. In their investigations an intense catalytic peak appeared upon adding CO_2 to the solution of the complex in cyclic voltammetry experiments (40 times more than that observed in the absence of any substrate or acid source). Controlled-potential electrolysis at 140 mV over potential together with Gas Chromatography coupled to thermal conductivity detector (GC-TCD) analysis confirmed that the peak is related to the CO_2 reduction to CO with a 94% faradic efficiency and 96% selectivity and turnover number (TON) of 17. By applying a slightly more negative potential (-1.3 V vs. SCE, 340 mV over potential), the same selectivity for CO was obtained with 87% FE with a TON of 64 after 8 hours electrolysis (0.68 mA/cm^2).[39]

Artero *et. al.* synthesized a family of complexes with the formula **Co-8** based on a κ^2-P_2 bidentate ligand $P^R{}_2N^R{}_2$ ($P^R{}_2N^R{}_2$= 1,5-diaza-3,7-diphosphacyclooctane where R= cyclohexyl, Benzyl, phenyl) with different substitution and two pendent amines, which were believed to act as proton relay. Most of the complexes were active for CO_2 reduction to formic acid with high faradic efficiency and selectivity. However, they suffered from long-term stability. All the catalysts showed potential dependent turnover frequency and turnover number over a range of applied potential E_{app} = -2-2.25 V vs $Fc/Fc^{0/+}$ in control potential electrolysis experiments. Among the series of catalysts, **Co-8.**1 showed higher catalytic activity with TON = 23 in the presence of 1.1 M of H_2O. Complex **Co-8**.4 showed lower catalytic activity with TON = 1.5 in 5.6 M H_2O and faradic efficiency of 38% for formic acid formation along with 67% for hydrogen production using mercury electrode as working electrode. This change in activity was attributed to the change in the substitution on the phosphorous and nitrogen atoms of the ligand backbone and was in agreement with low electron density of phosphine ligand. Density Functional Theory (DFT) calculations support the production of a Co^{II}-H species during

catalysis, which is involved in both proton and CO_2 reduction. Moreover, a prominent role of the pendant amine groups in the second coordination sphere of the complexes was elucidated to not only making hydride transfer thermodynamically favorable but also H-bond stabilization of the [Co-$HCOO^-$] intermediate with amine bonded water molecule.[40]

In 2016 Chapovetsky *et. al.* synthesized macrocyclic amino pyridine cobalt complexes of the type **Co-7** in **Figure 7**. These complexes were inspired by previous successful reports based on the presence of amines or hydroxyl groups in the second coordination sphere as well as the presence of the amino acid residuals in second coordination sphere of the [NiFe] CODHs enzyme. Cyclic voltammetry experiments of **Co-7**.1 showed increased current near to the $Co^{I/0}$ peak position (-2.75 V vs $Fc/Fc^{0/+}$) in the presence of the CO_2 and methanol or trifluoroethanol (TFE) as proton source, and glassy carbon electrode as working electrode in organic media. The origin of the increased current was confirmed as the CO_2 to CO reduction by controlled potential electrolysis experiment, together with detection of the products by GC-TCD. Moreover, the catalysts showed moderate stability (2h) for CO_2 reduction in control potential experiments with TOF and TON calculated to be 170 s^{-1} and 1.22×10^6 respectively with 98 % faradic efficiency for CO production for complex **Co-7.**1. To test the effect of the pendant amine on the catalytic activity of the complexes, **Co-7**.2 and **Co-7**.3 were synthesized and their electrochemistry investigated under the same experimental conditions as **Co-7**.1. The study showed not only a shift in the peak position of the catalytic wave of the new complexes as expected for substitutions with electron-donating groups such as methyl but also a decrease in TOF, TON and faradic efficiency of the complexes. This phenomena on substituted complexes is attributed to the lack of the stabilization of coordinated CO_2 by the intramolecular H-bond, which is caused by the presence of pendant amine in second coordination sphere of the **Co-7.**1. Later, DFT calculations showed that pendant amine does not directly transfer proton to coordinated CO_2 but instead binds to the acid in solution. This pendant amine facilitates the H-bond transfer network which enables direct proton transfer from acid to activate CO_2.[40–42]

Cobalt terpyridine complex **Co-3** in **Figure 7** was synthesized by Fontecave group in 2014. Cyclic voltammetry of the complex in DMF showed two reversible peaks which were attributed to the metal center $Co^{II/I}$ and ligand-based reduction processes ($tpy/tpy^{\cdot -}$), respectively. Control potential electrolysis experiments of the complex in the presence of the 5% H_2O and CO_2 showed the formation of H_2 and CO with sustained current for 3h and faradic efficiency of 17

% were calculated (12 (CO) and 5 (H_2)). The authors attributed the low faradic efficiencies for CO_2 reduction to the decomposition of the ligand involved in the electroreduction.[43,44]

Complex **Co-6** synthesized by Dey *et. al.* was submitted to electrochemical investigation in the presence of wet acetonitrile. Cyclic voltammetry experiments of the complex showed an increase in the current at the $Co^{II/I}$ peak position in the presence of CO_2. The origin of the increased current determined by control potential electrolysis and detection of the gas produced in the headspace of the cathodic side of the cell by GC-TCD was determined to be due to CO_2 to CO reduction. The complex showed moderate stability for 2h using glassy carbon (GC) electrode while a slight decay on the catalytic current was observed when a Hg-pool electrode was used, which was attributed to the high affinity of the thiol group to be adsorbed on Hg electrode surface. From electrochemical investigation group, conclude that protonation is the rate-determining step of the reaction. DFT calculations were used to support mechanistic elucidation. This study showed discoordination of one of phosphine arms upon CO_2 coordination and protonation of the thiolate in the presence of both H_2O and CO_2.[45]

Cobalt β-diketiminate complex **Co-4** reported by Holland group in 2019 was also shown to be active in the stoichiometric reduction of CO_2. They described a detailed analysis and the mechanism of the reaction. The cobalt(I) complex **Co-4** reacts with CO_2 yielding two products derived from C–O bond cleavage; the cobalt(I) monocarbonyl complex $L^{tBu}Co(CO)$ and the dicobalt(II) carbonate complex $(L^{tBu}Co)_2(\mu\text{-}CO_3)$, where L^{tBu}= 2,2,6,6-tetramethyl-3,5-bis[(2,6-diisopropylphenyl)imino]hept-4-yl.[46] More details on the family of β-diketiminate complexes used in CO_2RR and HER is given in Chapter 3 of this thesis.

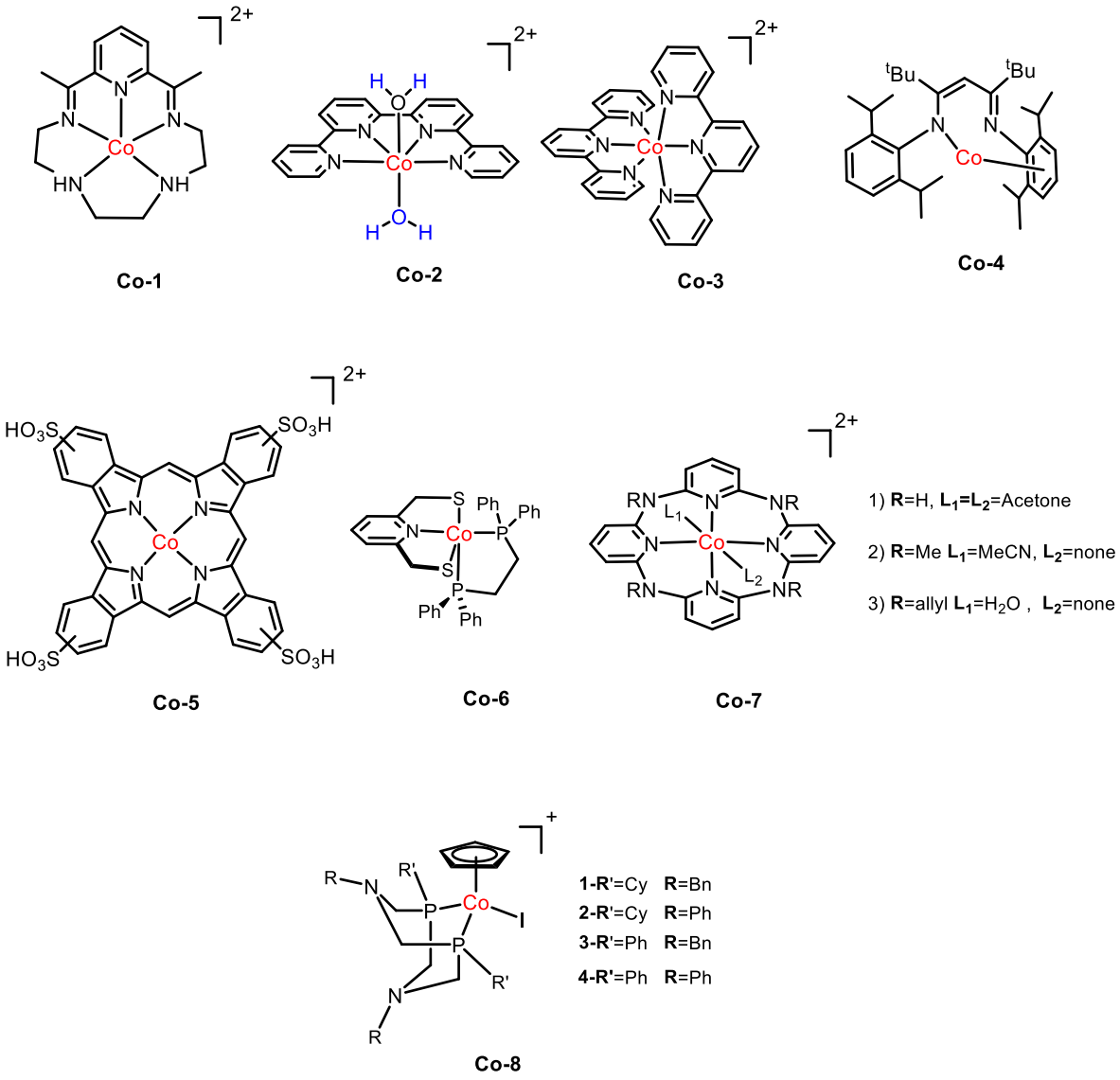

Figure 7- A selection of cobalt based molecular catalysts discussed in this chapter.

5.1.2- Iron base catalysts

Iron porphyrins is one of the most studied and successful candidate fir CO_2 reduction. The coordination compound base on iron porphyrin was introduced for first time in 1977 by Katsuhiro et.al, later, Saveant et.al studied the mechanism and activity of this family of the complexes in different media in prescence of weak Bronsted and Lewis acids. Iron porphyrins complexes **Fe-1** and **Fe-2**, when electrochemically reduced to the Fe^0 species, are among the most efficient molecular catalysts for the CO_2-to-CO conversion in aprotic solvent (DMF,

ACN), in terms of both efficiencies, catalytic rate and robustness.[47–50]

Robert et al. studied iron and Iron quatropyridine complexes **Fe-3 and Fe-4** for CO_2 to CO reduction reaction in prescence of phenol or TFE as proton source and glassy carbon as working electrode. Cyclic voltammetry of the complex showed increase in current intensity in $Fe^{II/I}$ peak position in prescence of the CO_2 and phenol as proton source along with appearance of the new peak upon back ward scan after catalytic wave. Author found this peak match with the oxidation peak upon purging the catalyst solution with CO. the nature of the increased current showed it is belonged to catalytic CO_2 to CO with high selectivity. To shed light to mechanistic pathway of the complex IR, UV (SEC) and DFT calculation were used. Calculation and experimental data had good agreement with each other, and all confirmed the formation of the $[Fe\ (qpy)\ CO]^0$ inactive adduct in catalytic cycle Moreover, group managed to increase the faradic efficiency to 70%, TON=12 with 100% selectivity for CO production by using visible light irridation (λ>420 nm) in conjunction with electrolysis(**Figure 8**).[39]

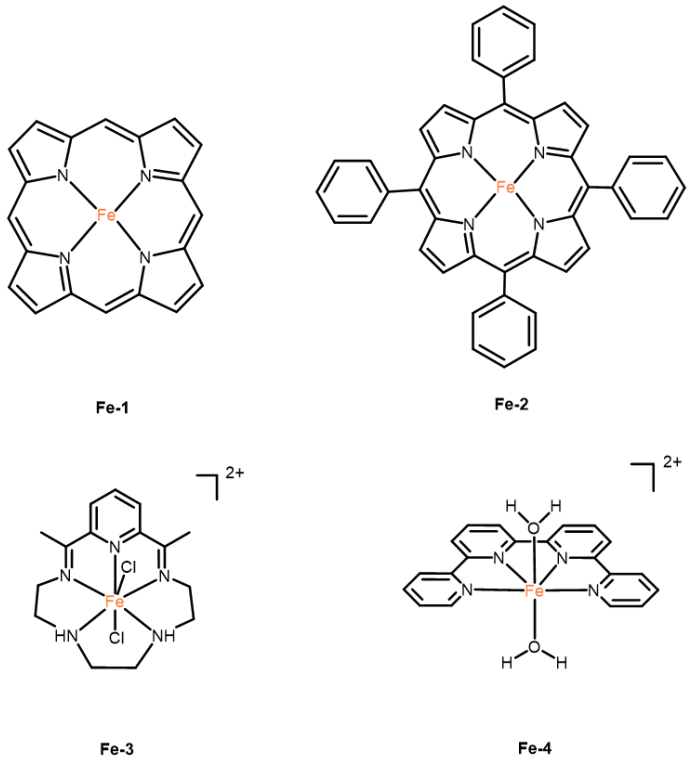

Figure 8- A selection of Iron based molecular catalysts discussed in this chapter.

5.1.3- Nickel based catalysts

One of the pioneering works on CO_2 reduction catalysis using first row metal complexes as catalysts were performed by Eisenberg et al in 1980 with series of the tetraazamacrocyclic Nickle **Ni-1** and **Ni-2** and Cobalt complexes. The importance of this paper was not only for its pioneering work with using non porphyrinic complexes but also Eisenberg for the first time in this paper, describe an indirect electrochemical reduction of CO_2 which involves the initial reduction of metal complexes and their subsequent reaction with CO_2. This approach facilitates reducing CO_2 at potentials near to the thermodynamic values. The metal complexes are thus redox-activated catalysts. Complexes showed electro reduction of the CO_2 to CO with high faradic efficiency accompanied by H_2 production in wet acetonitrile. Despite their high faradic efficiency and stability, complexes showed low turnover frequency.[51,52]

In 1984 Sauvage introduced complex **Ni-3** (1,4,8,11-tetra-azacyclotetradecane) Nickel (II) $[Ni^{II}(cyclam)]^{2+}$ as a selective electrocatalyst for the reduction of CO_2 to CO, in aqueous media, on the complex showed CO production with 99% selectivity, Max turnover number of 116 and turn over frequency of the $32h^{-1}$ the surface of the mercury electrode. Moreover, complex showed superior activity compared to its unsaturated or open cycle complexes. The complex after this pioneering work has gained lots of interest and studied with different research groups on various conditions and mediums.[53]

Complexes **Ni-4**,**Ni-5** and **Ni-6** have been developed by Jurss et.al g for electrochemical CO_2 reduction .The nickel complexes are competent, homogeneous electrocatalysts that operate with 100% overall Faradaic efficiency with no sign of deactivation. A structure–function relationship regarding catalytic activity and selectivity has been elucidated for the closely related 2,20 -bipyridine derivatized NHC ligands via electrochemical experiments. Their results showed a clear macrocyclic effect on catalytic activity across the series NHC ligands where increased rigidity of the redox-active macrocycle leads to enhanced selectivity for CO_2 reduction over the competing proton reduction reaction (HER). Their studies revealed importance between the metal and redox-active ligand that dictates the reaction pathway and highlights the importance of electronic structure of the resulted complexes development of the complexes.[54]

Complex **Ni-7** was introduced by Fontecave et.al Inspired by the metal active sites of formate dehydrogenase and CO-dehydrogenase, the Nickel complex contains a NiS_4 motif with two dithiolene ligands (quinoxaline-pyran-fused dithiolene ligand, **qpdt^{2-}**) mimicking molybdopterin present in the active site of formate dehydrogenase and CO dehydrogenase. the complex used for electrochemical CO_2 reduction reaction. During electro reduction, the complex showed an O_1-C_2 bond cleavage of the pyran ring upon a 4-electron reduction of the dithiolene ligand then the resulted complex catalyzes the reduction of CO_2 into formate as the major product, together with minor amounts of carbon monoxide and hydrogen, with reasonable overpotential requirement, good faradaic yield, and notable stability. Catalysis operates well on mercury electrode compared to glassy carbon electrode, as observed in the case of $[Ni(cyclam)]^{2+}$ complexes. Density functional theory (DFT) indicated the key role of a Ni(III)-hydride intermediate and provide insights into the different reaction pathways leading to HCOOH, CO, and H_2. This study opens the route toward a new, yet unexplored, class of mononuclear sulfur-coordinated Ni catalysts for CO_2 reduction (**Figure 9**).[55]

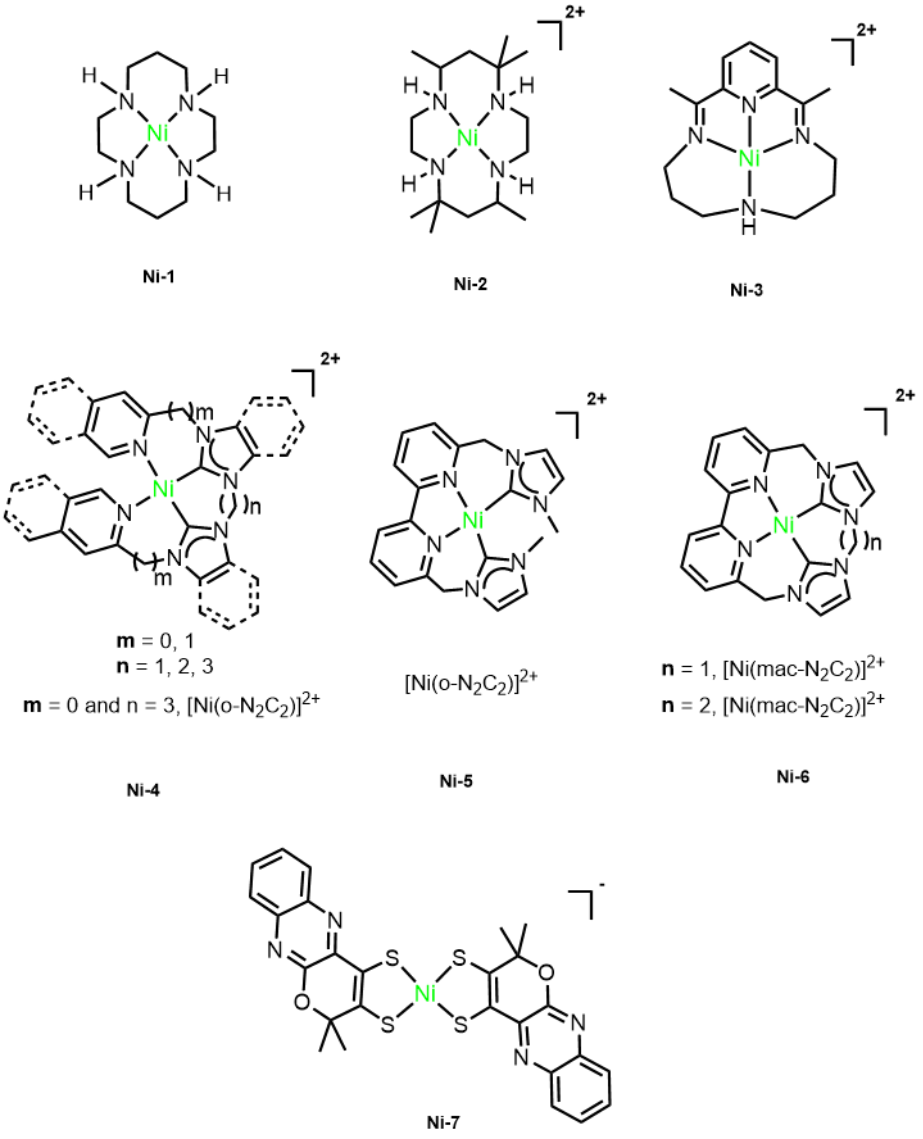

Figure 9- A selection of state -of- the -art molecular catalyst discussed on this chapter.

5.1.4- Mechanism of CO_2 reduction by molecular catalysts

As we discussed earlier, reduction of CO_2 to value-added compounds is highly depends on the number of electrons used in the reaction, consequently wide variety of compounds is produced in which most of the can have specific reaction mechanisms. Since most of the literature reports on CO_2 reduction reaction suggest $2e^-/2H^+$ catalysis of CO_2 to CO or HCOOH using molecular catalysts. herein we discussed the possible reaction pathways for production of this compounds because some of these steps can be common for production of other

compounds. The key challenge for CO_2 reduction is: **1**) The binding of CO_2 to a metal centre via the C atom instead of the more Lewis acidic O atom **2**) Weakening (activating) the strong C-O bonds by back bonding into the C-O π^* orbitals.[45] in general CO_2 reduction by molecular catalyst can be categorised to following steps.

1) The first step in activation of carbon dioxide by molecular Catalysts is the coordination of the of Carbon dioxide to the metal center, which determines reactivity of the catalysts for CO_2 reduction reaction. The coordination mood of the CO_2 to the metallic center determines expected product of the catalysis. For example, in the case of the HCOOH production metal hydride intermediate is involved in coordination of the CO_2 to the metallic center or in other cases, CO_2 coordinates via one of the oxygen molecules or carbon atom directly to the metallic center.

2) Second Step in activation of the CO_2 , is the weakening of the C-O bond with π-back donation to the C-O π^* orbitals. This parameter highly depends on the d-orbitals electron density of the metallic center. High-energy d-orbitals can achieve by reducing the metallic center to the low oxidation states.

3) Third step for CO or HCOOH production is the protonation of M-COO^- /M-$HCOO^-$ intermediate in which in case of CO production protonation should cause C-O bond cleaveage

4) Last step is dissociation of M-CO/M-HCOOH bond and release of resulted product.[27,45,49,56–59]

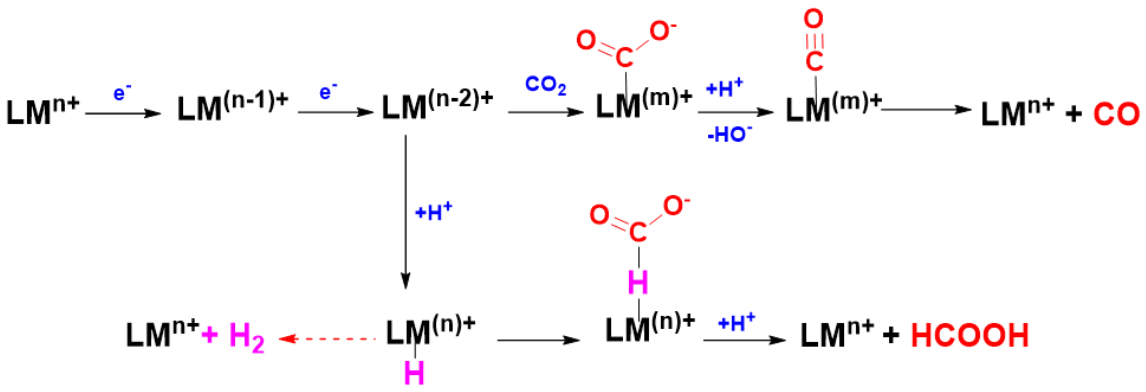

Scheme 1- General scheme for reduction of CO_2 to CO and COOH by molecular catalyst.

6- Hydrogen Evolution Reaction (HER)

The formation of one molecule of H_2 from water (or protons) is a simple reduction reaction which only requires two electrons and two protons. The kinetic and thermodynamic barrier for the reaction is small (0V at pH=0, 1 atmosphere and 298.15 K) compared to CO_2 or other reduction reactions. However, to perform the reaction even at fast rates and near thermodynamic potential, catalytic systems is required. For this purpose, platinum (Pt) and other noble metals has been used as excellent catalysts for electrolytic H_2-evolving reaction (HER). however, the development of earth-abundant electrocatalysts is necessary to process becomes economically viable.[60–62]

In nature, hydrogen production is catalysed reversibly by hydrogenase enzymes. These metalloenzymes are found on bacteria, archaea, and eukaryotes. So far, three class of hydrogenase enzymes has been found on nature which are classified based on composition of their metal center used on their active sites on three families. **1**) [FeFe] hydrogenase **2**) [NiFe] hydrogenase **3**) [Fe]-only hydrogenase. The structure of active site of [FeFe] hydrogenase contains two iron atoms in which each of the iron atoms is coordinated by one CO and one CN^- atom both in terminal binding mode. Two dithiolene ligands and one CO ligand bridge connected two iron metal centers to each other which completes the coordination sphere of the active site. One of the interesting structural aspects of this active site is the prescence of pendent amine on azadithiolene ligand. The pendent amine is in proximity of distal iron atom (Fe_d) which is believed that assists in heterolytic cleaveage of H_2. Another class of the active sites

like its counterpart has two metal center one Nickle atom and one iron atom. In [Ni Fe] hydrogenase, the Nickle atom is coordinated by four cysteinate-sulfur atoms, two of which bridge to the iron atom and the other ligands coordinated to iron atom are cyanide and carbon monoxide. The third class of the hydrogenase enzyme unlike its counterparts contains just one meal center (Fe) and like other active sites is coordinated by carbon monoxide ligands. This class of the hydrogenases unlike other active sits does not catalyse redox reaction of H_2 or protons reversible to each other. The enzyme contains [Fe]-only hydrogenase is called HMD and catalyses reversible transfer of a hydride from H_2 to the methanogenic cofactor methenyl tetrahydromethanopterin, reducing it to methylene tetrahydromethanopterin (**Figure 10**).[63–69]

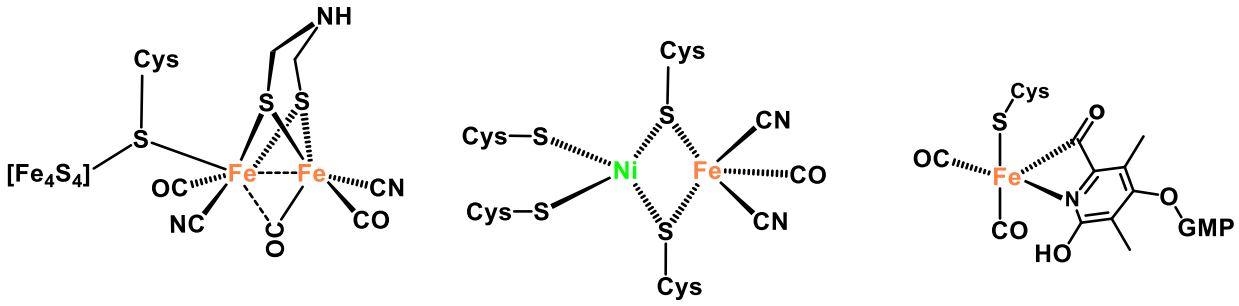

Figure 10- Structure of active sites on hydrogenase enzymes. [FeFe] hydrogenase (**right**), [NiFe] hydrogenase (**middle**) and [Fe] only hydrogenase (**left**).

6.1- Molecular catalysts for proton reduction reaction

Recent years have witnessed development of wide variety of coordination compounds based on first row transition complexes with different ligand Scaffolds for hydrogen production in aqueous or organic mediums in prescence of different proton sources using different methods such as photochemical or electrochemical technics. In this regard Nickle and Cobalt complexes has been most successful metal centers .Even though Cobalt is not used in the structure of the hydrogenase enzyme active sites, cobalt complexes are one of the most prevalent and studied metal complexes with different ligand back bones for hydrogen evolution reaction. Metal complexes for hydrogen evolution goes through production of metal hydride intermediate in which in the next step this intermediate can undergoes hydrogenation/ hydride coupling via

different pathways (homolytic or heterolytic) for hydrogen evolution.[62,70,71] Here in some of the state-of-the-art Cobalt and Nickle complexes for hydrogen evolution catalysis (**HEC**).

Complex **Co-9** is the first Cobalt based molecular catalyst for HEC which was introduced by Fisher and Eisenberg in 1980. Even though the catalyst was used for CO_2 reduction reaction in 2:1 water: acetonitrile mixture and pure water, its ability to produce hydrogen with high faradic efficiency nominated it as efficient proton reduction catalyst. The catalyst was able to produce H_2 from protons with 80% of Faradaic efficiency at -1.26 V and -1.36 V vs NHE on a Hg pool electrode.[14]

Dimethyl glyoxime is another class of the ligand scaffolds for synthesis of coordination compounds for hydrogen evolution reaction. Cobalt macrocycles based on Dimethyl glyoxime are called cobaloximes which has gained resurgence of interest over past decades because of their ease of synthesis and high catalytic activity for hydrogen production. The first Cobaloxime complexes $Co(dmgBF_2)_2(L)_2$ (**Co-10**, $dmgBF_2$) difluoroboryl-dimethylglyoxime) was reported by Connelly and Espenson in 1986. The complex was used for proton reduction in aqueous media in prescence of Cr^{2+} as stoichiometric electron donor. Later other related cobaloxime complexes **Co-11** and **Co-12** was used as electrochemically or photochemically for hydrogen production in different medias.[60,72–75]

Polypyridine ligands are another family of the ligand scaffolds used for synthesis of complexes for proton reduction reaction. The polypyridine complexes has two features compared to other ligand back bones; **1**) they can stabilize the low oxidation state of the metal center and consequently can shift the redox potential of the metal center to positive potentials consequently less overpotential will be necessary for catalysis **2**) since the polypyridine ligand back bones are redox active, they can induce ligand assisted hydrogen production. the first example of Co (II) poly pyridine (PN_4) complex for proton reduction reaction (**Co-13)c** was reported by change et al in 2010. the ligand was designed to stabilizes the metal center in low oxidation state and at the same time leaving one vacant site for coordination of the substrate. The resulted cobalt complex showed activity for proton reduction reaction at 400mV overpotential in prescence of TFA as proton source in 50% aqueous media. Later, the complex was inspiration for other research groups and lots of groups tried to enhance the catalytic activity of the complex by changing of the substitution on ligand back bone **(Co14)**.[76,77]

Another successful example of complexes was molecular cobalt complexes containing a tetraazamacrocyclic containing of a pyridine and two imines groups **(Co-15)**. The synthesis of the complex for first time reported by Brush and Long in 1970 while it was used for proton reduction reaction by Lauet.al. The electrocatalytic activity for proton reduction was examined in acetonitrile and aqueous solutions using p-cyanoanilinium and acetic acid as a proton source, respectively, with high Faradaic efficiency (>90%) and >50 TON in both media. Photochemical H_2 production was also carried out in a mixture of acetonitrile: water with $[Ir^{III}(ppy)_2(bpy)]^+$ (where ppy is 2-phenylpyridine and bpy is 2,2'-bipyridine) as a photosensitizer, acetic acid as proton source and triethanolamine as a sacrificial electron donor, reaching 180 TON under visible light.[78] Peters *et al.* also studied the same cobalt complex electrochemically reaching 17 TON with 92% of faradaic yield.[79] Compared to cobaloximes derivates, the complex with a ligand scaffold containing a pyridine and two imine groups shows slightly more negative redox potential but higher Faradaic efficiencies suggesting better stability in aqueous solutions.[79,80]

Ni-8 was developed by DuBois and co-workers with two 1,3-diethylphosphapropane (DEPP) ligands $[Ni(DEPP)_2]^{2+}$ capable of reversible cleave H_2 in the presence of 2,3-dichloroaniline to form a nickel hydrate and the protonated dichloroaniline. Inspired by natural hydrogenases, an amine base was incorporated in the backbone structure to facilitate the proton transfer rate resulting in a negative shift of 650 mV for the hydrogen oxidation but with a low reaction rate. DuBois' nickel catalysts are the perfect example of how a deep insight into the mechanism of the catalytic cycle can provide information to correlate the structure and the activity of a given catalyst, obtaining valuable information to design rationally better molecular catalysts. DuBois catalysts featured a high activity and stability in organic solvents in the presence of strong acids, but on the other hand they only operate with such high rate under large overpotential ($\eta > 0.6$ V) in non-aqueous medium.[81]

Recently our group developed two Nickel and cobalt complexes **Co-16** and **Ni-9** based on based on bis(imino) pyridine or (pyridinedimiino (PDI) ligands back bone with two phosphine arms for electrochemical proton reduction reaction. Redox non-innocent nature of the PDI ligands can act an electron reservoir storing electrons on either metal center or ligand back bone facilitating formation of high energetical intermediates on metal low oxidation states subsequently, lowering energy barrier for multi electron transformation on resulted complexes

as catalyst.[80-84]

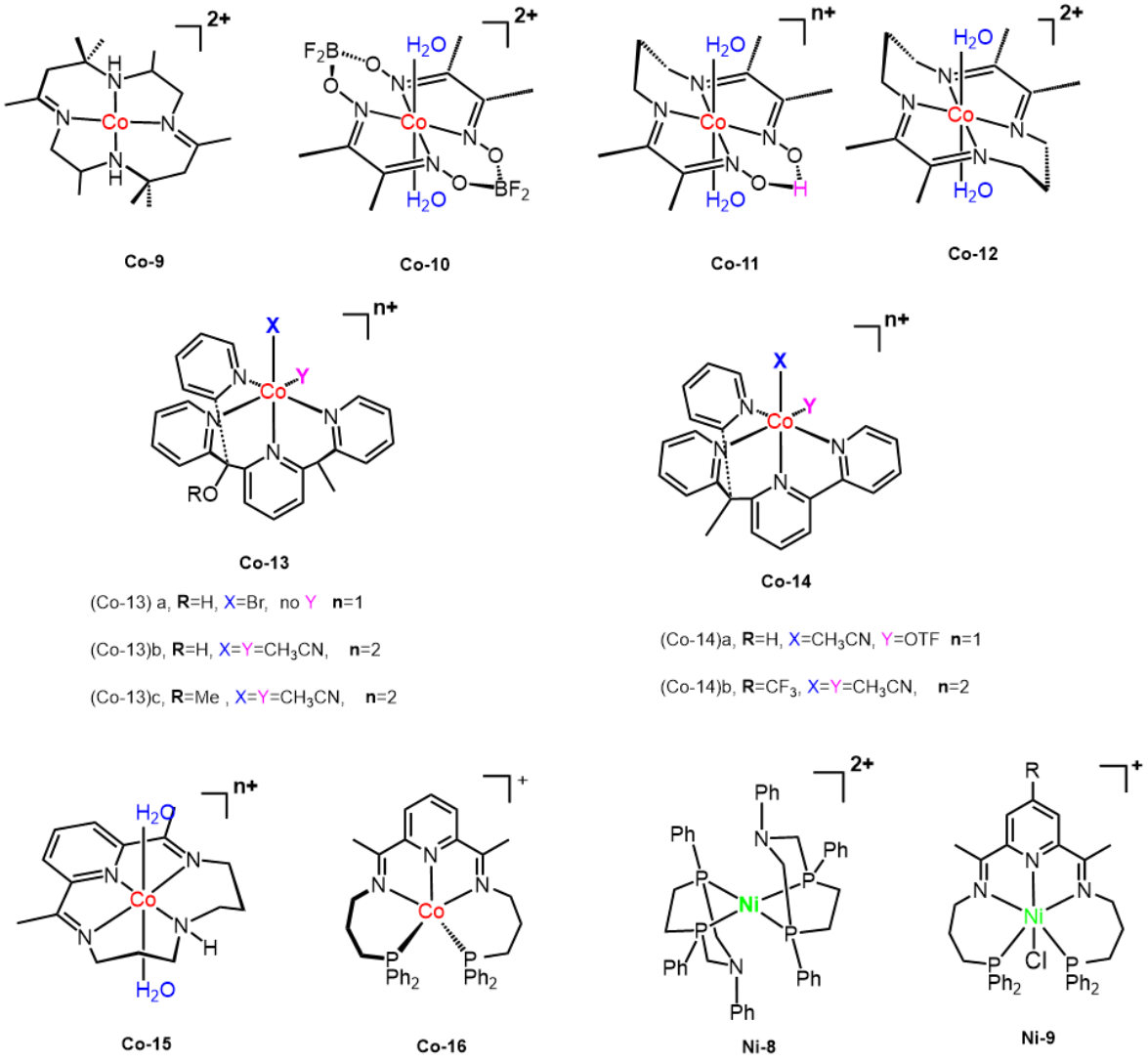

Figure 11- A selection of molecular catalysts discussed in this chapter.

6.2- Mechanism of proton reduction by molecular catalysts

The mechanism of the proton reduction by molecular catalyst can be divided to two pathways homolytic or heterolytic pathways. These two steps are competent and can done in parallel to each other which depends on lots of parameters like: the medium, pH, catalyst concentration ,the nature of the proton source used or etc. Regardless of the dominant mechanism pathway, the first step in proton reduction reaction by molecular catalyst is

reduction of metal center to low oxidation states (the oxidation number can be different based on metal center used) and protonation of the reduced metal center which produces hydride intermediate. The next step is crucial in determining the dominant mechanism pathways. After metal hydride production, **1**) The metal center can react with proton on medium and produces hydrogen and regenerating the initial M^{n+} catalyst or (heterolytic pathway) **2**)

the metal hydride intermediate can react with another metal hydride on medium which produces hydrogen as well as $M^{(n+1)+}$ (homolytic pathway) **3**) In this scenario produced metal hydride can further reduced and, in this case, reduced metal hydride can produces hydrogen via homolytic or heterolytic pathway. [14,60]

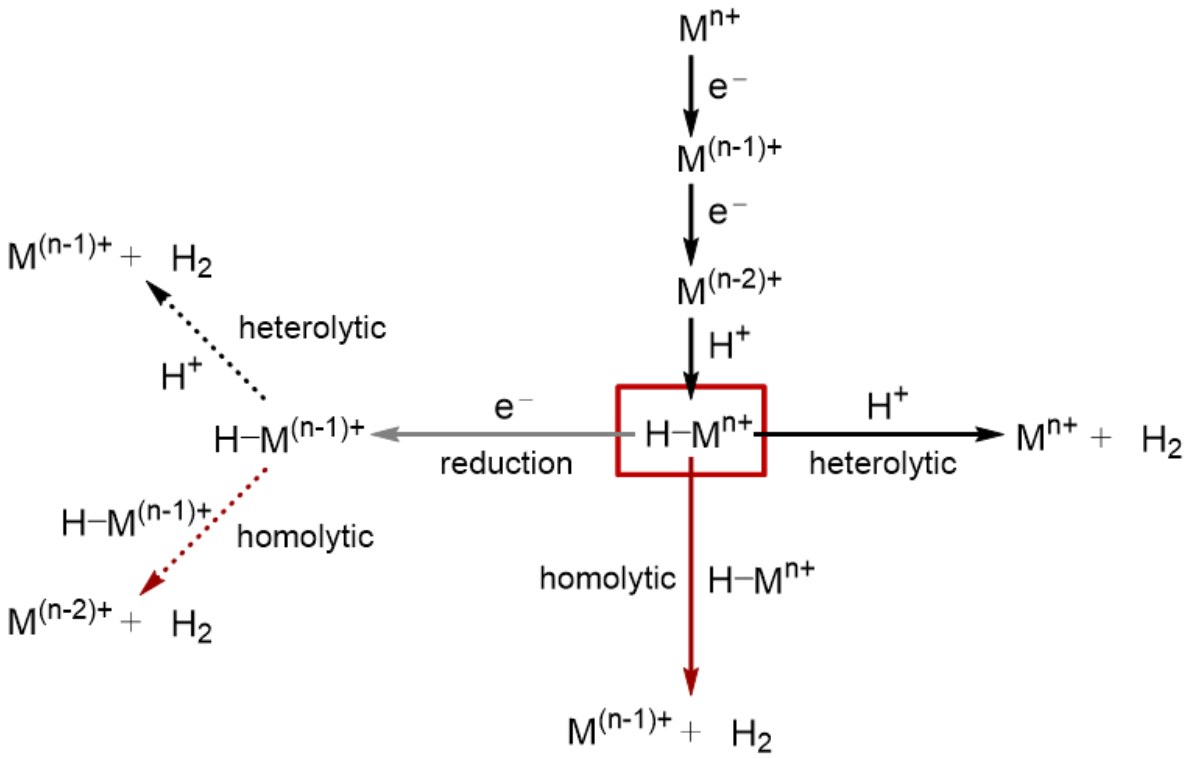

Scheme 2- Schematic representation of possible mechanism pathways for production of hydrogen using molecular catalysts.

7- References

(1) Li, L.; Gan, L.; Liu, M. Materials Advances. *Mater. Adv.* **2020**, *1*, 945–966. https://doi.org/10.1039/D1MA00814E.

(2) Anwar, M. N.; Fayyaz, A.; Sohail, N. F.; Khokhar, M. F.; Baqar, M.; Yasar, A.; Rasool, K.; Nazir, A.; Raja, M. U. F.; Rehan, M.; Aghbashlo, M.; Tabatabaei, M.; Nizami, A. S. CO2 Utilization: Turning Greenhouse Gas into Fuels and Valuable Products. *J. Environ. Manage.* **2020**, *260* (September 2019), 110059. https://doi.org/10.1016/j.jenvman.2019.110059.

(3) Nocera, D. G. The Artificial Leaf. *Acc. Chem. Res.* **2012**, *45* (5), 767–776. https://doi.org/10.1021/ar2003013.

(4) Obama, B. The Irreversible Momentum of Clean Energy. *Science (80-.).* **2017**, *355* (6321), 126–129. https://doi.org/10.1126/science.aam6284.

(5) Karl, T. R.; Trenberth, K. E. Modern Global Climate Change. *Science (80-.).* **2003**, *302* (5651), 1719–1723. https://doi.org/10.1126/science.1090228.

(6) Rockström, J.; Gaffney, O.; Rogelj, J.; Meinshausen, M.; Nakicenovic, N.; Schellnhuber, H. J. A Roadmap for Rapid Decarbonization. *Science (80-.).* **2017**, *355* (6331), 1269–1271. https://doi.org/10.1126/science.aah3443.

(7) Canadell, J. G.; Le Quéré, C.; Raupach, M. R.; Field, C. B.; Buitenhuis, E. T.; Ciais, P.; Conway, T. J.; Gillett, N. P.; Houghton, R. A.; Marland, G. Contributions to Accelerating Atmospheric CO2 Growth from Economic Activity, Carbon Intensity, and Efficiency of Natural Sinks. *Proc. Natl. Acad. Sci. U. S. A.* **2007**, *104* (47), 18866–18870. https://doi.org/10.1073/pnas.0702737104.

(8) Mac Dowell, N.; Fennell, P. S.; Shah, N.; Maitland, G. C. The Role of CO2 Capture and Utilization in Mitigating Climate Change. *Nat. Clim. Chang.* **2017**, *7* (4), 243–249. https://doi.org/10.1038/nclimate3231.

(9) Lewis S Nathan. Toward Cost-Effective Solar Energy Use. *Science (80-.).* **2007**, *315*

(1), 798–802.

(10) International Energy Agency. Global Energy Review 2021. *Glob. Energy Rev. 2020* **2021**, 1–36.

(11) Grahame, A.; Aguey-Zinsou, K. F. Properties and Applications of Metal (M) Dodecahydro-Closo-Dodecaborates (Mn=1,2B12H12) and Their Implications for Reversible Hydrogen Storage in the Borohydrides. *Inorganics* **2018**, *6* (4), 1–38. https://doi.org/10.3390/inorganics6040106.

(12) Najafpour, M. M. *ADVANCES IN PHOTOSYNTHESIS – FUNDAMENTAL ASPECTS Edited by Mohammad Mahdi Najafpour*.

(13) Najafpour, M. M.; Ghobadi, M. Z.; Larkum, A. W.; Shen, J. R.; Allakhverdiev, S. I. The Biological Water-Oxidizing Complex at the Nano-Bio Interface. *Trends Plant Sci.* **2015**, *20* (9), 559–568. https://doi.org/10.1016/j.tplants.2015.06.005.

(14) Zhang, B.; Sun, L. Artificial Photosynthesis: Opportunities and Challenges of Molecular Catalysts. *Chem. Soc. Rev.* **2019**, *48* (7), 2216–2264. https://doi.org/10.1039/c8cs00897c.

(15) Barber, J. Photosynthetic Energy Conversion: Natural and Artificial. *Chem. Soc. Rev.* **2009**, *38* (1), 185–196. https://doi.org/10.1039/b802262n.

(16) Messinger, J.; Lubitz, W.; Shen, J. R. Photosynthesis: From Natural to Artificial. *Phys. Chem. Chem. Phys.* **2014**, *16* (24), 11810–11811. https://doi.org/10.1039/c4cp90053g.

(17) Berardi, S.; Drouet, S.; Francàs, L.; Gimbert-Suriñach, C.; Guttentag, M.; Richmond, C.; Stoll, T.; Llobet, A. Molecular Artificial Photosynthesis. *Chem. Soc. Rev.* **2014**, *43* (22), 7501–7519. https://doi.org/10.1039/c3cs60405e.

(18) Kärkäs, M. D.; Verho, O.; Johnston, E. V.; Åkermark, B. Artificial Photosynthesis: Molecular Systems for Catalytic Water Oxidation. *Chem. Rev.* **2014**, *114* (24), 11863–12001. https://doi.org/10.1021/cr400572f.

(19) Yano, J.; Yachandra, V. Mn4Ca Cluster in Photosynthesis: Where and How Water Is

Oxidized to Dioxygen. *Chem. Rev.* **2014**, *114* (8), 4175–4205. https://doi.org/10.1021/cr4004874.

(20) Ferreira, K. N.; Iverson, T. M.; Maghlaoui, K.; Barber, J.; Iwata, S. Architecture of the Photosynthetic Oxygen-Evolving Center. *Science (80-.).* **2004**, *303* (5665), 1831–1838. https://doi.org/10.1126/science.1093087.

(21) Umena, Y.; Kawakami, K.; Shen, J. R.; Kamiya, N. Crystal Structure of Oxygen-Evolving Photosystem II at a Resolution of 1.9Å. *Nature* **2011**, *473* (7345), 55–60. https://doi.org/10.1038/nature09913.

(22) Suga, M.; Akita, F.; Hirata, K.; Ueno, G.; Murakami, H.; Nakajima, Y.; Shimizu, T.; Yamashita, K.; Yamamoto, M.; Ago, H.; Shen, J. R. Native Structure of Photosystem II at 1.95A° Resolution Viewed by Femtosecond X-Ray Pulses. *Nature* **2015**, *517* (7532), 99–103. https://doi.org/10.1038/nature13991.

(23) Cheng, J.; Deming, T. J. Synthesis of Polypeptides by ROP of NCAs. *Pept. Mater.* **2011**, *310* (June 2011), 1–26. https://doi.org/10.1007/128.

(24) Serhan, M.; Sprowls, M.; Jackemeyer, D.; Long, M.; Perez, I. D.; Maret, W.; Tao, N.; Forzani, E. Total Iron Measurement in Human Serum with a Smartphone. *AIChE Annu. Meet. Conf. Proc.* **2019**, *2019-Novem*. https://doi.org/10.1039/x0xx00000x.

(25) Gust, D.; Moore, T. A.; Moore, A. L. Solar Fuels via Artificial Photosynthesis. *Acc. Chem. Res.* **2009**, *42* (12), 1890–1898. https://doi.org/10.1021/ar900209b.

(26) Francke, R.; Schille, B.; Roemelt, M. Homogeneously Catalyzed Electroreduction of Carbon Dioxide - Methods, Mechanisms, and Catalysts. *Chem. Rev.* **2018**, *118* (9), 4631–4701. https://doi.org/10.1021/acs.chemrev.7b00459.

(27) Paparo, A.; Okuda, J. Carbon Dioxide Complexes: Bonding Modes and Synthetic Methods. *Coord. Chem. Rev.* **2017**, *334*, 136–149. https://doi.org/10.1016/j.ccr.2016.06.005.

(28) Lv, F.; Han, N.; Qiu, Y.; Liu, X.; Luo, J.; Li, Y. Transition Metal Macrocycles for

Heterogeneous Electrochemical CO2 Reduction. *Coord. Chem. Rev.* **2020**, *422*, 213435. https://doi.org/10.1016/j.ccr.2020.213435.

(29) Amanullah, S.; Saha, P.; Nayek, A.; Ahmed, M. E.; Dey, A. Biochemical and Artificial Pathways for the Reduction of Carbon Dioxide, Nitrite and the Competing Proton Reduction: Effect of 2nd sphere Interactions in Catalysis. *Chem. Soc. Rev.* **2021**, *50* (6), 3755–3823. https://doi.org/10.1039/d0cs01405b.

(30) Ragsdale, S. W.; Kumar, M. Nickel-Containing Carbon Monoxide Dehydrogenase/Acetyl-CoA Synthase. *Chem. Rev.* **1996**, *96* (7), 2515–2539. https://doi.org/10.1021/cr950058+.

(31) Can, M.; Armstrong, F. A.; Ragsdale, S. W. Structure, Function, and Mechanism of the Nickel Metalloenzymes, CO Dehydrogenase, and Acetyl-CoA Synthase. *Chem. Rev.* **2014**, *114* (8), 4149–4174. https://doi.org/10.1021/cr400461p.

(32) Jeoung, J. H.; Dobbek, H. Carbon Dioxide Activation at the Ni,Fe-Cluster of Anaerobic Carbon Monoxide Dehydrogenase. *Science (80-.).* **2007**, *318* (5855), 1461–1464. https://doi.org/10.1126/science.1148481.

(33) Dobbek, H.; Gremer, L.; Kiefersauer, R.; Huber, R.; Meyer, O. Catalysis at a Dinuclear [CuSMo(=O)OH] Cluster in a CO Dehydrogenase Resolved at 1.1-Å Resolution. *Proc. Natl. Acad. Sci. U. S. A.* **2002**, *99* (25), 15971–15976. https://doi.org/10.1073/pnas.212640899.

(34) Savéant, J. M. Molecular Catalysis of Electrochemical Reactions. Mechanistic Aspects. *Chem. Rev.* **2008**, *108* (7), 2348–2378. https://doi.org/10.1021/cr068079z.

(35) Rountree, E. S.; McCarthy, B. D.; Eisenhart, T. T.; Dempsey, J. L. Evaluation of Homogeneous Electrocatalysts by Cyclic Voltammetry. *Inorg. Chem.* **2014**, *53* (19), 9983–10002. https://doi.org/10.1021/ic500658x.

(36) Wang, J. W.; Liu, W. J.; Zhong, D. C.; Lu, T. B. Nickel Complexes as Molecular Catalysts for Water Splitting and CO_2 Reduction. *Coord. Chem. Rev.* **2019**, *378*, 237–261. https://doi.org/10.1016/j.ccr.2017.12.009.

(37) Dalle, K. E.; Warnan, J.; Leung, J. J.; Reuillard, B.; Karmel, I. S.; Reisner, E. Electro- and Solar-Driven Fuel Synthesis with First Row Transition Metal Complexes. *Chem. Rev.* **2019**, *119* (4), 2752–2875. https://doi.org/10.1021/acs.chemrev.8b00392.

(38) Wang, J. W.; Liu, W. J.; Zhong, D. C.; Lu, T. B. Nickel Complexes as Molecular Catalysts for Water Splitting and CO2 Reduction. *Coord. Chem. Rev.* **2019**, *378*, 237–261. https://doi.org/10.1016/j.ccr.2017.12.009.

(39) Cometto, C.; Chen, L.; Lo, P. K.; Guo, Z.; Lau, K. C.; Anxolabéhère-Mallart, E.; Fave, C.; Lau, T. C.; Robert, M. Highly Selective Molecular Catalysts for the CO2-to-CO Electrochemical Conversion at Very Low Overpotential. Contrasting Fe vs Co Quaterpyridine Complexes upon Mechanistic Studies. *ACS Catal.* **2018**, *8* (4), 3411–3417. https://doi.org/10.1021/acscatal.7b04412.

(40) Roy, S.; Sharma, B.; Pécaut, J.; Simon, P.; Fontecave, M.; Tran, P. D.; Derat, E.; Artero, V. Molecular Cobalt Complexes with Pendant Amines for Selective Electrocatalytic Reduction of Carbon Dioxide to Formic Acid. *J. Am. Chem. Soc.* **2017**, *139* (10), 3685–3696. https://doi.org/10.1021/jacs.6b11474.

(41) Chapovetsky, A.; Do, T. H.; Haiges, R.; Takase, M. K.; Marinescu, S. C. Proton-Assisted Reduction of Co2 by Cobalt Aminopyridine Macrocycles. *J. Am. Chem. Soc.* **2016**, *138* (18), 5765–5768. https://doi.org/10.1021/jacs.6b01980.

(42) Chapovetsky, A.; Welborn, M.; Luna, J. M.; Haiges, R.; Miller, T. F.; Marinescu, S. C. Pendant Hydrogen-Bond Donors in Cobalt Catalysts Independently Enhance CO_2 Reduction. *ACS Cent. Sci.* **2018**, *4* (3), 397–404. https://doi.org/10.1021/acscentsci.7b00607.

(43) Elgrishi, N.; Chambers, M. B.; Artero, V.; Fontecave, M. Terpyridine Complexes of First Row Transition Metals and Electrochemical Reduction of CO_2 to CO. *Phys. Chem. Chem. Phys.* **2014**, *16* (27), 13635–13644. https://doi.org/10.1039/c4cp00451e.

(44) Elgrishi, N.; Chambers, M. B.; Fontecave, M. Turning It off! Disfavouring Hydrogen Evolution to Enhance Selectivity for CO Production during Homogeneous CO_2 Reduction by Cobalt-Terpyridine Complexes. *Chem. Sci.* **2015**, *6* (4), 2522–2531.

https://doi.org/10.1039/c4sc03766a.

(45) Dey, S.; Ahmed, M. E.; Dey, A. Activation of Co(I) State in a Cobalt-Dithiolato Catalyst for Selective and Efficient CO2 Reduction to CO. *Inorg. Chem.* **2018**, *57* (10), 5939–5947. https://doi.org/10.1021/acs.inorgchem.8b00450.

(46) Roy, L.; Al-Afyouni, M. H.; Derosha, D. E.; Mondal, B.; Dimucci, I. M.; Lancaster, K. M.; Shearer, J.; Bill, E.; Brennessel, W. W.; Neese, F.; Ye, S.; Holland, P. L. Reduction of CO_2 by a Masked Two-Coordinate Cobalt(i) Complex and Characterization of a Proposed Oxodicobalt(Ii) Intermediate. *Chem. Sci.* **2019**, *10* (3), 918–929. https://doi.org/10.1039/c8sc02599a.

(47) Hammouche, M.; Lexa, D.; Savêant, J. M.; Momenteau, M. Chemical Catalysis of Electrochemical Reactions. Homogeneous Catalysis of the Electrochemical Reduction of Carbon Dioxide by Iron("0") Porphyrins. Role of the Addition of Magnesium Cations. *J. Am. Chem. Soc.* **1991**, *113* (22), 8455–8466. https://doi.org/10.1021/ja00022a038.

(48) Takahashi, K.; Hiratsuka, K.; Sasaki, H.; Toshima, S. Electrocatalytic Behavior of Metal Porphyrins in the Reduction of Carbon Dioxide. *Chem. Lett.* **1979**, *8* (4), 305–308. https://doi.org/10.1246/cl.1979.305.

(49) Mondal, B.; Rana, A.; Sen, P.; Dey, A. Intermediates Involved in the 2e-/2H+ Reduction of CO_2 to CO by Iron(0) Porphyrin. *J. Am. Chem. Soc.* **2015**, *137* (35), 11214–11217. https://doi.org/10.1021/jacs.5b05992.

(50) Talanquer, V.; Oxtoby, D.; Islam, M. F.; Zhang, J.; Collings, P. J.; Yodh, A. G.; Gleiter, H.; Perepezko, J.; Terrones, M.; Dwyer, J. R.; Jordan, R. E.; Miller, R. J.; Enomoto, M.; Lee, J. K.; Group, F.; Lekkerkerker, H. N.; Grier, D. G.; Weeks, E. R.; Schofield, A.; Pusey, P. N.; Weitz, D. A.; Blair, D. W.; Levine, A. J.; Guyer, R. A.; Dinsmore, A. D.; Alsayed, A. M.; Yodh, A. G.; Han, Y.; Megen, W. Van; Grier, D. G.; Dobry, A.; Diep, H. T.; Burakovsky, L.; Preston, D. L.; Silbar, R. R.; Grimvall, G.; Li, M.; Bongiorno, A.; Ostwald, W.; Li, M.; Denton, A. R.; Ashcroft, N. W.; Auer, S.; Frenkel, D.; Davidchack, R. L.; Moroni, D.; Bolhuis, P. G.; Lu, K.; Li, Y.; Jin, Z. H.; Gumbsch, P.;

Lu, K. Molecular Fe Catalyst. *Science (80-.).* **2012**, *338* (October), 90–94.

(51) Fisher, B.; Eisenberg, R. Electrocatalytic Reduction of Carbon Dioxide by Using Macrocycles of Nickel and Cobalt. *J. Am. Chem. Soc.* **1980**, *102* (24), 7361–7363. https://doi.org/10.1021/ja00544a035.

(52) Beley, M.; Collin, J. P.; Ruppert, R.; Sauvage, J. P. Nickel(Ii)-Cyclam: An Extremely Selective Electrocatalyst for Reduction of CO_2 in Water. *J. Chem. Soc. - Ser. Chem. Commun.* **1984**, *2* (19), 1315–1316. https://doi.org/10.1039/C39840001315.

(53) Froehlich, J. D.; Kubiak, C. P. Homogeneous CO 2 Reduction by Ni(Cyclam) at a Glassy Carbon Electrode. **2012**, 3932–3934.

(54) Su, X.; McCardle, K. M.; Panetier, J. A.; Jurss, J. W. Electrocatalytic CO2 Reduction with Nickel Complexes Supported by Tunable Bipyridyl-N-Heterocyclic Carbene Donors: Understanding Redox-Active Macrocycles. *Chem. Commun.* **2018**, *54* (27), 3351–3354. https://doi.org/10.1039/c8cc00266e.

(55) Fogeron, T.; Todorova, T. K.; Porcher, J.; Gomez-mingot, M.; Chamoreau, L.; Mellot-draznieks, C.; Li, Y.; Fontecave, M. A Bioinspired Nickel(Bis-Dithiolene) Complex as a Homogeneous Catalyst for Carbon Dioxide Electroreduction. **2018**. https://doi.org/10.1021/acscatal.7b03383.

(56) Grice, K. A. Carbon Dioxide Reduction with Homogenous Early Transition Metal Complexes: Opportunities and Challenges for Developing CO2 Catalysis. *Coord. Chem. Rev.* **2017**, *336*, 78–95. https://doi.org/10.1016/j.ccr.2017.01.007.

(57) Yin, X.; Moss, J. R. Recent Developments in the Activation of Carbon Dioxide by Metal Complexes. *Coord. Chem. Rev.* **1999**, *181* (1), 27–59. https://doi.org/10.1016/S0010-8545(98)00171-4.

(58) Takeda, H.; Cometto, C.; Ishitani, O.; Robert, M. Electrons, Photons, Protons and Earth-Abundant Metal Complexes for Molecular Catalysis of CO_2 Reduction. *ACS Catal.* **2017**, *7* (1), 70–88. https://doi.org/10.1021/acscatal.6b02181.

(59) Chen, L.; Guo, Z.; Wei, X. G.; Gallenkamp, C.; Bonin, J.; Anxolabéhère-Mallart, E.; Lau, K. C.; Lau, T. C.; Robert, M. Molecular Catalysis of the Electrochemical and Photochemical Reduction of CO_2 with Earth-Abundant Metal Complexes. Selective Production of CO vs HCOOH by Switching of the Metal Center. *J. Am. Chem. Soc.* **2015**, *137* (34), 10918–10921. https://doi.org/10.1021/jacs.5b06535.

(60) Wang, M.; Chen, L.; Sun, L. Recent Progress in Electrochemical Hydrogen Production with Earth-Abundant Metal Complexes as Catalysts. *Energy Environ. Sci.* **2012**, *5* (5), 6763–6778. https://doi.org/10.1039/c2ee03309g.

(61) Sakai, K.; Ozawa, H. Homogeneous Catalysis of Platinum(II) Complexes in Photochemical Hydrogen Production from Water. *Coord. Chem. Rev.* **2007**, *251* (21–24), 2753–2766. https://doi.org/10.1016/j.ccr.2007.08.014.

(62) Eckenhoff, W. T. Molecular Catalysts of Co, Ni, Fe, and Mo for Hydrogen Generation in Artificial Photosynthetic Systems. *Coord. Chem. Rev.* **2018**, *373*, 295–316. https://doi.org/10.1016/j.ccr.2017.11.002.

(63) Schilter, D.; Camara, J. M.; Huynh, M. T.; Hammes-Schiffer, S.; Rauchfuss, T. B. Hydrogenase Enzymes and Their Synthetic Models: The Role of Metal Hydrides. *Chem. Rev.* **2016**, *116* (15), 8693–8749. https://doi.org/10.1021/acs.chemrev.6b00180.

(64) Lubitz, W.; Ogata, H.; Ru, O.; Reijerse, E. Hydrogenases. **2014**.

(65) De Lacey, A. L.; Fernández, V. M.; Rousset, M.; Cammack, R. Activation and Inactivation of Hydrogenase Function and the Catalytic Cycle: Spectroelectrochemical Studies. *Chem. Rev.* **2007**, *107* (10), 4304–4330. https://doi.org/10.1021/cr0501947.

(66) Evans, D. J.; Pickett, C. J. Chemistry and the Hydrogenases. *Chem. Soc. Rev.* **2003**, *32* (5), 268–275. https://doi.org/10.1039/b201317g.

(67) Appel, A. M.; Bercaw, J. E.; Bocarsly, A. B.; Dobbek, H.; Dubois, D. L.; Dupuis, M.; Ferry, J. G.; Fujita, E.; Hille, R.; Kenis, P. J. A.; Kerfeld, C. A.; Morris, R. H.; Peden, C. H. F.; Portis, A. R.; Ragsdale, S. W.; Rauchfuss, T. B.; Reek, J. N. H.; Seefeldt, L. C.; Thauer, R. K.; Waldrop, G. L. Frontiers, Opportunities, and Challenges in

Biochemical and Chemical Catalysis of CO_2 Fixation. *Chem. Rev.* **2013**, *113* (8), 6621–6658. https://doi.org/10.1021/cr300463y.

(68) Tard, C.; Pickett, C. J. Structural and Functional Analogues of the Active Sites of the [Fe]-, [NiFe]-, and [FeFe]-Hydrogenases. *Chem. Rev.* **2009**, *109* (6), 2245–2274. https://doi.org/10.1021/cr800542q.

(69) Simmons, T. R.; Berggren, G.; Bacchi, M.; Fontecave, M.; Artero, V. Mimicking Hydrogenases: From Biomimetics to Artificial Enzymes. *Coord. Chem. Rev.* **2014**, *270–271* (1), 127–150. https://doi.org/10.1016/j.ccr.2013.12.018.

(70) Queyriaux, N.; Jane, R. T.; Massin, J.; Artero, V.; Chavarot-Kerlidou, M. Recent Developments in Hydrogen Evolving Molecular Cobalt(II)-Polypyridyl Catalysts. *Coord. Chem. Rev.* **2015**, *304–305*, 3–19. https://doi.org/10.1016/j.ccr.2015.03.014.

(71) Anxolabéhère-Mallart, E.; Costentin, C.; Fournier, M.; Nowak, S.; Robert, M.; Savéant, J. M. Boron-Capped Tris(Glyoximato) Cobalt Clathrochelate as a Precursor for the Electrodeposition of Nanoparticles Catalyzing H 2 Evolution in Water. *J. Am. Chem. Soc.* **2012**, *134* (14), 6104–6107. https://doi.org/10.1021/ja301134e.

(72) Dempsey, J. L.; Brunschwig, B. S.; Winkler, J. R.; Gray, H. B. Hydrogen Evolution Catalyzed by Cobaloximes. *Acc. Chem. Res.* **2009**, *42* (12), 1995–2004. https://doi.org/10.1021/ar900253e.

(73) Wiedner, E. S.; Bullock, R. M. Electrochemical Detection of Transient Cobalt Hydride Intermediates of Electrocatalytic Hydrogen Production. *J. Am. Chem. Soc.* **2016**, *138* (26), 8309–8318. https://doi.org/10.1021/jacs.6b04779.

(74) Baffert, C.; Artero, V.; Fontecave, M. Cobaloximes as Functional Models for Hydrogenases. 2. Proton Electroreduction Catalyzed by Difluoroborylbis(Dimethylglyoximato)Cobalt(II) Complexes in Organic Media. *Inorg. Chem.* **2007**, *46* (5), 1817–1824. https://doi.org/10.1021/ic061625m.

(75) Connolly, P.; Espenson, J. H. Cobalt-Catalyzed Evolution of Molecular Hydrogen. *Inorg. Chem.* **1986**, *25* (16), 2684–2688. https://doi.org/10.1021/ic00236a006.

(76) Bigi, J. P.; Hanna, T. E.; Harman, W. H.; Chang, A.; Chang, C. J. Electrocatalytic Reduction of Protons to Hydrogen by a Water-Compatible Cobalt Polypyridyl Platform. *Chem. Commun.* **2010**, *46* (6), 958–960. https://doi.org/10.1039/b915846d.

(77) Artero, V.; Chavarot-Kerlidou, M.; Fontecave, M. Splitting Water with Cobalt. *Angew. Chemie - Int. Ed.* **2011**, *50* (32), 7238–7266. https://doi.org/10.1002/anie.201007987.

(78) Leung, C.-F.; Chen, Y.-Z.; Yu, H.-Q.; Yiu, S.-M.; Ko, C.-C.; Lau, T.-C. Electro and Photocatalytic Hydrogen Generation in Acetonitrile and Aqueous Solutions by a Cobalt Macrocyclic Schiff-Base Complex. *Int. J. Hydrogen Energy* **2011**, *36* (18), 11640–11645. https://doi.org/10.1016/j.ijhydene.2011.06.062.

(79) McCrory, C. C. L.; Uyeda, C.; Peters, J. C. Electrocatalytic Hydrogen Evolution in Acidic Water with Molecular Cobalt Tetraazamacrocycles. *J. Am. Chem. Soc.* **2012**, *134* (6), 3164–3170. https://doi.org/10.1021/ja210661k.

(80) Leung, C. F.; Chen, Y. Z.; Yu, H. Q.; Yiu, S. M.; Ko, C. C.; Lau, T. C. Electro- and Photocatalytic Hydrogen Generation in Acetonitrile and Aqueous Solutions by a Cobalt Macrocyclic Schiff-Base Complex. *Int. J. Hydrogen Energy* **2011**, *36* (18), 11640–11645. https://doi.org/10.1016/j.ijhydene.2011.06.062.

(81) Fischer, G. References and Notes. *Sov. Oppos. to Stalin* **2014**, No. August, 201–217. https://doi.org/10.4159/harvard.9780674333987.c22.

Chapter 2

Objectives

Chapter 2. Objetives

As discussed in detail in Chapter 1, natural photosynthesis is an inspiring process for renewable energy storage and conversion. The process addresses excellent solutions for the transition from fossil fuels to sustainable energy utilisation. For this purpose, a combination of complex structures has been evolved in organisms and plants over billion years. Among them, enzymes as biological catalysts have played an important role. Recent years have witnessed development of new technologies inspired by natural photosynthesis (artificial photosynthesis), which try to use sunlight as the main energy source and convert it to fuels, thus called solar fuels. To develop systems based on artificial photosynthesis, robust, efficient, and selective catalysts for the fuel generation reaction are required. These catalytic systems in the heart of this technology play important roles such as making the technologies economically viable and the resulting devices highly efficient. In this context, the general goal of the present thesis is to develop efficient and stable catalysts capable of performing the hydrogen evolution reaction (HER) or the CO_2 reduction reaction (CO_2RR). The main goal mentioned above can be divided into the following specific objectives:

- Study a family of non-innocent ligands with potential to facilitate the multiple electron and proton transfers involved in the chemical reactions required for the formation of fuels such as hydrogen or reduced carbon derivatives in the context of artificial photosynthesis. In particular, the work will focus on β-diimino compounds as precursors to **β-diketiminate** ligands with different substituents and denticity including κ^2-N_2, κ^3-PN_2 and κ^4-P_2N_2 (**Figure 1**, left) and a family of tetradentate **dipicolinamido** ligands (κ^2-N_4) (**Figure 1**, right).

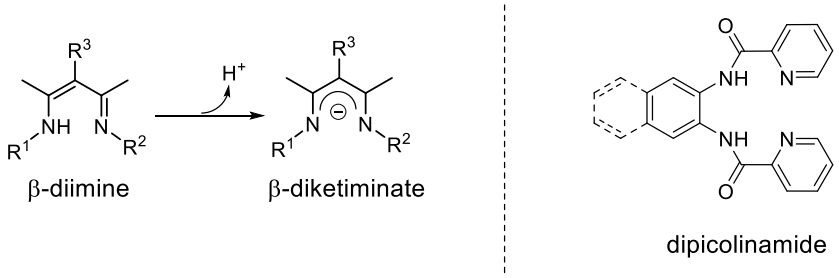

Figure 1- Ligands and ligand's precursors targeted in this thesis.

- Develop homogeneous catalysts for the HER and CO_2RR based on first-row transition

Chapter 2. Objetives

metal complexes such as **iron** or **nickel** containing β-diketiminate or dipicolinamido ligands, as inexpensive and effective molecular catalysts for the cathodic side of an artificial photosynthesis devices (**Figure 2**).

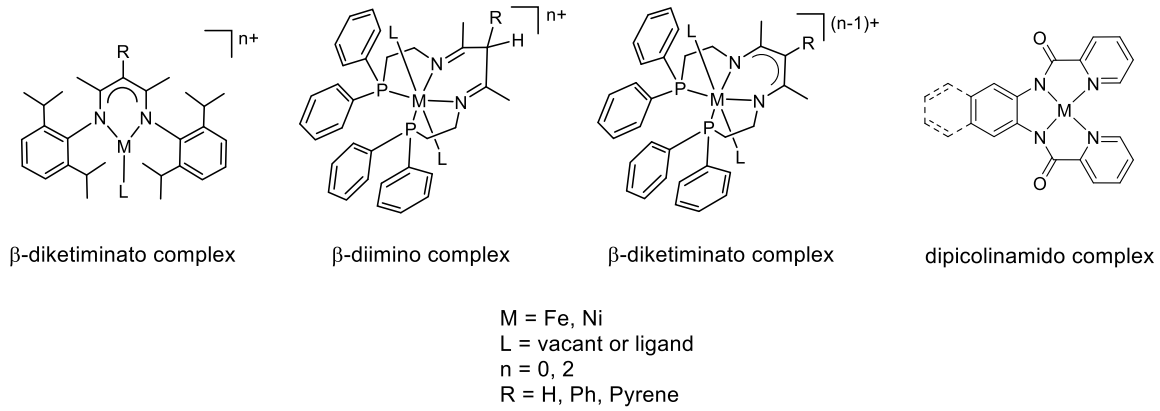

Figure 2- General structure of β-diimino, β-diketiminato and dipicolinamido complexes targeted in this study.

- In order advance towards an artificial photosynthesis device, the heterogenization of molecular catalysts will be tested by adding a proper functional group to the backbone of the ligand. In particular, a pyrene group will be attached to one of the β-diketiminate ligands in order to prepare metal complexes susceptible of anchoring in graphitic materials such as graphene or carbon nanotubes (**Figure 3**). This would allow to transfer the catalytic activity studied under homogeneous conditions to the heterogeneous phase. This is an important step towards building an artificial photosynthesis cell with real applications.

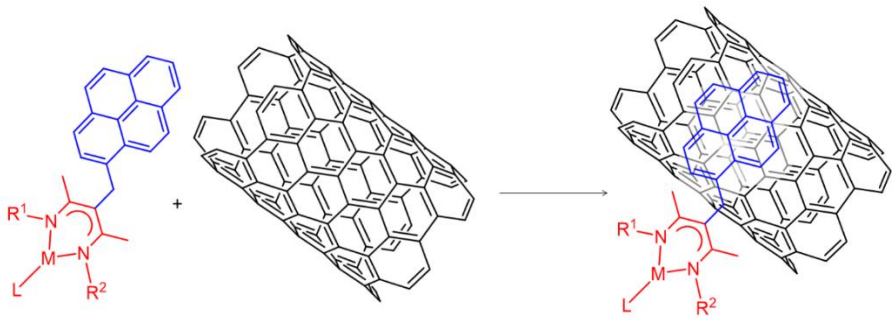

Figure 3- Attachment of a generic β-diketiminato metal complex functionalized with a pyrene derivative (in blue) to a carbon nanotube via π,π-stacking interactions.

Chapter 3

β-Diimino compounds as precursors to κ^2-N_2, κ^3-PN_2 and κ^4-P_2N_2β-diketiminate ligands

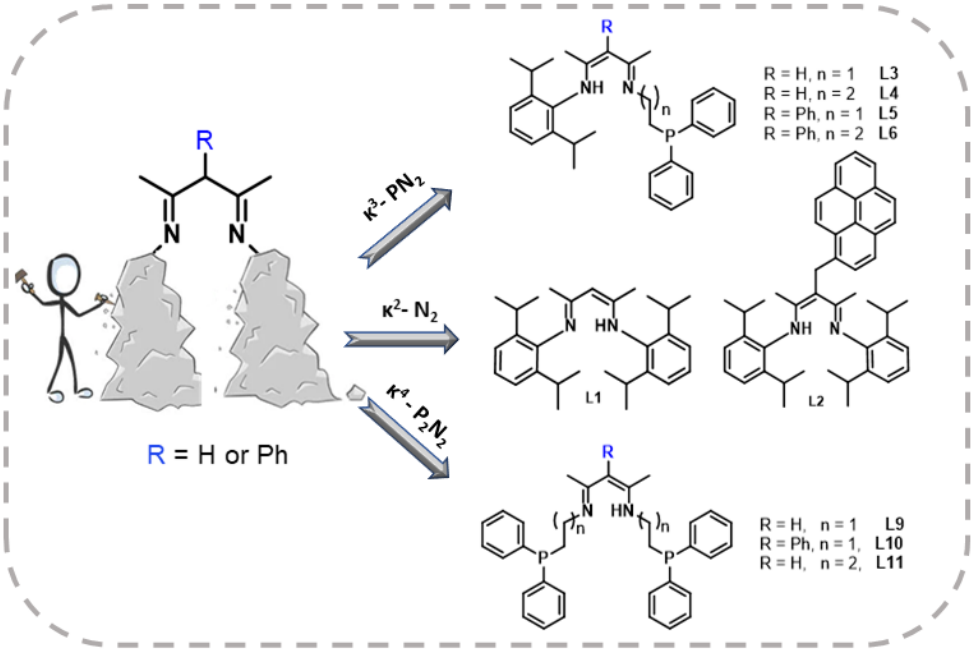

Chapter 3.

1- Introduction

β-diketiminates (often abbreviated as *nacnac* or BDK) are a family of ligands that have been widely used for synthesizing a large family of complexes with different metal centers, all across the periodic table.[1,2] Since their introduction in 1968,[3–6] BDK ligands have gained interest because of their versatility and tunability as well as their strong binding to metal centers. These characteristics not only enable the ligand to possess different steric and electronic configurations but also stabilize low coordination complexes with unusual oxidation states and geometries.[7] The variation of the ligand's steric and electronic properties is possible by changing the substituent on the imine N atom, the imine C atom or the α-carbon in the ligand backbone (**Figure 1**).[8–10] Varying the steric configuration of BDK ligands has a significant effect on the activity, selectivity, and structural properties of the resulting metal complexes in both stoichiometric and catalytic reactions. On the other hand, varying the electronic properties affects electron density of the metal center and changes the reactivity.[11] Although BDK ligands have been long considered spectator ligands, several reports show that they can also act as non-innocent ligands. [12–16]

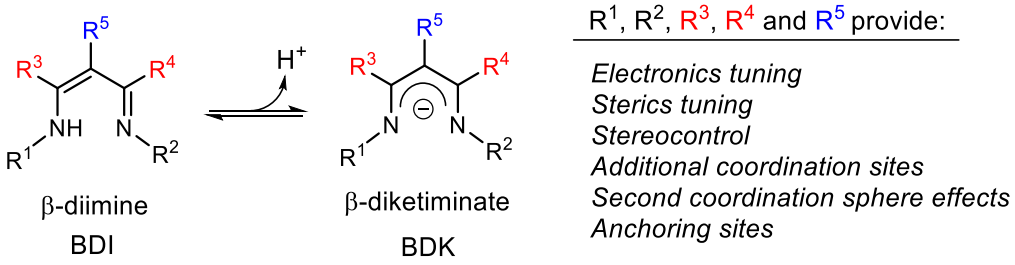

Figure 1. General structure of β-diimine compounds (BDI) and the conversion to β-diketiminate derivatives (BDK) through deprotonation. Modification of BDI and BDK compounds is possible by varying the substituents of the ligand's backbone at the imine N atom (R^1 and R^2), the imine C atom (R^3 and R^4) and the α-carbon (R^5).

There is a considerable diversity of bonding modes from pure σ to a combination of σ to π donation for *β*-diketiminato ligands to metal complexes, in which most of them the coordination modes are metal center dependent (**Figure 2**). The most common is the κ^2-N,N' bidentate coordination through the two nitrogen atoms, affording a six-membered metallacyclic ring (top of **Figure 2**). Monodentate coordination modes are less common and can happen through the N or the α-imino carbons (**Figure 2**, middle). Other rarer coordination of BDK might involve aromatic rings in pending groups acting as η^6 ligands or even boat

Chapter 3.

conformation metalacyclic complexes with a η^5 coordination mode of the BDK ligand, which is favored by the C-M bond formation with metals containing empty d orbitals with the appropriate geometry (**Figure 2**, bottom).

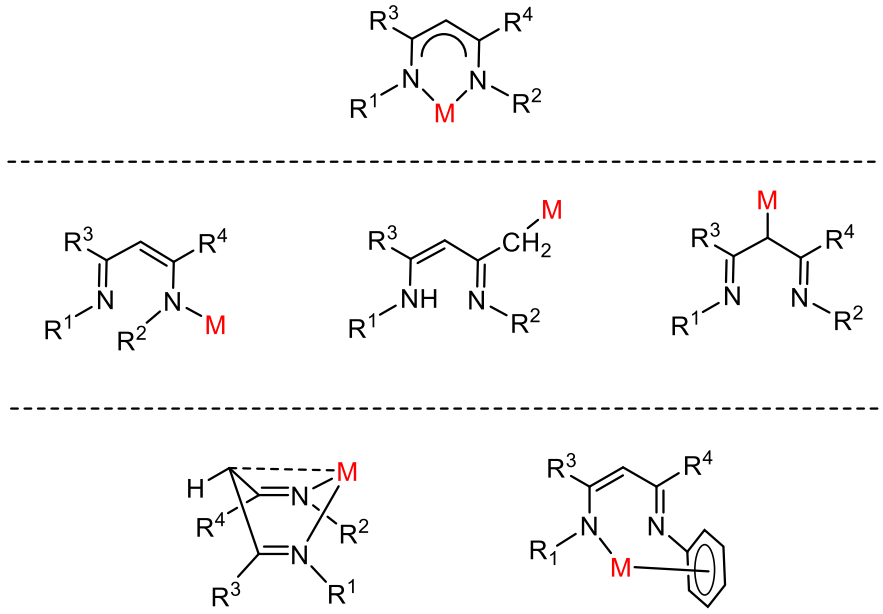

Figure 2. Diversity in bonding modes of β-diketiminato complexes. **Top:** κ^2-N,N' bidentate coordination; **middle:** monodentate coordination through the N or the α-imino carbons; **Bottom:** η^5 coordination mode in a boat conformation metallacycle (left) and η^6 coordination mode by a pending aromatic ring (right).

First row transition metal β-diketiminato complexes have been used for a wide variety of applications such as stoichiometric and catalytic transformations including polymerization and functionalization of alkenes, cross coupling reactions and energy related applications. In addition, late transition metal complexes have been used for synthesizing low coordination metal centers mimicking the active site of metalloproteins for the conversion of organic substrates but also the activation of small molecules such as carbon dioxide or nitrogen.[17–23]

Figure 3 collects the β-diketiminato complexes that have been used in carbon dioxide reduction (CO_2RR) and proton reduction (PRR) stoichiometric reactions. They are iron, cobalt or nickel complexes characterized by holding ligands with bulky substituents that allow for a low coordination number and stabilize low valent metal centers. The Holland group exploited the BDK ligand with R^1 = R^2 = 2,6-diisopropylphenyl, R^3 = R^4 = *tert*-butyl and R^5 = H coordinated to Fe(I) in a dinuclear fashion.[24] The complex was found to react with CO_2 releasing CO and a carbonate bridged diiron complex. An analogous complex with Ni(I) was

Chapter 3.

later reported by Lappert, showing similar reactivity but also the conversion of CO_2 to an oxalate dinickel complex, through a new C-C bond formation.[25] More recently, the Holland group isolated a mononuclear Co(I) complex, that was also active in CO_2 activation giving rise to carbonyl and carbonate complexes.[26,27] This complex is considered a masked two-coordinate cobalt(I) complex, because it readily converts into the common κ^2-N,N' bidentate coordination mode derivative in the presence of monodentate ligands such as triphenylphophine, carbon monoxide or pyridine. More recently, Meyer has published a dinuclear bis(β-diketiminato) complex bridged by a pyrazolate ring, which has been involved in stoichiometric PRR through a proposed metal-metal and metal-ligand cooperative two electron reductive process.[28,29]

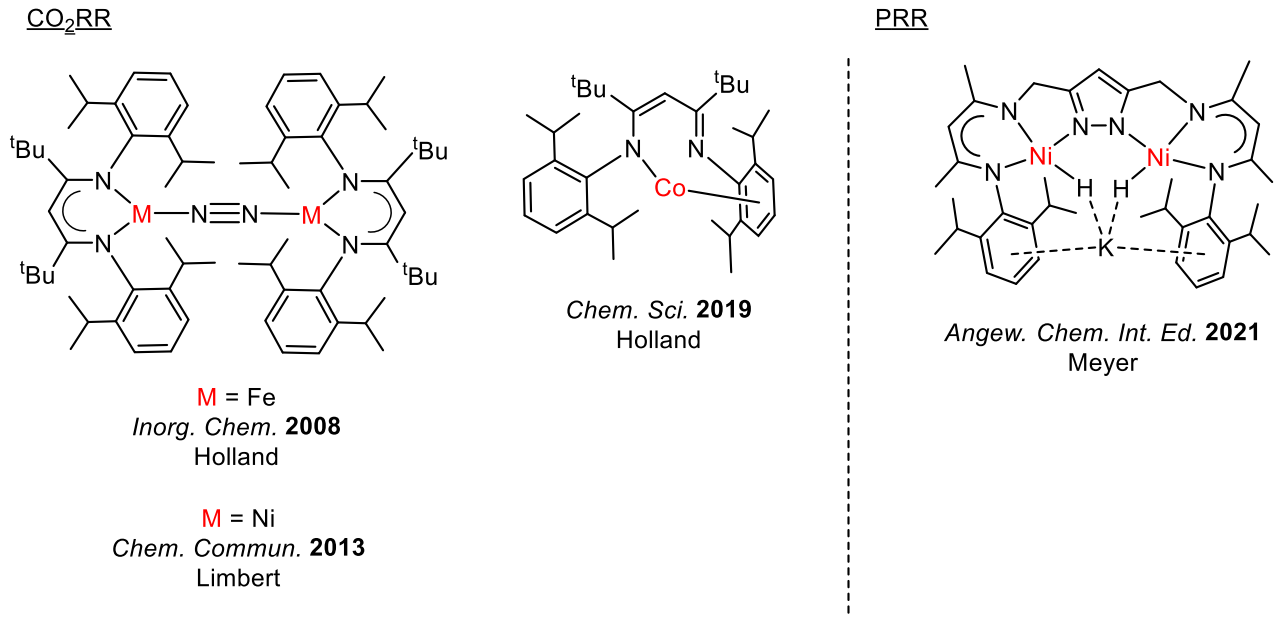

Figure 3. β-diketiminate complexes used in CO_2 or proton reduction reactions (CO_2RR and PRR, respectively).

This chapter reports on the synthesis of β-diimino (BDI) compounds as precursors to β-diketiminato ligands with different denticity. Inspired by the work of Holland, a κ^2-N_2 BDK ligand was derivatized with a pyrene group in the α-carbon position (R^5 in **Figure 1**) with the aim of anchoring the resulting compound and their metal complexes on graphitic surfaces. Anchoring molecular catalysts onto (photo)cathodes for the CO_2RR and PRR can modify their reaction pathways and/or improve the activity of the catalyst.[32–35] This would allow to explore

Chapter 3.

β-diketiminato complexes in CO_2RR electroreduction in heterogeneous phase for the first time. A second family of ligand precursors are asymmetric κ^3-PN_2 compounds, incorporating an aliphatic diphenylphosphine arm in the C-imine position (R^1 in Figure 1), which provides an extra coordination while allowing to stabilize metallic low oxidation states thanks to the π-back bonding ability of phosphine ligands. Finally, tetradentate symmetric κ^4-P_2N_2 diamine compounds, where $R^1 = R^2$ in Figure 1, will be prepared.

2- Results and discussions

2.1- κ^2-N_2 ligands L1 and L2

There are various synthetic routes to *β*-diimino compounds. The most common strategy involves the double condensation reaction of two equivalents of a primary amine with a *β*-diketone in the presence of a catalytic amount of acid.[2] Following this methodology, the BDK ligand precursor **L1** in Figure 4 was successfully prepared in 80% yield (**Figure 4**). Compound **L1** is isolated as its enamine tautomer as identified by the low field NH proton at 14.38 ppm (Figure S1 in the SI). It includes two bulky 2,6-diisopropylphenyl substituents providing a small pocket that when bound in the κ^2-N_2 mode, discourages the coordination of more than three ligands and in principle avoids dimerization, although this is not always possible (see the diiron and dinickel examples in **Figure 3**).[4,30,31]

Compound **L2**, containing a dangling pyrene group in the α-carbon position was prepared by deprotonation of **L1** with nBuLi followed by alkylation with 1-(bromomethyl)pyrene as shown in the bottom of **Figure 4**. Compound **L2** is isolated as a mixture of both tautomers in a ratio of 1:1.4 (imine:enamine) in a 39% overall yield. A small sample of the imine tautomer could be isolated in pure form and characterized by ^{1}H NMR spectroscopy (**Figure S6** in the SI). On the other hand, crystals of the enamine tautomer suitable for X-ray diffraction analysis were obtained after slow evaporation of a DCM solution of the mixture (**Figure S78** in the SI).

Chapter 3.

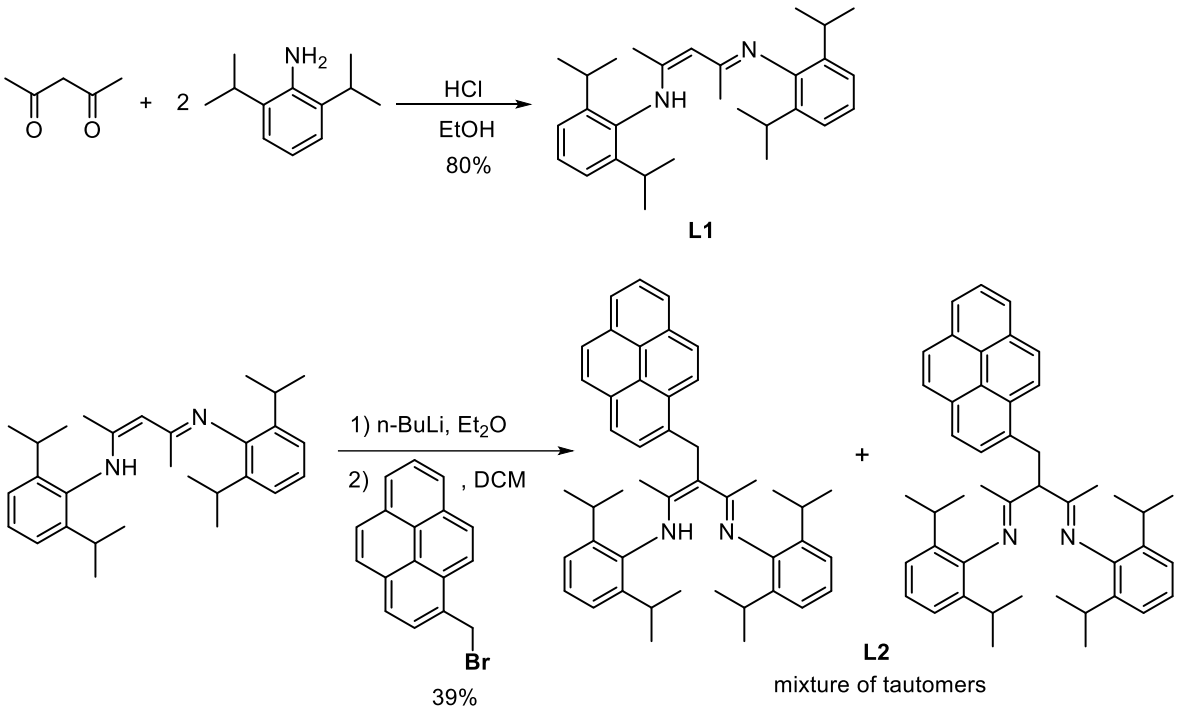

Figure 4. Synthesis of BDI compounds **L1** and **L2**.

Alternative routes starting from the β-diketone 3-(pyren-1-ylmethyl)pentane-2,4-dione (**Figure 5**) did not work presumably due to the low solubility of the substituted diketone substrate in common solvents needed for the condensation reaction as well as the electronic effects of the pyrene group. The low solubility of this compound is a consequence of the inter and intramolecular π-π interactions with other pyrene groups or the diisopropylphenyl substituent favoring aggregation. Noteworthy, the alkylation of the α-dicarbonylic position was successfully performed and the intermediate could be isolated in a 60 % yield, while traces of the bis(alkylated) product 3,3-bis(pyren-1-ylmethyl)pentane-2,4-dione could also be detected and crystallized (**Figures S79** and **S80** in the SI).

Chapter 3.

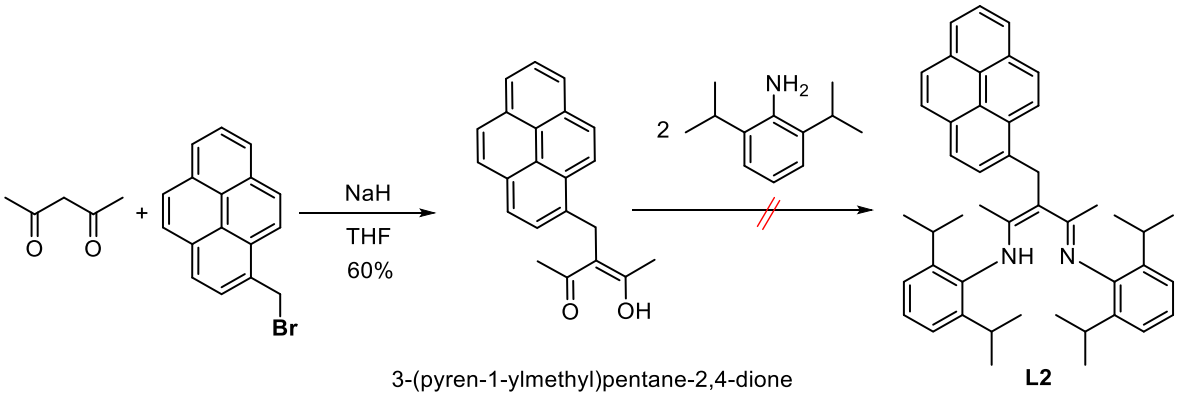

Figure 5. Attempt of preparing compound **L2** via direct condensation of 3-(pyren-1-ylmethyl)pentane-2,4-dione.

The presence of a pyrene moiety in the ligand backbone of **L2** will enable the resulting complexes to be anchored on graphitic substrates via π-π stacking interactions Compounds **L1** and **L2**, whose structure and overall reaction yields are summarized in **Table 1**, were used to prepare iron complexes, whose synthesis and characterization is presented in Chapter 4.

Table 1. Summary of κ^2-N_2 ligands.

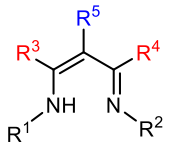

$R^3 = R^4 = CH_3$

Compound	R^1	R^2	R^5	Overall Yield (%)[a]	Drawing
L1	$(^i Pr)_2Ph$	$(^i Pr)_2Ph$	H	80 %	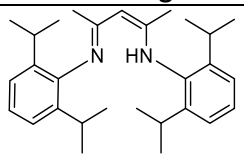
L2	$(^i Pr)_2Ph$	$(^i Pr)_2Ph$	(CH_2)Pyrene	31 %	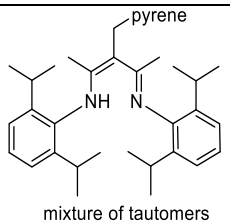

[a]From 2,4-pentanedione.

Chapter 3.

2.2- κ^3-PN_2 ligands L3-6 and κ^3-PNO ligand L7

This family of ligands are the result of the substitution of one of the bulky 2,6-diisopropylphenyl arms in ligand **L1** with a diphenylphosphinoalkyl arm, which provides an additional coordination site. The presence of the extra phosphorous atom can provide unique properties to the resulting complexes as compared to κ^2-N_2 ligands: i) increased stability due to the tridentate nature of the ligand; ii) stabilization of low oxidation states due to the π-acceptors character of the phosphine; iii) flexibility allowing the complex to adopt different geometries along catalytic cycles.

The preparation of the κ^3-PN_2 asymmetric ligands starts with the mono condensation reaction of a β-diketone derivative with one equivalent of 2,6-diisopropylaniline as indicated in the left of **Figure 6**. Three substrates were tested with different substituents in the α-carbon position (R = H, Ph or 2-CO_2H-Ph, **Figure 6**). As described in the literature, the substrate with R = H could be successfully prepared using catalytic amount of p-toluensulfonic acid (p-TsOH) in toluene using a Dean-Stark apparatus.[36] However, this method did not work for the other two compounds. For the phenyl derivative, an alternative solvent-free strategy based on microwave activation in the presence of catalytic amount of HCl was developed, allowing to isolate pure compound in a 27% yield. The low yields obtained for both reactions are associated with the formation of the bis(condensation) product (see **L1** in Figure 4). Finally, the third derivative could not be isolated, instead a side-product was detected by ^{1}H NMR that has been tentatively assigned to the enamine derivative in **Figure 6** (right), see also **Figure S30**. This compound is the result of a deacetylation reaction, presumably favored by the presence of the carboxylic acid in the ortho-phenyl position.

Chapter 3.

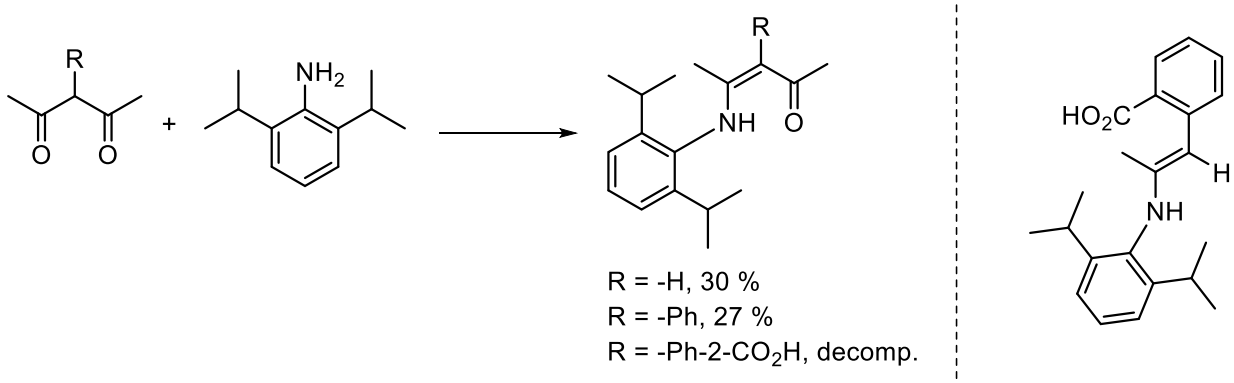

Figure 6. Left) Monocondensation reactions of β-diketones with 2,6-diisopropylaniline. Right) Side-product isolated from the reaction using the β-diketone with the group R = -Ph-CO_2H in the α-carbon position.

using p-TsOH in toluene in a Dean-Stark apparatus worked in all cases allowing to isolate ligands **L3**, **L4** and **L6** in moderate or low yields. Ligand **L5**, containing an ethyl(diphenyl)phosphine arm could not be isolated in pure form although the product could be identified in the reaction crude mixture together with starting materials in approximately 20 % conversion.

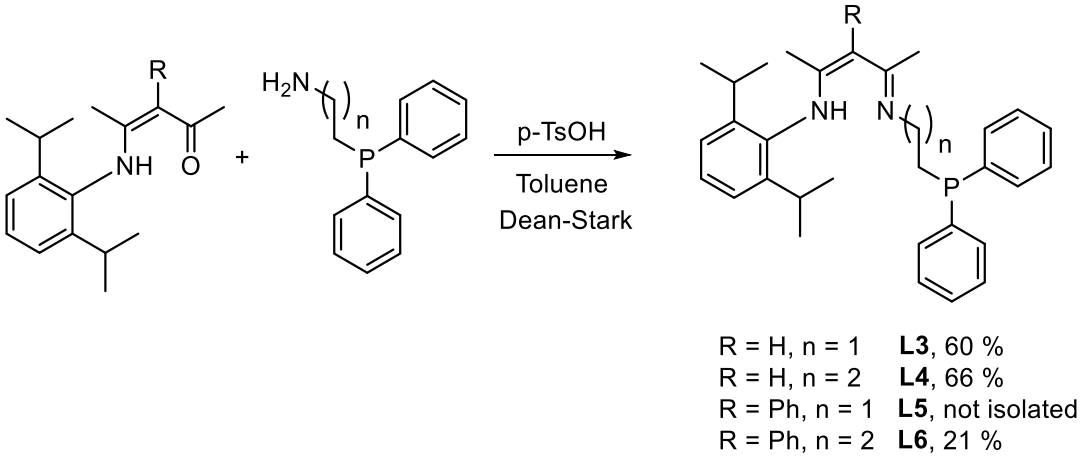

Figure 7. Synthesis of κ^2-PN_2 ligands **L3**-**L6**.

Finally, a last attempt to prepare ligand **L8** in **Figure 8** was carried out inverting the order of the condensation steps trying to avoid the unstable intermediate that lead to the product indicated in **Figure 6** (right, R = -Ph-CO_2H). First, the phosphine arm was introduced through

Chapter 3.

standard p-TsOH catalysis obtaining compound **L7** in 50% yield. Unfortunately, the final product **L8** could not be detected in the reaction crude mixtures of the next condensation reaction using p-TsOH in toluene. Instead, unidentified side-products were observed suggesting similar decomposition pathways to that observed for the intermediate in **Figure 6**. At this point, this derivative was no longer pursued.

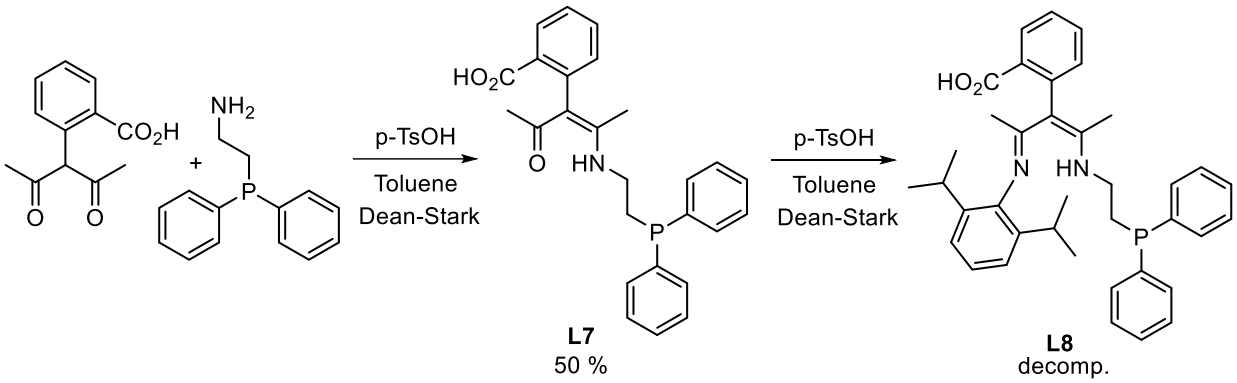

Figure 8. Attempt to prepare compound **L8** through intermediate **L7**.

Table 2. Summary of κ^3-PN_2 ligands and κ^3-PNO ligands.

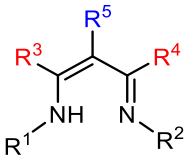

$R^3 = R^4 = CH_3$

Compound	R^1	R^2	R^5	Yield (%)[a]	Drawing
L3	$(^iPr)_2Ph$	$(CH_2)_2PPh_2$	H	18 %	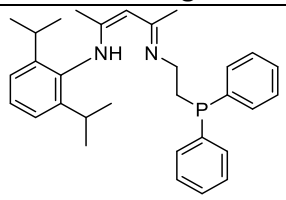
L4	$(^iPr)_2Ph$	$(CH_2)_3PPh_2$	H	20 %	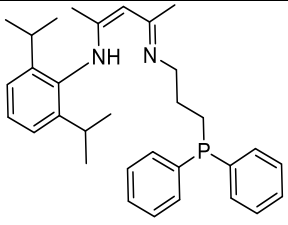

Chapter 3.

L6	$(^{i}Pr)_2Ph$	$(CH_2)_3PPh_2$	Ph	6 %	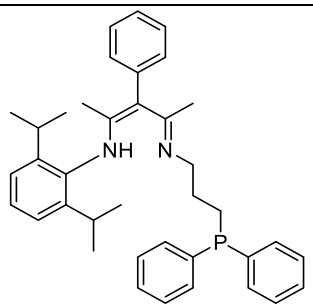
L7	-	$(CH_2)_2PPh_2$	2-CO_2H-Ph	50 %	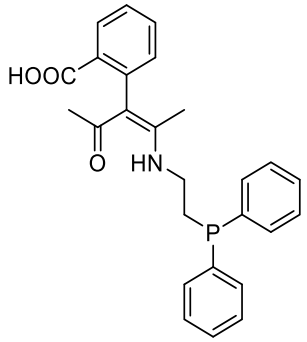

[a]From commercially available β-diketone.

2.3- κ^4-P_2N_2 ligands L9-L11

Symmetrical κ^4-P_2N_2 ligands derived from β-diketiminate are scarce in the literature, despite the well-known capacity of both BDK and phosphine groups to stabilize coordination complexes.[37] Following the series of ligands described in sections 3.1 and 3.2, three novel κ^4-P_2N_2 compounds resulting from the replacement of both bulky 2,6 diisopropylphenyl arms in **L1** with two diphenylphosphine alkyl groups are reported in this chapter **(Figure 9**).

First attempts to prepare the ligands through a double condensation reaction that worked for ligand **L1** (see top of Figure 4 for comparison) were unsuccessful, and only the monocondensation intermediate products could be isolated in excellent yields using standard condensation conditions with p-TsOH as catalyst in toluene solvent (**Figure 9**, left).

Chapter 3.

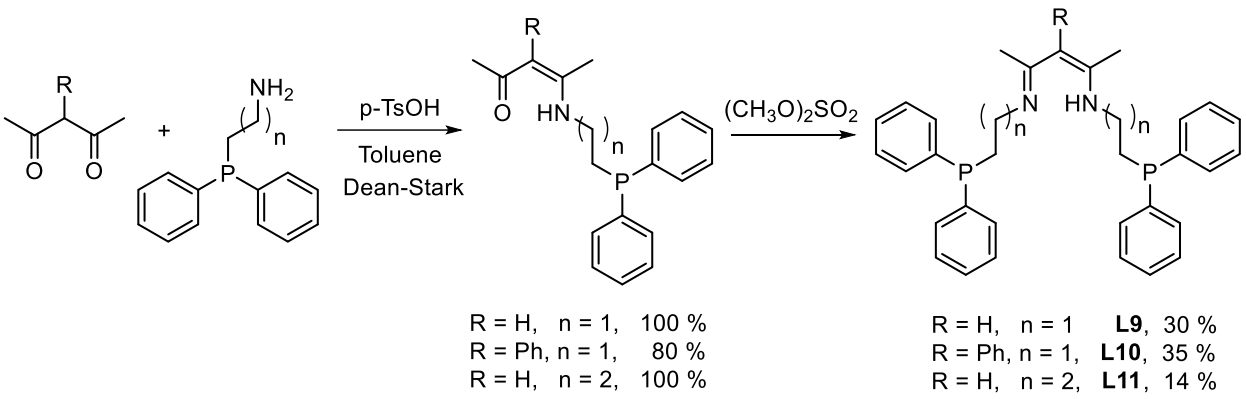

Figure 9. Synthesis of κ^4-P_2N_2 ligands **L9**-**L11**.

After exploring different alternative methods to introduce the second diphenylphosphinoalkyl arm, a route based on the use of dimethyl sulphate was found to be successful to prepare ligands **L9**-**L11** in moderate to low yields (**Figure 9**, right).[38–40] This reaction proceeds through the methylation of the carbonylic oxygen (**Figure 10**), making the group more electrophilic and enhancing the leaving group capacity of the oxygen. The reaction takes place in strictly anhydrous conditions and in a solvent free medium.

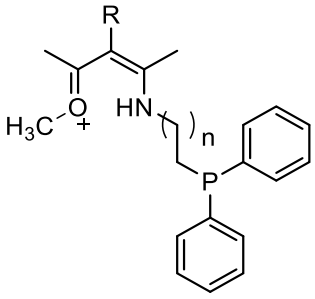

Figure 10. Intermediate species towards the second alkylation products.

Summarized in **Table 3** are the overall yields starting from commercially available β-diketones together with the structure of the three κ^4-P_2N_2 ligands that will be used in Chapters 4 and 5 to prepare iron and nickel complexes for the CO_2RR and PRR, respectively.

Chapter 3.

Table 3. Summary of κ^4-P_2N_2 ligands and ligands.

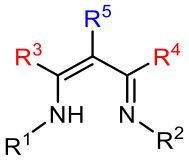

$R^3 = R^4 = CH_3$

Compound	$R^1 = R^2$	R^5	Yield (%)[a]	Drawing
L9	$(CH_2)_2PPh_2$	H	30 %	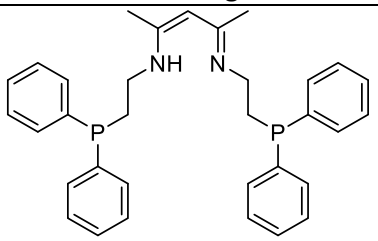
L10	$(CH_2)_2PPh_2$	Ph	28 %	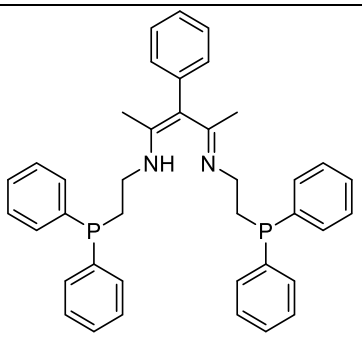
L11	$(CH_2)_3PPh_2$	H	14 %	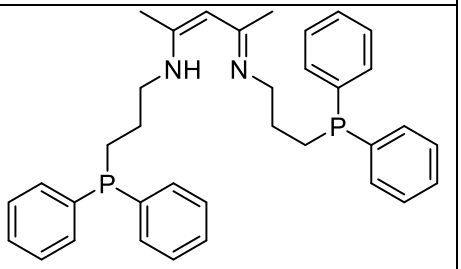

[a]From commercially available β-diketone.

3- Conclusions

In this chapter, nine BDI compounds have been reported with the aim of preparing BDI and BDK metallic complexes for the CO_2RR or PRR reactions with different coordination number, tuned electronic density as well as the ability to be anchored on graphitic solid supports. In particular, the imine nitrogen atoms have been modified to obtain a series of κ^3-PN_2 or κ^3-PNO asymmetric ligands and κ^2-N_2 or κ^4-P_2N_2 symmetric ligands (**Figure 11**). In addition, the α-intradiimino carbon has been successfully derivatized with phenyl or pyren-1-ylmethyl groups

Chapter 3.

(see ligands **L2**, **L6** and **L10**, **Figure 11**). All the ligands have been tested in complexation reactions using iron, nickel, and cobalt precursors. As illustrated in **Figure 11**, ligands **L2**, **L9** and **L10** were used to prepare Fe complexes for the CO_2RR and the results are described in detail in Chapter 5 of this manuscript. In addition, ligands **L9** and **L10** were also successfully used in the preparation of Ni complexes active for the PRR as described in detail in Chapter 4 of this manuscript. The preparation of metal derivatives of κ^3-PN_2 and κ^3-PNO ligands resulted more challenging due to the low reproducibility of the synthesis and the highly air-sensitivity nature of the resulting complexes and are not included in the framework of this thesis.

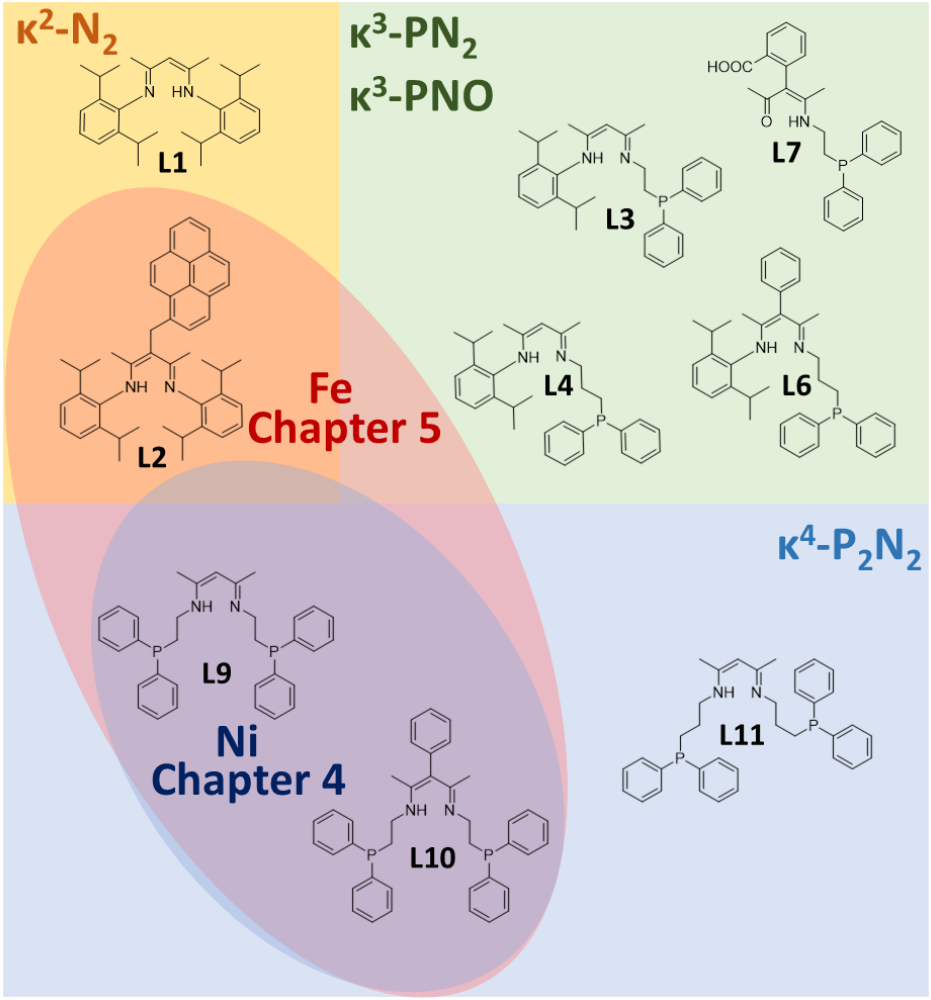

Figure 11. Ligands reported in this chapter classified according to denticity.

Chapter 3.

4- Experimental section

4.1- Synthesis of *N*-((2,4)-4-((2,6-diisopropylphenyl) imino)pent-2-en-2-yl)-2,6-diisopropylaniline, L1

Synthesis of **L1** was performed following a reported procedure.[4] To a mixture of 2,4-pentanedione (668 mg, 67 mmol) and 2,6-diisopropylaniline (23,8 g, 134 mmol) in 300 mL of ethanol in a two-neck 500 mL round-bottomed flask were added 4 mL of hydrochloric acid (12 M). The reaction mixture was heated to reflux with vigorous stirring for 3 days under nitrogen. The resulting slurry was allowed to cool down to room temperature. Then, the mixture was evaporated to dryness to yield a light brown solid. The solid residue was suspended in hexane and heated to reflux for 1h. After cooling down the mixture, the resulting solid was filtered, dried under reduced pressure, and identified as the pure desired compound by NMR spectroscopy (22.4 g, 53.6 mmol, 80 %). **^{1}H NMR (300 MHz, $CDCl_3$)** δ 12.11 (s, 1H), 7.13 (s, 5H), 4.88 (s, 1H), 3.12 (hept, *J* = 6.9 Hz, 4H), 1.72 (s, 6H), 1.23 (s, 6H), 1.13 (d, *J* = 6.8 Hz, 12H).**^{13}C NMR (101 MHz, $CDCl_3$)** δ 161.20, 142.48, 140.74, 125.10, 123.04, 93.25, 28.21, 24.24, 23.24, 20.77. **Anal. Calcd:** C, 83.20; H, 10.11; N, 6.69. **Found**: C, 83.019; H, 10.24; N, 6.64. **ESI-Mass**: Calcd for $[C_{29}H_{43}N_2]$ m/z=418.3, found $[M-H]^+$ m/z :419.3

4.2- Synthesis of *N*-((2*Z*,4*E*)-4-((2,6-diisopropylphenyl)imino)-3-(pyren-1-ylmethyl)pent-2-en-2-yl)-2,6-diisopropylaniline and (2*E*,4E)-*N*2,*N*4-bis(2,6-diisopropylphenyl)-3-(pyren-1-ylmethyl)pentane-2,4-diimine, L2 mixture of tautomers

To a solution of compound **L1** (708 mg, 1.69 mmol) in dried diethyl ether (50 mL) was added n-butyl lithium (0.68 mL, 2.5 M in n-hexane) dropwise at -20 ^{o}C under stirring. The reaction was allowed to warm up to room temperature. After 2 h a solution of 1-bromomethylpyrene (511 mg, 1.72 mmol) dissolved in dry DCM was added to the previous solution. The reaction mixture was stirred for three days at room temperature. After this time, the solution was dried under vacuum and the residue was treated with DCM and water. The yellow organic phase was separated, and the aqueous phase washed with additional DCM. The organic fractions were combined, dried with anhydrous sodium sulfate and evaporated to dryness. The resulting solid

was dissolved in n-hexane and the solution was stored overnight at -20 °C. A pale-yellow colored solid was formed, which was filtered, dried under vacuum and identified as a mixture of the enamine and imine forms of compound **L2** (420 mg, 0.66 mmol, 39 %). **^{1}H NMR (400 MHz, C_6D_6)** δ enamine: 14.4 (s, 1H, N*H*), 7.82-8.50 (m, 9H), 7.15-7.34 (m, 6H), 4.48. (s, 2H), 3.63. (hept, 4H), 1.82 (s, 6H), 1.39 (s, 24 H); imine: 7.82-8.68 (m, 9H), 7.17-7.27 (m, 6H), 4.78 (t, *J* = 4Hz, 1H), 4.38. (d, *J* = 4Hz, 2H), δ = 2.92 (hept, *J* = 6.9 Hz, 2H), 2.55. (hept, *J* = 6.9 Hz, 2H), 1.86 (s, 6H), 1.18 (d, *J* = 4Hz, 6H), 1.28. (d, *J* = 4Hz, 6H), 1.00 (d, *J* = 4Hz, 6H), 1.10. (d, *J* = 4Hz, 6H). **ESI-Mass:** Calcd for $[M + H]^+$: 633.42. **Found** 633.4.

4.3- Synthesis of 3-(pyren-1-ylmethyl)pentane-2,4-dione

2,4-pentanedione (0.242 mL, 2.34 mmol) was added into a suspension of NaH (62% suspended in oil, 103 mg, 2.6 mmol) in anhydrous THF. The mixture was stirred at room temperature for 2 h. After that, it was cooled down into an ice bath and 1-bromomethylpyrene (690 mg, 2.34 mmol) dissolved in dry THF was added. The mixture was stirred at room temperature for 2 days. After the addition of an aqueous 1M HCl solution into the reaction mixture at 0 °C, the organic phase was extracted with DCM and washed with water. The combined organic fractions were dried over Na_2SO_4 and then evaporated to afford a yellow solid, which was washed with a combined solution of ether and hexane to afford yellow crystalline solid (440 mg, 1.40 mmol, 60%). ^{1}H NMR in chloroform showed that the product was very pure and only exist in the enol form. **^{1}H NMR (400, $CDCl_3$)** δH: 8.43-8.39 (1H, d), 8.27-8.21 (3H, m), 8.18-8.15 (1H, d), 8.08-8.03 (3H, m), 7.80-7.76 (1H, d), 4.40 (2H, s), 2.10 (6H, s).

4.4- Synthesis of 4-((2,6-diisopropylphenyl) amino)pent-3-en-2-one

Synthesis of 4-((2,6-diisopropylphenyl)amino)pent-3-en-2-one was performed following a reported procedure.[20,36] In a 100 mL round bottom flask equipped with a Dean-Stark apparatus, acetyl acetone (2.4 mL, 21.2 mmol), 2,6-diisopropylaniline (4mL, 23.32 mmol) and a catalytic amount of (0.04 mg) of p-toluene sulfonic acid monohydrate were dissolved in 40 mL of dried and degassed toluene under nitrogen and the reaction mixture heated to reflux for 6 hours. After reaction, volatiles were removed by using rotary evaporator. The resulting residue was treated with water and extracted with diethyl ether (3 × 20ml). The combined organic fractions were

Chapter 3.

washed twice by diluted acidic solution (0.5M HNO_3). The organic solvent was removed under vacuum and the residue dissolved in hexane and kept at -30℃ overnight to afford a yellowish-white crystalline compound (0.164g, 6.36 mmol, 30 %). **^{1}H NMR (400 MHz, $CDCl_3$)** δ 7.41 – 7.33 (m, 1H), 7.28 – 7.22 (m, 2H), 5.29 (s, 1H), 3.11 (hept, *J* = 6.8 Hz, 2H), 2.20 (s, 3H), 1.71 (s, 3H), 1.29 (d, *J* = 6.9 Hz, 6H), 1.23 (d, *J* = 6.8 Hz, 6H).**^{13}C NMR (101 MHz, $CDCl_3$)** δ 196.02, 163.46, 146.41, 133.62, 128.38, 123.67, 95.71, 31.04, 29.19, 28.60, 24.71, 22.79, 19.29.

4.5- Synthesis of N-((2, 4)-4-((2-(diphenylphosphaneyl) ethyl) imino) pent-2-en-2-yl)-2, 6-diisopropylaniline, L3

Synthesis of **L3** was performed following a reported procedure. [20,36] 4-((2,6-diisopropylphenyl) amino)pent-3-en-2-one (1.13 g, 4.36 mmol), 2-(diphenylphosphino) ethylamine (1 g, 4.36 mmol) and a catalytic amount of p-toluene sulfonic acid (0.04 mg,) were dissolved in dry and degassed toluene (50 mL) and heated to reflux for 3 days using a Dean-stark apparatus. The volatiles were removed under vacuum and the residue was dissolved in methanol. Having placed the solution at -30 ℃ overnight and removing supernatant afford compound **L3** as a yellow oil (1.44 g, 2.61 mmol, 60%).**^{1}H NMR (400 MHz, C_6D_6)**: δ 7.49 – 7.40 (m, 4H), 7.36 – 7.31 (m, 2H), 7.31 – 7.20 (m, 2H), 7.19 – 7.09 (m, 6H), 4.80 (d, *J* = 0.8 Hz, 1H), 3.39 – 3.19 (m, 4H), 2.34 – 2.25 (m, 2H), 1.79 (s, 3H), 1.64 (d, *J* = 0.6 Hz, 3H), 1.35 (dd, *J* = 8.0, 6.9 Hz, 13H). **^{13}C NMR (126 MHz, C_6D_6)**: δ 166.30, 154.87, 147.19, 138.59, 138.13, 132.88, 132.69, 128.54 (d, *J* = 6.7 Hz), 123.08, 94.12, 40.15, 30.98, 28.36, 24.08, 22.87, 21.54, 18.78.**^{31}P NMR (202 MHz, C_6D_6)**: δ -18.26. **Anal. Calcd:** C, 79.11; H, 8.35; N, 5.95. **Found**: C, 78.34; H, 8.66; N, 5.53; **ESI-Mass**: Calcd for m/z: $[C_{31}H_{40}N_2P]^+$=470.3, Found m/z: 471.29.

4.6- Synthesis of N-((2, 4)-4-((3-(diphenylphosphaneyl) propyl) imino) pent-2-en-2-yl)-2, 6-diisopropylaniline, L4

Synthesis of **L4** was performed following a reported procedure.[20,36] 4-((2,6-diisopropylphenyl)amino)pent-3-en-2-one (1.066 g, 4.11 mmol), 2-(diphenylphosphino)ethanamine (1 g, 4.11 mmol) and a catalytic amount of p-toluene sulfonic acid (0.04 mg,) were dissolved in dry and degassed toluene (50 mL) under nitrogen and the

Chapter 3.

reaction mixture heated to reflux for 3 days using a Dean-stark apparatus. After 3 days, The volatiles were removed under reduced pressure .The residue was dissolved in dry and degassed methanol and the mixture kept at -30 ℃ overnight to afford compound **L4** as a yellow crystalline solid, which was filtered and dried under vacuum (1.32 g, 2.71 mmol, 66%).**^{1}H NMR (400 MHz, C_6D_6)** δ 11.14 (s, 1H), 7.41 – 7.30 (m, 4H), 7.24 – 7.10 (m, 5H), 7.03 (dtdd, *J* = 5.6, 4.3, 2.8, 1.3 Hz, 6H), 4.72 – 4.67 (m, 1H), 3.14 (p, *J* = 6.9 Hz, 2H), 2.92 (q, *J* = 6.1 Hz, 2H), 2.04 – 1.95 (m, 2H), 1.67 (s, 3H), 1.63 – 1.50 (m, 6H), 1.19 (dd, *J* = 17.2, 6.9 Hz, 13H).**^{13}C NMR (126 MHz, C_6D_6)** δ 166.72, 155.63, 147.58, 139.30, 139.16, 138.38, 133.16, 132.98, 123.38 (d, *J* = 6.2 Hz), 93.88, 44.02, 43.88, 28.59, 27.60, 27.44, 25.86, 25.73, 24.26, 23.12, 21.78, 19.13. **^{31}P NMR (202MHz, C_6D_6)** δ -13.31.

4.7- Synthesis of 4-((2, 6-diisopropylphenyl) amino)-3-phenylpent-3-en-2-one

A sealed microwave vial containing 3-phenylpentane-2,4-dione (1.9 g, 10.78 mmol), 2,6-diisopropylaniline (1.9 g, 10.78 mmol) and one drop of concentrated HCl was placed in a microwave reactor for 10 min at (300W 130 ℃) producing a dense red oil. After cooling to room temperature, the reaction mixture was transferred to a separatory funnel using dichloromethane and washed with water (3 × 30 mL). The organic phase was dried over Na_2SO_4 and evaporated to dryness leaving a dark brown solid, which was treated with pentane and filtered through frit. The filtrate was evaporated affording a dark red oil, which was treated with a little amount of pentane and kept at -30℃ causing the formation of pale brown crystals of 4-((2,6-diisopropylphenyl)amino)-3-phenylpent-3-en-2-one (1.05 g, 2.91mmol, 27%). **^{1}H NMR (300 MHz, $CDCl_3$)** δ 13.25 (s, 1H), 7.50 – 7.20 (m, 8H), 3.17 (hept, *J* = 6.9 Hz, 2H), 2.00 (s, 3H), 1.49 (s, 3H), 1.28 (dd, *J* = 6.9, 5.3 Hz, 12H).**^{13}C NMR (126 MHz, $CDCl_3$)** δ 195.56, 162.65, 146.31, 140.84, 134.17, 132.33, 128.76, 128.23, 126.79, 123.74, 29.32, 28.79, 24.73, 22.88, 17.99.

4.8- Synthesis of-((2, 4)-4-((3-(diphenylphosphaneyl)propyl) imino)-3-phenylpent-2-en-2-yl)-2,6-diisopropylaniline), L6

A round bottom flask equipped with a Dean-Stark apparatus containing (0.6g, 1.68mol) 4-((2, 6-diisopropylphenyl) amino)-3-phenylpent-3-en-2-one (0.6 g, 1.68 mmol) and a catalytic amount of p-toluene sulfonic acid (0.05 g) was subjected to vacuum-nitrogen cycles to provide

an inert atmosphere. Dry and degassed toluene was added to the reaction set-up using cannula. The reaction mixture was warmed up to 80℃ under nitrogen flow. After 1h, 2-(diphenylphosphino) propyl amine (1 g, 4.11 mmol) in dry and degassed toluene was added dropwise and the reaction mixture warmed up to reflux. Monitoring by ^{1}H NMR, the reaction judged to be complete after 3 days. After this time, the volatiles were removed by reduced pressure resulting in a yellow oil. Dry and degassed ethanol was added to dissolve the oily product and the mixture kept at -30℃ causing the precipitation of a white solid identified as compound **5** (200 mg, 0.4 mmol, 21%).**^{1}H NMR (400 MHz, C_6D_6)** δ 7.51 – 7.41 (m, 4H), 7.39 – 7.28 (m, 6H), 7.22 – 7.09 (m, 6H), 3.36 (p, *J* = 6.9 Hz, 2H), 3.12 (q, *J* = 6.4 Hz, 2H), 2.20 – 2.11 (m, 2H), 1.83 – 1.73 (m, 3H), 1.75 – 1.71 (m, 2H), 1.66 (s, 3H), 1.33 (t, *J* = 6.8 Hz, 12H).**^{13}C NMR (101 MHz, C_6D_6)** δ 167.60, 154.68, 146.96, 143.52, 139.32, 139.18, 138.48, 133.18, 133.12, 133.00, 132.53, 128.82, 128.75, 128.69, 126.37, 123.95, 123.54, 123.50, 106.66, 44.60, 44.46, 30.22, 29.08, 28.76, 27.49, 27.32, 26.16, 26.02, 24.63, 24.42, 23.21, 22.75, 21.84, 17.07.**^{31}P NMR (162 MHz, C_6D_6)** δ -13.06.

4.9- Synthesis of 2-(2-((2-(diphenylphosphaneyl) ethyl) amino)-4-oxopent-2-en-3-yl) benzoic acid, L7

A round bottom flask equipped with Dean-Stark apparatus containing 2-(1-acetyl-2-oxopropyl) benzoic acid (0.96 g, 4.36 mmol) and a catalytic amount of p-toluene sulfonic acid (0.05 g) was subjected to vacuum-nitrogen cycles to provide an inert atmosphere. Dry and degassed toluene was added to the reaction set-up using cannula. The reaction mixture was warmed up to 80℃ under nitrogen flow. After 1h, 2-(diphenylphosphino) ethylamine (1 g, 4.36 mmol) in dry and degassed toluene was added dropwise and the reaction mixture warmed up to reflux. Monitoring by ^{1}H NMR, the reaction judged to be complete after 24h. After this time, removing the volatiles by reduced pressure resulted in a yellow oil. Dry and degassed ethanol was added to dissolve the oily product and the mixture kept at -30℃ causing the precipitation of a white solid, which was identified as compound **L6** (100 mg, 2.18mmol, 50%).**^{1}H NMR (500 MHz, C_6D_6)** δ 8.77 (ddd, *J* = 8.0, 1.4, 0.8 Hz, 1H), 7.48 (tt, *J* = 7.4, 1.4 Hz, 3H), 7.17 – 7.14 (m, 6H), 7.08 (ddt, *J* = 7.4, 4.4, 1.4 Hz, 4H), 7.02 (dddd, *J* = 8.4, 6.0, 2.3, 1.2 Hz, 2H), 3.93 (d, *J* = 8.5 Hz, 2H), 2.31 – 2.24 (m, 2H), 2.05 (s, 3H), 1.53 (s, 3H).**^{13}C NMR (126 MHz, C_6D_6)** δ 161.50, 137.99 (d, *J* = 13.3 Hz), 135.43, 133.33, 132.80 (d, *J* = 19.1 Hz), 132.16, 126.26, 124.82, 122.68, 119.17, 41.69 (d, *J* = 28.5 Hz), 32.37, 26.97 (d, *J* = 15.4 Hz), 16.38.**^{31}P**

Chapter 3.

NMR (202 MHz, C_6D_6) δ -20.83.

4.10- Synthesis of 4-((2-(diphenylphosphaneyl) ethyl) amino) pent-3-en-2-one,

A round bottom flask equipped with a Dean-Stark apparatus was charged with a catalytic amount of p-toluene sulfonic acid (0.04 g) and the set-up subjected to vacuum-nitrogen cycles to provide an inert atmosphere. A solution of acetyl acetone (0.43 g, 4.36 mmol) in 20 mL of dry and degassed toluene was added by cannula and the mixture stirred under nitrogen atmosphere at RT. After 1 h of stirring, 2-diphenylphosphinoethylamine (1 g, 4.36 mmol) in 20 mL of dry and degassed toluene was added and the reaction mixture warmed up to reflux under nitrogen atmosphere. After 24 h the reaction was cooled down to room temperature and the volatiles removed by reduced pressure resulting in a yellow oily compound, identified as the desired compound by NMR spectroscopy (1.35 g, 4.36 mmol, 100%). **^{1}H NMR (500 MHz, C_6D_6)** δ 11.36 (s, 1H), 7.38 – 7.29 (m, 4H), 7.16 – 7.08 (m, 6H), 4.92 (s, 1H), 3.00 – 2.91 (m, 2H), 2.13 (s, 3H), 2.05 – 1.95 (m, 2H), 1.32 (s, 3H). **^{13}C NMR (126 MHz, C_6D_6)** δ 194.62, 161.49, 138.65 – 138.54 (m), 133.24, 95.76, 40.24, 29.12, 18.31. **^{31}P NMR (202 MHz, C_6D_6)** δ -18.22.

4.11- Synthesis of (2, 4)-N-(2-(diphenylphosphaneyl) ethyl (diphenylphosphaneyl) ethyl) imino) pent-2-en-2-amine, L9

Inside the glove box, 4-((2-(diphenylphosphaneyl) ethyl) amino) pent-3-en-2-one (1 g, 3.21 mmol) and dimethyl sulfate (0.4 mL, 4.4 mmol) were stirred for 30 min. During this time, fume appeared and the reaction mixture became dense. The reaction mixture was maintained overnight without stirring. Then, 2-diphenylphosphinoethylamine (1 g, 4.36 mmol) in 2 mL of dry and degassed methanol were added and stirred forming a viscous red oil. After 3h, sodium methoxide (0.17g 3.21 mmol) dissolved in 10 mL of dry and degassed methanol was added and immediately after the mixture became cloudy and a white precipitate started to appear. The reaction stirring continued for another 3 h. The white precipitate was filtered, washed with 100 mL of MeOH and dried under vacuum (500 mg, 0.96 mmol, 30%).**^{1}H NMR (500 MHz, C_6D_6)** δ 7.59 – 7.49 (m, 8H), 7.16 – 7.07 (m, 12H), 4.63 (s, 1H), 3.49 – 3.37 (m, 4H), 2.59 – 2.52 (m, 4H), 1.66 (s, 6H).**^{13}C NMR (126 MHz, C_6D_6)** δ 160.15, 139.94, 139.82, 133.44, 133.29, 95.36, 43.98, 43.83, 31.62 (d, J = 10.7 Hz), 19.41.**^{31}P NMR (202 MHz, C_6D_6)** δ -17.26. **Anal. Calcd:**

Chapter 3.

C, 75.84; H, 6.94; N, 5.36; P, 11.85 **Found**: C, 75.04; H, 6.62; N, 5.26; P, 11.85 ; **ESI-Mass**: Calcd for, $[C_{33}H_{36}N_2P_2]$ =522.2, Found $[M-H]^+$ m/z: 523.2.

4.12- Synthesis of 4-((2-(diphenylphosphaneyl) ethyl) amino)-3-phenylpent-3-en-2-one

A round bottom flask equipped with a Dean-Stark apparatus containing a catalytic amount of p-toluene sulfonic acid (0.04 g) and 3-phenyl-2,4-pentanedione (0.76 g, 4.36 mmol) was subjected to vacuum-nitrogen cycles to provide an inert atmosphere. 20 mL of dry and degassed toluene were added by cannula and the mixture stirred under nitrogen atmosphere at RT. After 1 h, a solution of 3-diphenylphosphinoethylamine (1 g, 4.36 mmol) in 20 mL of dry and degassed toluene was added and the reaction mixture heated up to reflux under nitrogen. After 24 h, the refluxing of the reaction was stopped and the volatiles removed under reduced pressure. The resulting yellow oil was identified as the desired compound (1.2 g, 3.48 mmol, 80 %).**^{1}H NMR (500 MHz, C_6D_6)** δ 12.63 (s, 1H), 7.41 – 7.33 (m, 3H), 7.27 – 7.20 (m, 3H), 7.20 – 7.06 (m, 9H), 3.12 – 3.03 (m, 2H), 2.21 – 2.11 (m, 2H), 2.08 (s, 3H), 1.30 (s, 3H).**^{13}C NMR (126 MHz, C_6D_6)** δ 194.21, 160.59, 142.05, 141.82, 138.91, 138.66, 138.55, 133.17, 133.01, 132.68, 132.57 (d, *J* = 2.6 Hz), 131.55, 131.46 – 131.19 (m), 131.00, 130.92, 129.12, 128.84 (dd, *J* = 13.6, 6.7 Hz), 126.86, 126.60, 109.86, 40.81, 40.60, 37.26, 37.09, 36.97, 32.35, 30.22, 29.94, 29.83, 29.47, 29.17, 29.06, 23.13, 22.85, 21.20, 16.39, 16.19, 14.38, 1.41.**^{31}P NMR (202 MHz, C_6D_6)** δ -18.04.

4.13- Synthesis of (2,4)-N-(2-(diphenylphosphaneyl)ethyl)-4-((2-(diphenylphosphaneyl)ethyl)imino)-3-phenylpent-2-en-2-amine, L10

Inside the glove box, (2, 4)-N-(2-(diphenylphosphaneyl) ethyl)-4-((2-(diphenylphosphaneyl) ethyl) imino)-3-phenylpent-2-en-2-amine (1.4 g, 4.36 mmol) and dimethyl sulfate (0.4 mL, 4.36mmol) were stirred for 30 min. During this time, fume appeared, and the mixture became dense. The reaction mixture was maintained overnight without stirring, producing a very dense red-orange oily mixture. A solution of 2-diphenylphosphinoethylamine (1 g, 4.36 mmol) in 2 mL of dry and degassed methanol was added. 20 min after the addition, a white dense solid appeared, which was diluted in 2 mL of methanol in order to make the reaction mixture easier to stir. After 3 h, a solution of sodium methoxide (0.23 g, 4.36 mmol) in 10 mL of dry and degassed methanol was added and immediately a white precipitate

appeared. Stirring continued for another 3 h. The resulting white solid was filtered off, washed with 100 mL of MeOH and dried under vacuum (900 mg, 1.526 mmol, 35%).**^{1}H NMR (500 MHz, C_6D_6)** δ 13.27 (s, 1H), 7.60 – 7.50 (m, 7H), 7.29 – 7.19 (m, 8H), 7.19 – 7.05 (m, 10H), 3.52 (dt, *J* = 9.6, 7.4 Hz, 4H), 2.63 (dd, *J* = 8.2, 6.6 Hz, 4H), 1.57 (s, 6H).**^{13}C NMR (126 MHz, C_6D_6)** δ 160.17, 144.43, 139.89, 139.77, 133.44, 133.27 (d, *J* = 5.5 Hz), 126.17, 44.27, 44.11, 31.60 (d, *J* = 10.6 Hz), 17.79.**^{31}P NMR (202 MHz, C_6D_6)** δ -17.19. **Anal. Calcd:** C, 78.24; H, 6.73; N, 4.68; P, 11.85 **Found:** C, 78.18; H, 6.66; N, 4.53; ESI-**Mass**: Calcd for m/z: $[C_{31}H_{40}N_2P]$ =598.3, Found $[M-H]^+$ m/z: 599.29

4.14- Synthesis of 4-((3-(diphenylphosphaneyl) propyl) amino) pent-3-en-2-one

A round bottom flask equipped with a Dean-Stark apparatus containing p-toluene sulfonic acid (0.04 g) was subjected to vacuum-nitrogen cycles to provide an inert atmosphere. A solution of acetyl acetone (0.41 g, 4.11 mmol) in 20 mL of dry and degassed toluene was added by cannula. The reaction mixture was stirred under nitrogen atmosphere at RT. After 1 h, 3-diphenylphosphinopropylamine (1 g, 4.11 mmol) in 20 mL of dry and degassed toluene was added and the reaction mixture heated up to reflux under nitrogen. After 24 h, the reaction was completed, and the volatiles removed under reduced pressure. The resulting yellow oil was identified as the desired compound (1.33g, 4.11 mmol, 100 %).**^{1}H NMR (400 MHz, C_6D_6)** δ 11.37 (s, 1H), 7.52 (ddt, *J* = 7.3, 5.8, 1.5 Hz, 4H), 7.24 – 7.12 (m, 6H), 4.99 (s, 1H), 2.76 (q, *J* = 6.6 Hz, 2H), 2.17 (s, 3H), 2.01 – 1.92 (m, 2H), 1.56 – 1.46 (m, 2H), 1.45 (s, 3H).**^{13}C NMR (101 MHz, C_6D_6)** δ 194.20, 161.64, 138.87, 132.95, 95.31, 43.08, 28.73, 26.84, 25.11, 18.05.**^{31}P NMR (162 MHz, C_6D_6)** δ -14.04.

4.15- Synthesis of (2, 4)-N-(3-(diphenylphosphaneyl) propyl)-4-((3-(diphenylphosphaneyl) propyl) imino) pent-2-en-2-amine, L11

Inside the glove box, 4-((3-(diphenylphosphaneyl) propyl) amino) pent-3-en-2-one (1.33g, 4.11mmol) and dimethyl sulfate (0.6ml, 4.11mmol) were stirred for 30 min. During this time, fume appeared, and the mixture become dense. The reaction was maintained overnight without stirring producing a very viscose orange mixture. A solution of 2-diphenylphosphinopropylamine (1g, 4.11mmol) in 2 mL of dry and degassed methanol was added and the reaction mixture stirred. After 3 h, a solution of sodium methoxide (0.22 g, 4.11

mmol) in 10 mL of dry and degassed methanol were added causing the immediate formation of a cloudy mixture and the formation of a white precipitate. Stirring continued for another 3 h. The white solid was filtered off, washed with 100mL of MeOH and dried under vacuum (300 mg, 0.5 mmol, 14%).**^{1}H NMR (500 MHz, C_6D_6)** δ 11.55 (s, 1H), 7.53 (tt, *J* = 7.1, 1.5 Hz, 8H), 7.21 – 7.10 (m, 12H), 4.66 (s, 1H), 3.22 (t, *J* = 6.6 Hz, 4H), 2.22 – 2.15 (m, 4H), 1.87 – 1.77 (m, 4H), 1.73 (s, 6H).**^{13}C NMR (126 MHz, C_6D_6)** δ 160.49, 139.99, 133.39, 95.35, 47.65, 28.62, 26.38, 19.49.**^{31}P NMR (202 MHz, C_6D_6)** δ -13.41.

5- References

(1) Camp, C.; Arnold, J. On the Non-Innocence of "Nacnacs": Ligand-Based Reactivity in β-Diketiminate Supported Coordination Compounds. *Dalt. Trans.* **2016**, *45* (37), 14462–14498. https://doi.org/10.1039/c6dt02013e.

(2) Bourget-merle, L.; Lappert, M. F.; Severn, J. R. The Chemistry of -Diketiminatometal Complexes. *Chem. Rev.* 2002, 102, 9, 3031–3066

(3) Dugan, T. R.; Bill, E.; Macleod, K. C.; Brennessel, W. W.; Holland, P. L. Synthesis, Spectroscopy, and Hydrogen/Deuterium Exchange in High-Spin Iron(II) Hydride Complexes. *Inorg. Chem.* **2014**, *53* (5), 2370–2380. https://doi.org/10.1021/ic4013137.

(4) Vela, J.; Vaddadi, S.; Cundari, T. R.; Smith, J. M.; Gregory, E. A.; Lachicotte, R. J.; Flaschenriem, C. J.; Holland, P. L. Reversible Beta-Hydrogen Elimination of Three-Coordinate Iron(II) Alkyl Complexes: Mechanistic and Thermodynamic Studies. *Organometallics* **2004**, *23* (22), 5226–5239. https://doi.org/10.1021/om049415+.

(5) Honeybourne, C. L.; Webb, G. A. Some Metal Complexes of 1,3-Di-Imines. *Chem. Commun.* **1968**, No. 13, 739–740. https://doi.org/10.1039/C19680000739.

(6) Bonnett, R.; Bradley, D. C.; Fisher, K. J. Bis-(NN′-Diethylbutane-2,4-Di-Iminato)Cobalt(II), a Tetrahedral Cobalt Derivative of a New Nitrogen Chelate Group. *Chem. Commun.* **1968**, No. 15, 886–887. https://doi.org/10.1039/C19680000886.

Chapter 3.

(7) Holland, P. L.; Cundari, T. R.; Perez, L. L.; Eckert, N. A.; Lachicotte, R. J. Electronically Unsaturated Three-Coordinate Chloride and Methyl Complexes of Iron, Cobalt, and Nickel. *J. Am. Chem. Soc.* **2002**, *124* (48), 14416–14424. https://doi.org/10.1021/ja025583m.

(8) Webster, R. L. β-Diketiminate Complexes of the First Row Transition Metals: Applications in Catalysis. *Dalt. Trans.* **2017**, *46* (14), 4483–4498. https://doi.org/10.1039/c7dt00319f.

(9) Landolsi, K.; Rzaigui, M.; Bouachir, F. Synthesis and Structure of Cationic Nickel Allyl Complexes Supported by β-Diimine Ligands. *Tetrahedron Lett.* **2002**, *43* (51), 9463–9466. https://doi.org/10.1016/S0040-4039(02)02187-1.

(10) Feldman, J.; McLain, S. J.; Parthasarathy, A.; Marshall, W. J.; Calabrese, J. C.; Arthur, S. D. Electrophilic Metal Precursors and a β-Diimine Ligand for Nickel(II)- and Palladium(II)-Catalyzed Ethylene Polymerization. *Organometallics* **1997**, *16* (8), 1514–1516. https://doi.org/10.1021/om960968x.

(11) Chen, C.; Bellows, S. M.; Holland, P. L. Tuning Steric and Electronic Effects in Transition-Metal β-Diketiminate Complexes. *Dalt. Trans.* **2015**, *44* (38), 16654–16670. https://doi.org/10.1039/c5dt02215k.

(12) Khusniyarov , M. M.; Bill, E.; Weyhermüller, T.; Bothe, E.; Wieghardt, K. Hidden Noninnocence: Theoretical and Experimental Evidence for Redox Activity of a β-Diketiminate(1−) Ligand. *Angew. Chemie* **2011**, *123* (7), 1690–1693. https://doi.org/10.1002/ange.201005953.

(13) Gondzik, S.; Bläser, D.; Wölper, C.; Schulz, S. Non-Innocence of β -Diketiminato Ligands. **2015**, *783*, 92–95.

(14) Takaichi, J.; Morimoto, Y.; Ohkubo, K.; Shimokawa, C.; Hojo, T.; Mori, S.; Asahara, H.; Sugimoto, H.; Fujieda, N.; Nishiwaki, N.; Fukuzumi, S.; Itoh, S. Redox Chemistry of Nickel(II) Complexes Supported by a Series of Noninnocent β-Diketiminate Ligands. *Inorg. Chem.* **2014**, *53* (12), 6159–6169. https://doi.org/10.1021/ic5006693.

Chapter 3.

(15) Moilanen, J.; Javier, B. G.; Roesler, R.; Tuononen, H. M. Paramagnetic Aluminium β-Diketiminate. *Chem. Commun.* **2012**, *48* (71), 8949–8951. https://doi.org/10.1039/c2cc34051h.

(16) McKenzie, I.; Percival, P. W.; Clyburne, J. A. C. A Computational Study of the Reactions of a β-Diketiminatoaluminium(I) Complex with the Hydrogen Atom and the Electron. *Chem. Commun.* **2005**, No. 9, 1134–1136. https://doi.org/10.1039/b414665d.

(17) Erdogan, G.; Grotjahn, D. B. Supported Imidazolylphosphine Catalysts for Highly (E)-Selective Alkene Isomerization. *Org. Lett.* **2014**, *16* (11), 2818–2821. https://doi.org/10.1021/ol500327k.

(18) Thacker, N. C.; Lin, Z.; Zhang, T.; Gilhula, J. C.; Abney, C. W.; Lin, W. Robust and Porous β-Diketiminate-Functionalized Metal-Organic Frameworks for Earth-Abundant-Metal-Catalyzed C-H Amination and Hydrogenation. *J. Am. Chem. Soc.* **2016**, *138* (10), 3501–3509. https://doi.org/10.1021/jacs.5b13394.

(19) Rodriguez, M. M.; Bill, E.; Brennessel, W. W.; Holland, P. L. N2 Reduction and Hydrogenation to Ammonia by a Molecular Iron-Potassium Complex. *Science (80).* **2011**, *334* (6057), 780–783. https://doi.org/10.1126/science.1211906.

(20) Yao, T.; Xu, P.; Xu, X. Scandium Complexes Containing β-Diketiminato Ligands with Pendant Phosphanyl Groups: Competition between Sc/γ-C [4 + 2] Cycloaddition and Sc/P Frustrated Lewis Pair Reactions. *Dalt. Trans.* **2019**, *48* (22), 7743–7754. https://doi.org/10.1039/c9dt01035a.

(21) Mukhopadhyay, T. K.; Flores, M.; Groy, T. L.; Trovitch, R. J. A β-Diketiminate Manganese Catalyst for Alkene Hydrosilylation: Substrate Scope, Silicone Preparation, and Mechanistic Insight. *Chem. Sci.* **2018**, *9* (39), 7673–7680. https://doi.org/10.1039/c8sc02768d.

(22) Kirmse, W. Copper Carbene Complexes: Advanced Catalysts, New Insights. *Angew. Chemie - Int. Ed.* **2003**, *42* (10), 1088–1093. https://doi.org/10.1002/anie.200390290.

(23) Casey, K. C.; Appiah, J. K.; Robinson, J. R. Low-Symmetry β-Diketimine Aryloxide

Chapter 3.

Rare-Earth Complexes: Flexible, Reactive, and Selective. *Inorg. Chem.* **2020**, *59* (20), 14827–14837. https://doi.org/10.1021/acs.inorgchem.0c02170.

(24) Sadique, A. R.; Brennessel, W. W.; Holland, P. L. Reduction of CO_2 to CO Using Low-Coordinate Iron: Formation of a Four-Coordinate Iron Dicarbonyl Complex and a Bridging Carbonate Complex. *Inorg. Chem.* **2008**, *47* (3), 784–786. https://doi.org/10.1021/ic701914m.

(25) Pfirrmann, S.; Yao, S.; Ziemer, B.; Stösser, R.; Driess, M.; Limberg, C. β-Diketiminato Nickel(I) Complexes with Very Weak Ligation Allowing for H_2 and N_2 Activation. *Organometallics* **2009**, *28* (24), 6855–6860. https://doi.org/10.1021/om9007983.

(26) Dugan, T. R.; Sun, X.; Rybak-Akimova, E. V.; Olatunji-Ojo, O.; Cundari, T. R.; Holland, P. L. A Masked Two-Coordinate Cobalt(I) Complex That Activates C-F Bonds. *J. Am. Chem. Soc.* **2011**, *133* (32), 12418–12421. https://doi.org/10.1021/ja2052914.

(27) Roy, L.; Al-Afyouni, M. H.; Derosha, D. E.; Mondal, B.; Dimucci, I. M.; Lancaster, K. M.; Shearer, J.; Bill, E.; Brennessel, W. W.; Neese, F.; Ye, S.; Holland, P. L. Reduction of CO2 by a Masked Two-Coordinate Cobalt(i) Complex and Characterization of a Proposed Oxodicobalt(Ii) Intermediate. *Chem. Sci.* **2019**, *10* (3), 918–929. https://doi.org/10.1039/c8sc02599a.

(28) Duan, P.; Schulz, R. A.; Römer, A.; Van Kuiken, B. E.; Dechert, S.; Demeshko, S.; Cutsail, G. E.; DeBeer, S.; Mata, R. A.; Meyer, F. Ligand Protonation Triggers H_2 Release from a Dinickel Dihydride Complex to Give a Doubly "T"-Shaped Dinickel(I) Metallodiradical . *Angew. Chemie* **2021**, *133* (4), 1919–1924. https://doi.org/10.1002/ange.202011494.

(29) Stevens, H.; Duan, P. C.; Dechert, S.; Meyer, F. Competing H2 versus Intramolecular C-H Activation at a Dinuclear Nickel Complex via Metal-Metal Cooperative Oxidative Addition. *J. Am. Chem. Soc.* **2020**, *142* (14), 6717–6728. https://doi.org/10.1021/jacs.0c00758.

(30) Mehn, M. P.; Peters, J. C. Mid- to High-Valent Imido and Nitrido Complexes of Iron. *J.*

Inorg. Biochem. **2006**, *100* (4), 634–643. https://doi.org/10.1016/j.jinorgbio.2006.01.023.

(31) Holland, P. L. Electronic Structure and Reactivity of Three-Coordinate Iron Complexes. *Acc. Chem. Res.* **2008**, *41* (8), 905–914. https://doi.org/10.1021/ar700267b.

(32) Garrido-Barros, P.; Gimbert-Surinifach, C.; Moonshiram, D.; Picón, A.; Monge, P.; Batista, V. S.; Llobet, A. Electronic I-Delocalization Boosts Catalytic Water Oxidation by Cu(II) Molecular Catalysts Heterogenized on Graphene Sheets. *J. Am. Chem. Soc.* **2017**, *139* (37), 12907–12910. https://doi.org/10.1021/jacs.7b06828.

(33) Matheu, R.; Moreno-Hernandez, I. A.; Sala, X.; Gray, H. B.; Brunschwig, B. S.; Llobet, A.; Lewis, N. S. Photoelectrochemical Behavior of a Molecular Ru-Based Water-Oxidation Catalyst Bound to TiO2-Protected Si Photoanodes. *J. Am. Chem. Soc.* **2017**, *139* (33), 11345–11348. https://doi.org/10.1021/jacs.7b06800.

(34) Creus, J.; Matheu, R.; Peñafiel, I.; Moonshiram, D.; Blondeau, P.; Benet-Buchholz, J.; García-Antón, J.; Sala, X.; Godard, C.; Llobet, A. A Million Turnover Molecular Anode for Catalytic Water Oxidation. *Angew. Chemie - Int. Ed.* **2016**, *55* (49), 15382–15386. https://doi.org/10.1002/anie.201609167.

(35) Garrido-Barros, P.; Matheu, R.; Gimbert-Suriñach, C.; Llobet, A. Electronic, Mechanistic, and Structural Factors That Influence the Performance of Molecular Water Oxidation Catalysts Anchored on Electrode Surfaces. *Curr. Opin. Electrochem.* **2019**, *15*, 140–147. https://doi.org/10.1016/j.coelec.2019.04.027.

(36) Xu, P.; Yao, Y.; Xu, X. Frustrated Lewis Pair-Like Reactivity of Rare-Earth Metal Complexes: 1,4-Addition Reactions and Polymerizations of Conjugated Polar Alkenes. *Chem. - A Eur. J.* **2017**, *23* (6), 1263–1267. https://doi.org/10.1002/chem.201605622.

(37) Zovko, C.; Bestgen, S.; Schoo, C.; Görner, A.; Goicoechea, J. M.; Roesky, P. W. A Phosphine Functionalized β-Diketimine Ligand for the Synthesis of Manifold Metal Complexes. *Chem. - A Eur. J.* **2020**, *26* (58), 13191–13202. https://doi.org/10.1002/chem.202001357.

Chapter 3.

(38) Pichlmair, S. Spotlight 79. *Synlett* ***2004****(1): 195-196*. https://doi.org/10.1055/s-2003-44976.

(39) Bradley, A. Z.; Thorn, D. L.; Glover, G. V. Efficient Synthesis of Alkyl -Diketimines. *J. Org. Chem.* ***2008****, 73, 8673–8674*

(40) Benson, B. R. E.; Cairns, T. L.; Benson, *Dalt. Trans.*. **1992**, *208* (2), 2115–2118.

Supporting information

Table of contents

Chapter 3.

1- NMR spectroscopy

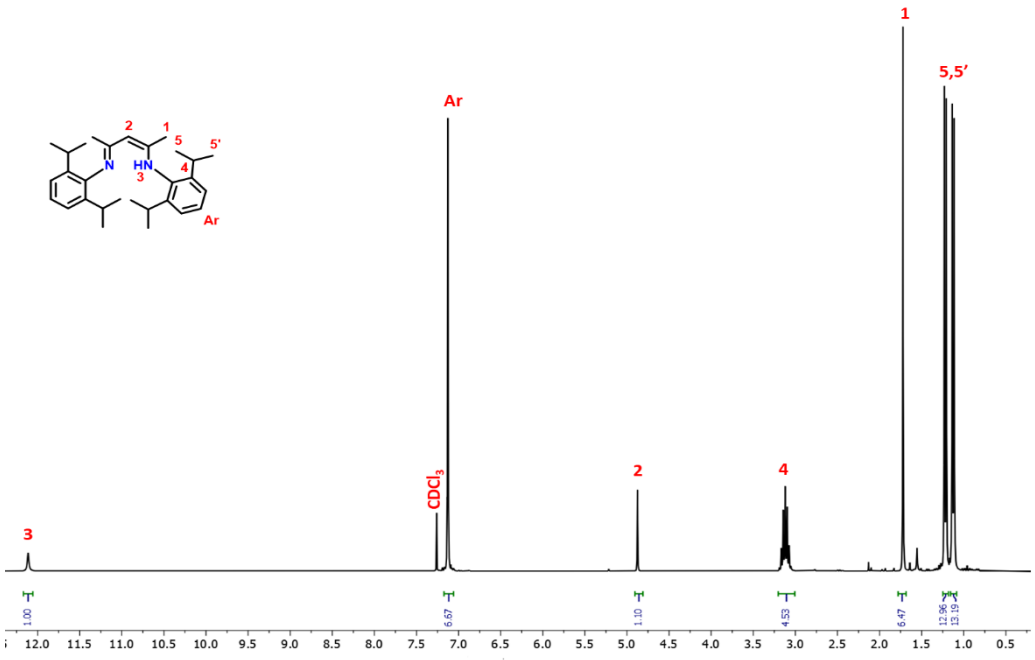

Figure S1. ^{1}H-NMR of **L1** (300MHZ, $CDCl_3$)

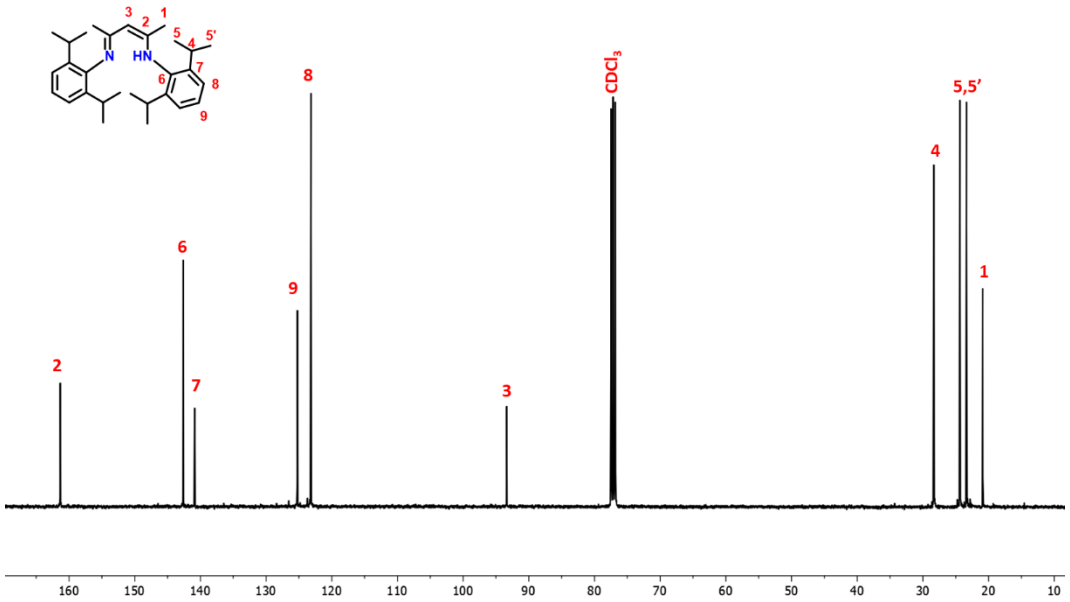

Figure S2. ^{13}C NMR of **L1** (101 MHZ, $CDCl_3$)

Chapter 3.

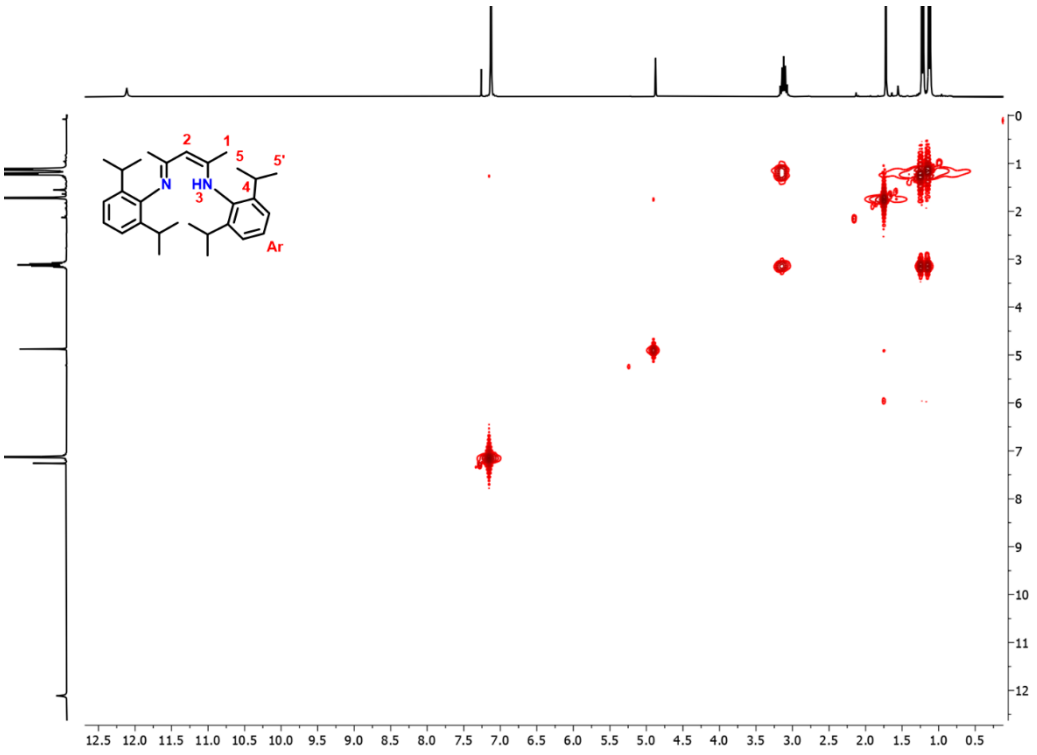

Figure S3. ^{1}H-^{1}H Cosy NMR of **L1** (300MHZ, $CDCl_3$)

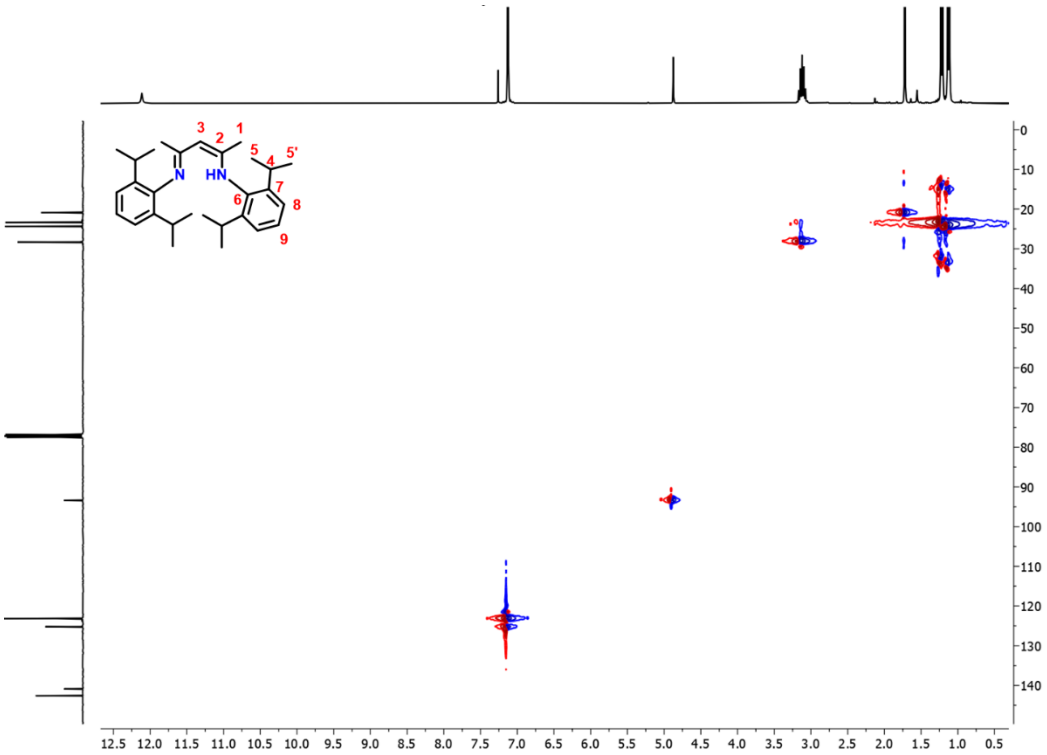

Figure S4. ^{1}H- ^{13}C HSQC NMR of **L1** (300MHZ, $CDCl_3$)

Chapter 3.

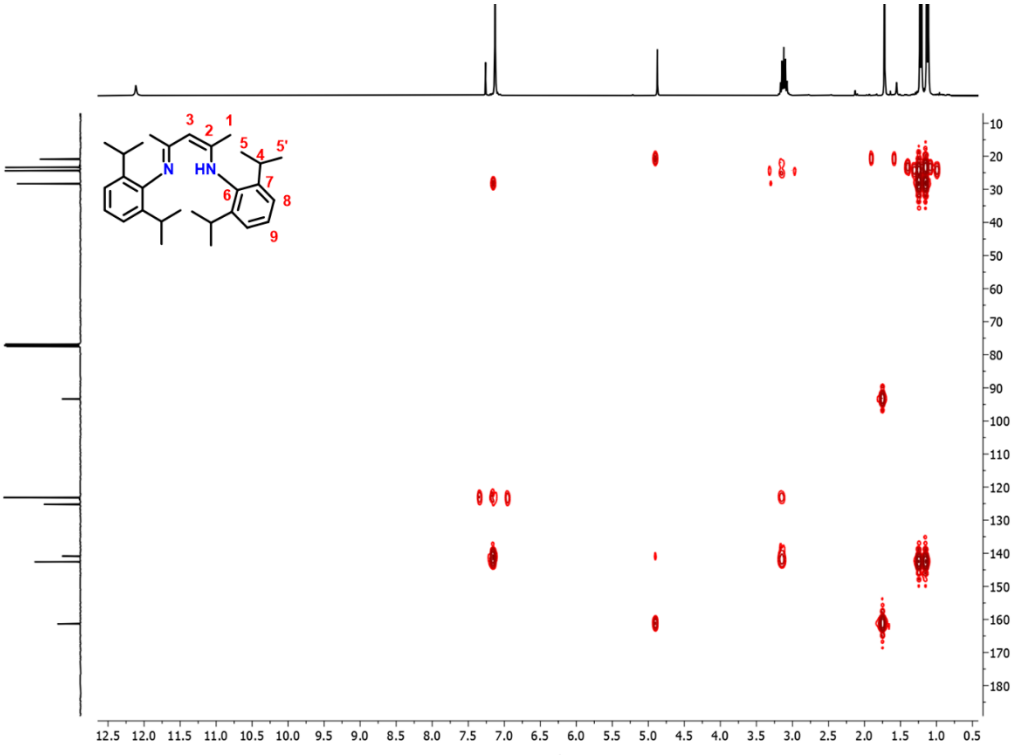

Figure S5. ^{1}H- ^{13}C HMBC NMR of **L1** (300MHZ, $CDCl_3$)

Chapter 3.

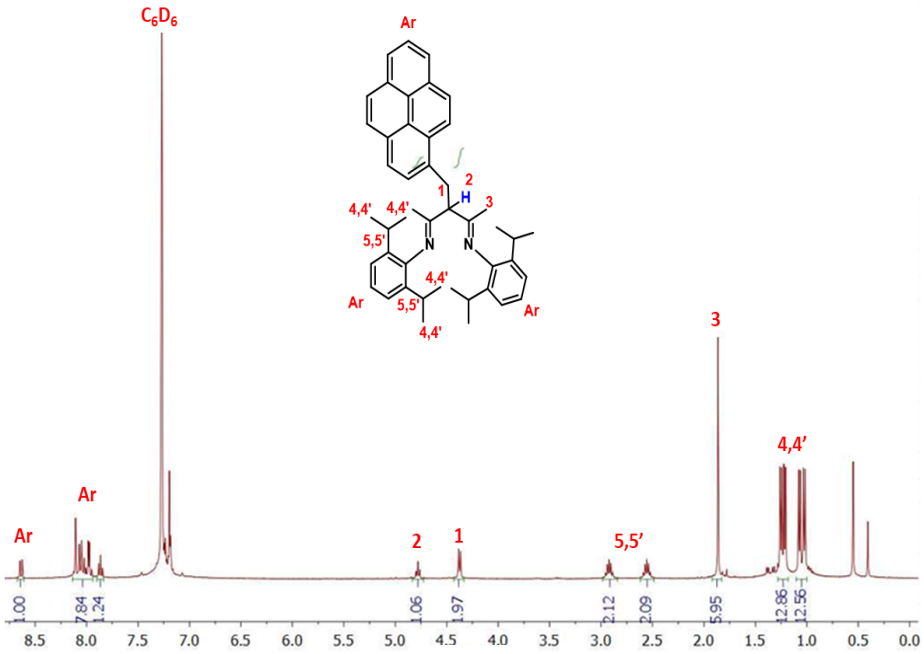

Figure S6. [1]H-NMR of imine form of **L2** (300MHZ, C_6D_6)

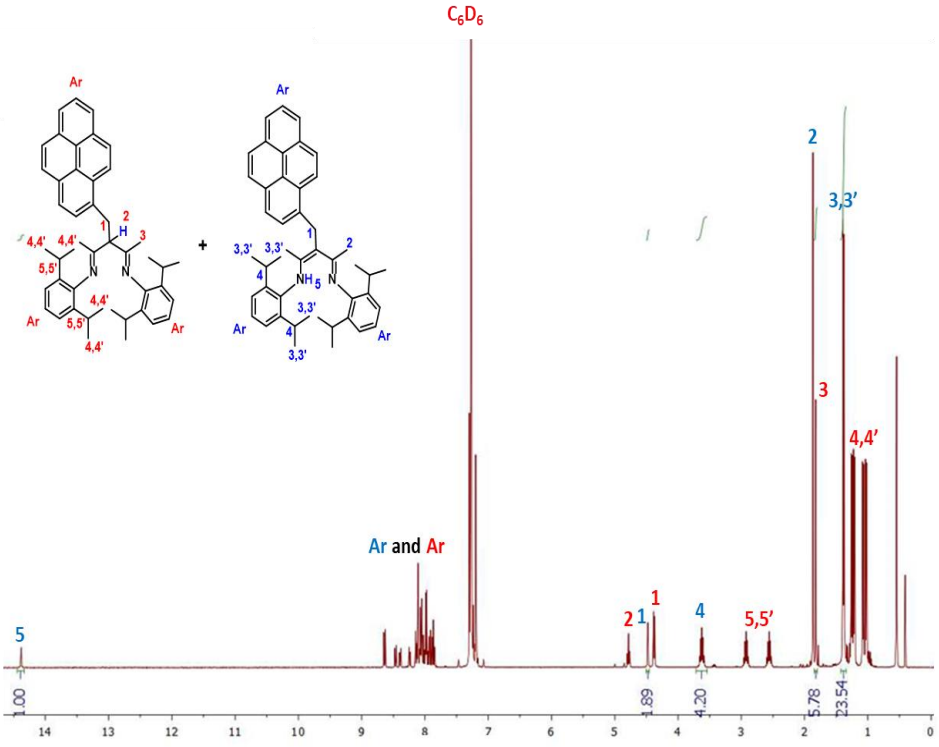

Figure S7. [1]HNMR of **L2** mixture of tautomers (300 MHZ, C_6D_6)

Chapter 3.

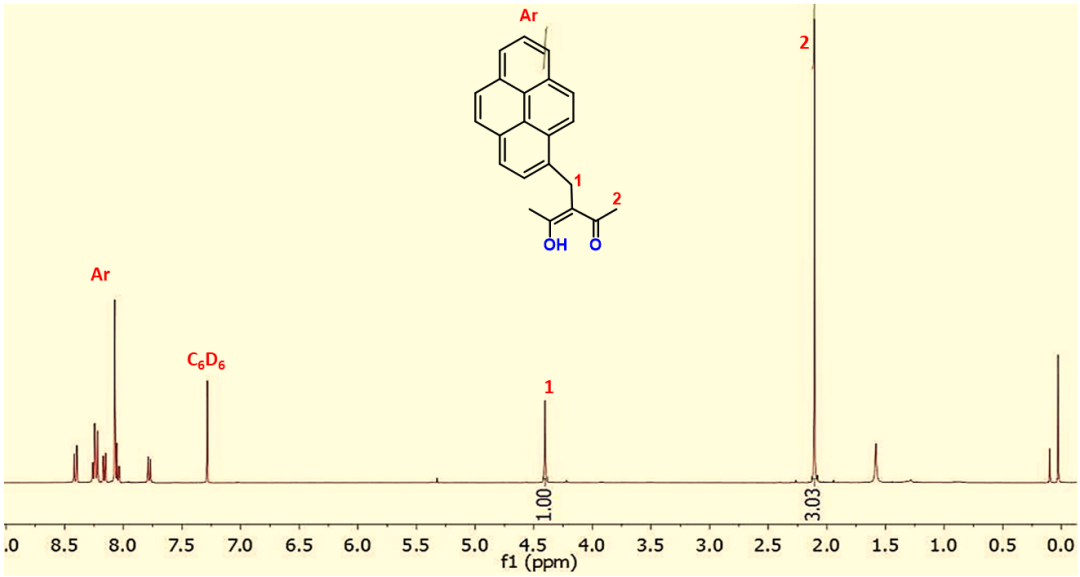

Figure S8. ^{1}H-NMR of 3-(pyren-1-ylmethyl)pentane-2,4-dione (300MHZ, $CDCl_3$)

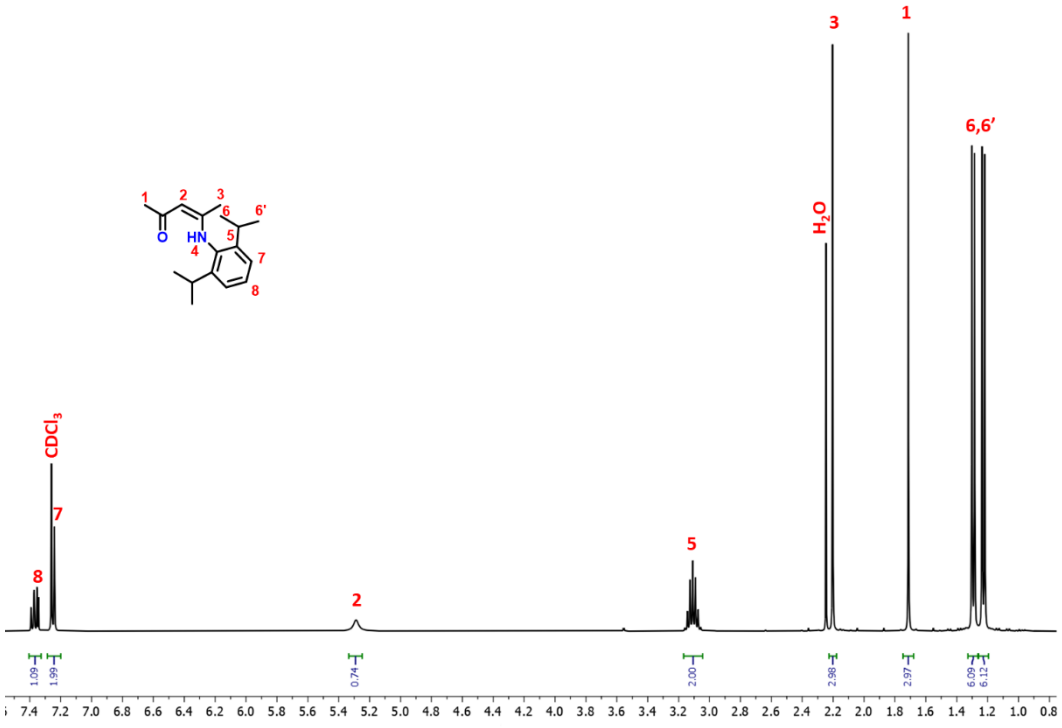

Figure S9. ^{1}H-NMR of (2-((2, 6-diisopropylphenyl) imido)-2-penten-4-one) (400MHZ, $CDCl_3$)

Chapter 3.

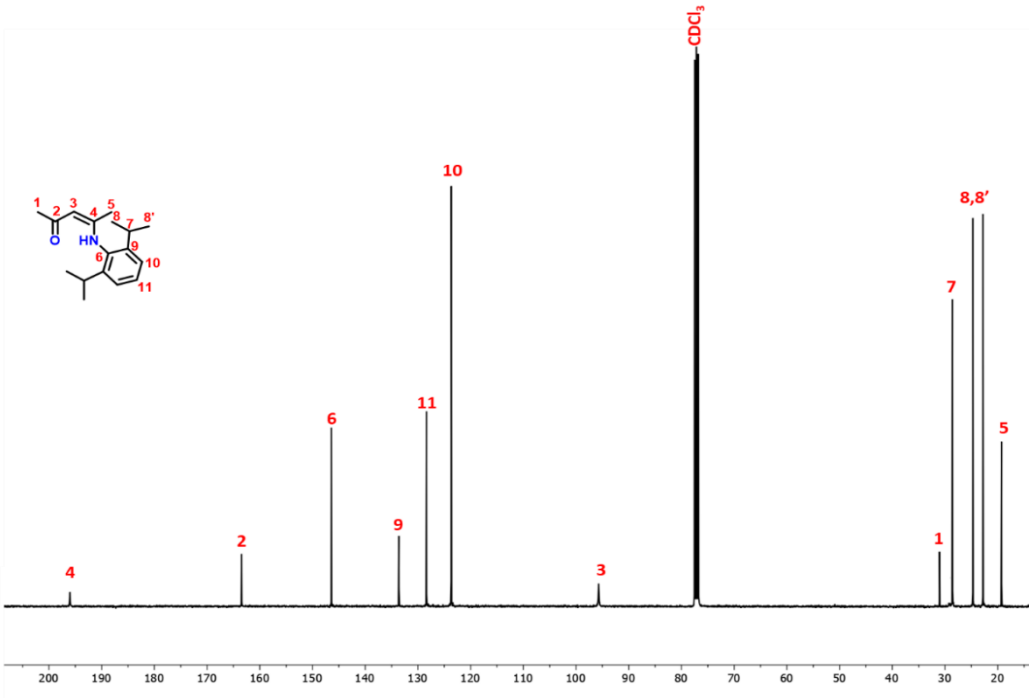

Figure S10. ^{13}C NMR of (2-((2, 6-diisopropylphenyl) imido)-2-penten-4-one) (101MHZ, $CDCl_3$)

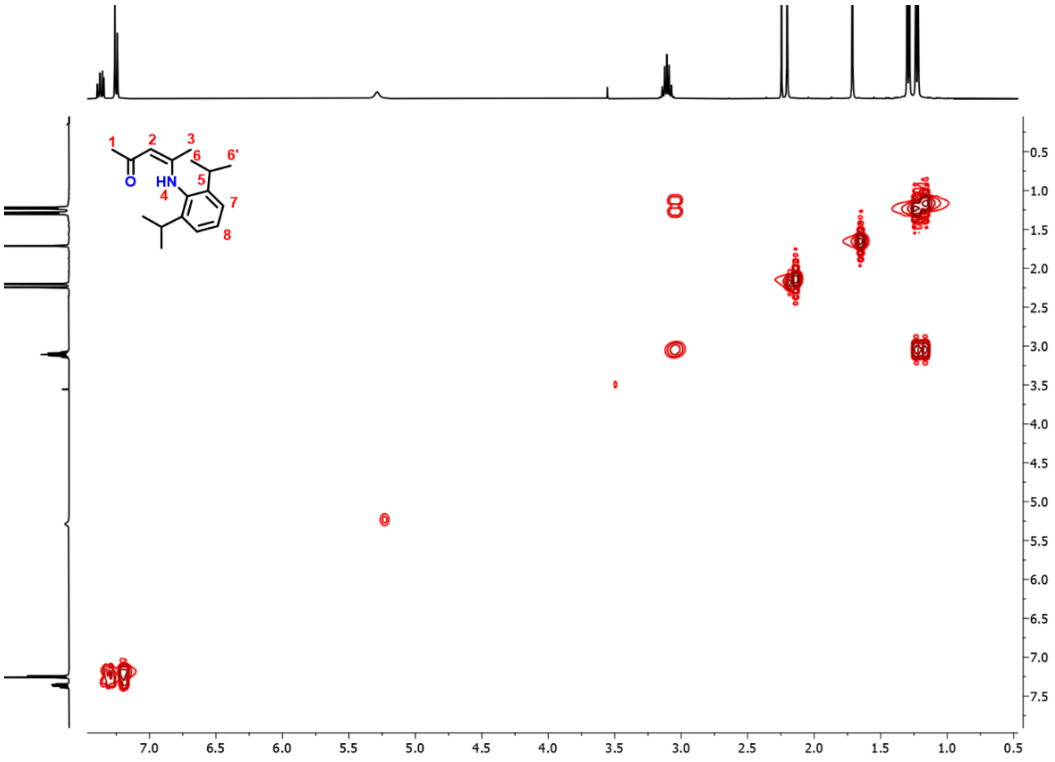

Figure S11. ^{1}H-^{1}H Cosy NMR of (2-((2, 6-diisopropylphenyl) imido)-2-penten-4-one) (400MHZ, $CDCl_3$)

Chapter 3.

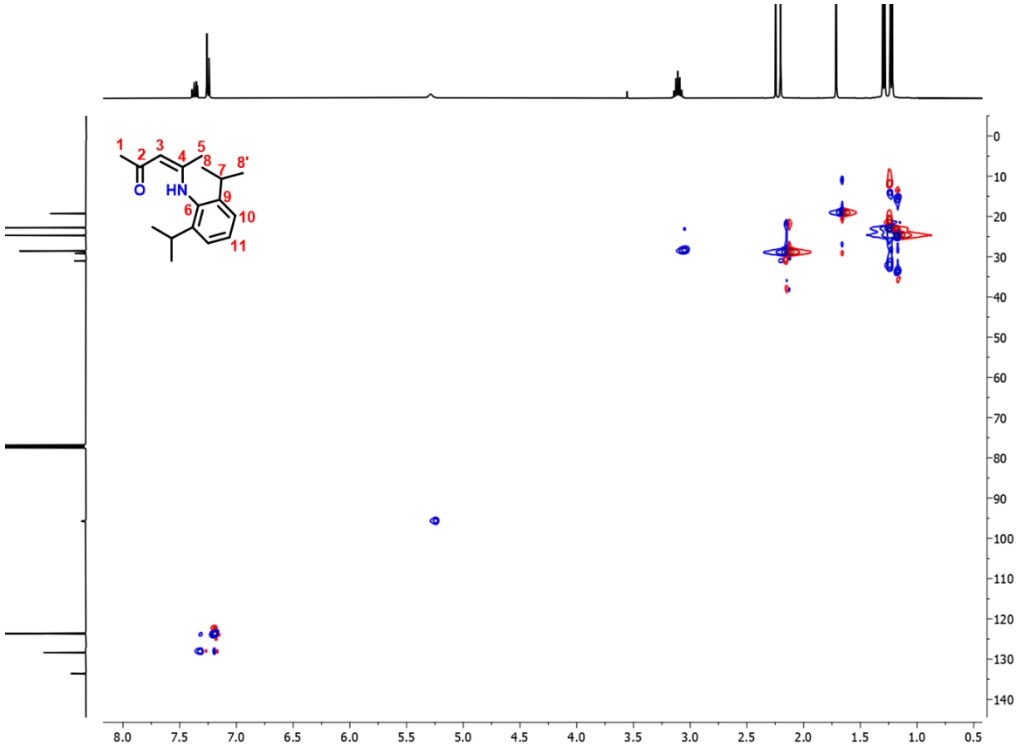

Figure S12: ^{1}H- ^{13}C HSQC NMR of (2-((2, 6-diisopropylphenyl) imido)-2-penten-4-one) (400MHZ, $CDCl_3$)

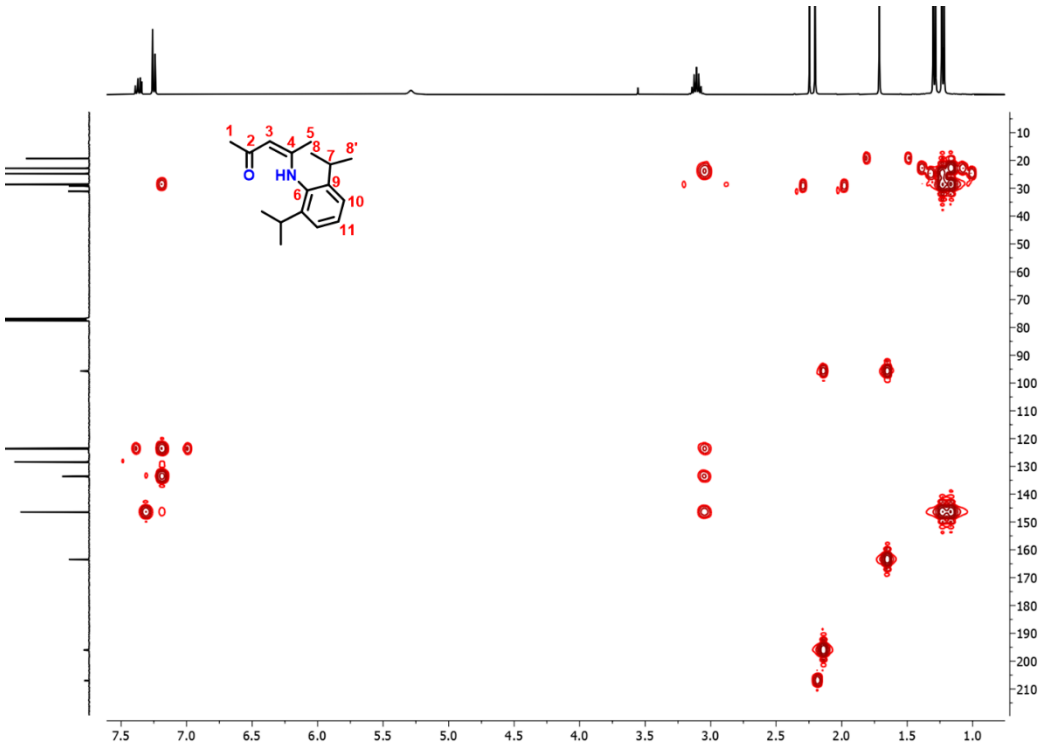

Figure S13: ^{1}H- ^{13}C HMBC NMR of (2-((2, 6-diisopropylphenyl) imido)-2-penten-4-one) (400MHZ, $CDCl_3$)

Chapter 3.

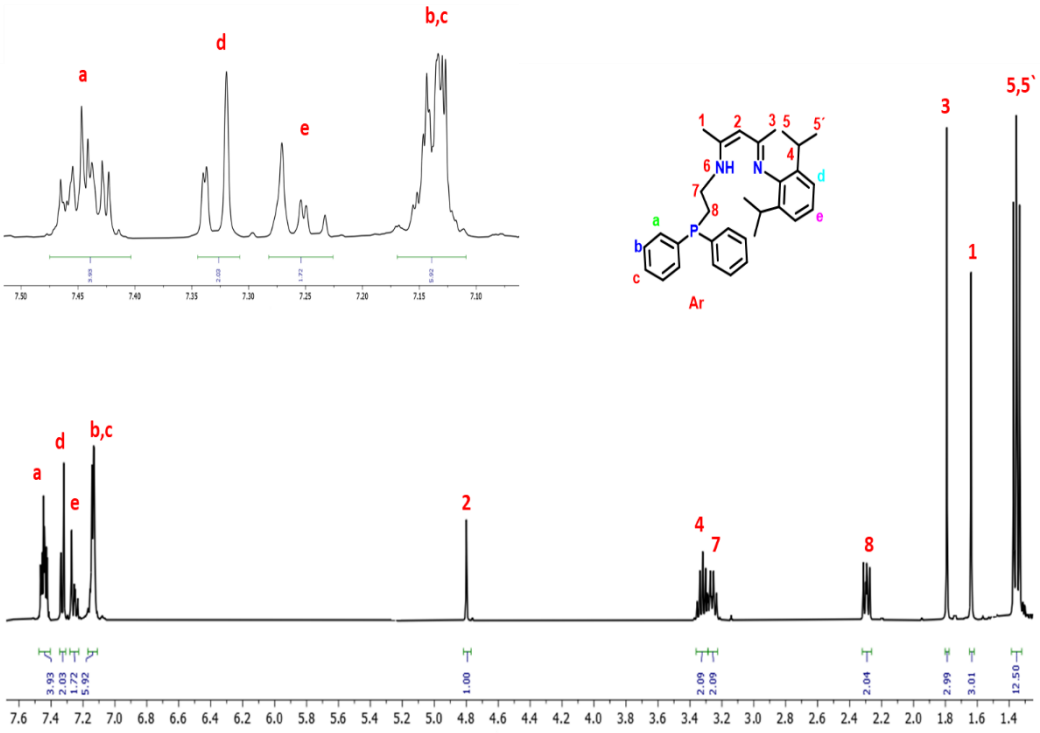

Figure S14: ^{1}H-NMR of **L3** (400MHZ C_6D_6)

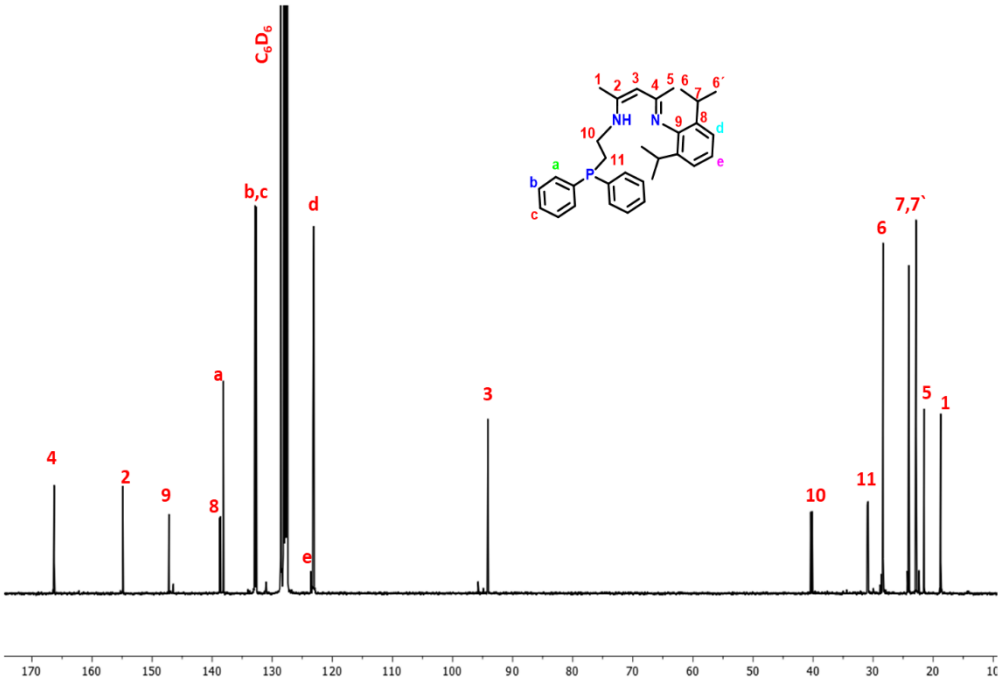

Figure S15: ^{13}C NMR of **L3** (126 MHZ C_6D_6)

Chapter 3.

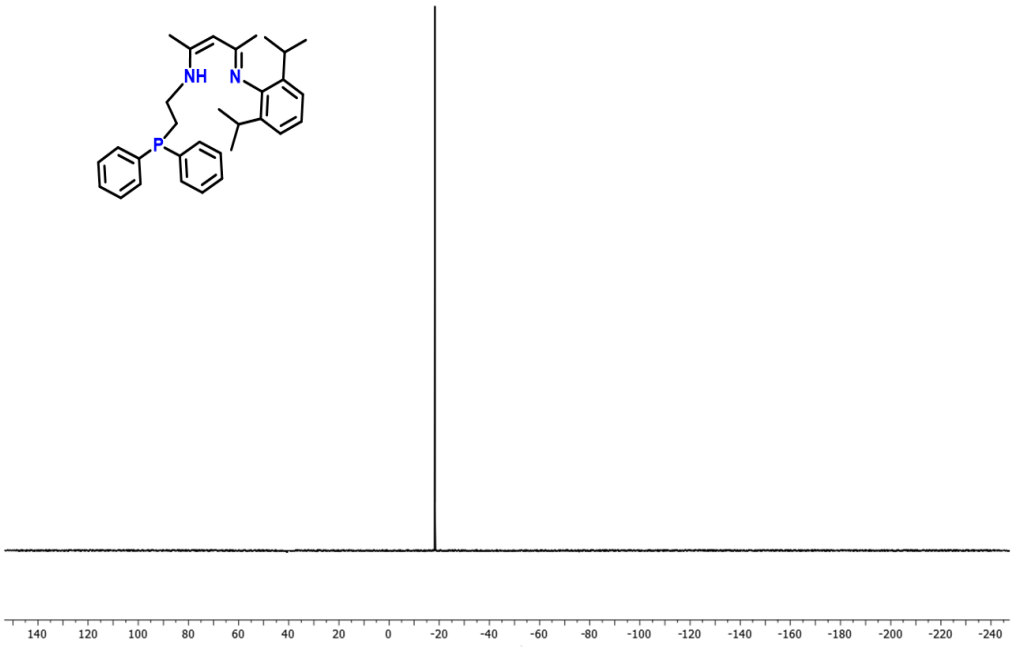

Figure S16: ^{31}P {^{1}H} NMR of **L3** (202MHZ C_6D_6)

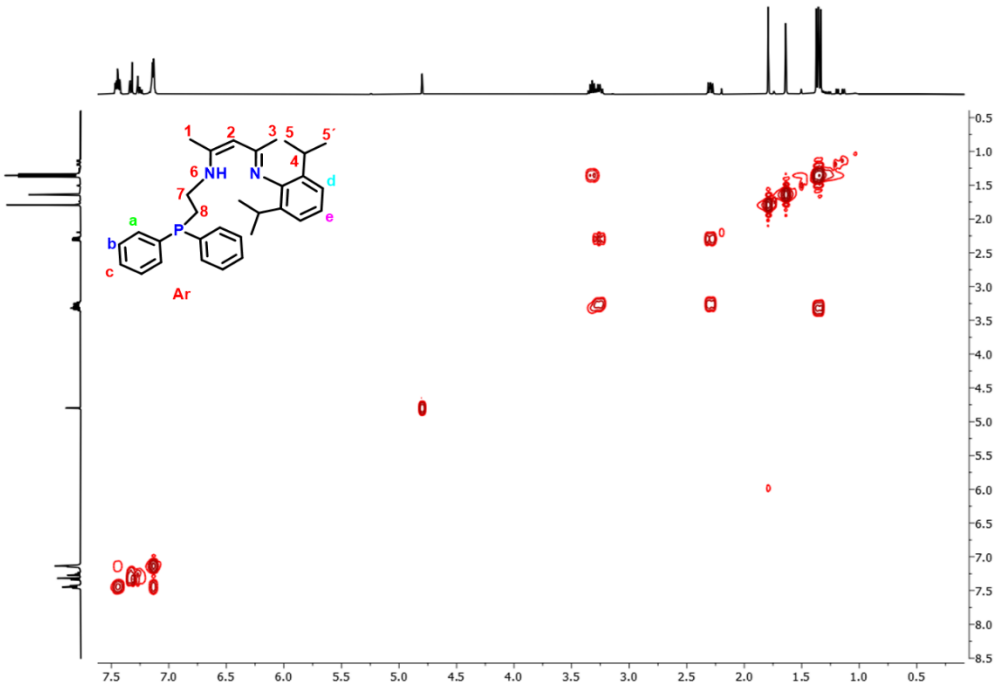

Figure S17:^{1}H-^{1}H Cosy NMR of **L3** (400MHZ C_6D_6)

Chapter 3.

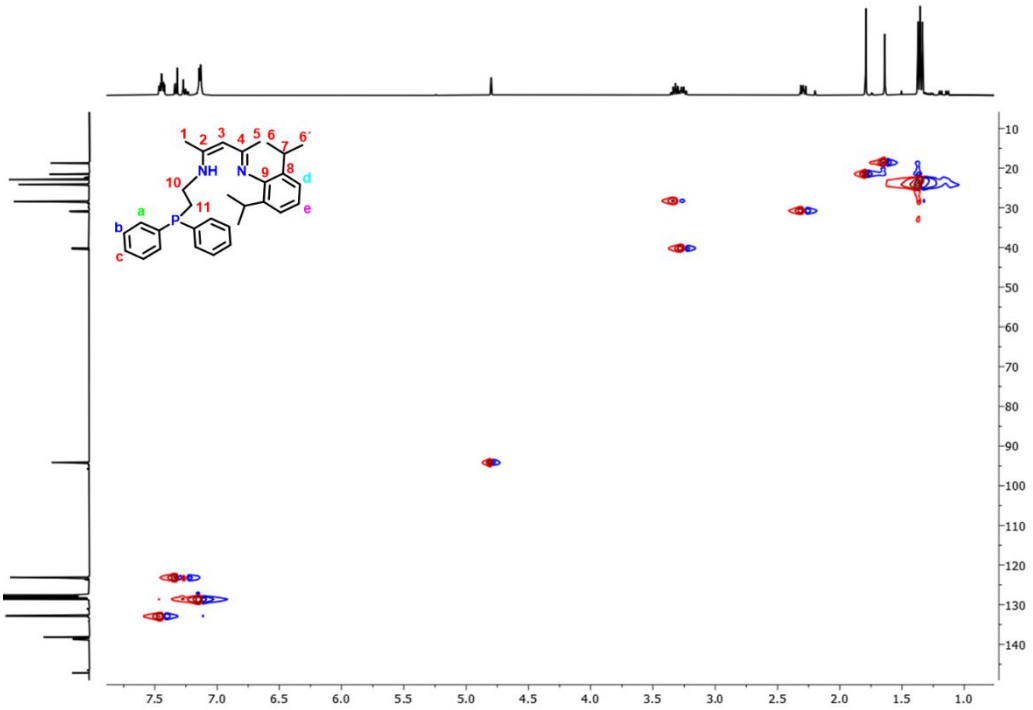

Figure S18: ^{1}H- ^{13}C HSQC NMR of **L3** (400MHZ C_6D_6)

Chapter 3.

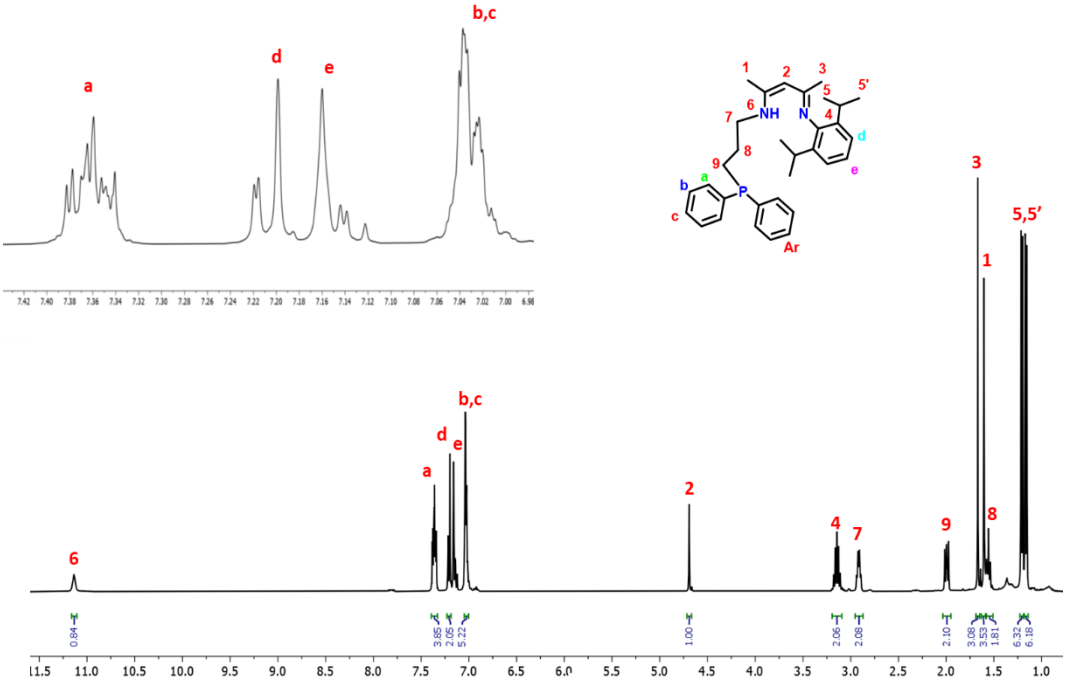

Figure S19: ^{1}H-NMR of **L4** (400MHZ C_6D_6)

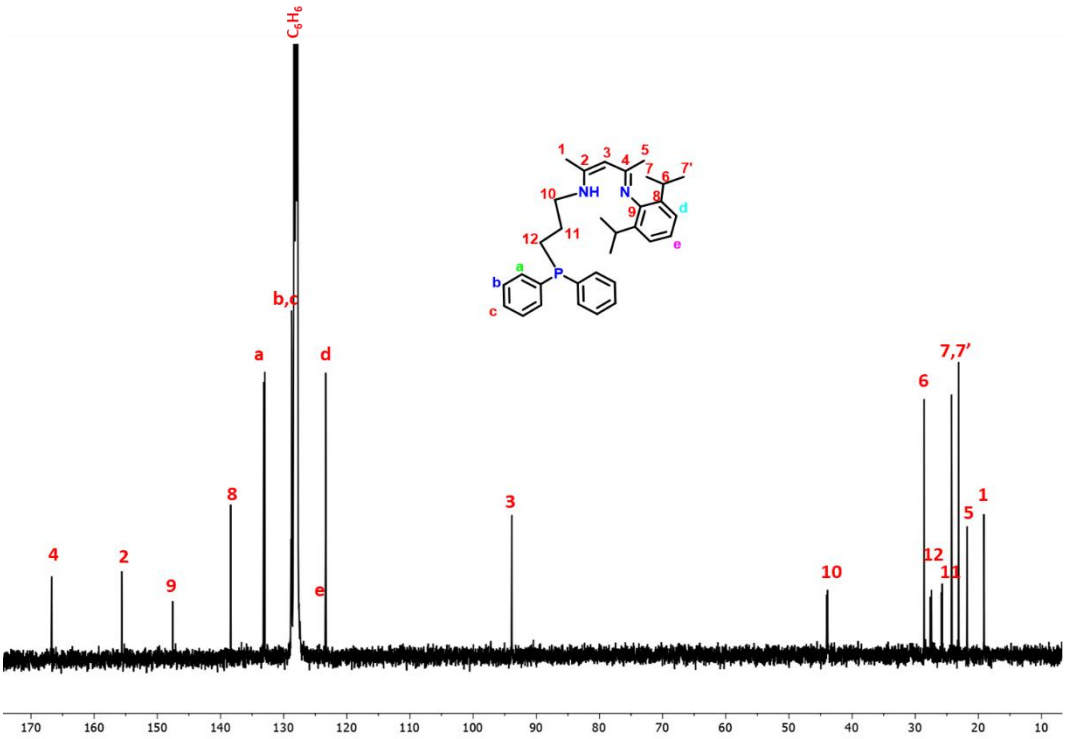

Figure S20: ^{13}C NMR of **L4** (126 MHZ C_6D_6)

Chapter 3.

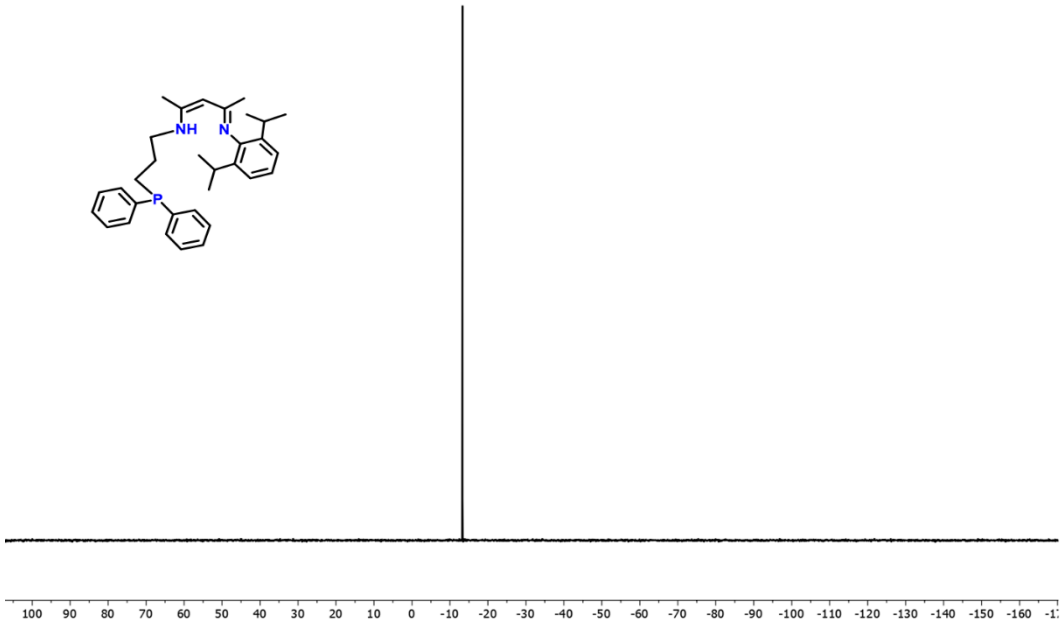

Figure S21: ^{13}P {^{1}H} NMR of **L4** (202 MHZ C_6D_6)

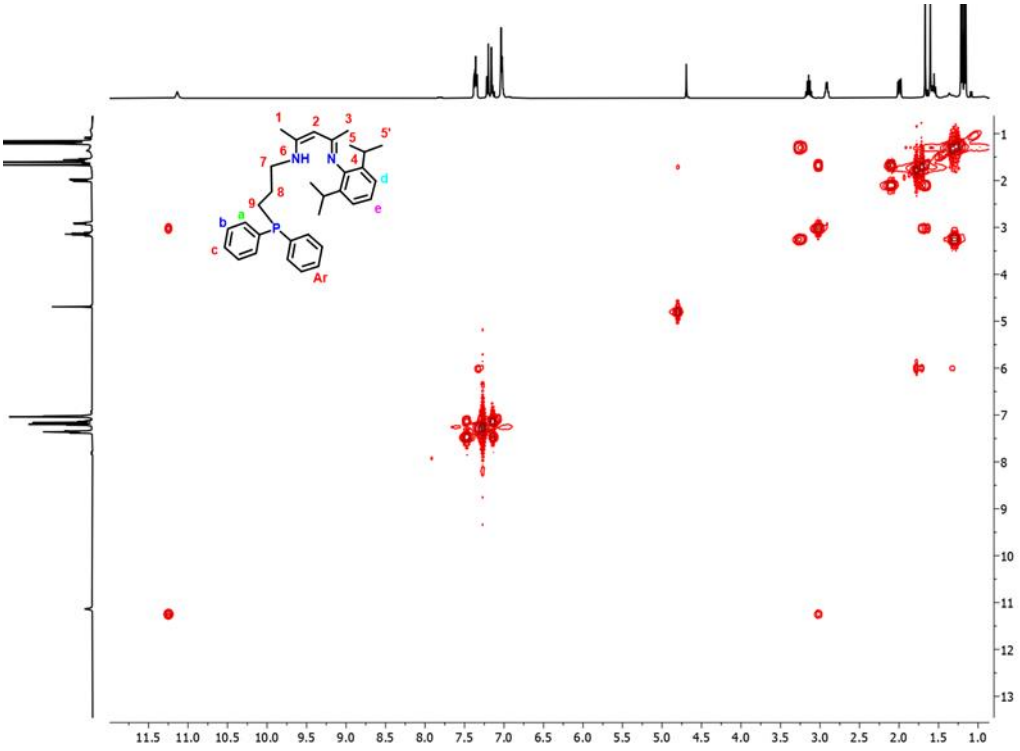

Figure S22: ^{1}H-^{1}H Cosy NMR of **L4** (400MHZ C_6D_6)

Chapter 3.

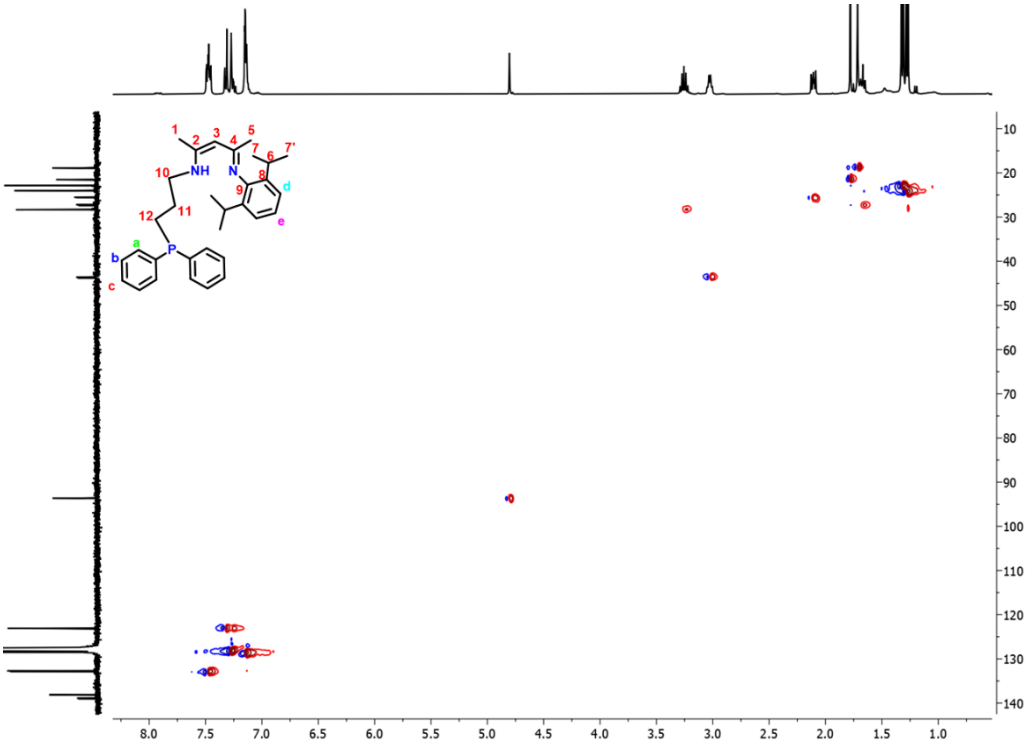

Figure S23: ^{1}H- ^{13}C HSQC NMR of **L4** (400MHZ C_6D_6)

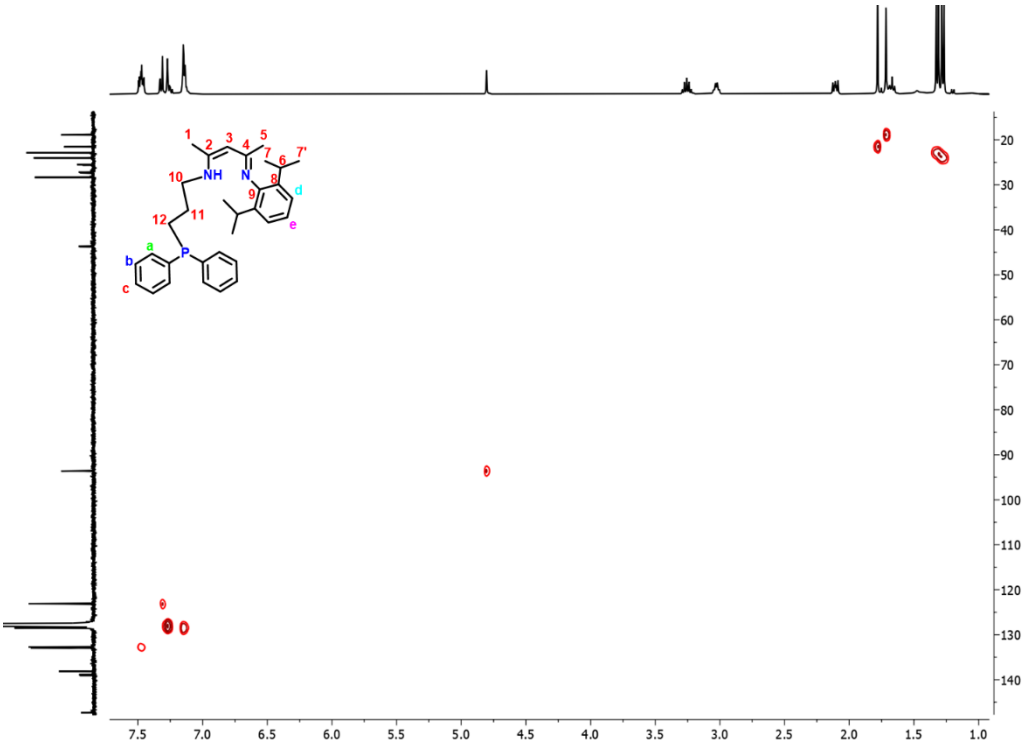

Figure S24: ^{1}H- ^{13}C HMBC NMR of **L4** (400MHZ C_6D_6)

Chapter 3.

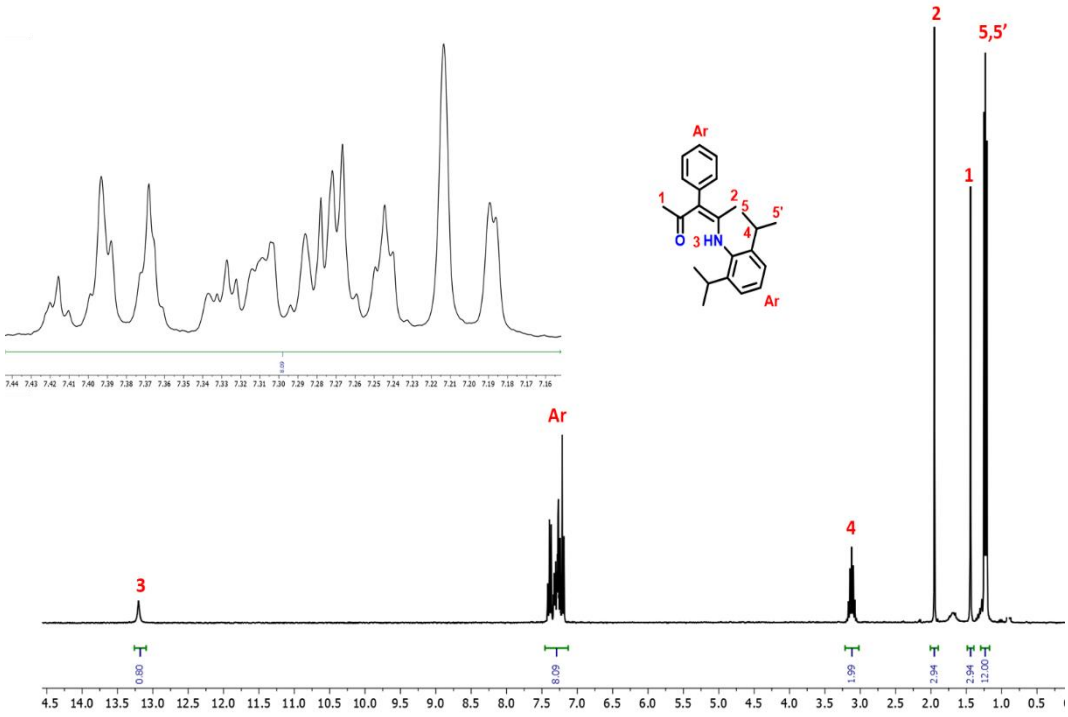

Figure S25: [1]H NMR of 4-((2, 6-diisopropylphenyl) amino)-3-phenylpent-3-en-2-one (300MHZ $CDCl_3$)

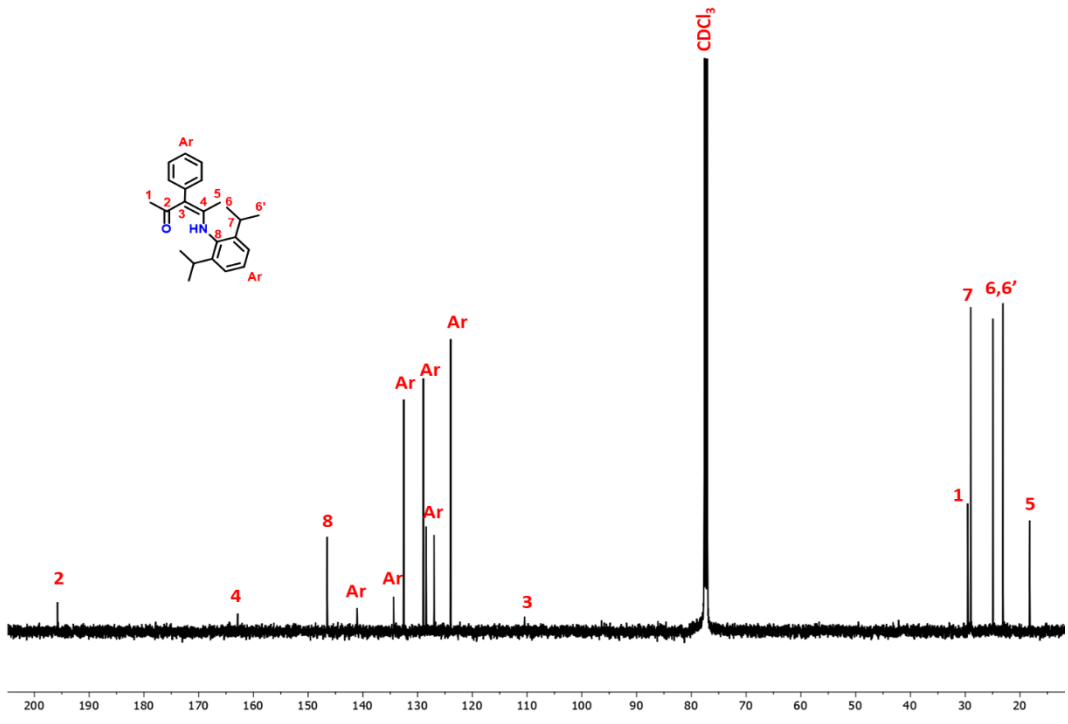

Figure S26: [13]C NMR of 4-((2, 6-diisopropylphenyl) amino)-3-phenylpent-3-en-2-one (126 MHZ $CDCl_3$)

Chapter 3.

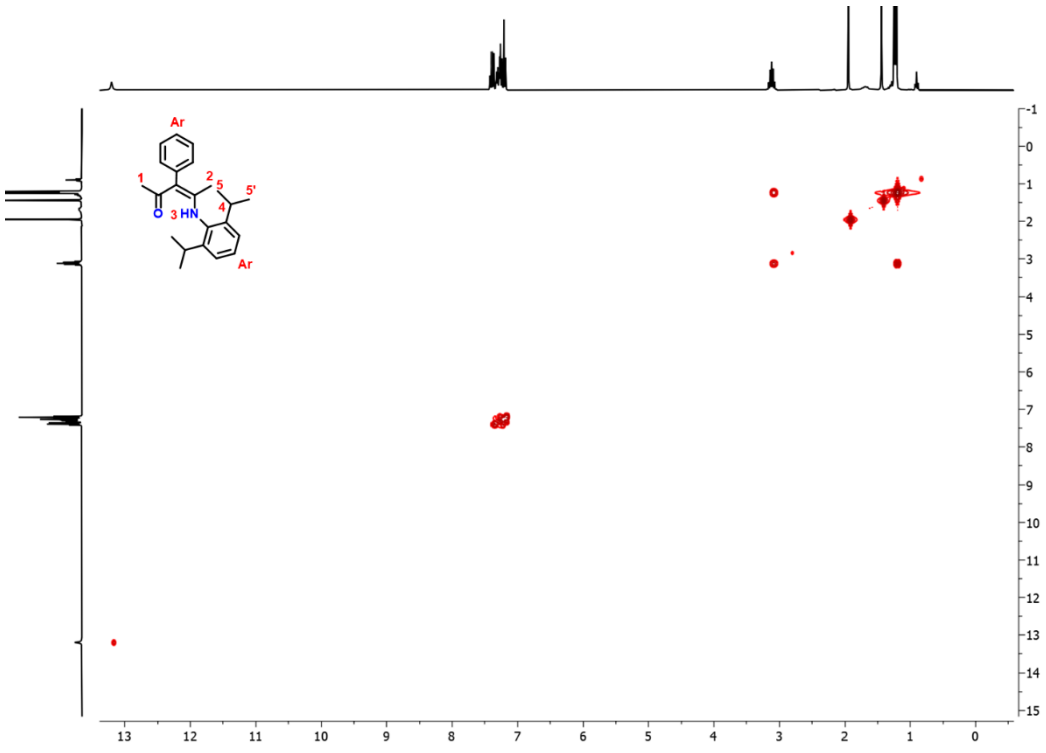

Figure S27 : ^{1}H-^{1}H Cosy NMR of 4-((2, 6-diisopropylphenyl) amino)-3-phenylpent-3-en-2-one (300MHZ $CDCl_3$)

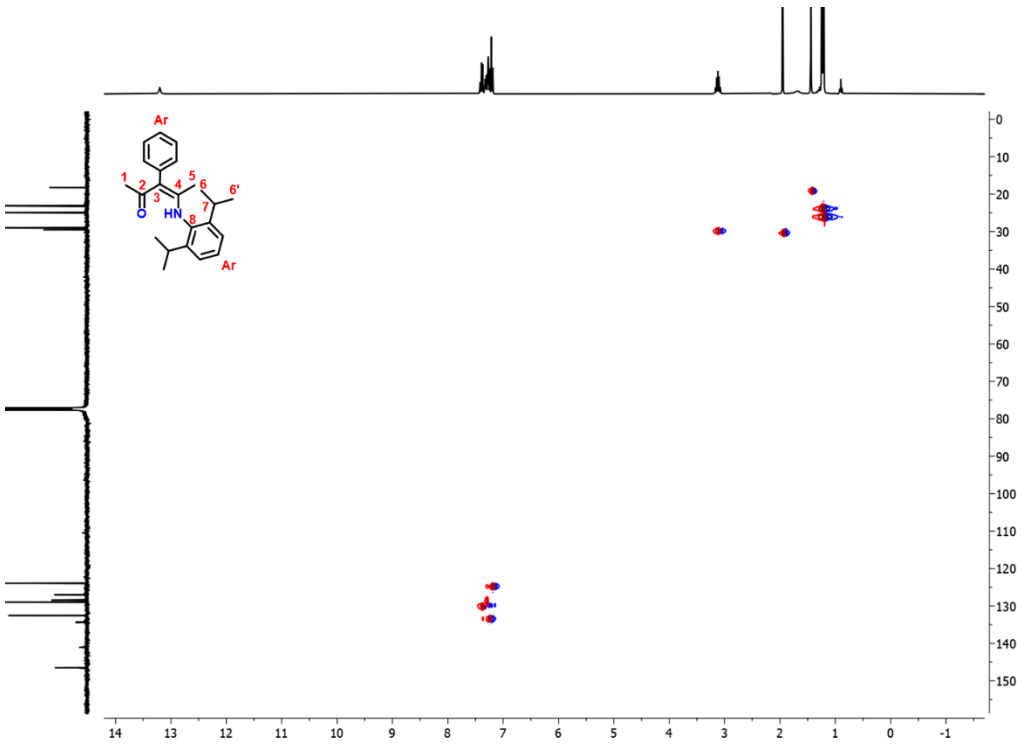

Figure S28: ^{1}H- ^{13}C HSQC NMR of 4-((2, 6-diisopropylphenyl) amino)-3-phenylpent-3-en-2-one (300MHZ $CDCl_3$)

Chapter 3.

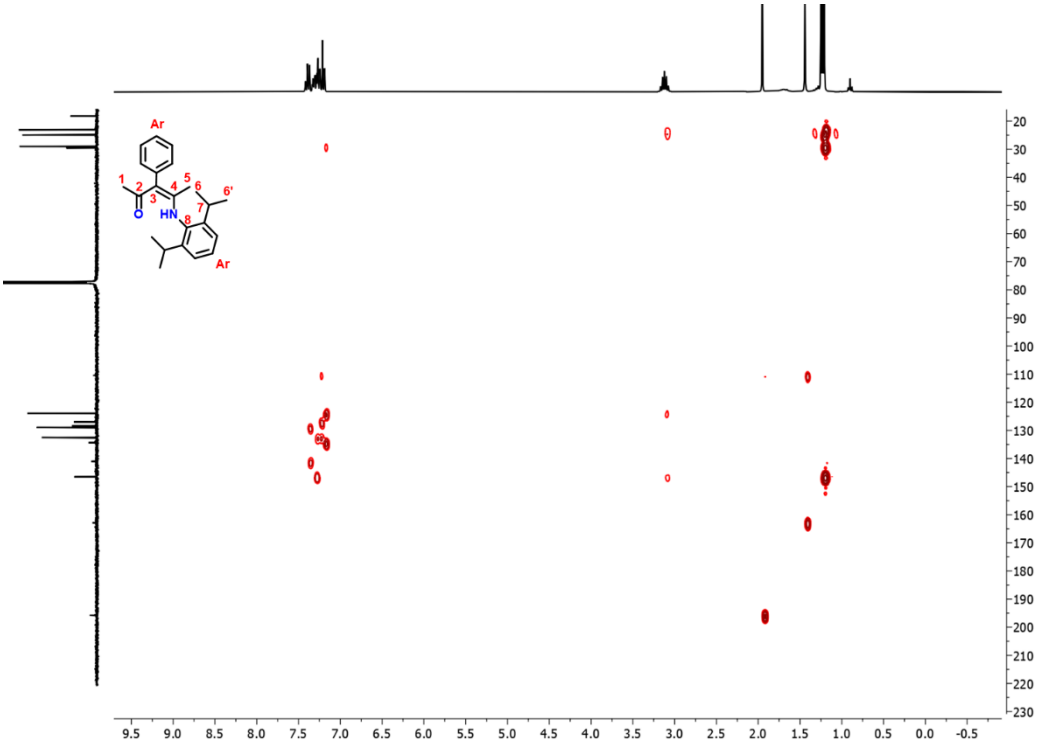

Figure S29: ^{1}H- ^{13}C HMBC NMR of 4-((2, 6-diisopropylphenyl) amino)-3-phenylpent-3-en-2-one (300MHZ $CDCl_3$)

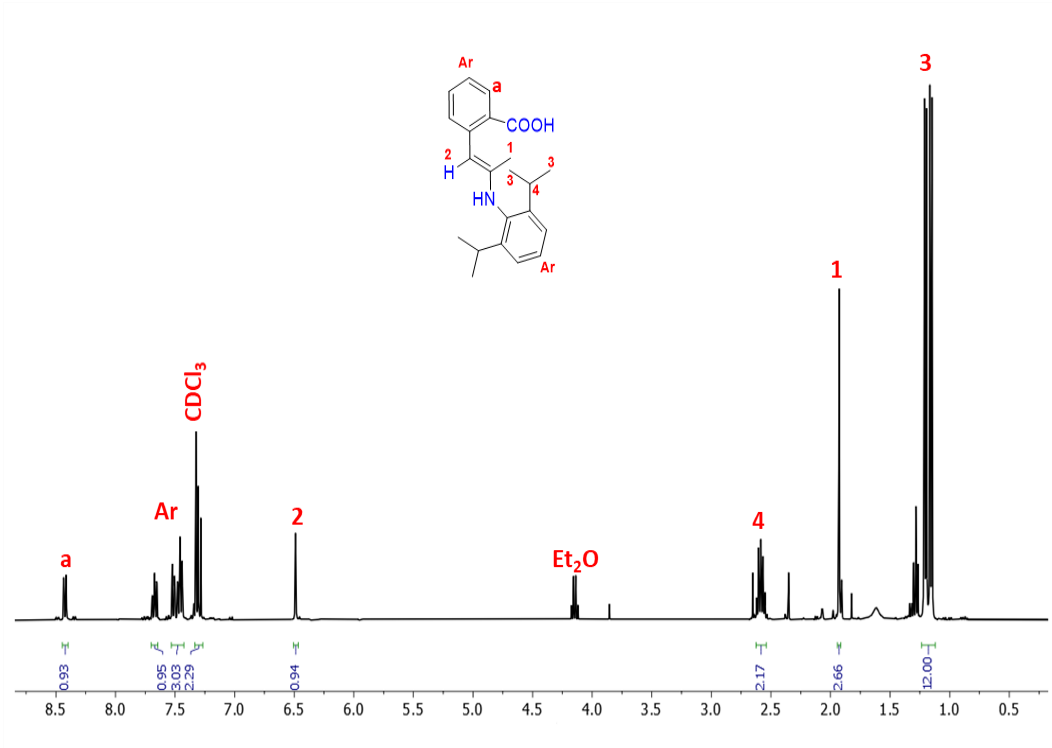

Figure S30: ^{1}H NMR of 2-(2-((2,6-diisopropylphenyl)amino)prop-1-en-1-yl)benzoic acid (300MHZ $CDCl_3$). This side-product was not purified, thus the spectrum shows additional peaks related to impurities, including Et_2O solvent.

Chapter 3.

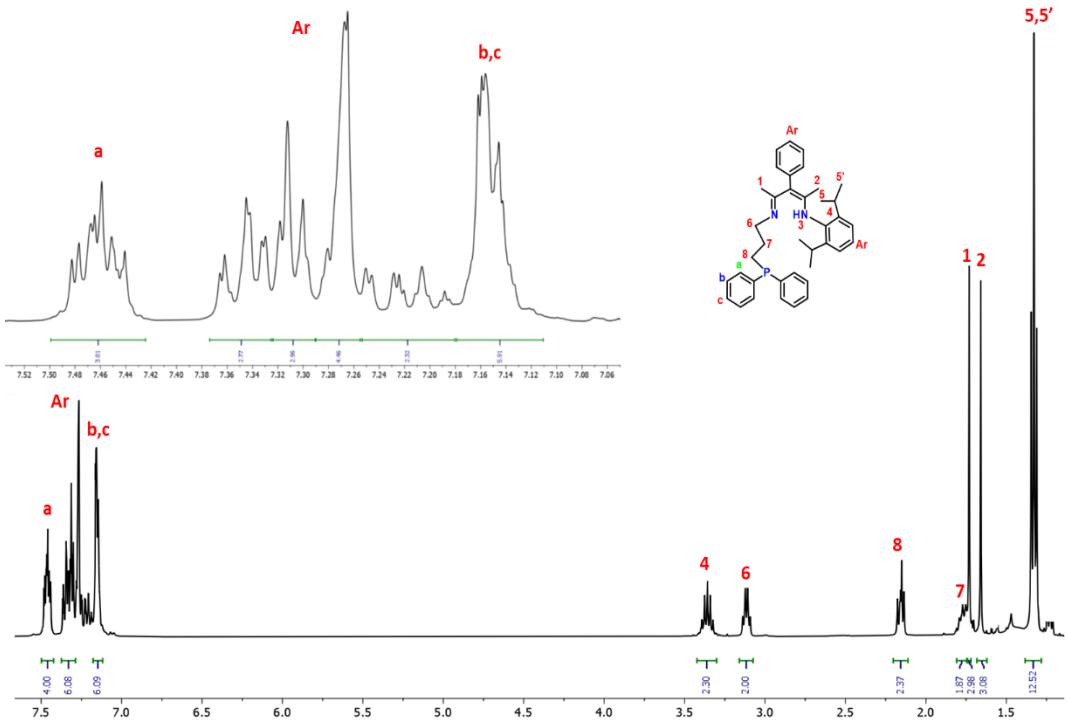

Figure S31:[1]H NMR of **L6** (400MHZ C_6D_6)

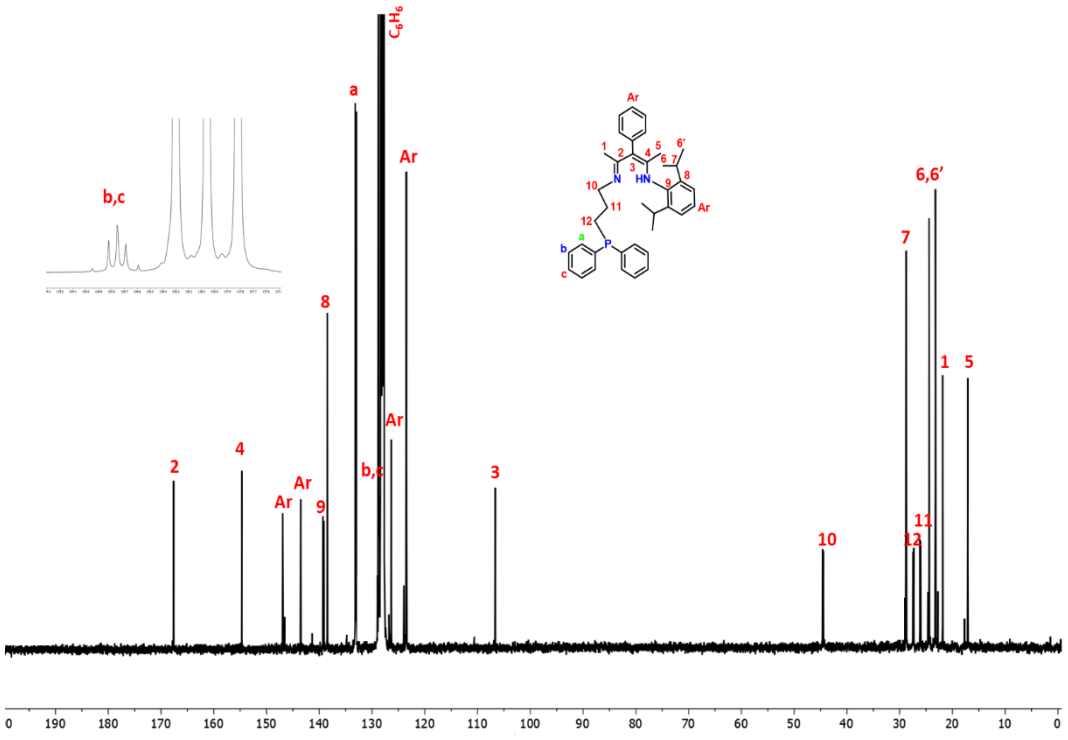

Figure S32: [13]C NMR of **L6** (101 MHZ C_6D_6)

Chapter 3.

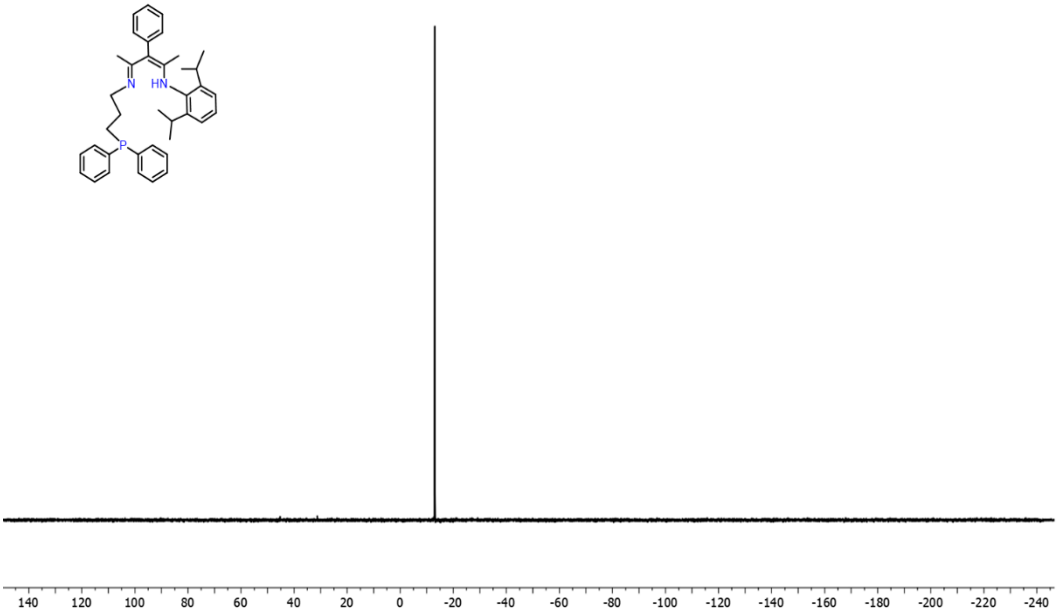

Figure S33: ^{31}P $\{^{1}H\}$ NMR of **L6**(202 MHZ C_6D_6)

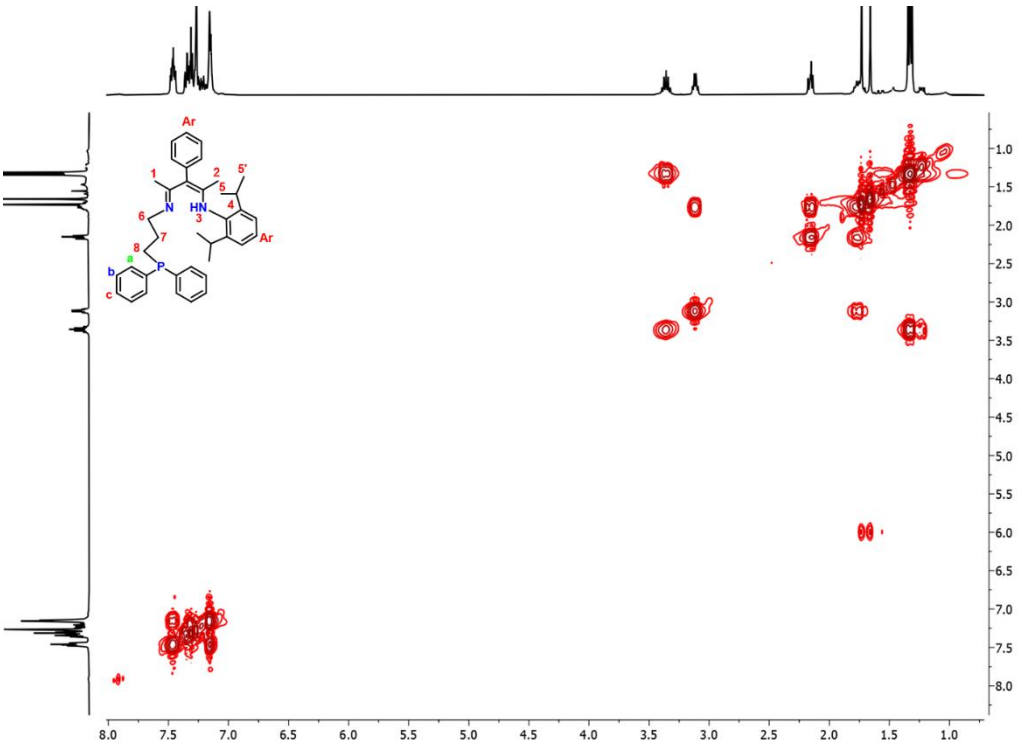

Figure S34: ^{1}H-^{1}H COSY NMR of **L6** (400MHZ C_6D_6)

Chapter 3.

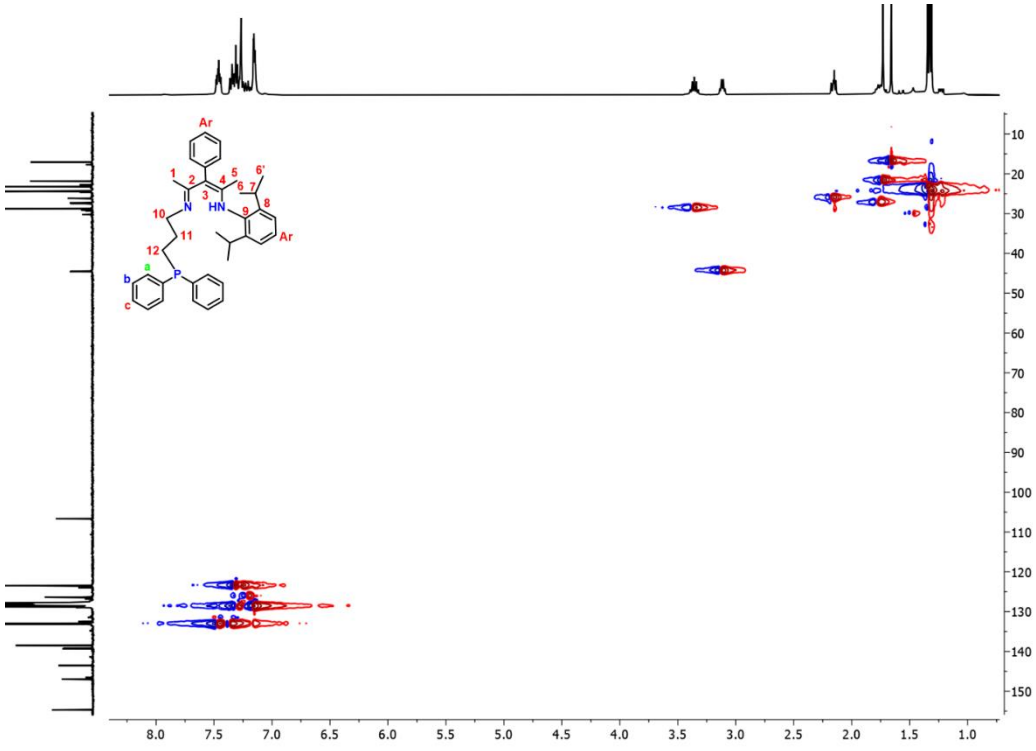

Figure S35: ^{1}H- ^{13}C HSQC NMR of **L6** (400MHZ C_6D_6)

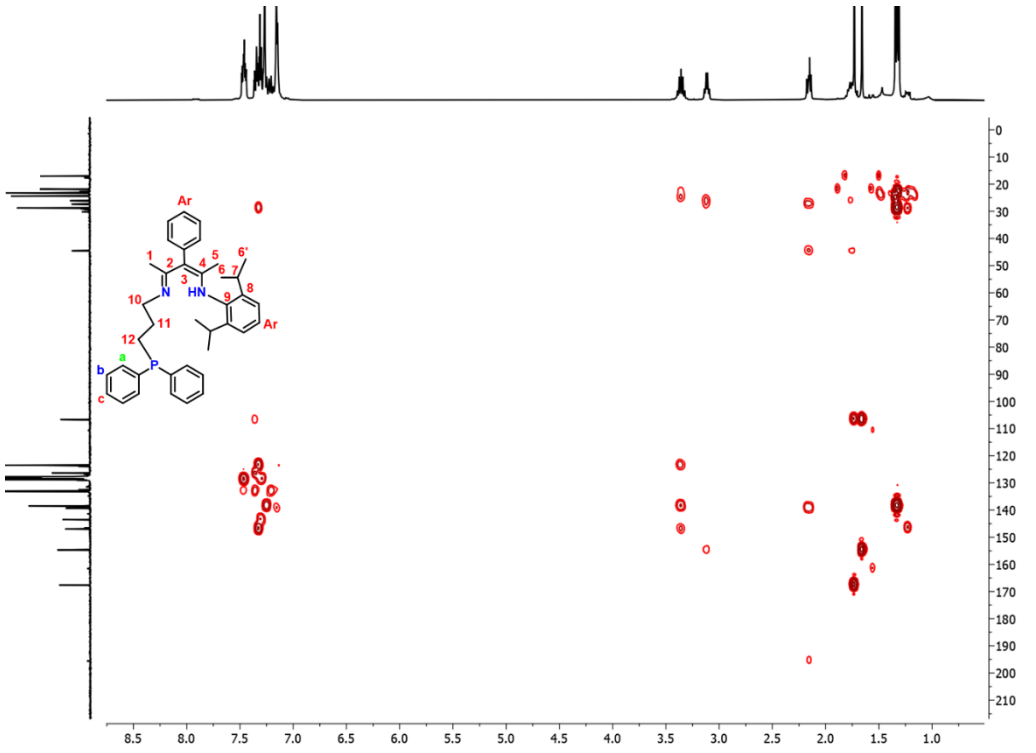

Figure S36: ^{1}H- ^{13}C HMBC NMR of **L6** (400MHZ C_6D_6)

Chapter 3.

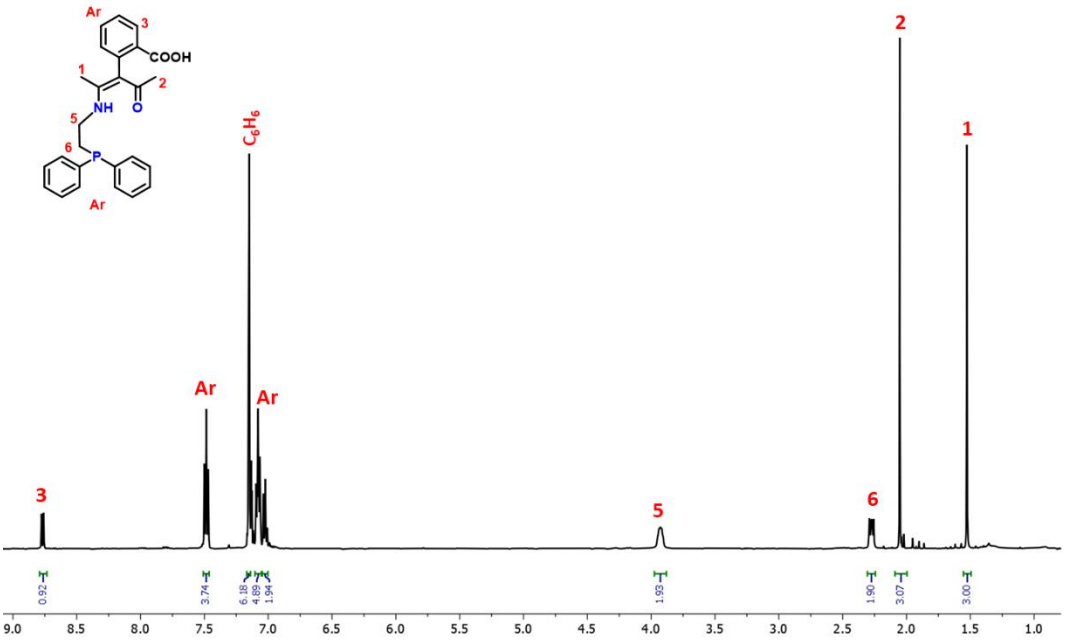

Figure S37: ^{1}H NMR of **L7** (400MHZ C_6D_6)

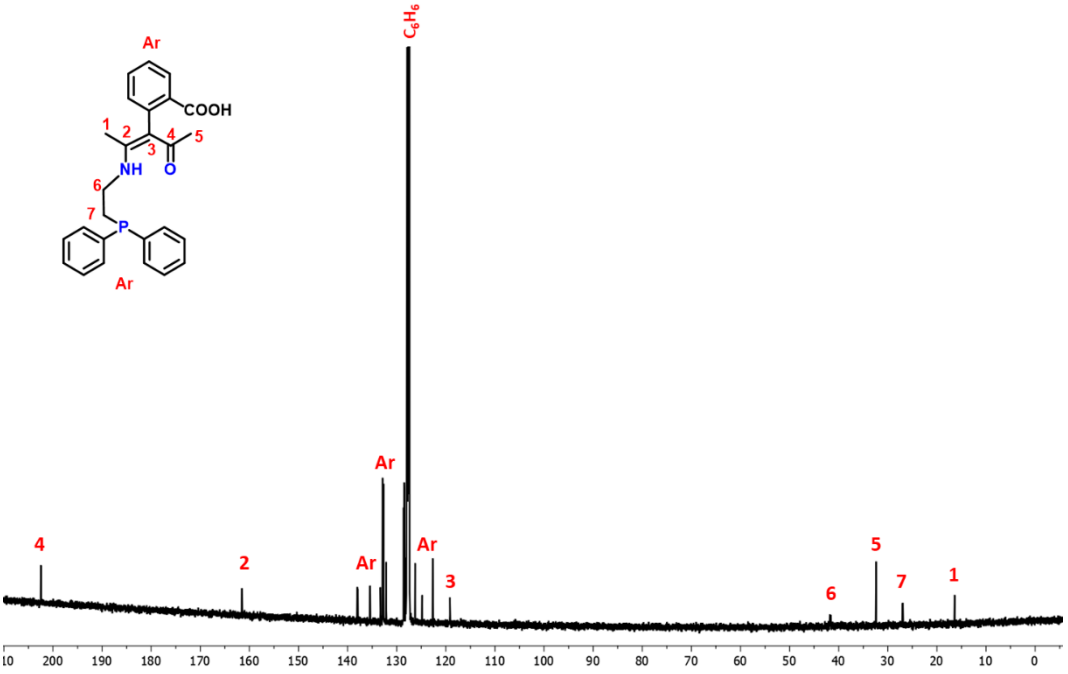

Figure S38: ^{13}C NMR of **L7** (126 MHZ C_6D_6)

Chapter 3.

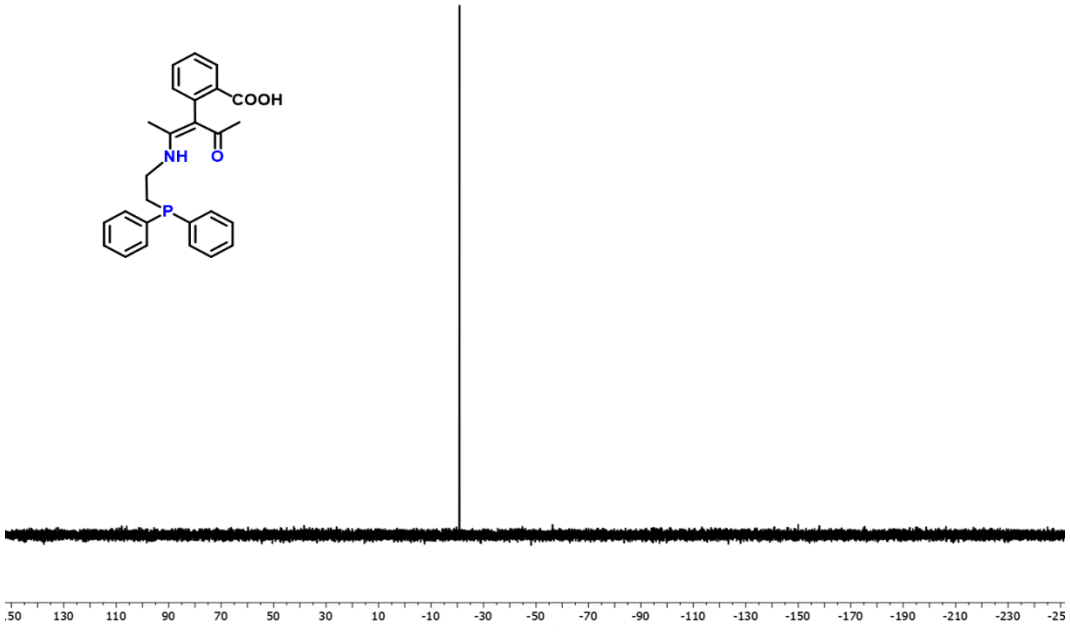

Figure S39: ^{31}P {^{1}H} NMR of **L7** (202 MHZ C_6D_6)

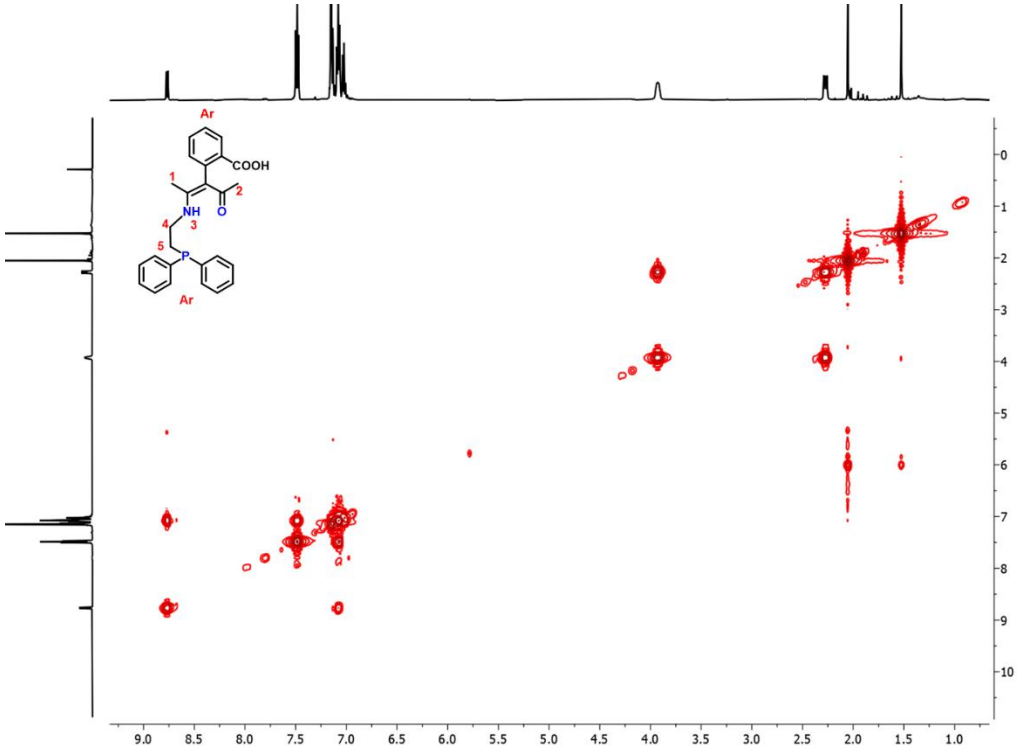

Figure S40: ^{1}H-^{1}H COSY NMR of **L7** (400MHZ C_6D_6)

Chapter 3.

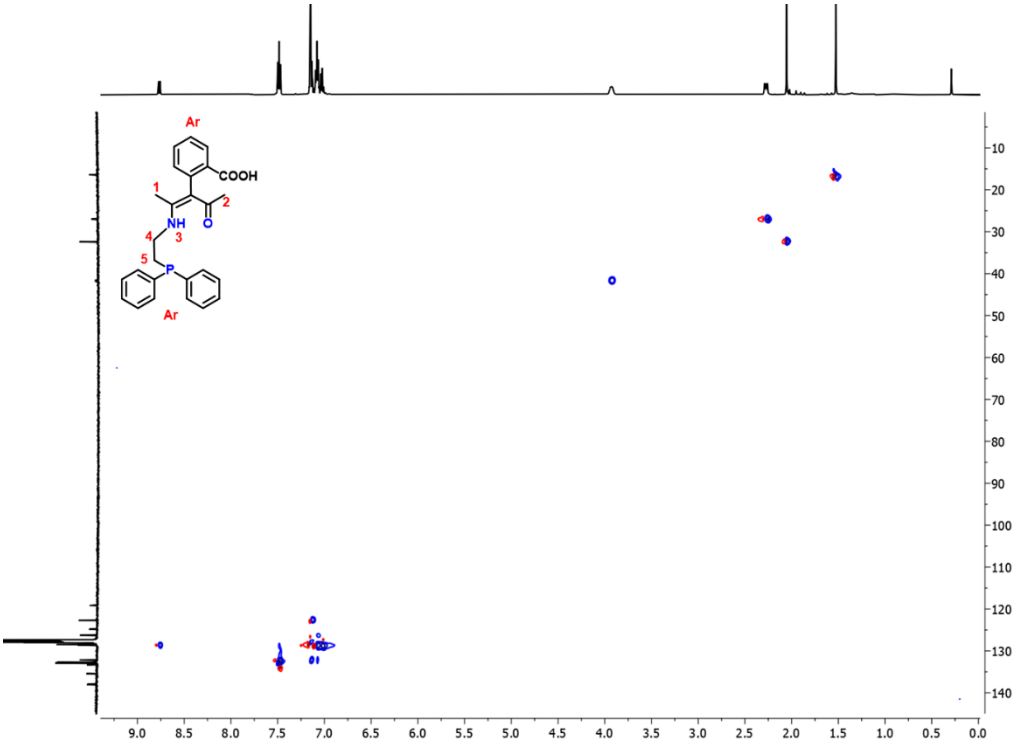

Figure S41: ^{1}H- ^{13}C HSQC NMR of **L7** (400MHZ C_6D_6)

Chapter 3.

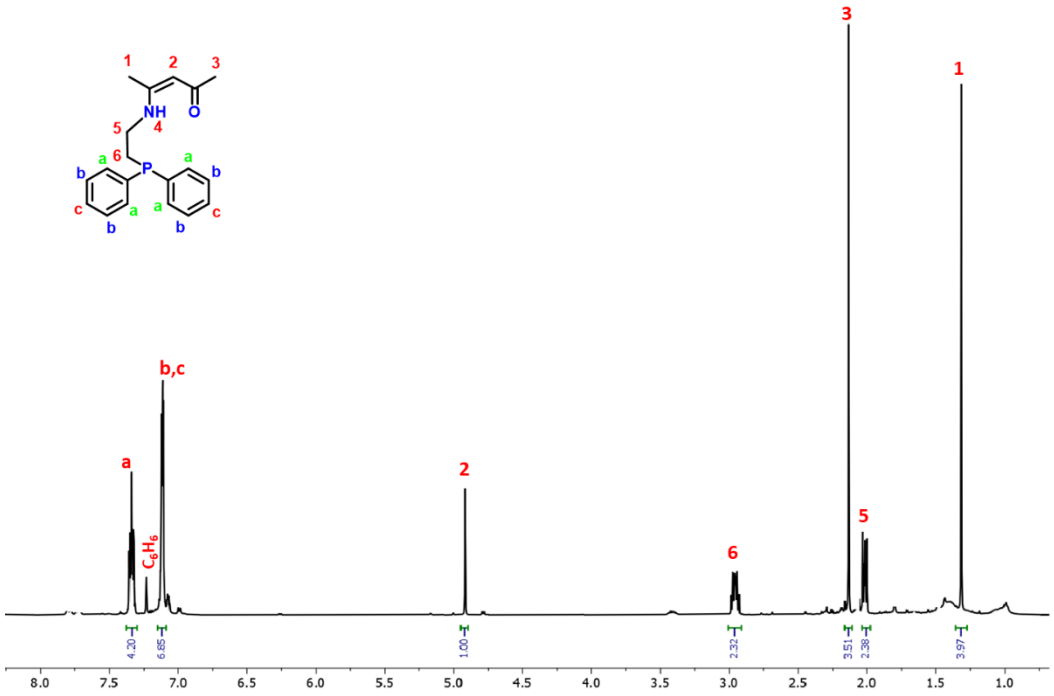

Figure S42: ^{1}H NMR of 4-((2-(diphenylphosphaneyl) ethyl) amino) pent-3-en-2-one (500MHZ C_6D_6)

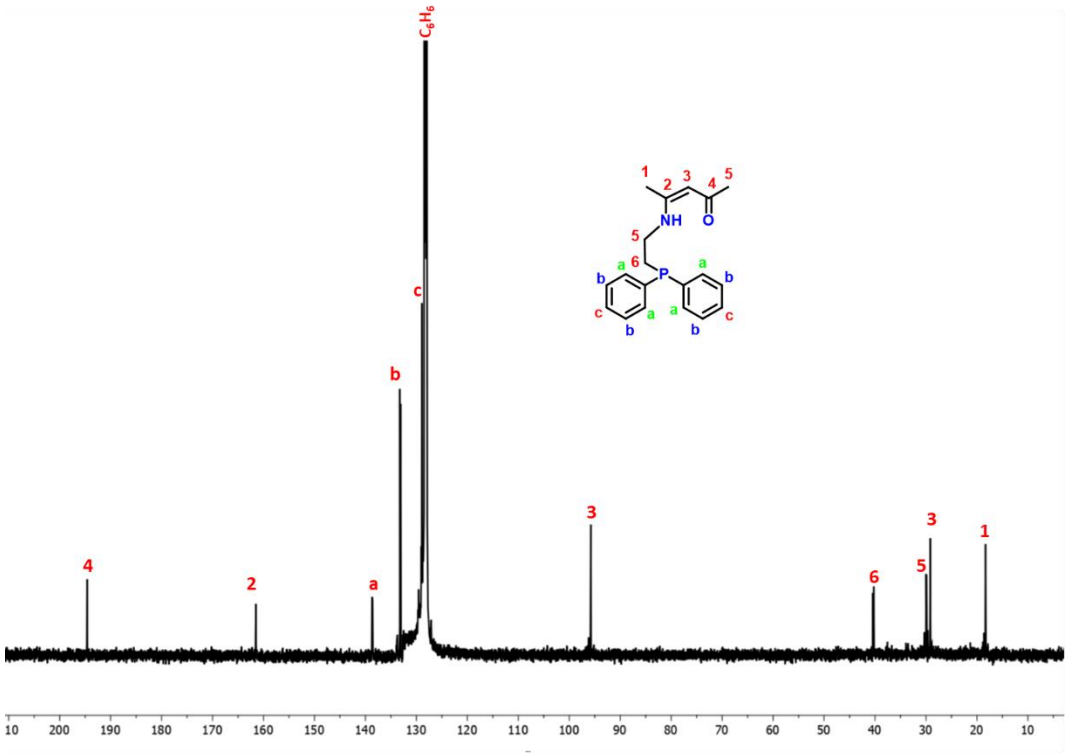

Figure S43: ^{13}C NMR of 4-((2-(diphenylphosphaneyl) ethyl) amino) pent-3-en-2-one (126 MHZ C_6D_6)

Chapter 3.

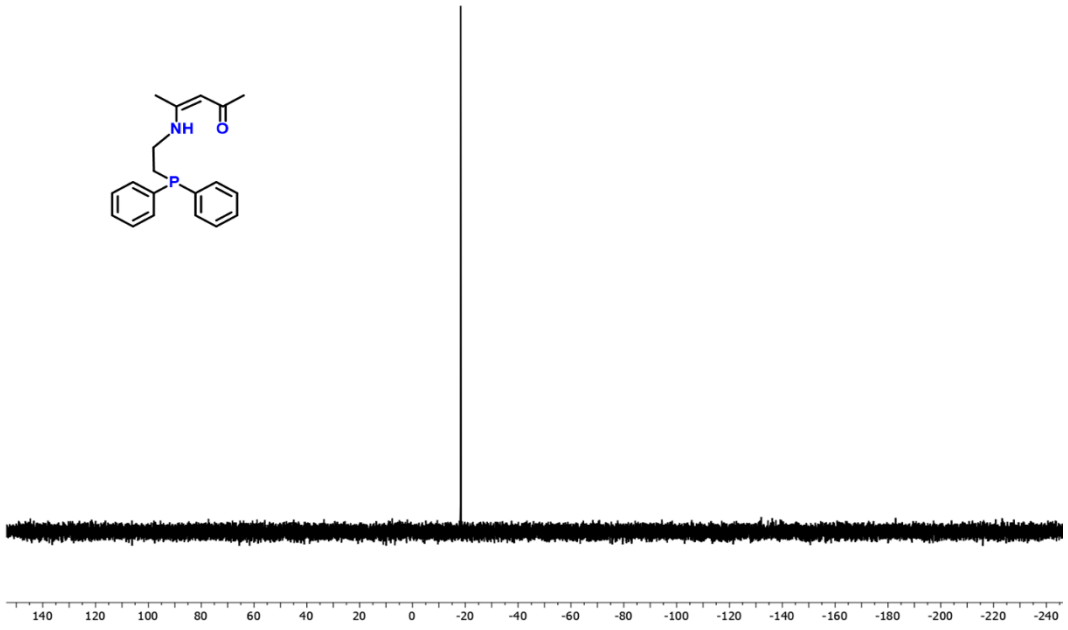

Figure S44: ^{31}P {^{1}H} NMR of 4-((2-(diphenylphosphaneyl) ethyl) amino) pent-3-en-2-one (202 MHZ C_6D_6)

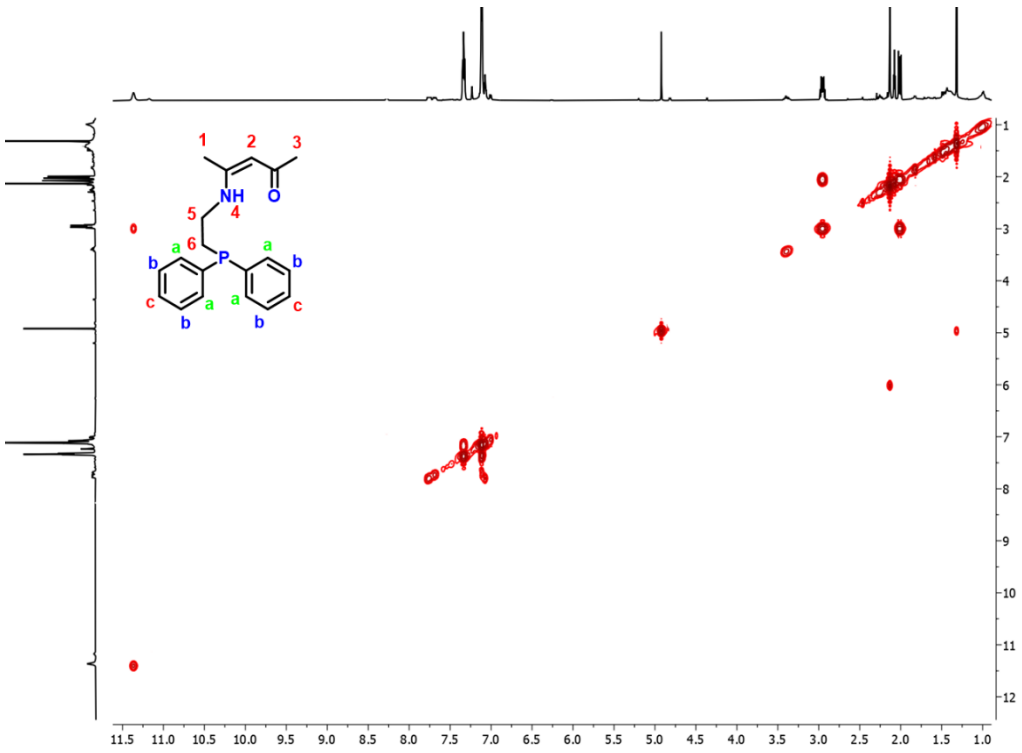

Figure S45: ^{1}H-^{1}H COSY NMR of 4-((2-(diphenylphosphaneyl) ethyl) amino) pent-3-en-2-one (500MHZ C_6D_6)

Chapter 3.

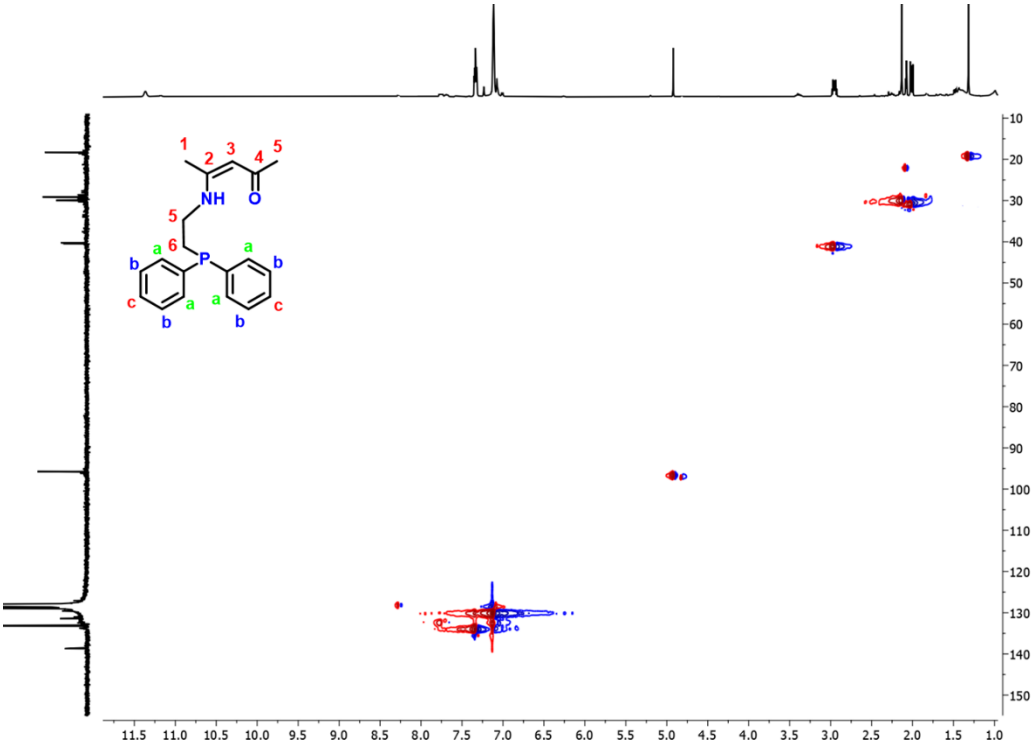

Figure S46: ^{1}H- ^{13}C HSQC NMR of 4-((2-(diphenylphosphaneyl) ethyl) amino) pent-3-en-2-one (500MHZ C_6D_6)

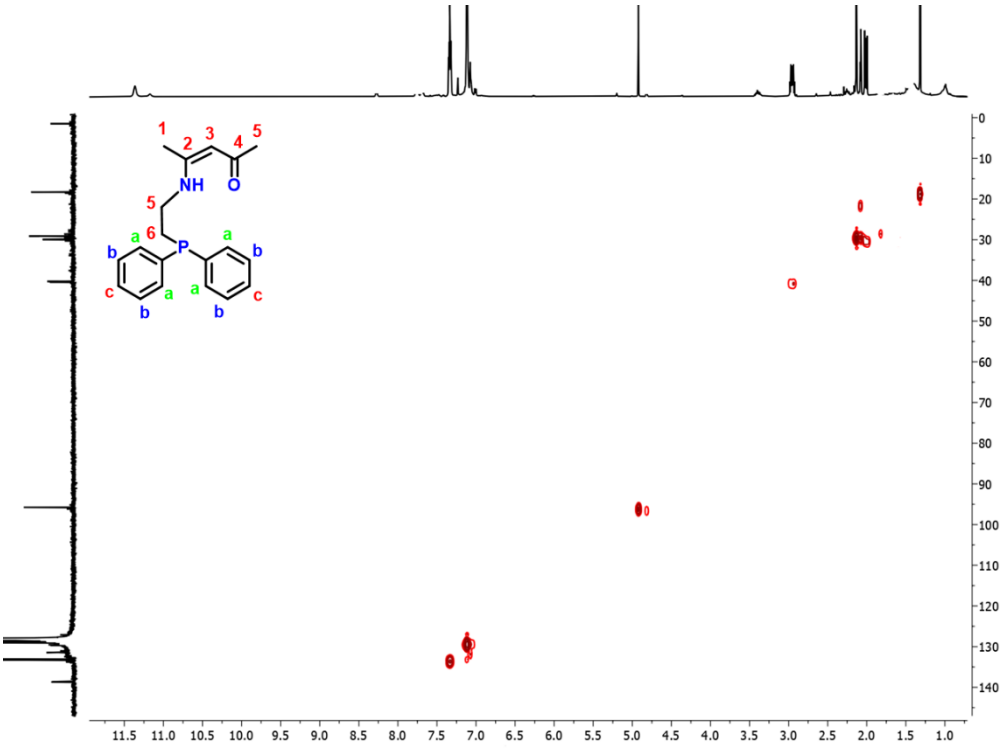

Figure S47: ^{1}H- ^{13}C HMBC NMR of 4-((2-(diphenylphosphaneyl) ethyl) amino) pent-3-en-2-one (500MHZ C_6D_6)

Chapter 3.

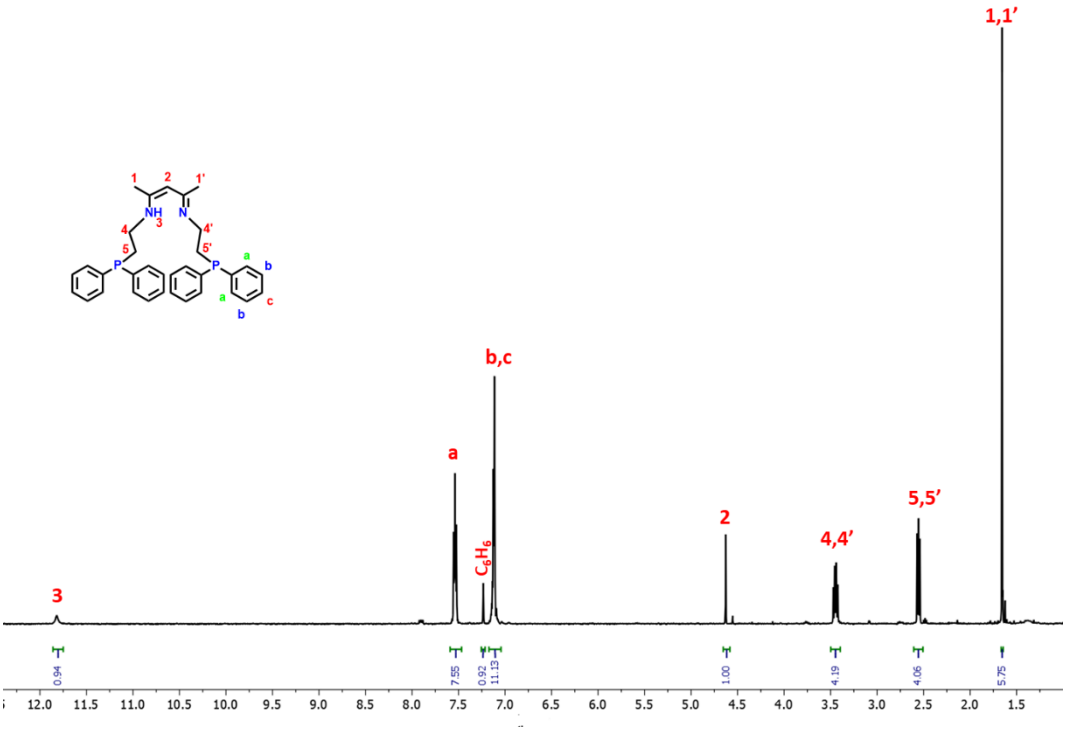

Figure S48: ^{1}H NMR of **L9** (500MHZ C_6D_6)

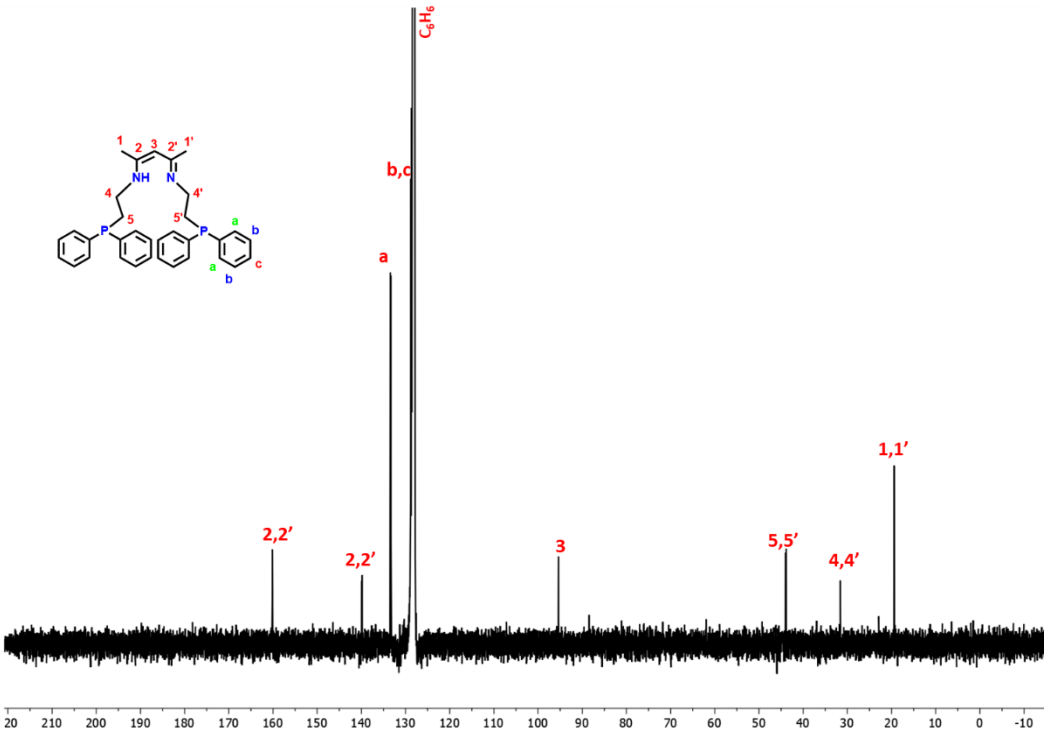

Figure S49: ^{13}C NMR of **L9** (126 MHZ C_6D_6)

Chapter 3.

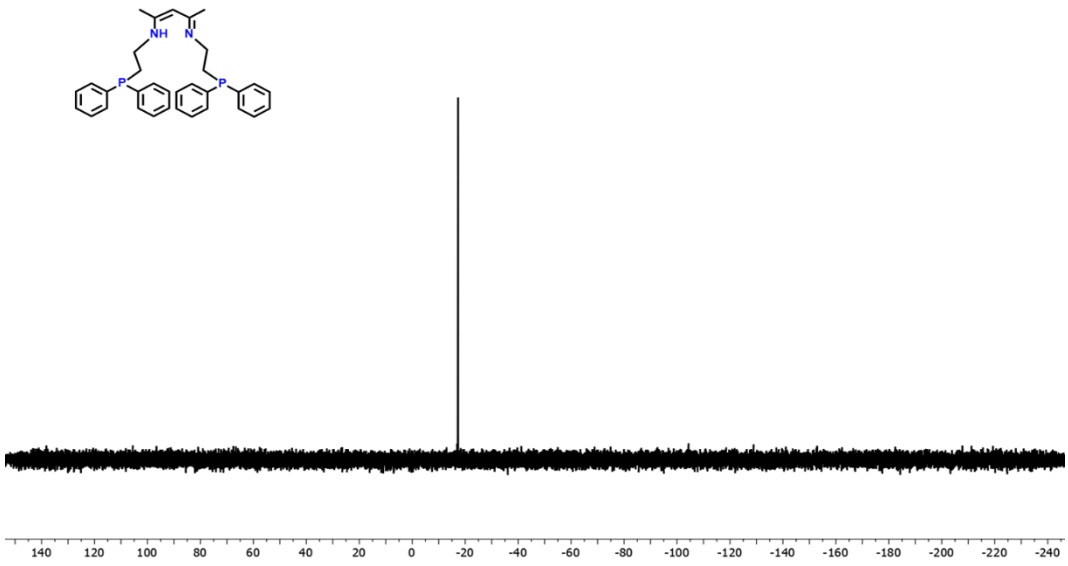

Figure S50: ^{31}P {^{1}H} NMR of **L9** (202 MHZ C_6D_6

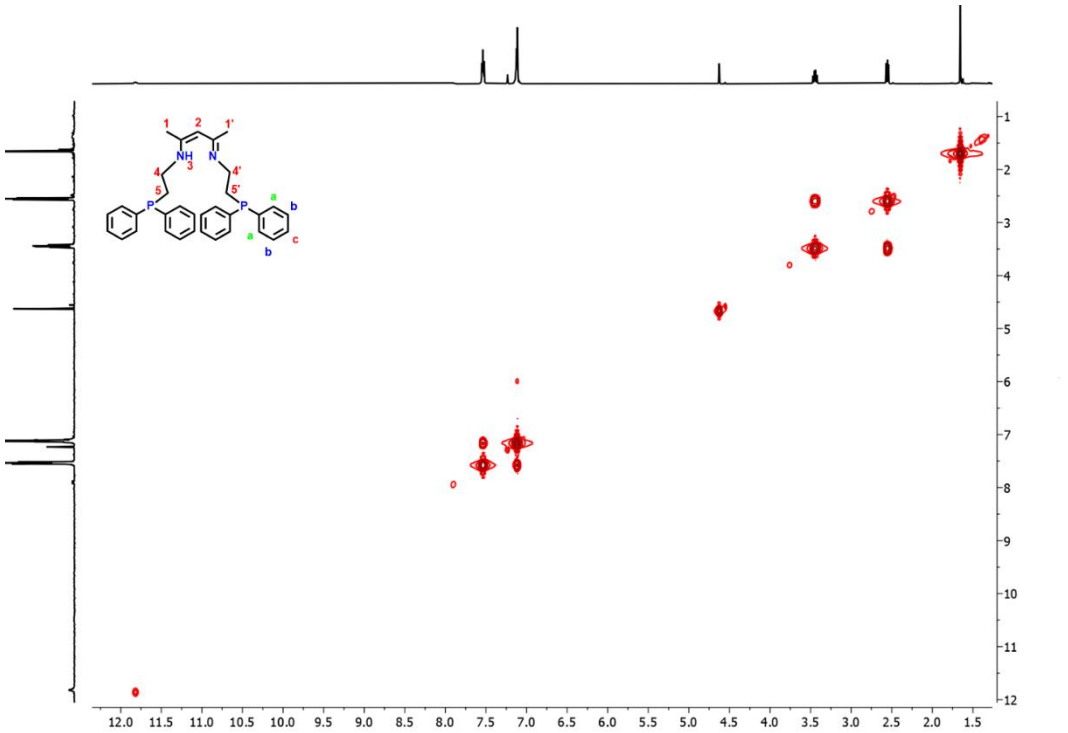

Figure S51: ^{1}H-^{1}H COSY NMR of **L9** (500MHZ C_6D_6)

Chapter 3.

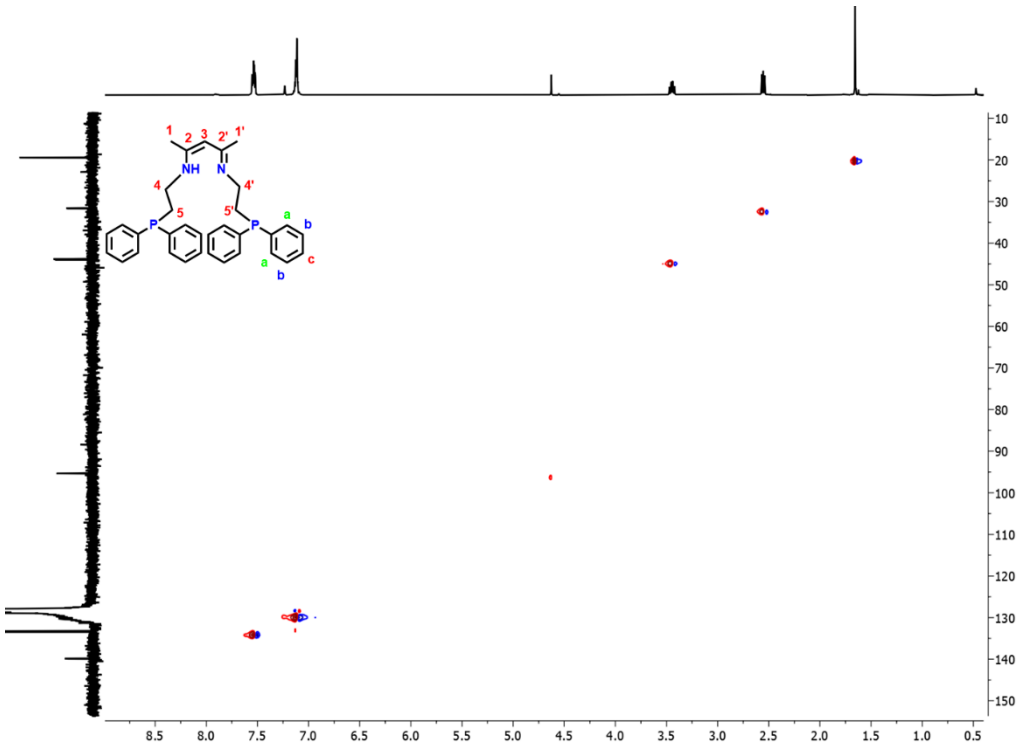

Figure S52: ^{1}H- ^{13}C HSQC NMR of **L9** (500MHZ C_6D_6)

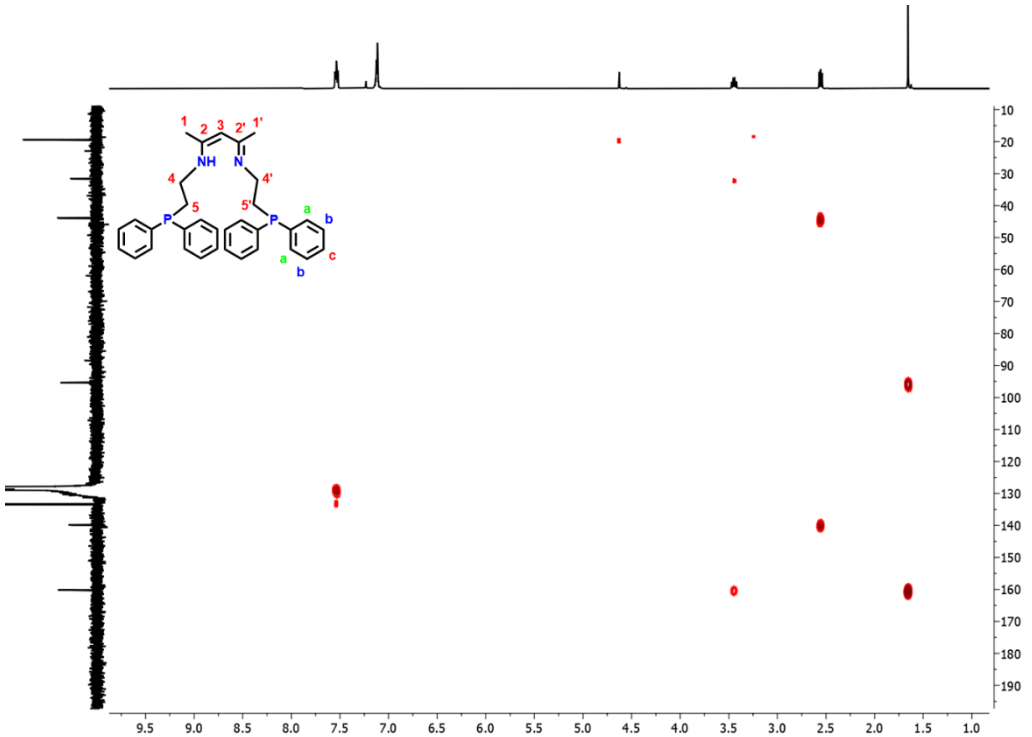

Figure S53: ^{1}H- ^{13}C HMBC NMR of **L9** (500MHZ C_6D_6)

Chapter 3.

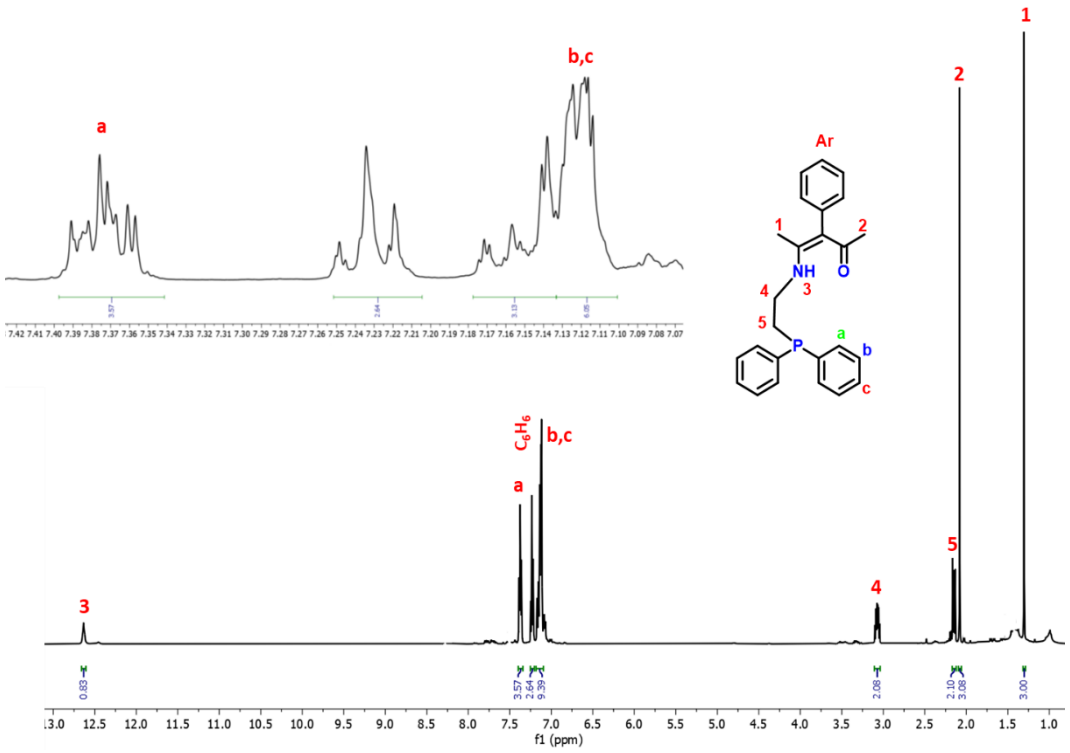

Figure S54: ^{1}H NMR of 4-((2-(diphenylphosphaneyl) ethyl) amino)-3-phenylpent-3-en-2-one (500MHZ C_6D_6)

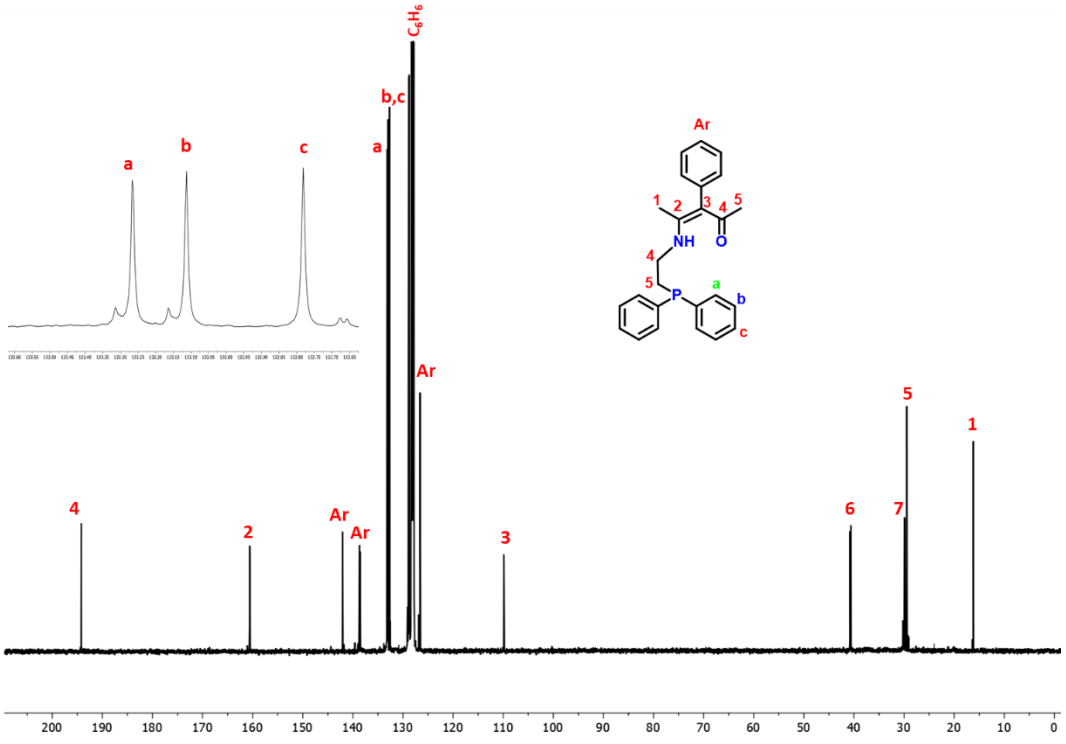

Figure S55: ^{13}C NMR of 4-((2-(diphenylphosphaneyl) ethyl) amino)-3-phenylpent-3-en-2-one (126 MHZ C_6D_6)

Chapter 3.

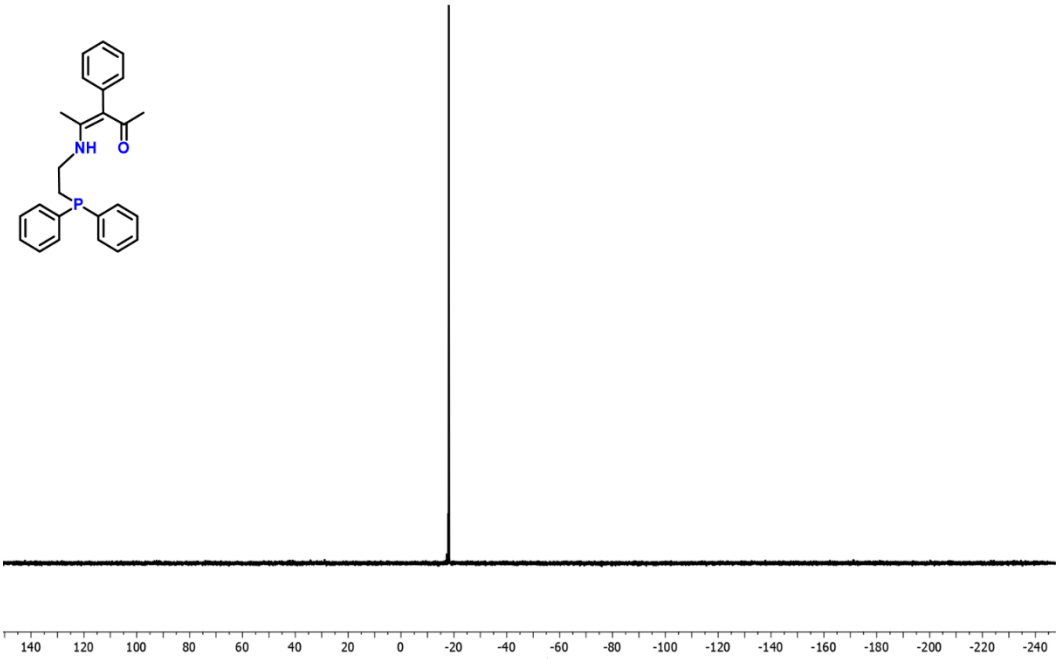

Figure S56: ^{31}P {^{1}H} NMR of 4-((2-(diphenylphosphaneyl) ethyl) amino)-3-phenylpent-3-en-2-one (202 MHZ C_6D_6)

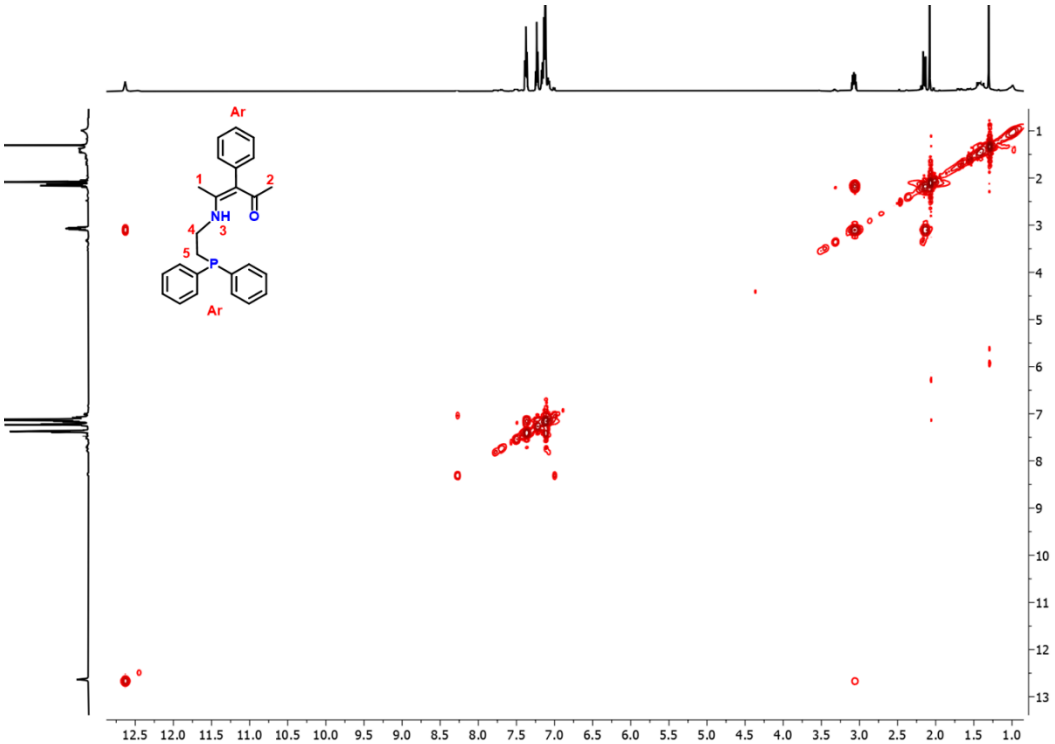

Figure S57: ^{1}H-^{1}H COSY NMR of 4-((2-(diphenylphosphaneyl) ethyl) amino)-3-phenylpent-3-en-2-one (500MHZ C_6D_6)

Chapter 3.

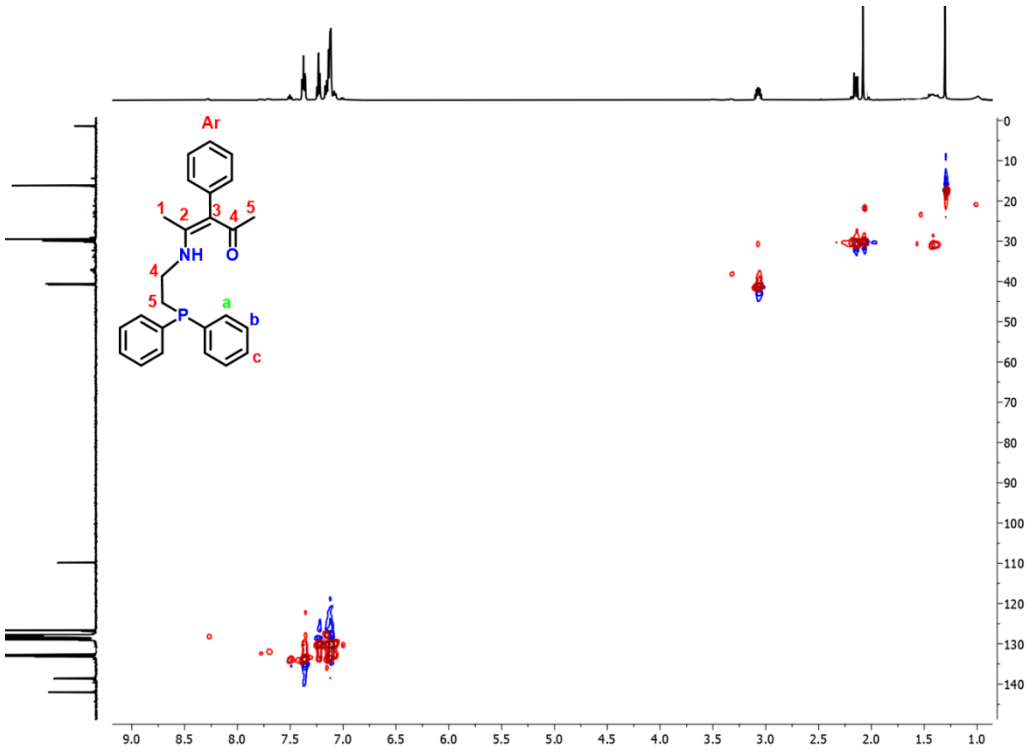

Figure S58: ^{1}H- ^{13}C HSQC NMR of 4-((2-(diphenylphosphaneyl) ethyl) amino)-3-phenylpent-3-en-2-one (500MHZ C_6D_6)

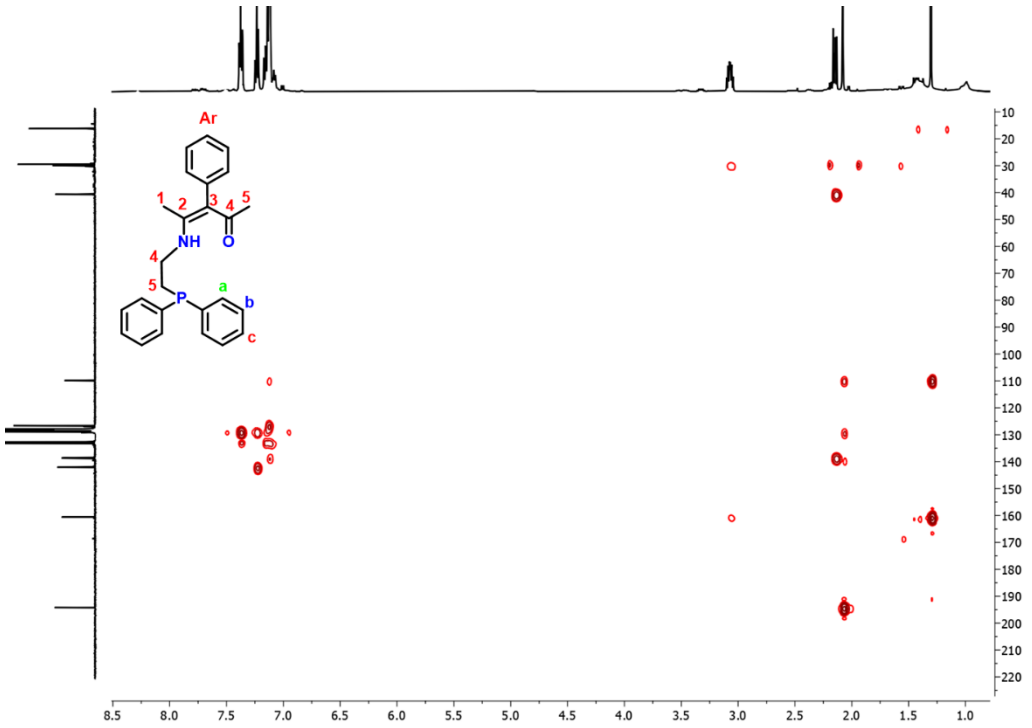

Figure S59: ^{1}H- ^{13}C HMBC NMR of 4-((2-(diphenylphosphaneyl) ethyl) amino)-3-phenylpent-3-en-2-one (500MHZ C_6D_6)

Chapter 3.

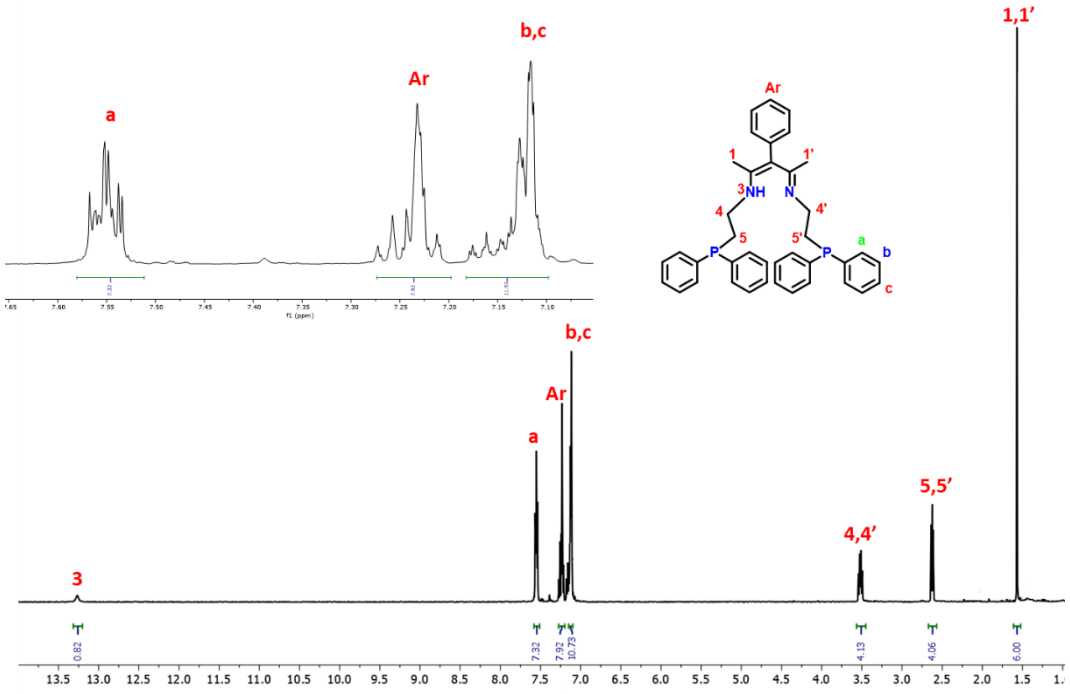

Figure S60: ^{1}H NMR of **L10** (500MHZ C_6D_6)

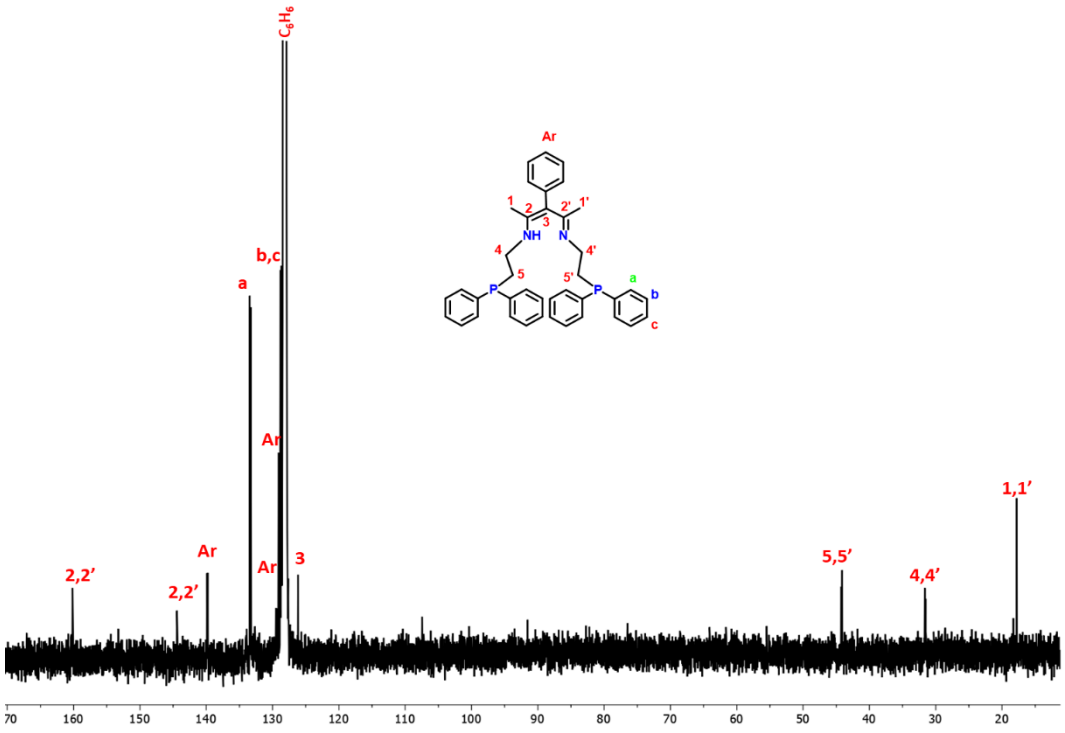

Figure S61: ^{13}C NMR of **L10** (126 MHZ C_6D_6)

Chapter 3.

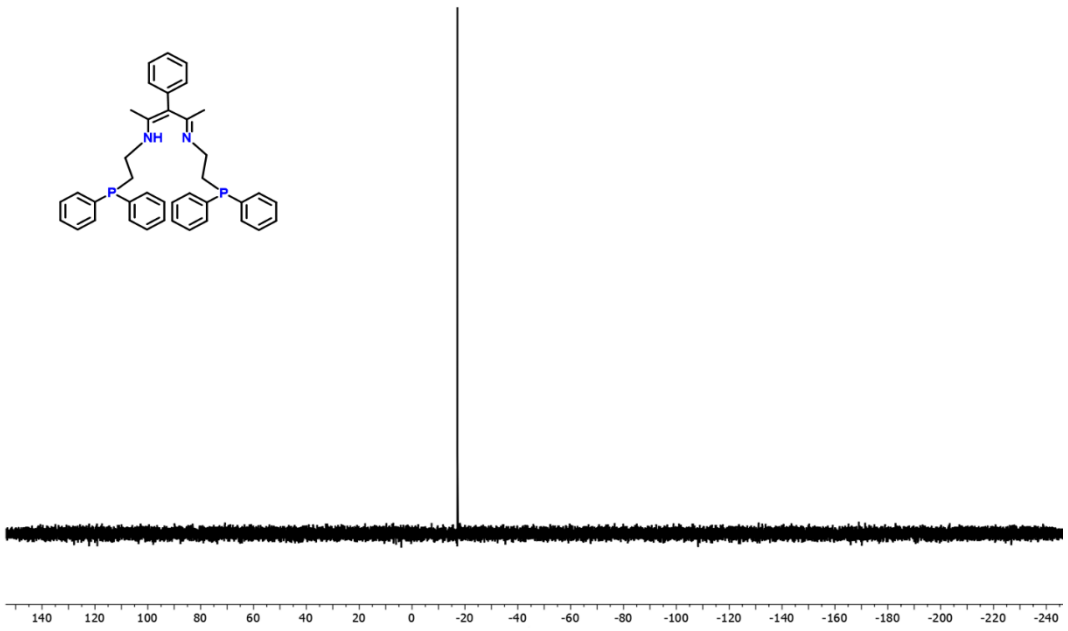

Figure S62: ^{31}P {^{1}H} NMR of **L10** (202 MHZ C_6D_6)

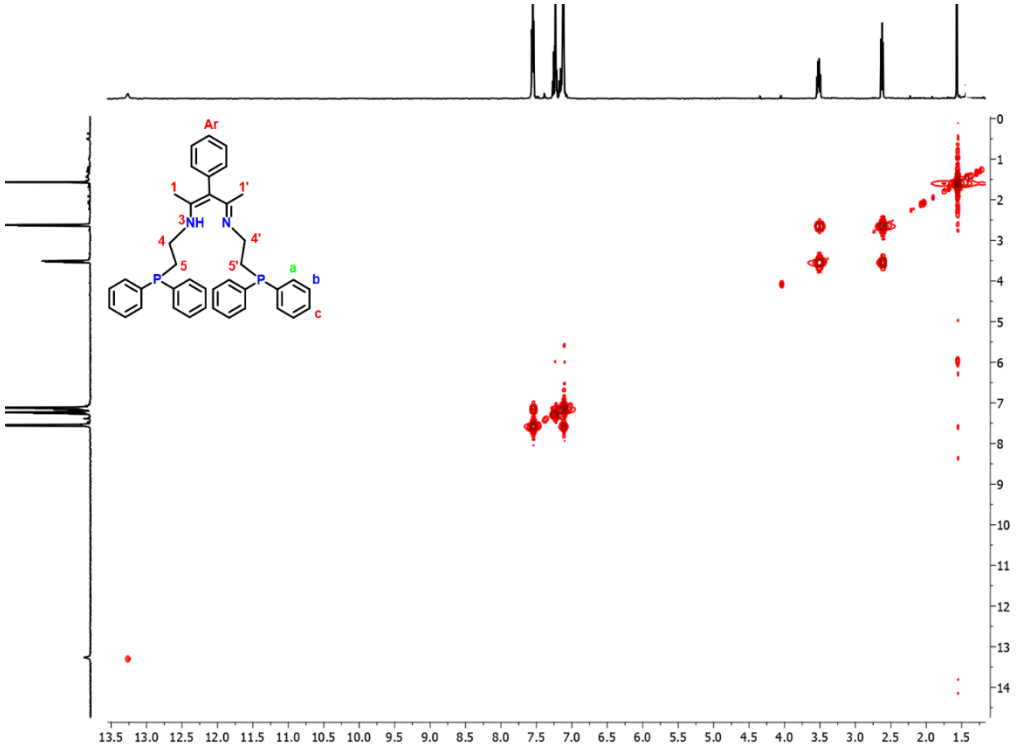

Figure S63: ^{1}H-^{1}H COSY NMR of **L10** (500MHZ C_6D_6)

Chapter 3.

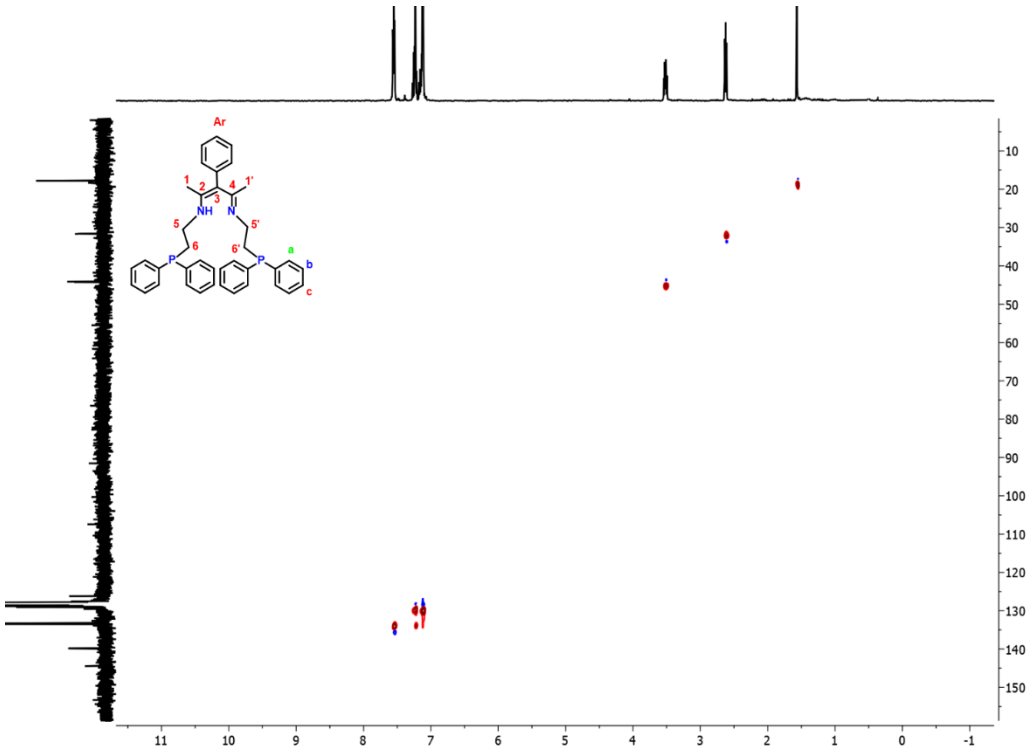

Figure S64: ^{1}H- ^{13}C HSQC NMR of **L10**(500MHZ C_6D_6)

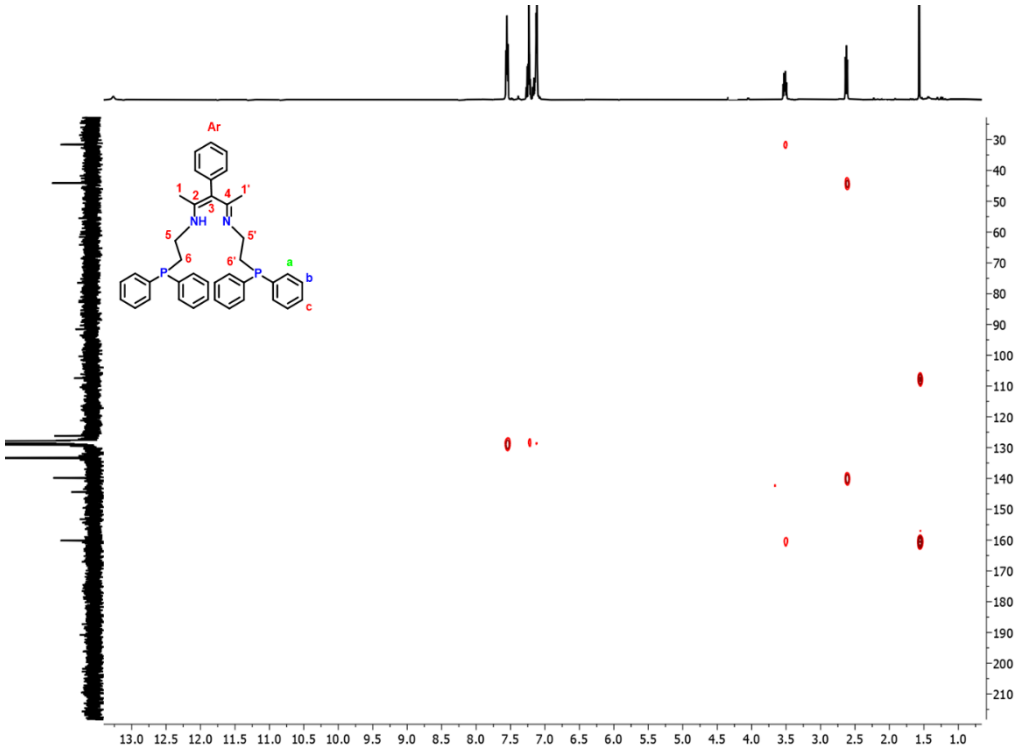

Figure S65: ^{1}H- ^{13}C HMBC NMR of **L10** (500MHZ C_6D_6)

Chapter 3.

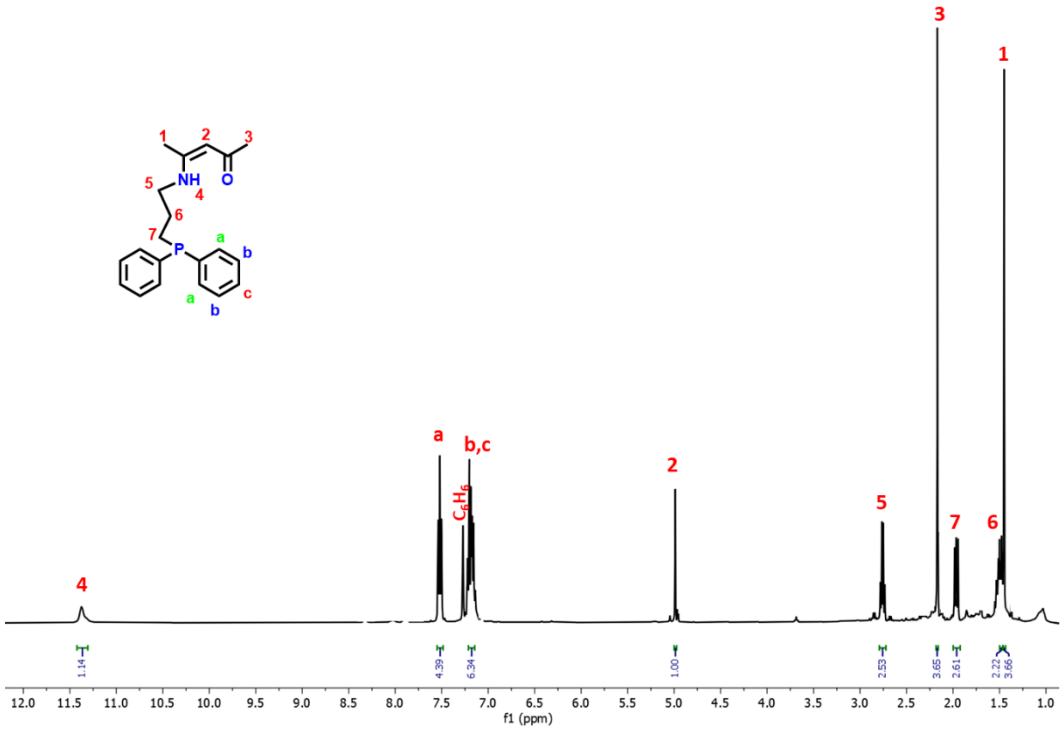

Figure S66: ^{1}H NMR of 4-((3-(diphenylphosphaneyl) propyl) amino) pent-3-en-2-one (400MHZ C_6D_6)

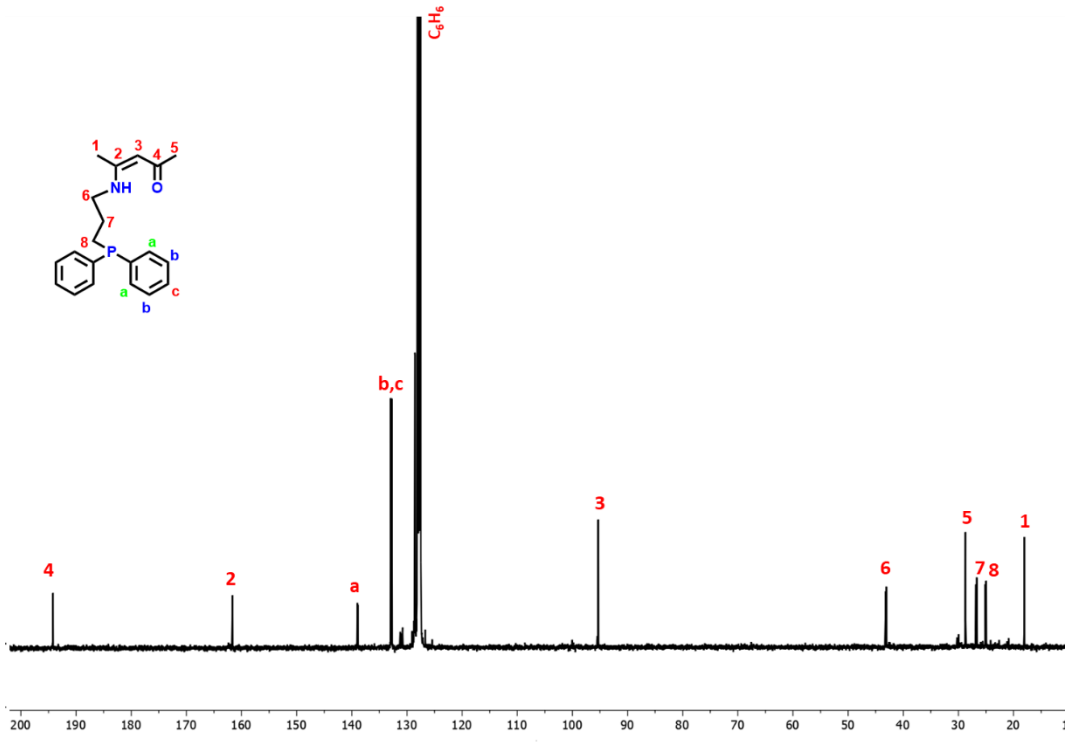

Figure S67: ^{13}C NMR of 4-((3-(diphenylphosphaneyl) propyl) amino) pent-3-en-2-one (101 MHZ C_6D_6)

Chapter 3.

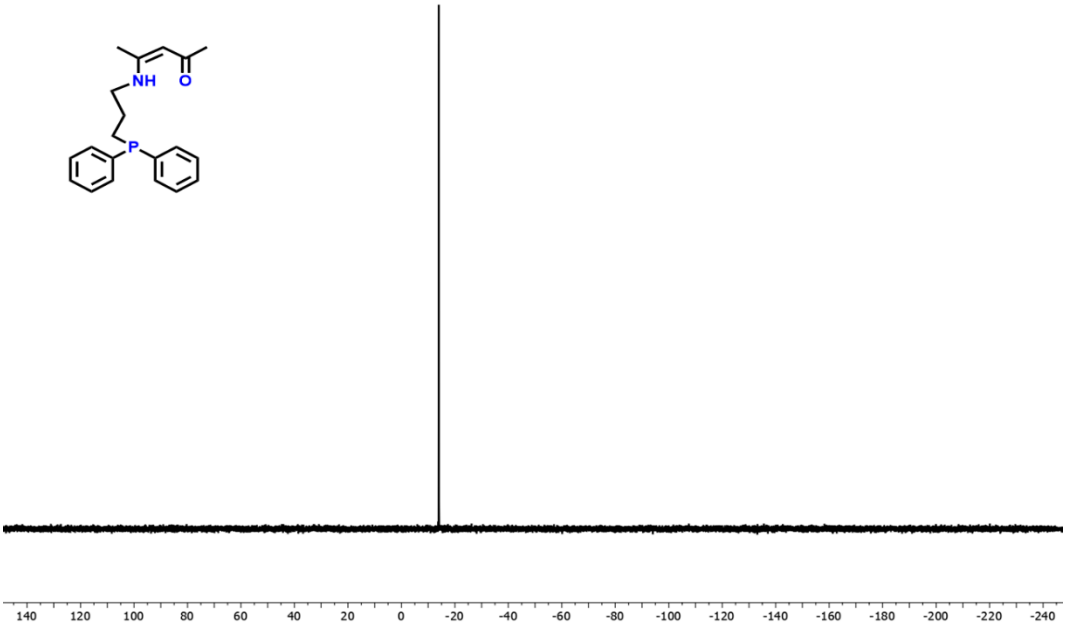

Figure S68: ^{31}P {^{1}H} NMR of 4-((3-(diphenylphosphaneyl) propyl) amino) pent-3-en-2-one (162 MHZ C_6D_6)

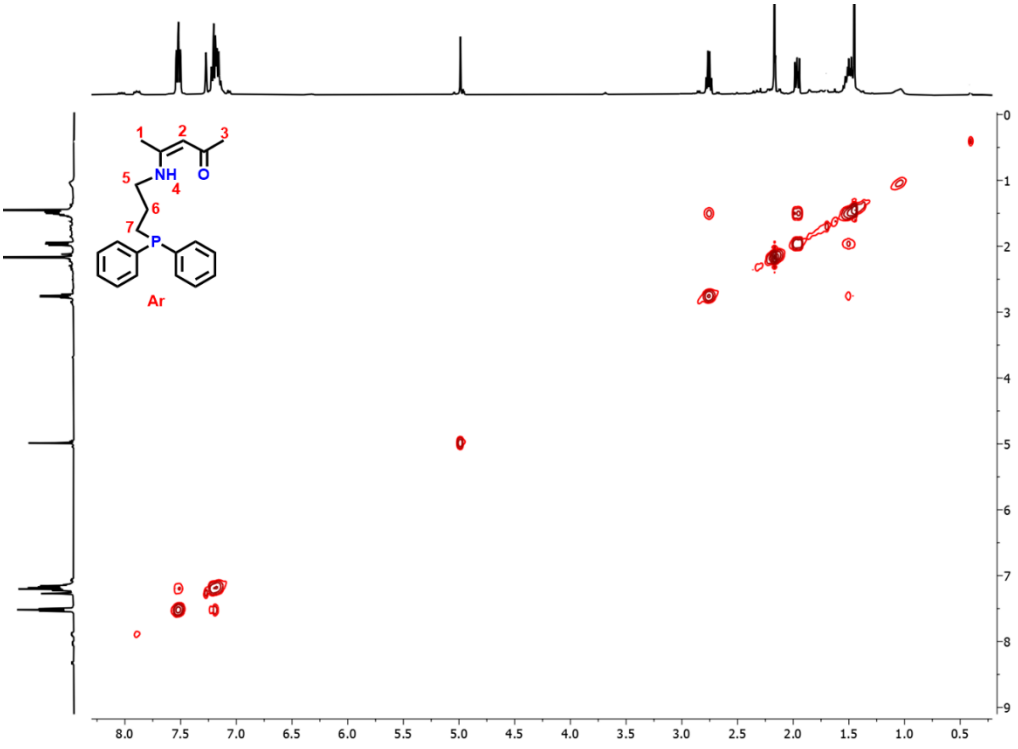

Figure S69: ^{1}H-^{1}H COSY NMR of 4-((3-(diphenylphosphaneyl) propyl) amino) pent-3-en-2-one (400MHZ C_6D_6)

Chapter 3.

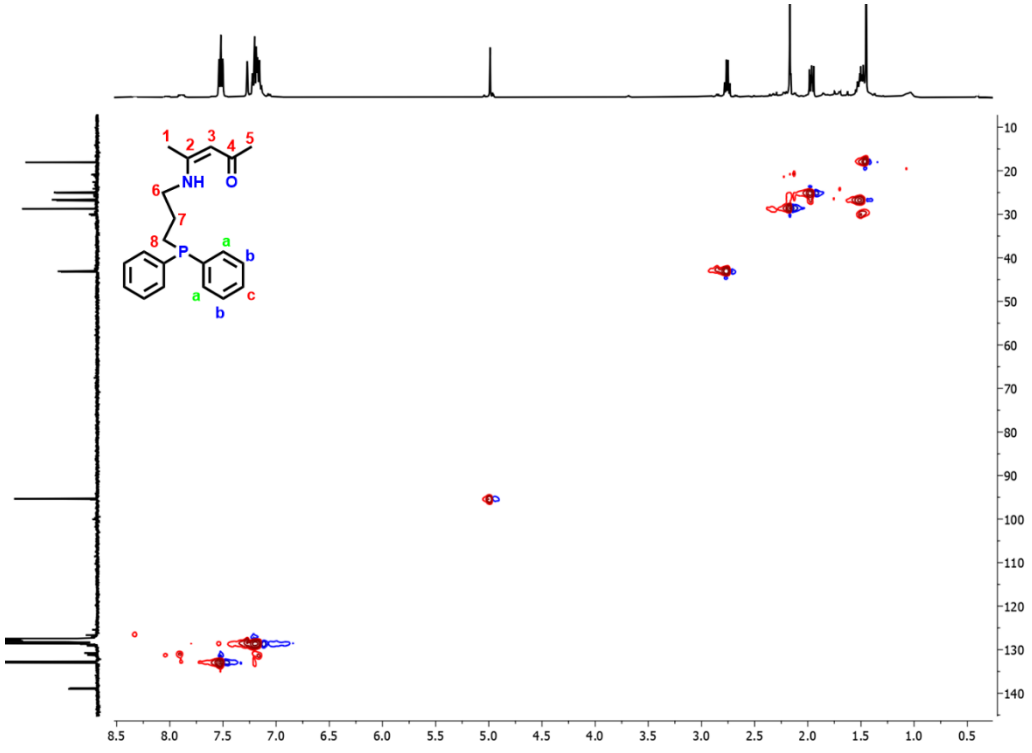

Figure S70: ^{1}H- ^{13}C HSQC NMR of 4-((3-(diphenylphosphaneyl) propyl) amino) pent-3-en-2-one (400MHZ C_6D_6)

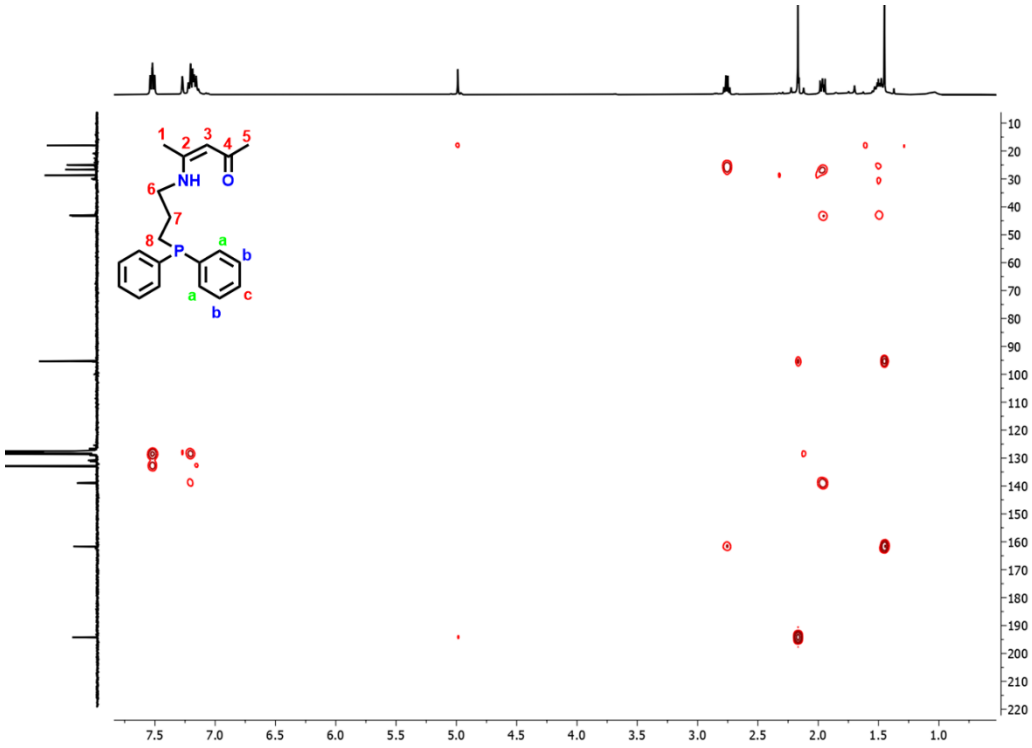

Figure S71: ^{1}H- ^{13}C HMBC NMR of 4-((3-(diphenylphosphaneyl) propyl) amino) pent-3-en-2-one (400MHZ C_6D_6)

Chapter 3.

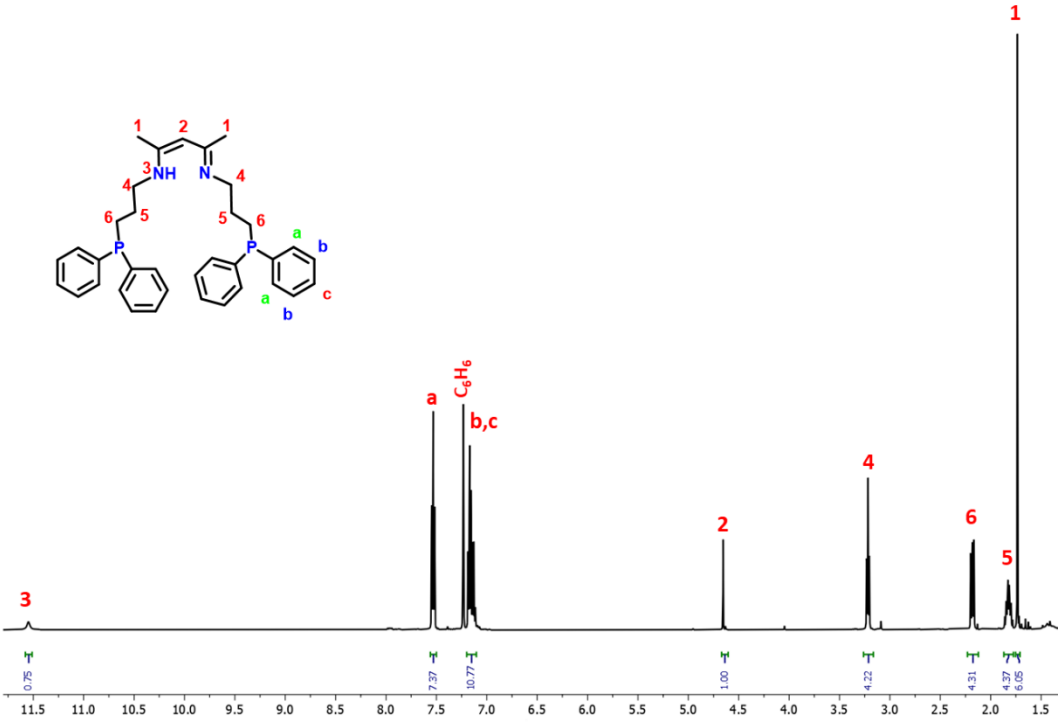

Figure S72- ^{1}H NMR of **L11** (500MHZ C_6D_6)

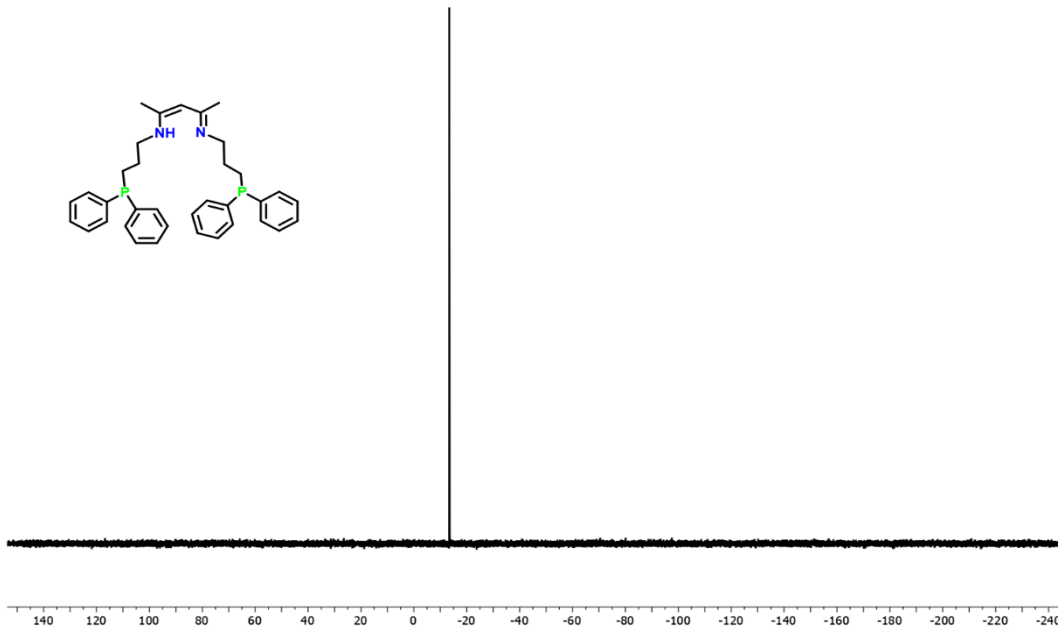

Figure S73- ^{31}P {^{1}H} NMR of **L11** (202 MHZ C_6D_6)

Chapter 3.

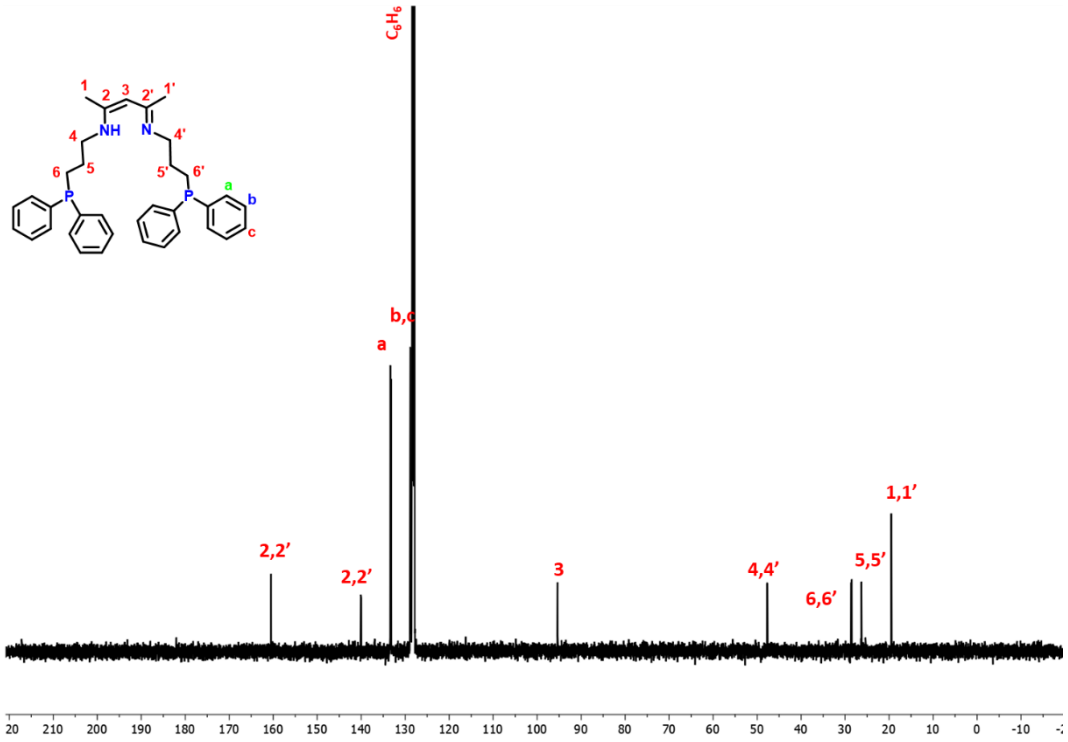

Figure S74- ^{13}C NMR of **L11** (126 MHZ C_6D_6)

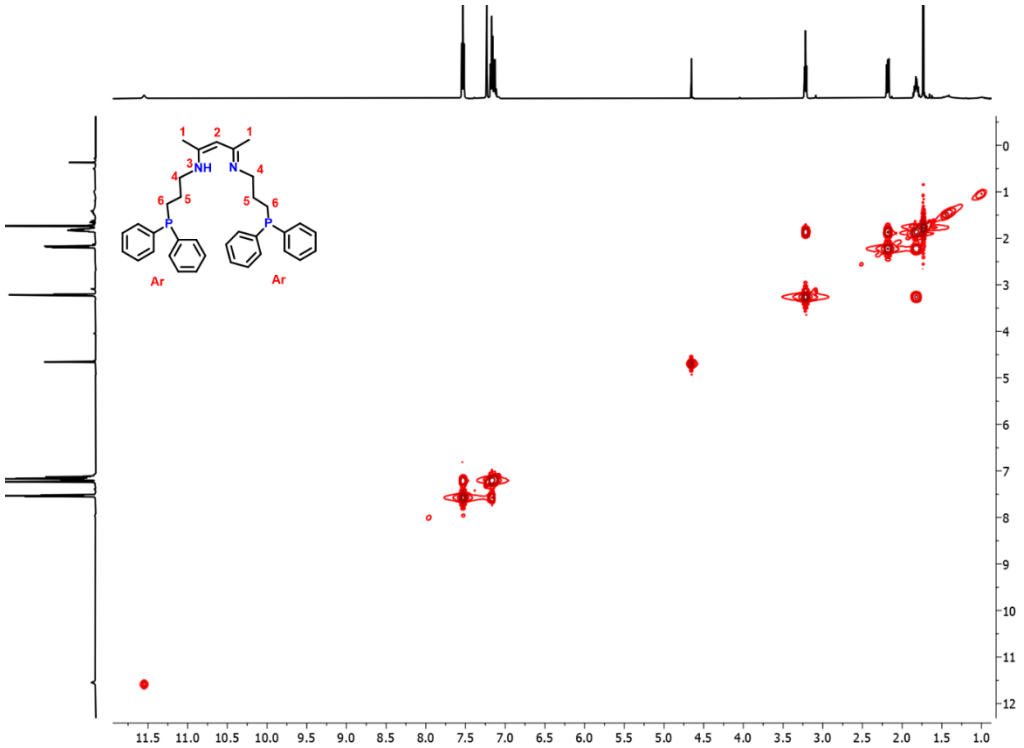

Figure S75- ^{1}H-^{1}H COSY NMR of **L11** (500MHZ C_6D_6)

Chapter 3.

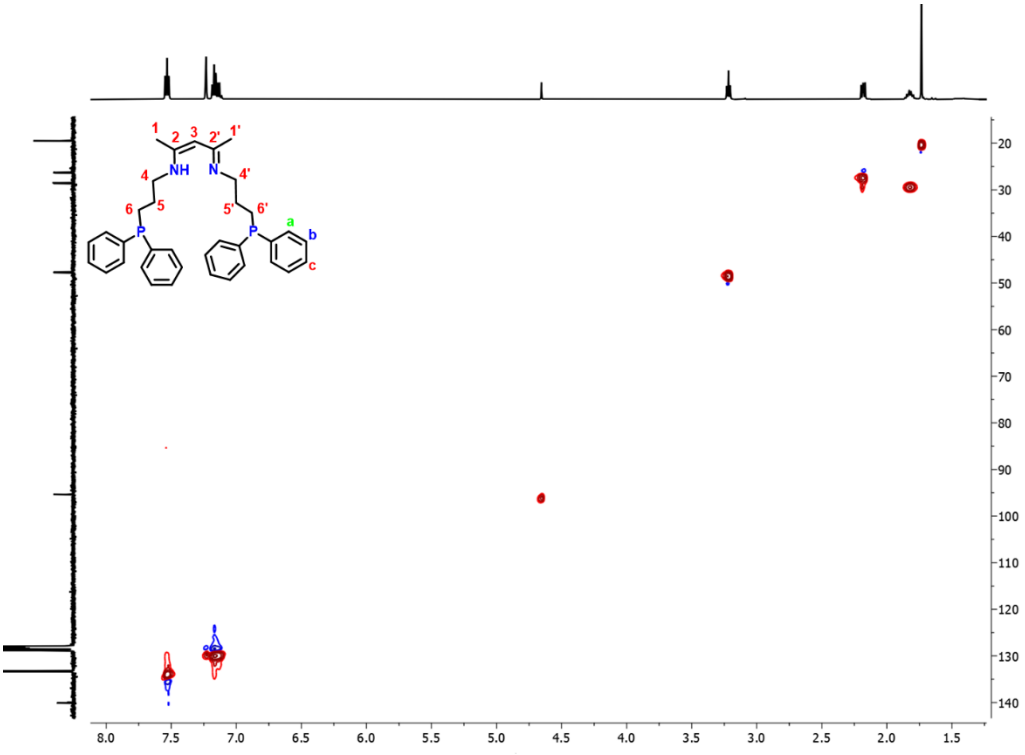

Figure S76- ^{1}H- ^{13}C HSQC NMR of **L11** (500MHZ C_6D_6)

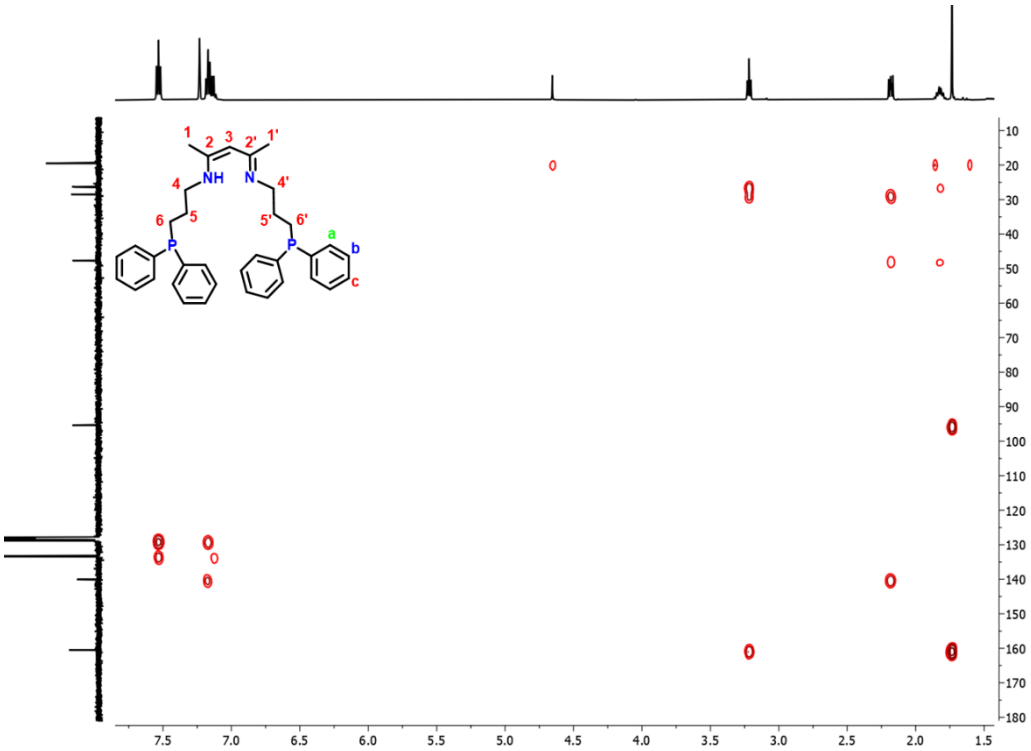

Figure S77- ^{1}H- ^{13}C HMBC NMR of **L11** (500MHZ C_6D_6)

Chapter 3.

2- X-ray diffraction analysis

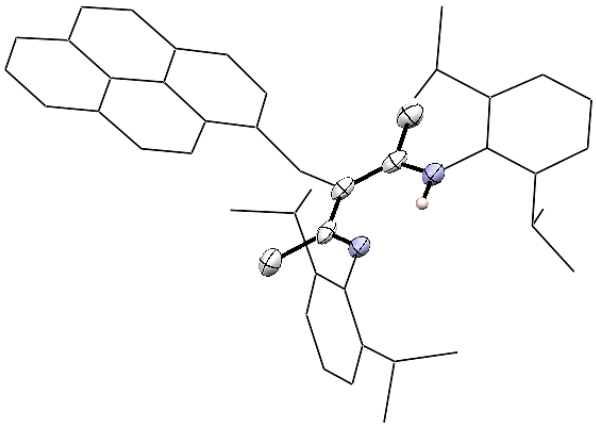

Figure S78. Picture of the X-ray diffraction structure of the enamine tautomer of ligand **L2**.

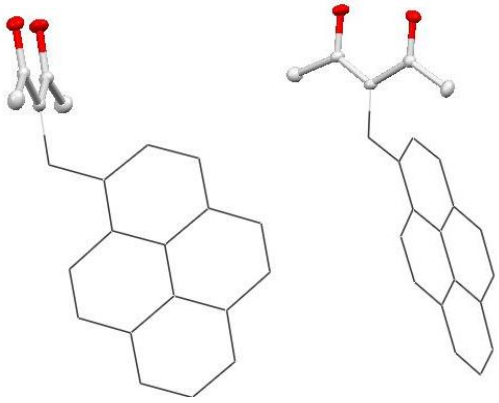

Figure S79. Picture of the X-ray diffraction structure of the enol tautomer of 3-(pyren-1-ylmethyl)pentane-2,4-dione.

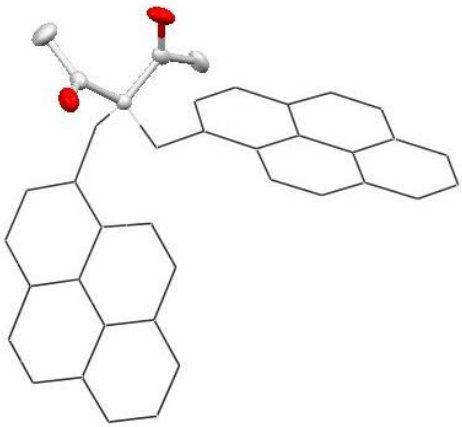

Figure S80. Picture of the X-ray diffraction structure of 3,3-bis(pyren-1-ylmethyl)pentane-2,4-dione.

Chapter 4

Interplay between β-diimino and β-diketiminato ligands in nickel complexes active in the proton reduction reaction

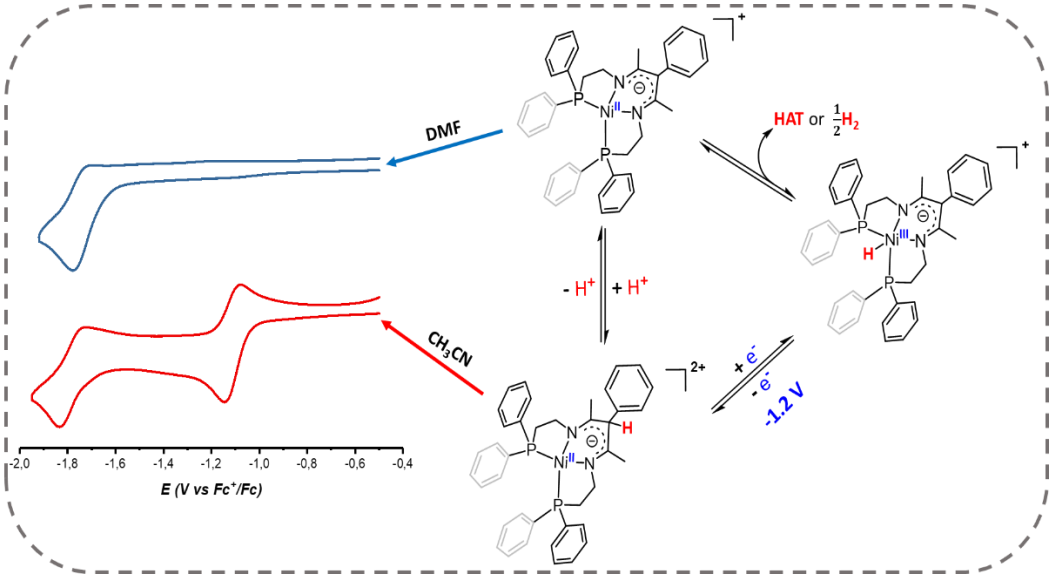

Chapter 4.

1- Introduction

Increasing carbon dioxide concentration on earth's atmosphere caused by anthropogenic processes has caused global warming which has had severe environmental impact. To tackle this problem, transferring from fossil fuel-based economy to renewable energies-based economy is imperative. Renewable energy resources, such as sunlight or wind energy, are intermittent and should be stored to be able to be used whenever and wherever needed.[1,2] Over billions of years, Nature has been using one of the most excellent strategies: natural photosynthesis, which consists of capturing the sunlight energy and storing it in the form of chemical bonds.[3,4] Inspired by natural photosynthesis the concept of the artificial photosynthesis has evolved, focusing on capturing photons from the sunlight and using them to produce solar fuels as energy careers, as described in detail in Chapter 1 of this manuscript. To make artificial photosynthetic devices economically feasible and viable, development of catalytic systems that facilitate the involved chemical reactions is necessary. These catalytic systems not only should make thermodynamically and kinetically uphill water oxidation half reaction feasible but also facilitate the utilization of the electrons obtained from water oxidation to reduce protons and/or carbon dioxide to hydrogen and carbon fuels as energy carriers, respectively.[5–7] For this purpose, metal complexes have received increasing interest because their electronic and structural properties can easily be tuned by ligand modification. This versatility can affect their stability, selectivity, and catalytic activities.[8] Following this strategy, in the recent years we have witnessed the emergence of robust molecular complexes with different ligand backbones and metal centers for catalyzing multi-electron and multi- proton chemical reactions including water oxidation[9–13] , CO_2 [14–19] and proton reduction (see also Chapter 1 of this manuscript).[20–23] In this context, β-diketiminato (BDK) ligands have recently gained resurgence for their versatility regarding ligand backbone tunability (**Figure 1**, see also Chapter 3). BDK ligands have been used in many coordination compounds using metals all across the periodic table, which have found applications in many disciplines including energy related applications[24,25] and catalysis.[26–29]

In this work, we describe the synthesis, spectroscopic and electrochemical characterization of two novel β-diimine complexes (BDI, Figure 1, left) with two different substituents in the α-carbon position and their conversion to the corresponding β-diketiminate derivative (BDK, **Figure 1**, right) in the context of the proton reduction reaction to produce hydrogen.

Chapter 4.

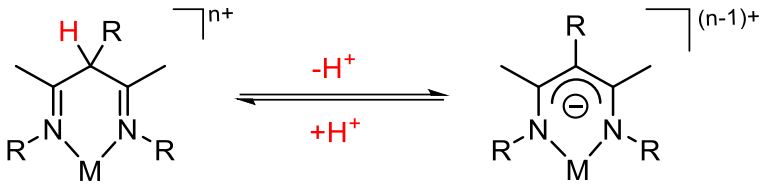

Figure 1. β-Diimino (left) and β-diketiminato (right) metallic complexes.

2- Results and discussion

2.1- Synthesis and structural characterization of complexes $1(BF_4)_2$ and $2(BF_4)_2$

HBDI and PhBDI ligands in Scheme 1 are two novel tetradentate ligands with two nitrogen and two phosphorous donors, that differ on the substituent of the α-C position (H for HBDI and Ph for PhBDI). The synthesis of ligands HBDI and PhBDI was performed through two consecutive condensation steps in oxygen and moisture free conditions. Briefly, the first condensation was performed by refluxing the corresponding acetylacetone and 2-(diphenylphosphaneyl)ethylamine in the presence of a catalytic amount of acid in toluene and the second condensation was performed using dimethylsulfate in a solvent free reaction with overall yields of 30 % and 35 % for HBDI and PhBDI, respectively (**Scheme 1**, see also Chapter 3). The synthesis of Ni complexes from ligands HBDI and PhBDI is straightforward using $Ni(BF_4)_2{\cdot}6H_2O$ as metal precursor, obtaining moderate to good reaction yields (36 % and 96 % for complexes **$1(BF_4)_2$** and **$2(BF_4)_2$** respectively).

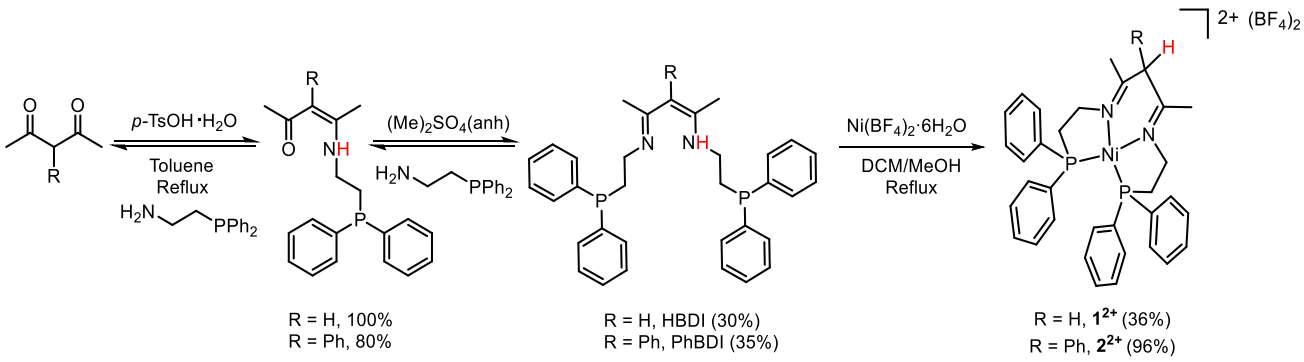

Scheme 1. Synthesis of ligands and complexes described in this work.

Chapter 4.

The resulting Ni(II) d^8 complexes **1(BF$_4$)$_2$** and **2(BF$_4$)$_2$** are diamagnetic. They were fully characterized by NMR spectroscopy (**Figure S1-S26** in the Supporting information). The ^{1}H NMR spectra in CD_3CN show the characteristic resonances of the α-imino protons of the sp^3 carbon at 4.29 ppm integrating 2H for **1(BF$_4$)$_2$** and at 5.50 ppm integrating 1H for **2(BF$_4$)$_2$**. A single set of resonances per methylene group of the ligand scaffold is indicative of a symmetric structure of the complexes. This is confirmed by the ^{31}P{H} NMR spectra in CD_3CN which show a unique singlet resonance for the two phosphine ligands at 49.64 ppm and 47.15 ppm for **1(BF$_4$)$_2$** and **2(BF$_4$)$_2$**, respectively.

All the resonances corresponding to complex **1(BF$_4$)$_2$** are significantly shifted when the NMR analysis is performed in deuterated dimethylformamide (DMF-d7) (Figure 2 and Figure S23-S24 in the SI). In particular, the α-imino proton appears at 5.31 ppm, accounting for a 1.02 ppm downfield shift compared to the resonance in CD_3CN. In addition, it integrates for one proton instead of two, suggesting a deprotonation of the neutral β-diimino ligand to form a negatively charged β-diketiminate derivative (**Figure 1**). This is confirmed by the ^{13}C NMR spectrum, where the chemical shift of the C=N imino carbon is upfield shifted from 179.97 ppm in CD_3CN to 161.81 ppm in DMF-d7 and the α-carbon is downfield shifted from 53.71 ppm in CD_3CN to 102.16 ppm in DMF-d7. The assignment of the α-carbon is confirmed by the clear crossed signals in the HSQC spectra (see **Figure 3** and **Figures S5** and **S6** in the SI). This impressive shift can only be explained by the changes in hybridization and formal charge of the carbon atoms going from a β-diimino to a β-diketiminate ligand. A similar phenomenon is observed for complex **2(BF$_4$)$_2$** where the resonance corresponding to the α-CH proton disappears (Figure S25). Likewise, the C=N carbon shifts from 181.52 ppm in CD_3CN to 144.81 ppm in DMF-d7 and the α-carbon from 67.97 ppm in CD_3CN to 112.96 ppm in DMF-d7 (**Figure S26**). ^{2}D-NMR experiments of both complexes in DMF-d7 rule out the possible α-imino proton exchange with the solvent and supports the deprotonation of the β-diimino ligand (**Figure S27**). Indeed, the acidity of the α-CH proton is rather high and it is increased once coordinated to the metal center, so that even very weak bases such as DMF induce the deprotonation of the ligand.[30,31]

Chapter 4.

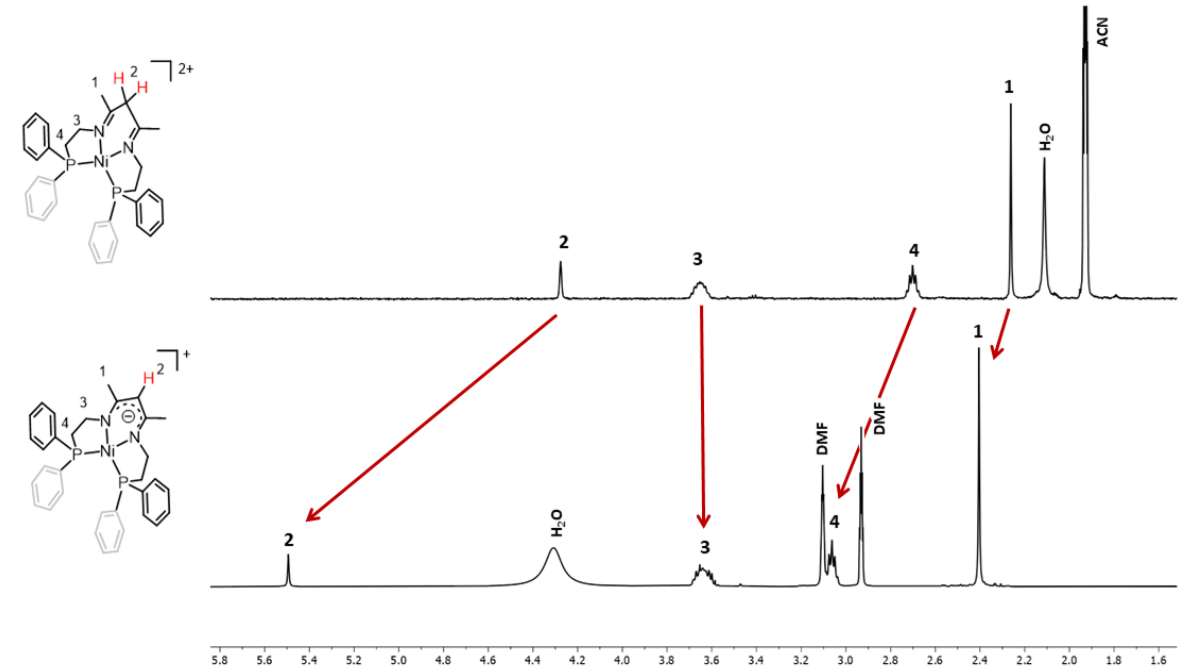

Figure 2. Comparison ^{1}H NMR spectra of Complex **1(BF$_4$)$_2$** in CD_3CN (**top**) and DMF-d_7 (**bottom**).

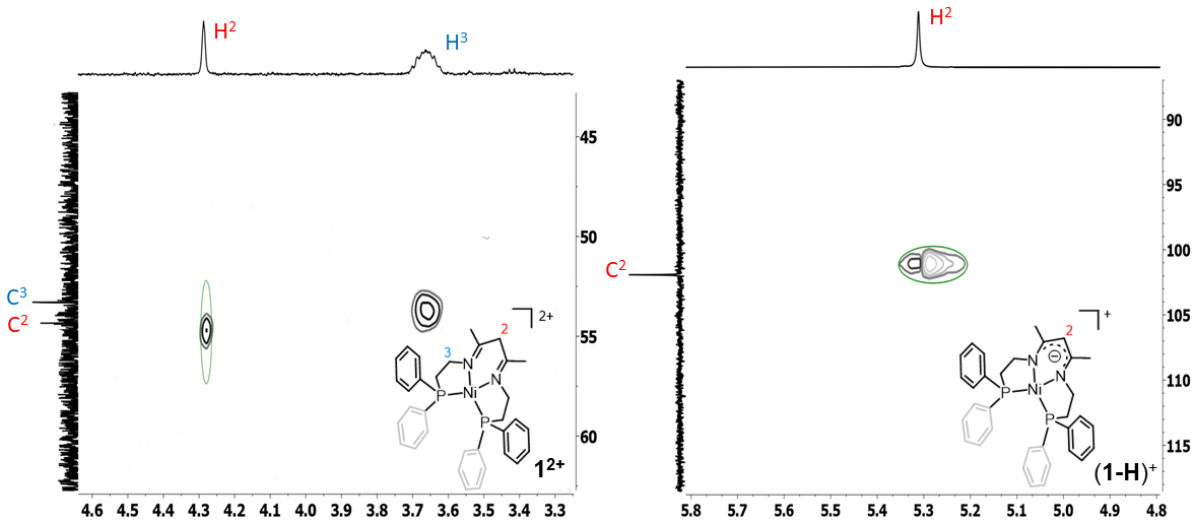

Figure 3. Zoom of the HSQC spectra of **1(BF$_4$)$_2$** in CD_3CN (left) and DMF-d_7 (right).

The β-diimino compounds **1(BF$_4$)$_2$** and **2(BF$_4$)$_2$** and the β-diketiminato derivatives (here after (**1-H**)**BF$_4$** and (**2-H**)**BF$_4$**) where characterized by UV-Vis spectroscopy (**Figure 4**). Complex **1(BF$_4$)$_2$** in acetonitrile shows an intense absorption below 300 nm and two well-

Chapter 4.

defined absorption bands at 323 nm (ε = 3720 $M^{-1} \times cm^{-1}$) and 348 nm (ε = 4528 $M^{-1} \times cm^{-1}$) with a shoulder at 414 nm (ε = 460.72 $M^{-1} \times cm^{-1}$) (black trace in **Figure 4a**). These bands are attributed to intra ligand π-π* transitions. Finally, a very weak absorption band at 512 nm (ε = 196.56 $M^{-1} \times cm^{-1}$) appears that is assigned to d-d transition of the low spin square planar Ni(II) complex.[32]

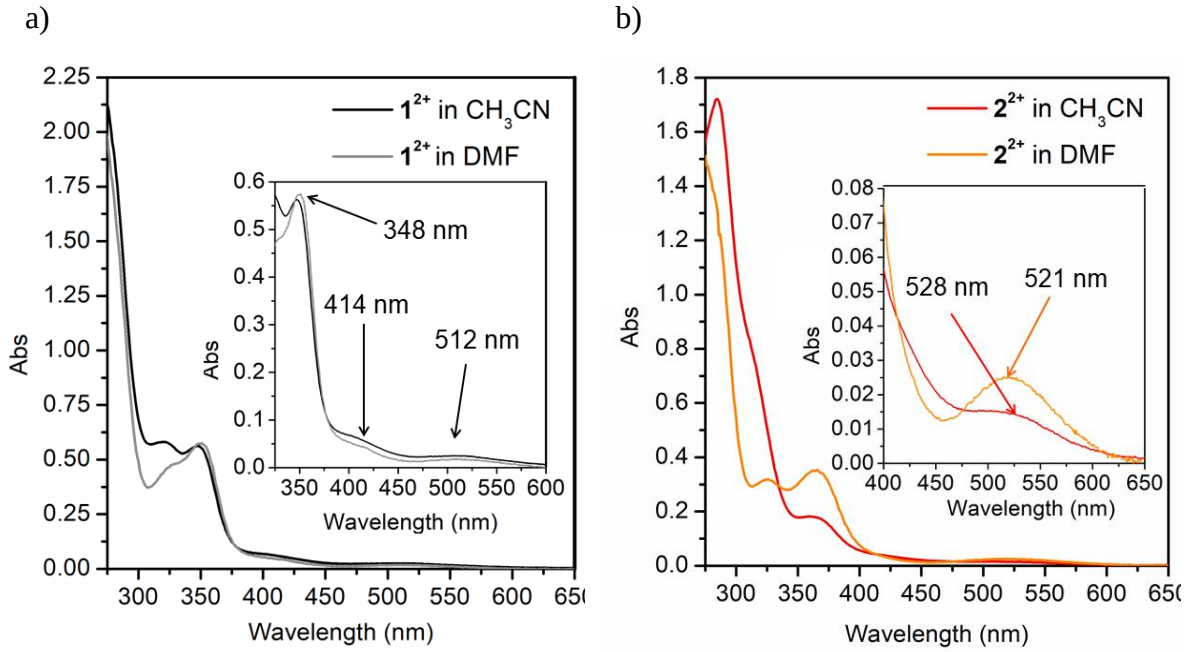

Figure 4. UV-Vis spectra of a 0.125 mM of (a) **1(BF4)2** in CH_3CN (black) and DMF (grey) and (b) **2(BF4)2** in CH_3CN (red) and DMF (orange).

As discussed above, dissolving **1(BF4)2** in DMF affords the β-diketiminate derivative, which shows a very similar UV-Vis spectrum (grey trace in **Figure 4a**) with exactly the same bands but less intense at 323 nm (ε = 3720 $M^{-1} \times cm^{-1}$), shoulder at 414 nm (ε = 356.56$M^{-1} \times cm^{-1}$) and 512 nm (ε = 134.24 $M^{-1} \times cm^{-1}$). In contrast, the band at 348 nm (ε = 4578 $M^{-1} \times cm^{-1}$) is slightly more intense (**Figure 4a**, inset). The differences in the absorption spectra of **2(BF4)2** and (**2-H**)**BF4** are more pronounced although the band positions are also very similar (**Figure 4b**, red and orange traces respectively). The spectrum in CH_3CN shows bands at 284 nm (ε = 13770 $M^{-1} \times cm^{-1}$), a shoulder at 313 nm (ε = 6499 $M^{-1} \times cm^{-1}$), and two other bands at 365 nm (ε = 1507 $M^{-1} \times cm^{-1}$) and 528 nm (ε = 112.72 $M^{-1} \times cm^{-1}$). In comparison, **2(BF4)2** in DMF shows bands at 270 nm partially overlapped with the solvent subtraction noise, at 325 nm (ε = 2526 $M^{-1} \times cm^{-1}$), 365 nm (ε = 2832 $M^{-1} \times cm^{-1}$) and 528nm (ε = 193.6 $M^{-1} \times cm^{-1}$).

Chapter 4.

Single crystals suitable for x-ray diffraction analysis were grown by layering Et_2O on top of a saturated solution of complexes **1(BF$_4$)$_2$** or **2(BF$_4$)$_2$** in CH_3CN while keeping the mixture at -30 °C. The ORTEP representations of the cationic part of both complexes, shown in **Figure 5**, reveal a distorted square planar geometry with angles of 94.56º (N1-Ni-N2), 83.06º (N2-Ni-P2), 86.48º (N1-Ni-P1) and 95.85º (P1-Ni- P2) for $\mathbf{1}^{2+}$ and 92.60º (N1-Ni-N2), 86.93º (N1-Ni-P1), 83.28º (N2-Ni-P2) and 96.64º (P1-Ni- P2) for $\mathbf{2}^{2+}$. The imine C=N bond lengths ranging from 1.279(8) Å to 1.281(1) Å are significantly shorter than the C-N bonds linking the phosphine arms, which are in the range of 1.476(4)-1.495(3) Å. These results are in agreement with localized imine double bonds within a non-planar ligand core with the sp^3 hybridized α-carbon lying above the plane of the back bone giving rise to a boat conformation.[33]

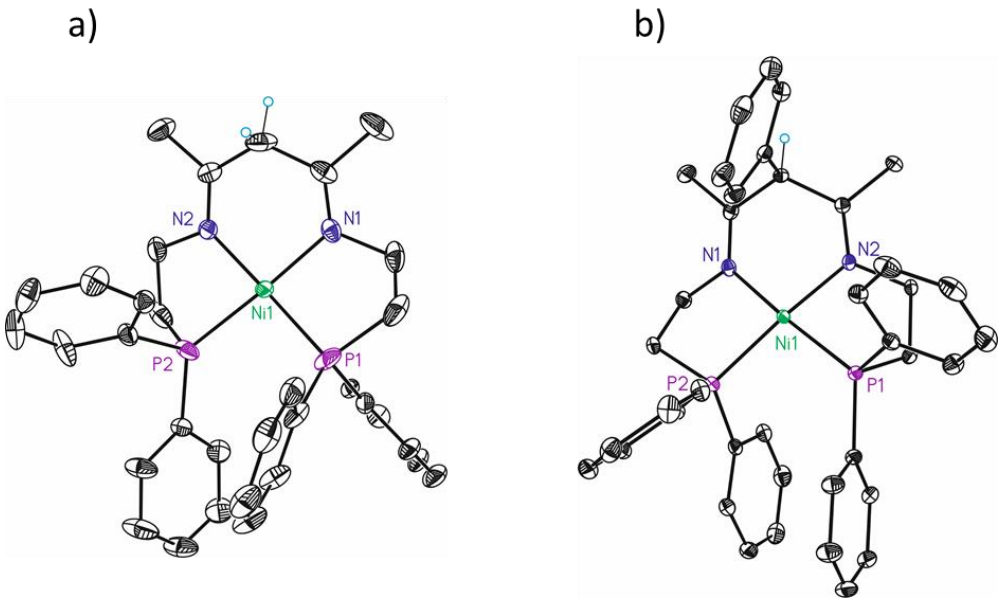

Figure 5. ORTEP representation of $\mathbf{1}^{2+}$(**a**) and $\mathbf{2}^{2+}$(**b**) at 50% probability level (hydrogens are omitted for further clarification except for α-carbon hydrogen) **Color code**: **C**, Dark gray; **N**, Blue; **Ni**, green; **P**, purple.

2.2- Electrochemical Characterization

The redox properties of complexes $\mathbf{1}^{2+}$ and $\mathbf{2}^{2+}$ were investigated by cyclic voltammetry (CV) in anhydrous acetonitrile or dimethylformamide containing 0.1M [(*n*-Bu)$_4$ N](PF$_6$) (TBAP) as supporting electrolyte in a three electrode one-compartment cell consisting of a glassy carbon working electrode, Pt as counter electrode and Ag/$AgNO_3$ solution in acetonitrile

(0.01 M $Ag/AgNO_3$, 0.1 M $TBAP_6$) as reference electrode, under nitrogen atmosphere. Ferrocene was used as the internal reference, which was added at the end of each experiment.

Cyclic voltammetry of $\mathbf{1}^{2+}$ in acetonitrile solution shows two reduction waves. The first one is irreversible with E_{pc}= -1.20 vs $Fc^{+/0}$ and the second one is quasi-reversible with $E_{1/2}$ = -1.76 V vs $Fc^{+/0}$ (ΔE = 66 mV) (**Figure 6a**, black trace, see also **Table 1**). At higher scan rates ($\upsilon \geq$ 0.3 V/s) the first reduction peak becomes reversible ($E_{1/2}$ = -1.17 V vs $Fc^{+/0}$, ΔE = 60 mV, **Figure 6b**) indicating that a chemical reaction follows the electrochemical step.[34] A plot of redox peak current varies linearly with the square root of the scan rate (i_{pc}, i_{pa} vs $\upsilon^{1/2}$) for both redox events, which is expected from homogenous diffusion controlled electrochemical events (**Figure S28** in the SI).

The electrochemical behavior of complex $\mathbf{2}^{2+}$ is similar to that of $\mathbf{1}^{2+}$ showing a first redox wave at $E_{1/2}$ = -1.11 V vs $Fc^{+/0}$ (ΔE = 59 mV) and a second one at $E_{1/2}$ = -1.78 V vs $Fc^{+/0}$ (ΔE = 90 mV), accounting for an anodic shift of 67 mV for the former and only 20 mV of cathodic shift for the latter (**Figure 6a**, red trace, see also Figure S29 in the SI). Thus, the first redox event from a formal Ni(II) to Ni(I) is influenced by the electron-withdrawing nature of the phenyl ring in the α-position of the diimino complex. The reversibility of this first redox wave at slow scan rates of ($\leq$ 0.2V/s) is fully reversible for $\mathbf{2}^{2+}$ as opposed to $\mathbf{1}^{2+}$, suggesting that the chemical reaction following the first reduction is less favored for $\mathbf{2}^{2+}$.

Chapter 4.

a) b)

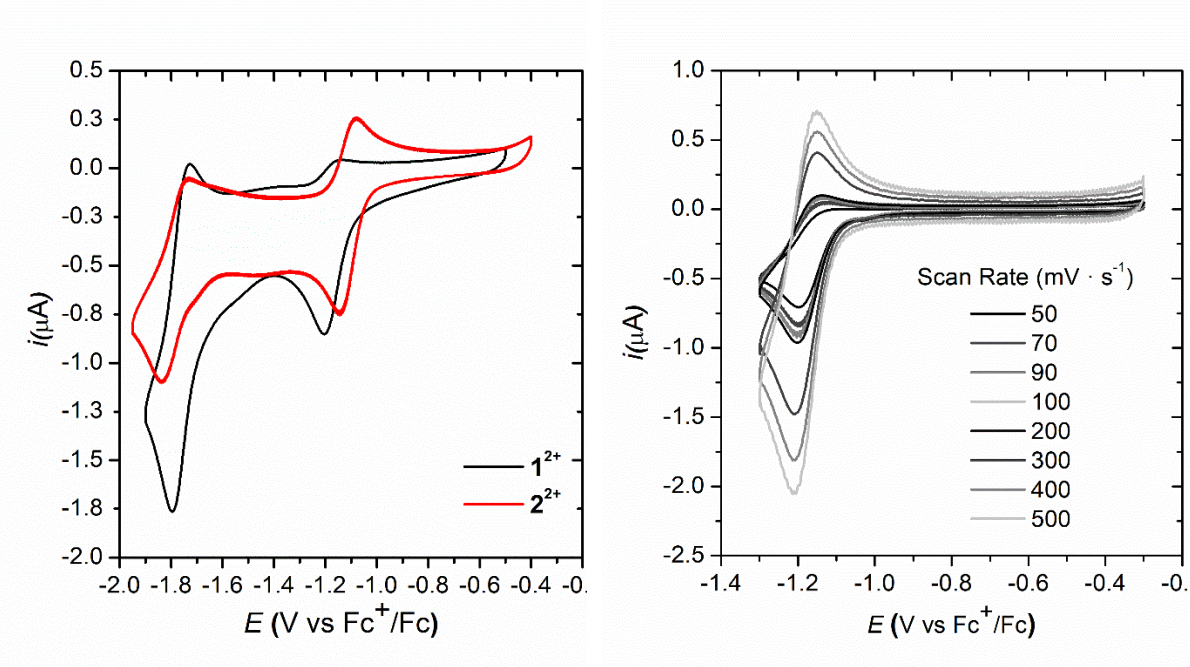

Figure 6. a) Cyclic voltammetry experiments of 0.5 mM solution of $\mathbf{1}^{2+}$ **(black)** and $\mathbf{2}^{2+}$ **(red)** in CH_3CN and scan rate of 100 mV/s. **b**) Comparison of voltammograms of $\mathbf{1}^{2+}$ in CH_3CN at different scan rates.

Table 1: Redox potentials data for complexes 1^{2+} and 2^{2+} in CH_3CN and DMF. All potentials are reported in V versus $Fc^{+/0}$.

Solvent	complex	E^1_{pa}	E^1_{pc}	$E^1_{1/2}$	ΔE^1(mV)	E^2_{pa}	E^2_{pc}	$E^2_{1/2}$	ΔE^2(mV)
CH_3CN	$\mathbf{1}^{2+}$	-1.14	-1.20	-1.17	60[a]	-1.73	-1.79	-1.76	66
	$\mathbf{2}^{2+}$	-1.08	-1.14	-1.11	59	-1.74	-1.83	-1.78	90
DMF	$\mathbf{1}^{2+}$	-	-	-	-	-1.72	-1.8	-1.76	80
	$\mathbf{2}^{2+}$	-	-	-	-	-1.72	-1.8	-1.76	80

[a]Peak separation potential at high Scan rates (υ = 0.3 V/s).

Cyclic voltammetry of the β-diketiminate derivatives $(\mathbf{1\text{-}H})^+$ and $(\mathbf{2\text{-}H})^+$ show only one quasi-reversible peak appearing at the same potential for both complexes with $(\mathbf{2\text{-}H})^+$ showing lower reversibility ($E_{1/2}$ = -1.76 V vs $Fc^{+/0}$ ΔE = 80 mV, **Figure 7-8a** and **Table 1**, see also

Figures S30 and **S31** in the SI). Spectroelectrochemical experiments in an optically transparent thin layer electrochemical (OTTLE) cell show isosbestic points for the conversion of (**1-H**)$^+$ and (**2-H**)$^+$ to the neutral **1-H** and **2-H** derivatives, respectively (**Figures S33** and **S34** in the SI). The process is reversible as demonstrated by the full recovery of the initial species in the reverse scan. Thus, the low reversibility of the redox process in DMF is associated to a slow electrochemical process, which is enhanced in the case of the α-phenyl substituted derivative (**2-H**)$^+$ suggesting that geometrical rearrangement is involved in the process and is hindered by the bulky phenyl group.

The low potential of the reduction of (**1-H**)$^+$ and (**2-H**)$^+$ ($E_{1/2}$ = -1.76 V) compared to the first reduction observed for the parent complexes **1**$^{2+}$ ($E_{1/2}$ = -1.17 V) and **2**$^{2+}$ ($E_{1/2}$ = -1.11 V) accounts for a cathodic shift of 580 mV and 650 mV, respectively, and is in agreement with the negatively charged nature of the β-diketiminate versus the neutral β-diimine ligands.

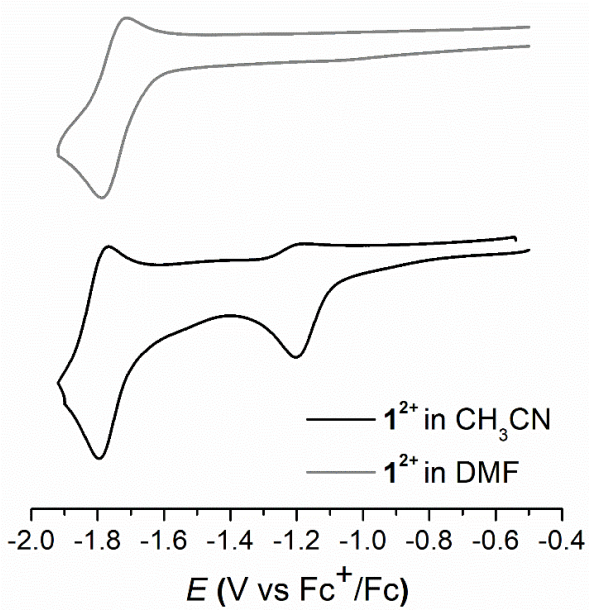

Figure 7. Cyclic voltammogram of **1**$^{2+}$ in CH_3CN (bottom) and DMF (top).

The peak position of the unique redox event observed for (**1-H**)$^+$ and (**2-H**)$^+$ exactly matches that of the second redox event observed for **1**$^{2+}$ and **2**$^{2+}$ (compare black and grey in **Figure 7** and red and orange in **Figure 8a**, see also **Table 1**). These results suggest a putative conversion of the mono-reduced β-diimino complexes **1**$^+$ and **2**$^+$ to the β-diketiminate complex (**1-H**)$^+$ and

Chapter 4.

(**2-H**)$^+$ within the time-scale of the experiment. This hypothesis is supported by spectroscopic analysis of the one electron reduced species derived from **2**$^{2+}$. This was achieved by performing a bulk electrolysis (BE) experiment at -1.3 V vs Fc$^{+/0}$ of a solution of the β-diimino complex **2**$^{2+}$ in acetonitrile (**Figure 8** and **Figures S35** in the SI). UV-Vis analysis of the resulting mixture matches the profile of the spectrum of the β-diketiminate (**2-H**)$^+$ (**Figure 8b**). An analogous experiment using compound **1**$^{2+}$ lead to decomposition of the complex during the long time of the bulk electrolysis experiment highlighting the lower stability of this complex compared to the α-phenyl substituted analog **2**$^{2+}$.

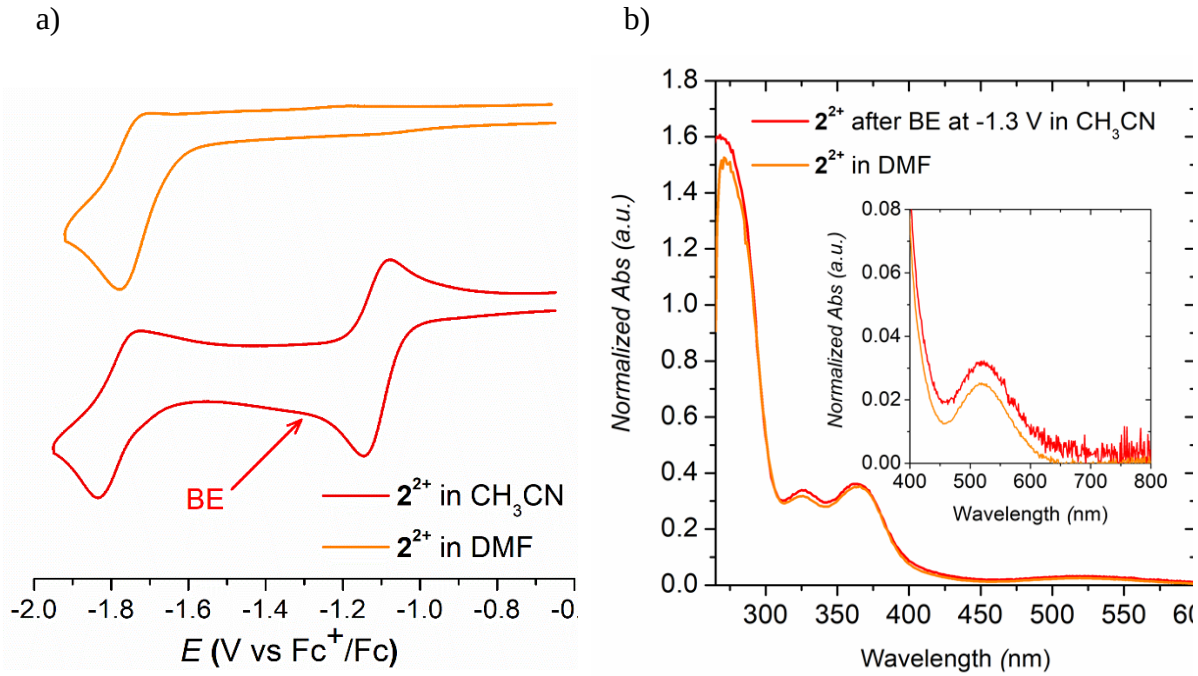

Figure 8. (a) Cyclic voltammogram of **2**$^{2+}$ in CH_3CN (bottom) and DMF (top). The red arrow indicates the applied potential in the bulk electrolysis (BE) experiment (E_{app} = -1.3 V vs Fc$^{+/0}$). b) UV-Vis spectra of **2**$^{2+}$ after bulk BE at E_{app} = -1.3 V vs Fc$^{+/0}$ (red) compared to the UV-Vis of (**2-H**)$^+$ in DMF (orange). See Figure S35 for the details in the BE experiment.

H cleavage releasing a molecule of H_2 or to a hydrogen atom abstraction by a solvent molecule via metal hydride hydrogen atom transfer (MHAT) pathways, producing in both cases the β-diketiminato derivatives (**1-H**)$^+$ and (**2-H**)$^+$ (Scheme 2, top-right).[36,37,28] The latter show the same electroreduction feature in CH_3CN and in DMF at $E_{1/2}$ = -1.76 V (Scheme 2, bottom). The transformation of diimino to diketiminate upon reduction and hydrogen atom loss, either

Chapter 4.

by H_2 evolution or by a MHAT process, evidences the non-innocent nature of this type of ligands that can get involved in cooperative metal-ligand reactivity. In this context, a recent report has demonstrated both meta-metal and metal-β-diketiminate ligand cooperative stoichiometric hydrogen evolution by a bimolecular dihydride nickel complex in the presence of a proton source (see **Figure 3** in Chapter 3). In this report, the dihydride derivative is stable enough to be isolated and characterized but only in the presence of an acid source, and thanks to the cooperative protonation of the BKI ligand, the complex is able to evolve H_2 gas.[38] In contrast, in the case of complexes $\mathbf{1}^{2+}$ and $\mathbf{2}^{2+}$ reported here, the putative hydride species $\mathbf{1'}^{+}$ and $\mathbf{2'}^{+}$ are too reactive to be isolated and they rapidly transform into $(\mathbf{1\text{-}H})^{+}$ and $(\mathbf{2\text{-}H})^{+}$, respectively. Time resolved spectroscopic techniques as well as stoichiometric hydrogen evolution detection experiments at E_{app} = -1.3 V could help to fully characterize the reaction pathway towards $(\mathbf{1\text{-}H})^{+}$ and $(\mathbf{2\text{-}H})^{+}$ and give information of the lifetime of the involved intermediate species, but are beyond the scope of this thesis.

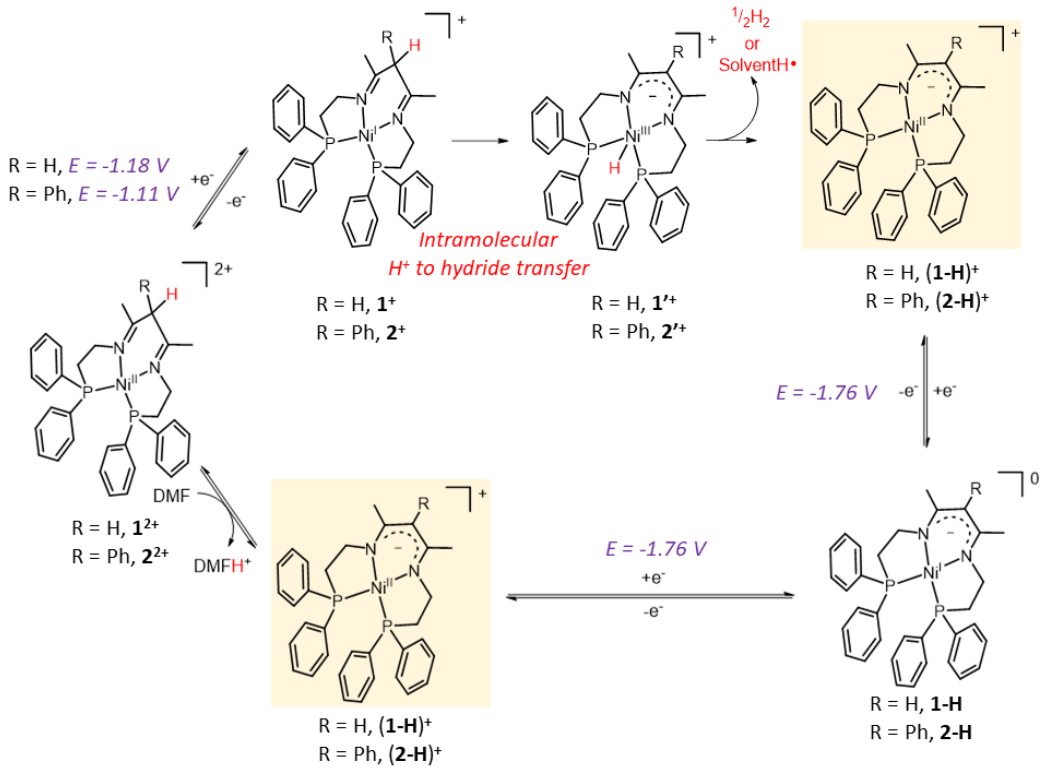

Scheme 2. Proposed electrochemical and chemical events during reduction of $\mathbf{1}^{2+}$ and $\mathbf{2}^{2+}$ in CH_3CN (top) and DMF (bottom) showing the interconversion between β-diimino and β-diketiminato complexes.

Chapter 4.

2.3- Electrochemical proton reduction

The electrochemical behaviour of $\mathbf{1}^{2+}$ and $\mathbf{2}^{2+}$ in the presence of acid was performed in CH_3CN and DMF using *p*- toluene sulfonic acid (p-TsOH) (pK_a = 8.6 in CH_3CN).[39] In acetonitrile solution, addition of acid results in a slight increase in current of the first reduction wave for both complexes $\mathbf{1}^{2+}$ and $\mathbf{2}^{2+}$ and a loss of reversibility for $\mathbf{2}^{2+}$ (**Figure 9** and **Figure S38** in the SI). Upon further addition, the peak intensity continues to increase but quickly reaches a plateau after adding approximately 2-3 equivalents of acid (**Figure 9**, inset). A similar phenomenon is observed when [DMFH](CF_3O_3) is used as acid (pK_a = 6.8 in CH_3CN, **Figure S39** in the SI). The early saturation of the wave intensity suggests an irreversible reaction promoted by the presence of acid but with poor or null hydrogen evolution catalytic nature. Indeed, a bulk electrolysis experiments at E_{app} = -1.2 V vs $Fc^{+/0}$ in the presence of 20 equivalents of p-TsOH·H_2O did not generate any hydrogen gas as confirmed by analysing the head space of the cathodic compartment of the electrochemical cell using gas chromatography coupled to thermal conductivity detector (GC-TCD). Thus, we propose that under these conditions the one-electron reduced species $\mathbf{1}^{+}$ and $\mathbf{2}^{+}$ or their Ni(III)-hydride derivatives $\mathbf{1'}^{+}$ and $\mathbf{2'}^{+}$ protonate to form the intermediate species $(\mathbf{1+H})^{2+}$ and $(\mathbf{2+H})^{2+}$ respectively (**Scheme 3**). Such species could lead to the electroreduction of one or two of the imino ligands to form the amino counterparts (formal hydrogenation of the C=N group). Such transformations have been proposed and even confirmed for related nickel and cobalt complexes containing imino ligands.[40–42] Since the irreversible conversion of complexes $\mathbf{1}^{2+}$ and $\mathbf{2}^{2+}$ prevented the hydrogen evolution reaction we did not further investigate this process but focused on the proton reduction ability of $\mathbf{1}^{2+}$ and $\mathbf{2}^{2+}$ in DMF at lower potential.

Chapter 4.

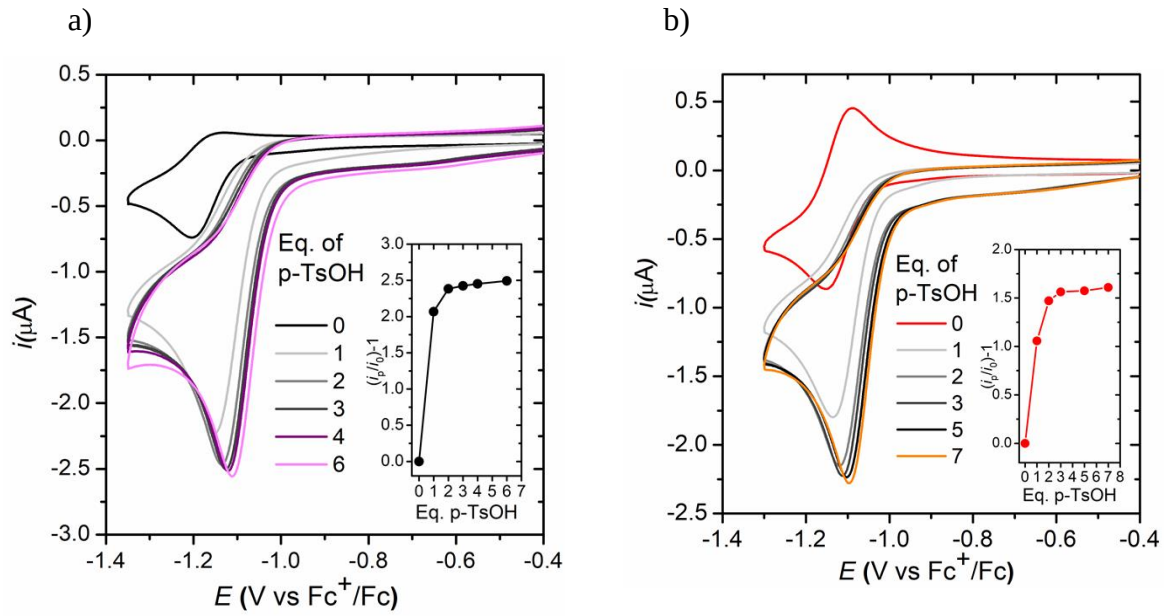

Figure 9. Cyclic voltammetry experiments of $\mathbf{1}^{2+}$(**a**) and $\mathbf{2}^{2+}$ (**b**) in CH_3CN solution with successive addition of p-TsOH·H_2O at scan rate 0.1V/s. The inset figures show the growth of peak intensity (i_p) relative to the peak in the absence of acid (i_0).

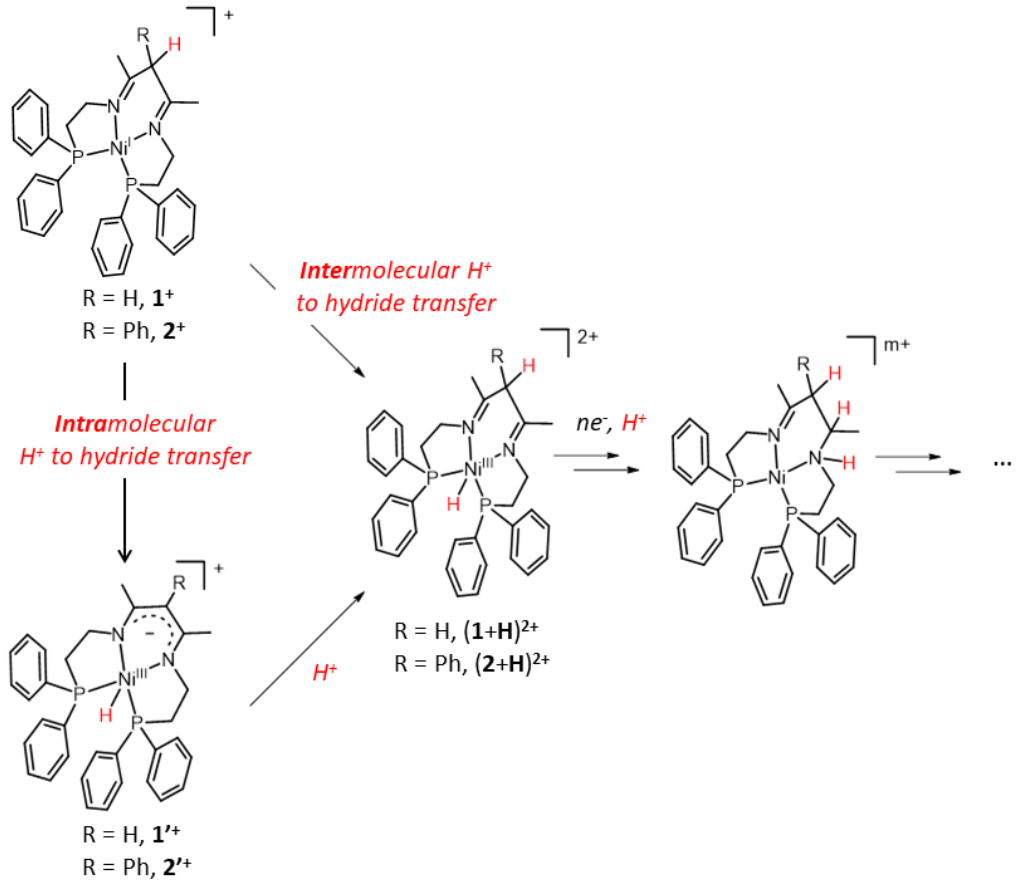

Scheme 3. Proposed reaction pathways after one-electron reduction of $\mathbf{1}^{2+}$ or $\mathbf{2}^{2+}$ in the presence of an acid source.

Chapter 4.

Figures 10a and **11a** show the cyclic voltammetry profile after successive additions of p-TsOH in a solution of $\mathbf{1}^{2+}$ and $\mathbf{2}^{2+}$ in DMF, respectively. The reversible wave at -1.8 V associated with the one-electron reduction of $(\mathbf{1\text{-}H})^{+}$ and $(\mathbf{2\text{-}H})^{+}$ becomes irreversible and increases in intensity with increasing concentration of acid. In addition, an increase in current is also observed at E < -1.8 V for both complexes, which cannot be attributed solely to the blank (see **Figure S40** in the SI). A slight increase in current is also observed at $E_{onset} \approx$ -1.3 V for $\mathbf{1}^{2+}$ and at $E_{onset} \approx$ -1.1 V for $\mathbf{2}^{2+}$ that we attribute to the redox signature of the first reduction of $\mathbf{1}^{2+}$ and $\mathbf{2}^{2+}$, which result from the protonation of $(\mathbf{1\text{-}H})^{+}$ and $(2\text{-}\mathbf{H})^{+}$ after a few additions of acid. This phenomenon is more evident for compound $\mathbf{2}^{2+}$ with the characteristic reversible wave at E = -1.1 V showing very clear at 9 equivalents of p-TsOH (Figure 10a, inset). These results show how subtle changes in acid concentration and acid strength can displace the equilibrium between the β-diimino and the β-diketiminato complexes (**Scheme 4**).[43–45]

In order to assess the proton reduction ability of $\mathbf{1}^{2+}$ and $\mathbf{2}^{2+}$ in DMF, a bulk electrolysis experiment at E_{app} = -1.8 V vs $Fc^{+/0}$ in the presence of 60 equivalents of p-TsOH was performed. After 20 minutes the headspace of the electrochemical cell was analysed by GC-TCD, confirming the formation of hydrogen gas (**Figures 10b, 11b** and **Figure S42** in the SI).

Chapter 4.

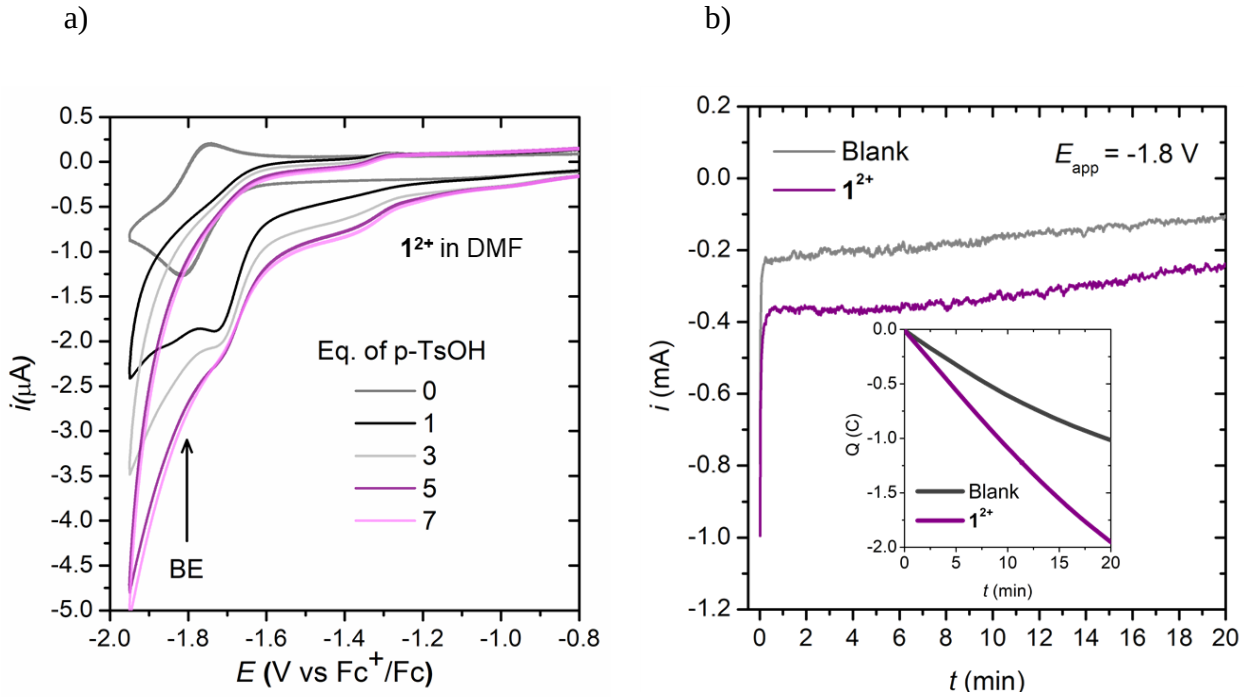

Figure 10. (**a**) Cyclic voltammetry experiments of a 0.5 mM solution of $\mathbf{1}^{2+}$ in DMF (0.1 M $TBAPF_6$) after consecutive addition of p-TsOH·H_2O at scan rate 0.1V/s; **WE**: GC (Φ = 1mm), **CE**: Pt, **REF** electrode: Ag/$AgNO_3$ (Ag wire in a 0.01 M solution of $AgNO_3$ and 0.1 M $TBAPF_6$). (**b**) Bulk electrolysis experiments at E_{app} = -1.8V vs $Fc/Fc^{+/0}$ in the presence of 60 eq. p-TsOH·H_2O in the presence (purple) and in the absence (grey) of a 0.5 mM solution of $\mathbf{1}^{2+}$ in DMF (0.1 M $TBAPF_6$); **WE**; GC rod (S = 3.1 cm^2), **CE**: Pt mesh, **REF** electrode: Ag/$AgNO_3$ (Ag wire in a 0.01 M solution of $AgNO_3$ and 0,1 M $TBAPF_6$), $V_{cathode} = V_{anode}$ = 5 mL.

The accumulated charge as well as accumulated hydrogen gas in the bulk electrolysis experiments are significantly higher than those observed for analogous experiments performed in the absence of complexes confirming the role of $\mathbf{1}^{2+}$ and $\mathbf{2}^{2+}$ in promoting the hydrogen evolution reaction (**Figures 10b, 11b and Figure S43**in the SI). While complex $\mathbf{2}^{2+}$ shows a fairly stable current over the whole 20 min period at about -0.60 mA (-0.19 mA/cm^2), complex $\mathbf{1}^{2+}$ shows a lower current intensity (-0.36 mA, -0.11 mA/cm^2) that starts to decrease slowly after 8 min, suggesting a higher stability for the former. Cyclic voltammetry experiments performed immediately after the bulk electrolysis experiments show the characteristic redox feature of complex $\mathbf{2}^{2+}$ at E = -1.1 V (after 1.8 turnover numbers), while complex $\mathbf{1}^{2+}$ is more difficult to identify due to the irreversible nature of the first reduction which shows to be very broad and pointing to partial decomposition (**Figure S41** in the SI). Faradaic efficiency of 33%

Chapter 4.

and 35% were obtained for $\mathbf{1}^{2+}$ and $\mathbf{2}^{2+}$ respectively. A rinse test of the working electrode performed after the bulk electrolysis experiment suggests that part of the decomposition might be related to deposited species on the electrode since a broad reduction wave in the range of *E* = -1.1 to -1.7 V vs $Fc^{+/0}$ is observed in both cases ($\mathbf{1}^{2+}$ and $\mathbf{2}^{2+}$). Importantly, no significant increase in the current is observed at the bulk electrolysis potential (E_{app} = -1.8 V vs $Fc^{+/0}$) for the rinsed electrode when compared to a blank electrode, supporting the homogeneous molecular nature of the catalytic process (**Figure S42** in the SI).

a) b)

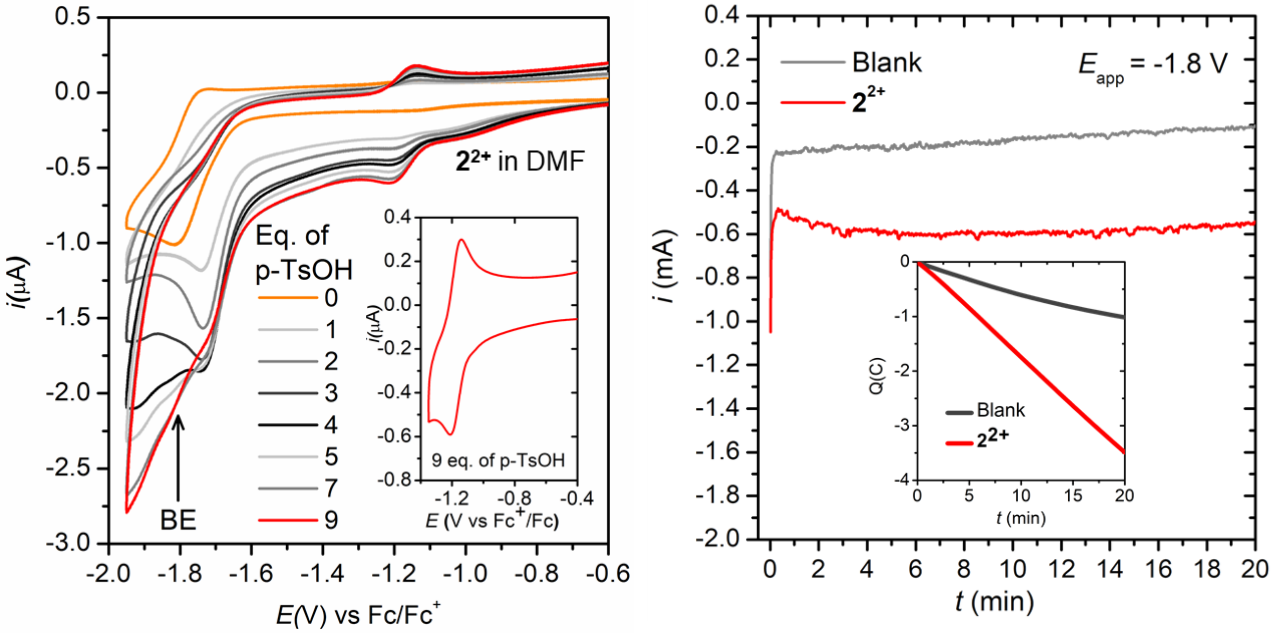

Figure 11. (**a**) Cyclic voltammetry experiments of a 0.5 mM solution of $\mathbf{2}^{2+}$ in DMF (0.1 M $TBAPF_6$) after consecutive addition of p-TsOH·H_2O at scan rate 0.1V/s; **WE**: GC (Φ = 1mm), **CE**: Pt, **REF** electrode: $Ag/AgNO_3$ (Ag wire in a 0.01 M solution of $AgNO_3$ and 0.1 M $TBAPF_6$). (**b**) Bulk electrolysis experiments at E_{app} = -1.8V vs $Fc/Fc^{+/0}$ in the presence of 60 eq. p-TsOH·H_2O in the presence (red) and in the absence (grey) of a 0.5 mM solution of $\mathbf{2}^{2+}$ in DMF (0.1 M $TBAPF_6$); **WE**; GC rod (S = 3.1 cm^2), **CE**: Pt mesh, **REF** electrode: $Ag/AgNO_3$ (Ag wire in a 0.01 M solution of $AgNO_3$ and 0.1 M $TBAPF_6$), $V_{cathode} = V_{anode}$ = 5 mL.

Chapter 4.

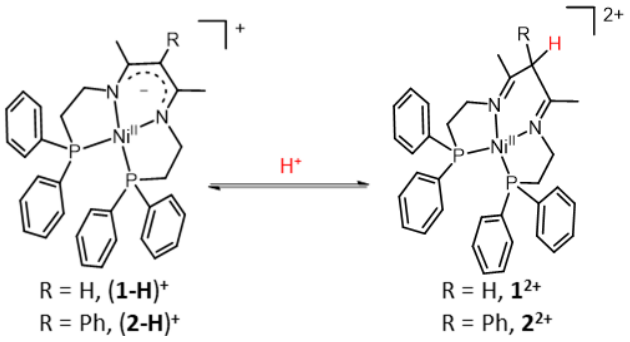

Scheme 4. Equilibria between β-diketiminato and β-diimino complexes (**1-H**)$^{+}$/**1**$^{2+}$ and (**2-H**)$^{+}$/**2**$^{2+}$, highly dependent on acid concentration and acid strength.

The fact that **1**$^{2+}$ and **2**$^{2+}$ are able to trigger hydrogen evolution in the presence of protons in DMF at E_{app} = -1.76 V suggests that at this low potential the decomposition pathways of the intermediate species **1**$^{+}$, **2**$^{+}$, **1'**$^{+}$ and **2'**$^{+}$ governing the electrochemistry at higher potentials shown in **Scheme 3** are avoided.

In the bottom of **Scheme 5** the reduction of the key hydride species **1'**$^{+}$ and **2'**$^{+}$ is proposed as the driving force of the hydrogen evolution reaction through a formal Ni(II) hydride species **1'** and **2'**. Alternatively, the formal Ni(I) diimino derivatives **1**$^{+}$ and **2**$^{+}$ could also be reduced to formal Ni(0) complexes that could lead to hydrogen, most likely through a Ni(I) hydride complex. However, the latter route seems less likely taking into account the possible conversion of the involved β-diimino species to the β-diketiminato derivatives by fast intramolecular proton to hydride transfer as indicated by the vertical arrows in **Scheme 5**.

Chapter 4.

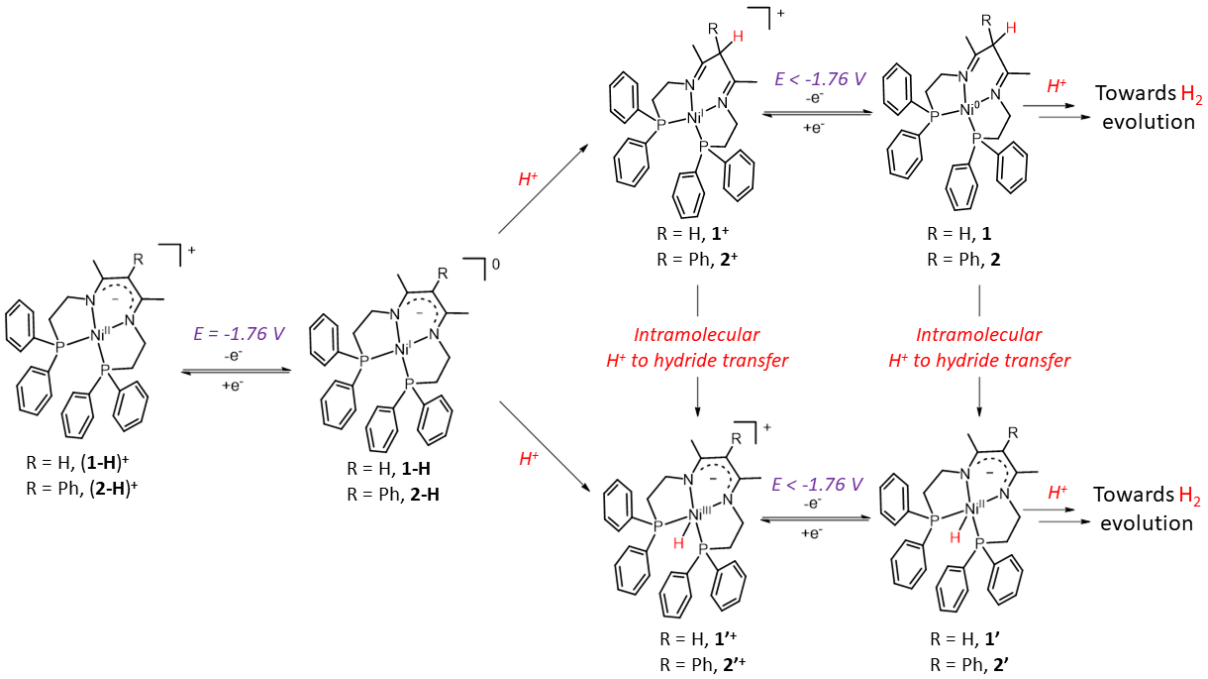

Scheme 5. Proposed routes toward the hydrogen evolution reaction from (**1-H**)$^+$ and (2-**H**)$^+$.

3- Conclusions

The spectroscopic and electrochemical characterisation of two novel nickel κ^4-P_2N_2 β-diimine (BDI) complexes $\mathbf{1}^{2+}$ and $\mathbf{2}^{2+}$ show the interconversion of the BDI ligand to a β-diketiminate (BDK) ligand upon reduction and hydrogen atom loss. Two possible pathways are proposed for this transformation, both starting from a metal based reduction of the initial Ni(II) in $\mathbf{1}^{2+}$ and $\mathbf{2}^{2+}$ to form a formal Ni(I) species that rapidly evolves to a Ni(III)-hydride derivative $\mathbf{1'}^{+}$ and $\mathbf{2'}^{+}$ upon intramolecular deprotonation of the α-carbon acidic proton in the BDI ligand. At this point, $\mathbf{1'}^{+}$ and $\mathbf{2'}^{+}$ can be involved either in hydrogen evolution through bimolecular reductive elimination or in metal hydride induced hydrogen atom transfer (MHAT) reaction to the acetonitrile solvent. Both routes would lead to the formation of the BDK complexes (**1**-H)$^+$ and (**2**-H)$^+$.

Hydrogen detection experiments in the presence of acid sources rule out a hydrogen evolution reaction in the first reduction wave of $\mathbf{1}^{2+}$ and $\mathbf{2}^{2+}$ (E_{app} = -1.2 V vs $Fc^{+/0}$), presumably due to the electroreduction of the imino ligands that evolve to the amino derivatives in the presence of protons and blocking the reductive elimination route towards H_2. In contrast, hydrogen evolution is demonstrated in the second reduction wave where the decomposition

Chapter 4.

route is partially overcome by further reduction of intermediates **1'**$^{+}$ and **2'**$^{+}$ at low potentials (E_{app} = -1.8 V vs $Fc^{+/0}$). Importantly, the conversion of (**1**-H)$^{+}$ and (**2**-H)$^{+}$ to **1**$^{2+}$ and **2**$^{2+}$ respectively in the presence of acid is clearly demonstrated by the recovery of the first reduction wave of **2**$^{2+}$ in DMF. Overall, these results highlight the easy interconversion between BDI and BDK ligands, depending on subtle changes in acid strength of species in the media and their concentration.

4- Experimental section

Synthesis of ligands HBDI (**L9**) and PhBDI **(L10**) were prepared as described in detail in Chapter 3 of this manuscript.

4.1- Synthesis of 1(BF$_4$)$_2$

In a round bottom flask equipped with reflux condenser Nickel (II) tetrafluoroborate hexahydrate (60mg, 0.177mmol) was dissolved in 30 mL anhydrous and degassed acetonitrile affording a blue solution. Ligand HBDI (**L9**, 100 mg, 0.177 mmol) was dissolved in 15 mL of DCM inside the glovebox and the resulting yellow solution was transferred to the dissolved Nickel salt solution by cannula outside the glovebox. Upon addition, the color of the reaction changed from blue to red. The reaction mixture was stirred at 65℃ under nitrogen overnight. The volatiles were removed under reduced pressure leaving a red oily compound, which was dissolved in the minimum amount of acetonitrile. To this acetonitrile solution, Et_2O was added, and the color of the solution became cloudy. It was placed at -30℃, causing green crystals to appear that were filtered and washed with Et_2O. (40 mg, 0.0637 mmol, 36%). Crystals suitable for single crystal X-ray diffraction analysis were grown by slow diffusion of Et_2O to a saturated acetonitrile solution. **^{1}H NMR (500 MHz, CD$_3$CN)** δ 7.55 (t, *J* = 7.5 Hz, 3H), 7.47 – 7.43 (m, 9H), 7.35 (t, *J* = 7.6 Hz, 8H), 4.29 (s, 2H), 3.66 (s, 4H), 2.74 – 2.68 (m, 4H), 2.27 (s, 6H). **^{13}C NMR (126 MHz, CD$_3$CN)** δ 179.97, 133.87, 133.24, 129.76, 117.60,53.71,52.68 23.37,**^{31}P NMR (202 MHz, CD$_3$CN)** δ 49.64.

^{1}H NMR (500 MHz, DMF-(d$_7$) δ 7.63 (ddd, *J* = 8.2, 6.7, 3.1 Hz, 8H), 7.55 (t, *J* = 7.5 Hz, 4H), 7.36 (t, *J* = 7.6 Hz, 8H), 5.31 (s, 1H), 3.45 (ddt, *J* = 19.6, 13.3, 6.5 Hz, 4H), 2.88 (p, *J* = 6.4 Hz, 4H), 2.22 (s, 6H). **^{13}C NMR (126 MHz, DMF)** δ 135.12 (t, J = 5.2 Hz), 133.17, 130.10, 128.28 – 126.94 (m), 102.16, 52.02 33.81 24.58. **^{31}P NMR (202 MHz, DMF(d$_7$))** δ 57.64.

Anal. Calcd: $[C_{33}H_{36}N_2NiP_2](BF_4)_2$ + Et_2O: C, 52.55; H, 5.17; N, 3.51; **Found**: **:** $[C_{33}H_{36}N_2NiP_2](BF_4)_2$ + Et_2O: C, 52.30; H, 4.60; N, 3.50 **ESI-Mass:** Calcd for m/z: $[C_{33}H_{36}N_2NiP_2]^{2+}$ =580.2; **Found**: $[M-H]^+$ m/z: 579.16.

4.2- Synthesis of $2(BF_4)_2$

In a round bottom flask equipped with a reflux condenser Nickel (II) tetrafluoroborate hexahydrate (56 mg, 0.167 mmol) was dissolved in 30 mL of anhydrous and degassed acetonitrile under nitrogen affording a blue solution. Ligand PhBDI (**L10**, 100 mg, 0.167 mmol) was dissolved in 15 mL DCM inside the glovebox and the resulting yellow solution was transferred to the Nickel salt solution by cannula outside the glovebox. Upon addition of the ligand, the color of the reaction changed from blue to red. The reaction mixture was heated to 65°C under nitrogen overnight. Removing volatiles under reduced pressure afforded a red oily compound, which was dissolved in the minimum amount of acetonitrile. To this acetonitrile solution, Et_2O was added, which caused the precipitation of a yellow solid that filtered and washed with Et_2O (80 mg, 0.16 mmol, 96 %). Crystals suitable for single crystal X-ray diffraction analysis were grown by slow diffusion of Et_2O to an acetonitrile solution of **2(OTf)$_2$**. **^{1}H NMR (500 MHz, CD_3CN)** δ 7.76 – 7.70 (m, 2H), 7.66 – 7.54 (m, 4H), 7.52 – 7.26 (m, 16H), 7.26 – 7.19 (m, 3H), 5.50 (s, 1H), 3.75 (ddt, *J* = 29.1, 14.8, 8.0 Hz, 5H), 2.97 (dp, *J* = 12.6, 6.9 Hz, 2H), 2.62 (dt, *J* = 13.9, 7.0 Hz, 3H), 2.31 (d, *J* = 0.9 Hz, 7H). **^{13}C NMR (126 MHz, CD_3CN)** δ 181.52, 133.65 – 133.49, 133.41, 133.08, 130.59, 130.22 , 129.74, 128.88, 117.61, 67.97,53,38,30,53,28,29, 23.19. **^{31}P NMR (202 MHz, CD_3CN)** δ 47.15.

^{1}H NMR (**500 MHz, DMF**) δ 8.04 (s, 2H), 7.70 – 7.33 (m, 10H), 7.22 – 7.14 (m, 1H), 3.72 (s, 14H), 3.56 (dt, *J* = 29.9, 6.2 Hz, 1H), 3.56 (s, 1H), 2.97 – 2.89 (m, 2H), 2.80 – 2.74 (m, 3H), 1.95 (s, 2H). **^{13}C NMR** (**101 MHz, DMF**) δ ,144.81, 134.12 , 132.19 ,130.10 – 128.48, 128.34 – 125.61, 112.96, 52.13, 34.26 , 23.27. **^{31}P NMR** (**162 MHz, DMF-d7**) δ 57.87. **Anal. Calcd:** $[C_{39}H_{40}N_2NiP_2](BF_4)_2$ + Et_2O: C, 56.21; H, 5.18; N, 3.37; **Found**: $[C_{39}H_{40}N_2NiP_2](BF_4)_2$+$Et_2O$: C, 56.20; H, 5.10; N, 3.20**; ESI-Mass**: Calcd for m/z: $[C_{39}H_{40}N_2NiP_2]^{2+}$ = 656.2, Found; $[M-H]^+$ = 655.

Chapter 4.

5- References

(1) Obama, B. The Irreversible Momentum of Clean Energy. *Science (80-.).* **2017**, *355* (6321), 126–129. https://doi.org/10.1126/science.aam6284.

(2) Labrador, G. A. Heat Energy Recapture and Recycle and Its New Applications. https://doi.org/10.1126/science.aad1920.22.

(3) Matheu, R.; Garrido-Barros, P.; Gil-Sepulcre, M.; Ertem, M. Z.; Sala, X.; Gimbert-Suriñach, C.; Llobet, A. The Development of Molecular Water Oxidation Catalysts. *Nat. Rev. Chem.* **2019**, *3* (5), 331–341. https://doi.org/10.1038/s41570-019-0096-0.

(4) Najafpour, M. M.; Renger, G.; Hołyńska, M.; Moghaddam, A. N.; Aro, E. M.; Carpentier, R.; Nishihara, H.; Eaton-Rye, J. J.; Shen, J. R.; Allakhverdiev, S. I. Manganese Compounds as Water-Oxidizing Catalysts: From the Natural Water-Oxidizing Complex to Nanosized Manganese Oxide Structures. *Chem. Rev.* **2016**, *116* (5), 2886–2936. https://doi.org/10.1021/acs.chemrev.5b00340.

(5) Berardi, S.; Drouet, S.; Francàs, L.; Gimbert-Suriñach, C.; Guttentag, M.; Richmond, C.; Stoll, T.; Llobet, A. Molecular Artificial Photosynthesis. *Chem. Soc. Rev.* **2014**, *43* (22), 7501–7519. https://doi.org/10.1039/c3cs60405e.

(6) Sala, X.; Llobet, A. Redox Catalysis for Artificial Photosynthesis. *Eur. J. Inorg. Chem.* **2019**, *2019* (15), 2017–2019. https://doi.org/10.1002/ejic.201900289.

(7) Kärkäs, M. D.; Åkermark, B. Water Oxidation Using Earth-Abundant Transition Metal Catalysts: Opportunities and Challenges. *Dalt. Trans.* **2016**, *45* (37), 14421–14461. https://doi.org/10.1039/c6dt00809g.

(8) Garrido-Barros, P.; Gimbert-Suriñach, C.; Matheu, R.; Sala, X.; Llobet, A. How to Make an Efficient and Robust Molecular Catalyst for Water Oxidation. *Chem. Soc. Rev.* **2017**, *46* (20), 6088–6098. https://doi.org/10.1039/c7cs00248c.

(9) Garrido-Barros, P.; Funes-Ardoiz, I.; Drouet, S.; Benet-Buchholz, J.; Maseras, F.; Llobet, A. Redox Non-Innocent Ligand Controls Water Oxidation Overpotential in a

New Family of Mononuclear Cu-Based Efficient Catalysts. *J. Am. Chem. Soc.* **2015**, *137* (21), 6758–6761. https://doi.org/10.1021/jacs.5b03977.

(10) Gil-Sepulcre, M.; Lindner, J. O.; Schindler, D.; Velasco, L.; Moonshiram, D.; Rüdiger, O.; Debeer, S.; Stepanenko, V.; Solano, E.; Würthner, F.; Llobet, A. Surface-Promoted Evolution of Ru-Bda Coordination Oligomers Boosts the Efficiency of Water Oxidation Molecular Anodes. *J. Am. Chem. Soc.* **2021**, *143* (30), 11651–11661. https://doi.org/10.1021/jacs.1c04738.

(11) Matheu, R.; Ertem, M. Z.; Gimbert-Suriñach, C.; Sala, X.; Llobet, A. Seven Coordinated Molecular Ruthenium-Water Oxidation Catalysts: A Coordination Chemistry Journey. *Chem. Rev.* **2019**, *119* (6), 3453–3471. https://doi.org/10.1021/acs.chemrev.8b00537.

(12) Hoque, M. A.; Gil-Sepulcre, M.; de Aguirre, A.; Elemans, J. A. A. W.; Moonshiram, D.; Matheu, R.; Shi, Y.; Benet-Buchholz, J.; Sala, X.; Malfois, M.; Solano, E.; Lim, J.; Garzón-Manjón, A.; Scheu, C.; Lanza, M.; Maseras, F.; Gimbert-Suriñach, C.; Llobet, A. Water Oxidation Electrocatalysis Using Ruthenium Coordination Oligomers Adsorbed on Multiwalled Carbon Nanotubes. *Nat. Chem.* **2020**, *12* (11), 1060–1066. https://doi.org/10.1038/s41557-020-0548-7.

(13) Vereshchuk, N.; Matheu, R.; Benet-Buchholz, J.; Pipelier, M.; Lebreton, J.; Dubreuil, D.; Tessier, A.; Gimbert-Suriñach, C.; Ertem, M. Z.; Llobet, A. Second Coordination Sphere Effects in an Evolved Ru Complex Based on Highly Adaptable Ligand Results in Rapid Water Oxidation Catalysis. *J. Am. Chem. Soc.* **2020**, *142* (11), 5068–5077. https://doi.org/10.1021/jacs.9b11935.

(14) Angamuthu, R.; Byers, P.; Lutz, M.; Spek, A. L.; Bouwman, E. Electrocatalytic CO_2 Conversion to Oxalate by a Copper Complex. *Science (80-.).* **2010**, *327* (5963), 313–315. https://doi.org/10.1126/science.1177981.

(15) Cometto, C.; Kuriki, R.; Chen, L.; Maeda, K.; Lau, T. C.; Ishitani, O.; Robert, M. A Carbon Nitride/Fe Quaterpyridine Catalytic System for Photostimulated CO_2-to-CO Conversion with Visible Light. *J. Am. Chem. Soc.* **2018**, *140* (24), 7437–7440. https://doi.org/10.1021/jacs.8b04007.

Chapter 4.

(16) Costentin, C.; Drouet, S.; Robert, M.; Savéant, J. M. A Local Proton Source Enhances CO2 Electroreduction to CO by a Molecular Fe Catalyst. *Science (80-.).* **2012**, *338* (6103), 90–94. https://doi.org/10.1126/science.1224581.

(17) Elgrishi, N.; Chambers, M. B.; Wang, X.; Fontecave, M. Molecular Polypyridine-Based Metal Complexes as Catalysts for the Reduction of CO_2. *Chem. Soc. Rev.* **2017**, *46* (3), 761–796. https://doi.org/10.1039/c5cs00391a.

(18) Ma, B.; Chen, G.; Fave, C.; Chen, L.; Kuriki, R.; Maeda, K.; Ishitani, O.; Lau, T. C.; Bonin, J.; Robert, M. Efficient Visible-Light-Driven CO_2 Reduction by a Cobalt Molecular Catalyst Covalently Linked to Mesoporous Carbon Nitride. *J. Am. Chem. Soc.* **2020**, *142* (13), 6188–6195. https://doi.org/10.1021/jacs.9b13930.

(19) Gonglach, S.; Paul, S.; Haas, M.; Pillwein, F.; Sreejith, S. S.; Barman, S.; De, R.; Müllegger, S.; Gerschel, P.; Apfel, U. P.; Coskun, H.; Aljabour, A.; Stadler, P.; Schöfberger, W.; Roy, S. Molecular Cobalt Corrole Complex for the Heterogeneous Electrocatalytic Reduction of Carbon Dioxide. *Nat. Commun.* **2019**, *10* (1), 1–10. https://doi.org/10.1038/s41467-019-11868-5.

(20) Dempsey, J. L.; Brunschwig, B. S.; Winkler, J. R.; Gray, H. B. Hydrogen Evolution Catalyzed by Cobaloximes. *Acc. Chem. Res.* **2009**, *42* (12), 1995–2004. https://doi.org/10.1021/ar900253e.

(21) Gimbert-Suriñach, C.; Albero, J.; Stoll, T.; Fortage, J.; Collomb, M. N.; Deronzier, A.; Palomares, E.; Llobet, A. Efficient and Limiting Reactions in Aqueous Light-Induced Hydrogen Evolution Systems Using Molecular Catalysts and Quantum Dots. *J. Am. Chem. Soc.* **2014**, *136* (21), 7655–7661. https://doi.org/10.1021/ja501489h.

(22) Bhugun, I.; Lexa, D.; Savéant, J. M. Homogeneous Catalysis of Electrochemical Hydrogen Evolution by Iron(0) Porphyrins. *J. Am. Chem. Soc.* **1996**, *118* (16), 3982–3983. https://doi.org/10.1021/ja954326x.

(23) Wiedner, E. S.; Bullock, R. M. Electrochemical Detection of Transient Cobalt Hydride Intermediates of Electrocatalytic Hydrogen Production. *J. Am. Chem. Soc.* **2016**, *138* (26), 8309–8318. https://doi.org/10.1021/jacs.6b04779.

(24) Rodriguez, M. M.; Bill, E.; Brennessel, W. W.; Holland, P. L. N_2 Reduction and Hydrogenation to Ammonia by a Molecular Iron-Potassium Complex. *Science (80-.).* **2011**, *334* (6057), 780–783. https://doi.org/10.1126/science.1211906.

(25) Roy, L.; Al-Afyouni, M. H.; Derosha, D. E.; Mondal, B.; Dimucci, I. M.; Lancaster, K. M.; Shearer, J.; Bill, E.; Brennessel, W. W.; Neese, F.; Ye, S.; Holland, P. L. Reduction of CO2 by a Masked Two-Coordinate Cobalt(i) Complex and Characterization of a Proposed Oxodicobalt(Ii) Intermediate. *Chem. Sci.* **2019**, *10* (3), 918–929. https://doi.org/10.1039/c8sc02599a.

(26) Kim, D.; Pillon, G.; Diprimio, D. J.; Holland, P. L. Highly Z-Selective Double Bond Transposition in Simple Alkenes and Allylarenes through a Spin-Accelerated Allyl Mechanism. *J. Am. Chem. Soc.* **2021**, *143* (8), 3070–3074. https://doi.org/10.1021/jacs.1c00856.

(27) McWilliams, S. F.; Broere, D. L. J.; Halliday, C. J. V.; Bhutto, S. M.; Mercado, B. Q.; Holland, P. L. Coupling Dinitrogen and Hydrocarbons through Aryl Migration. *Nature* **2020**, *584* (7820), 221–226. https://doi.org/10.1038/s41586-020-2565-5.

(28) Shevick, S. L.; Wilson, C. V.; Kotesova, S.; Kim, D.; Holland, P. L.; Shenvi, R. A. Catalytic Hydrogen Atom Transfer to Alkenes: A Roadmap for Metal Hydrides and Radicals. *Chem. Sci.* **2020**, *11* (46), 12401–12422. https://doi.org/10.1039/d0sc04112b.

(29) Vela, J.; Smith, J. M.; Yu, Y.; Ketterer, N. A.; Flaschenriem, C. J.; Lachicotte, R. J.; Holland, P. L. Synthesis and Reactivity of Low-Coordinate Iron(II) Fluoride Complexes and Their Use in the Catalytic Hydrodefluorination of Fluorocarbons. *J. Am. Chem. Soc.* **2005**, *127* (21), 7857–7870. https://doi.org/10.1021/ja042672l.

(30) Camp, C.; Arnold, J. On the Non-Innocence of "Nacnacs": Ligand-Based Reactivity in β-Diketiminate Supported Coordination Compounds. *Dalt. Trans.* **2016**, *45* (37), 14462–14498. https://doi.org/10.1039/c6dt02013e.

(31) Pegis, M. L.; Roberts, J. A. S.; Wasylenko, D. J.; Mader, E. A.; Appel, A. M.; Mayer, J. M. Standard Reduction Potentials for Oxygen and Carbon Dioxide Couples in Acetonitrile and N,N-Dimethylformamide. *Inorg. Chem.* **2015**, *54* (24), 11883–11888.

https://doi.org/10.1021/acs.inorgchem.5b02136.

(32) Ohtsu, H.; Tanaka, K. Equilibrium of Low- and High-Spin States of Ni(II) Complexes Controlled by the Donor Ability of the Bidentate Ligands. *Inorg. Chem.* **2004**, *43* (9), 3024–3030. https://doi.org/10.1021/ic035486.

(33) Landolsi, K.; Rzaigui, M.; Bouachir, F. Synthesis and Structure of Cationic Nickel Allyl Complexes Supported by β-Diimine Ligands. *Tetrahedron Lett.* **2002**, *43* (51), 9463–9466. https://doi.org/10.1016/S0040-4039(02)02187-1.

(34) Elgrishi, N.; Rountree, K. J.; McCarthy, B. D.; Rountree, E. S.; Eisenhart, T. T.; Dempsey, J. L. A Practical Beginner's Guide to Cyclic Voltammetry. *J. Chem. Educ.* **2018**, *95* (2), 197–206. https://doi.org/10.1021/acs.jchemed.7b00361.

(35) Helm, M. L.; Stewart, M. P.; Bullock, R. M.; Dubois, M. R.; Dubois, D. L. A Synthetic Nickel Electrocatalyst. *Science (80-.).* **2011**, *333* (August), 863–866.

(36) Gu, N. X.; Oyala, P. H.; Peters, J. C. An S = 1/2 Iron Complex Featuring N_2, Thiolate, and Hydride Ligands: Reductive Elimination of H_2 and Relevant Thermochemical Fe-H Parameters. *J. Am. Chem. Soc.* **2018**, *140* (20), 6374–6382. https://doi.org/10.1021/jacs.8b02603.

(37) Gu, N. X.; Oyala, P. H.; Peters, J. C. H_2 Evolution from a Thiolate-Bound Ni(III) Hydride. *J. Am. Chem. Soc.* **2020**, *142* (17), 7827–7835. https://doi.org/10.1021/jacs.0c00712.

(38) Duan, P.; Schulz, R. A.; Römer, A.; Van Kuiken, B. E.; Dechert, S.; Demeshko, S.; Cutsail, G. E.; DeBeer, S.; Mata, R. A.; Meyer, F. Ligand Protonation Triggers H 2 Release from a Dinickel Dihydride Complex to Give a Doubly "T"-Shaped Dinickel(I) Metallodiradical . *Angew. Chemie* **2021**, *133* (4), 1919–1924. https://doi.org/10.1002/ange.202011494.

(39) McCarthy, B. D.; Martin, D. J.; Rountree, E. S.; Ullman, A. C.; Dempsey, J. L. Electrochemical Reduction of Brønsted Acids by Glassy Carbon in Acetonitrile-Implications for Electrocatalytic Hydrogen Evolution. *Inorg. Chem.* **2014**, *53* (16),

8350–8361. https://doi.org/10.1021/ic500770k.

(40) Anxolabéhère-Mallart, E.; Costentin, C.; Fournier, M.; Nowak, S.; Robert, M.; Savéant, J. M. Boron-Capped Tris(Glyoximato) Cobalt Clathrochelate as a Precursor for the Electrodeposition of Nanoparticles Catalyzing H 2 Evolution in Water. *J. Am. Chem. Soc.* **2012**, *134* (14), 6104–6107. https://doi.org/10.1021/ja301134e.

(41) Lee, K. J.; McCarthy, B. D.; Dempsey, J. L. On Decomposition, Degradation, and Voltammetric Deviation: The Electrochemist's Field Guide to Identifying Precatalyst Transformation. *Chem. Soc. Rev.* **2019**, *48* (11), 2927–2945. https://doi.org/10.1039/c8cs00851e.

(42) Martin, D. J.; McCarthy, B. D.; Donley, C. L.; Dempsey, J. L. Electrochemical Hydrogenation of a Homogeneous Nickel Complex to Form a Surface Adsorbed Hydrogen-Evolving Species. *Chem. Commun.* **2015**, *51* (25), 5290–5293. https://doi.org/10.1039/c4cc08662g.

(43) Gianetti, T. L.; Nocton, G.; Minasian, S. G.; Tomson, N. C.; Kilcoyne, A. L. D.; Kozimor, S. A.; Shuh, D. K.; Tyliszczak, T.; Bergman, R. G.; Arnold, J. Diniobium Inverted Sandwich Complexes with μ-H6:H6-Arene Ligands: Synthesis, Kinetics of Formation, and Electronic Structure. *J. Am. Chem. Soc.* **2013**, *135* (8), 3224–3236. https://doi.org/10.1021/ja311966h.

(44) Venugopal, A.; Ghosh, M. K.; Jürgens, H.; Törnroos, K. W.; Swang, O.; Tilset, M.; Heyn, R. H. (β-Diketiminato)Dimethylgold(III): Synthesis, Structure, and Reactivity. *Organometallics* **2010**, *29* (10), 2248–2253. https://doi.org/10.1021/om100038f.

(45) Shaffer, D. W.; Ryken, S. A.; Zarkesh, R. A.; Heyduk, A. F. Ligand Effects on the Oxidative Addition of Halogens to (Dpp-Nacnac R)Rh(Phdi). *Inorg. Chem.* **2012**, *51* (22), 12122–12131. https://doi.org/10.1021/ic300733j.

Supporting information

Table of contents

Chapter 4.

1- Materials and reagents

All organic reagents, salts for buffers and metal precursors were purchased from Sigma-Aldrich and used without further purification, unless otherwise stated. Anhydrous solvents were taken from a solvent purification system (SPS®).

2- General Methods and Instrumentations

2.1- Crystallography data collection

Measured crystals were prepared under inert conditions immersed in perfluoropolyether as protecting oil for manipulation.

Crystal structure determination for **1(BF$_4$)$_2$** and **2(BF$_4$)$_2$** was carried out using an Apex DUO Kappa 4-axis goniometer equipped with an APPEX 2 4K CCD area detector, a Microfocus Source E025 IuS using MoK$_\alpha$ radiation, Quazar MX multilayer Optics as monochromator and an Oxford Cryosystems low temperature device Cryostream 700 plus (T = -173 °C). Full-sphere data collection was used with ω and φ scans. *Programs used:* Data collection APEX-2[1], data reduction Bruker Saint[2] V/.60A and absorption correction SADABS[3]

2.2- Structure solution and refinement

Crystal structure solution was achieved using the computer program SHELXT[4] . Visualization was performed with the program SHELXle[5]. Missing atoms were subsequently located from difference Fourier synthesis and added to the atom list. Least-squares refinement on F^2 using all measured intensities was carried out using the program SHELXL 2015[6]. All non-hydrogen atoms were refined including anisotropic displacement parameters.

[1] Data collection with APEX II version v2013.4-1. Bruker (2007). Bruker AXS Inc., Madison, Wisconsin, USA.
[2] Data reduction with Bruker SAINT version V8.30c. Bruker (2007). Bruker AXS Inc., Madison, Wisconsin, USA.
[3] SADABS: V2012/1 Bruker (2001). Bruker AXS Inc., Madison, Wisconsin, USA. Blessing, Acta Cryst. **1995**, A51, 33-38.
[4]SHELXT; V2018/2. Sheldrick, G.M. *Acta Cryst*. **2015** A71, 3-8.
[5]SHELXle; C.B. Huebschle, G.M. Sheldrick & B. Dittrich; J.Appl.Cryst. (2011) 44, 1281-1284.
[6] SHELXL; SHELXL-2018/3. Sheldrick, G.M. *Acta Cryst*. **2015** C71, 3-8.

Chapter 4.

2.3- Comments to the structure: Compound 1$(BF_4)_2$

The asymmetric unit contains one molecule of the Nickel metal-complex, two BF_4^- anions and 0.15 molecules of water. In the main molecule three of the aromatic rings are disordered in two orientations (approximated ratio 60:40). The BF_4^- anions are also disordered in two orientations. Additionally, one of the disordered BF_4^- anions is sharing its position (coordinated with the disorder) with 0.15 molecules of water.

Compound 1$(BF_4)_2$: The asymmetric unit contains one molecule of the cationic metal-complex and two BF_4 anions.

2.4- Electrochemical methods and instrumentations

Glassy Carbon electrodes (1mm diameter), Platinum Disk Electrodes, and reference electrodes ($AgNO_3$/Ag) were purchased from IJ-Cambria Ldt. Pads and alumina for polishing were also purchased from the same company. Cyclic voltammetry experiments were performed with a CHI660D potentiostat in a one-compartment cell, three electrode system using glassy carbon (GC) disk as working electrode, platinum disk as counter electrode and standard calomel electrode (SCE) or $AgNO_3$/Ag reference electrodes.

2.5- Spectro electrochemistry

Spectroelectrochemistry experiments were performed in a custom-made Optically Transparent Thin Layer Electrochemical (OTTLE) cell (University of Reading) with platinum mesh working electrode, platinum wire counter electrode and silver wire pseudo-reference electrode.

2.6- UV-vis equipment

UV-Vis measurements were carried out on a Lambda 1050 PerkinElmer spectrophotometer equipped with a PMT, InGaAs and PbS detectors system, double beam optics, double monochromator and D2 and W light sources.

Chapter 4.

2.7- High-resolution mass spectrometry

(HRMS) was recorded on a Thermo Finnigan MAT95XL spectrometer (for CI) and a Thermo Fisher Scientific LTQ-Orbitrap spectrometer (for ESI).

2.8- NMR spectroscopy for ligands

^{1}H and ^{13}C NMR spectra were recorded on a *Bruker Avance 400* spectrometer fitted with a 5 mm i.d. BBFO+ probe carefully tuned to the recording frequency of 400.13 MHz (for ^{1}H) and 100.61 MHz (for ^{13}C). The spectra are referenced to the solvent in which they were run (7.26 ppm for ^{1}H $CDCl_3$ and 77.16 ppm for ^{13}C $CDCl_3$, 2.5 ppm for ^{1}H DMSO, and 39.52 ppm for ^{13}C DMSO). Chemical shifts (δ) are given in ppm, coupling constants (J) are given in Hz with the following splitting abbreviations: s = singlet, d = doublet, t = triplet, q = quartet, qt = quintet, sx = sextuplet, sp = septuplet, m = massif and br = broad. All assignments were confirmed with the aid of two-dimensional ^{1}H, ^{1}H (COSY), or ^{1}H, ^{13}C (HSQC, HMBC) experiments using standard pulse programs.

2.9- NMR Spectroscopy for Ni complexes

^{1}H NMR, ^{13}C NMR, ^{31}P NMR, and spectra were recorded on a Bruker 400 MHz or a Bruker 500 MHz. Chemical shifts (δ) are reported in ppm and peak multiplicity is designated as s (singlet), d (doublet), t (triplet), m (multiplet), dd (doublet of doublets), dt (doublet of triplets), tt (triplet of triplets) and br (broad). All the collected spectra were referenced on residual solvent signal according to Nudelman et al.[2] Aqueous samples were recorded on an NMR spectrometer Bruker Avance 500 MHz spectrometer equipped with a Cryoprobe^{TM} and denoted with a "*" at the synthetic description.

Chapter 4.

3- NMR Spectra of $1(BF_4)_2$ and $2(BF_4)_2$

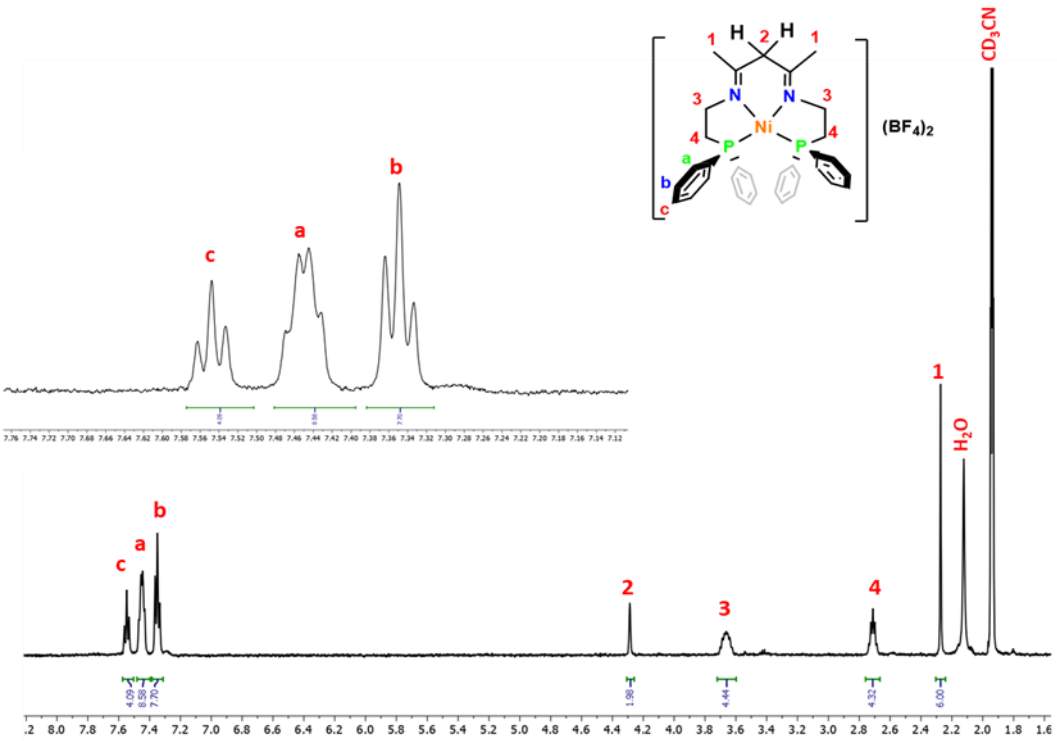

Figure S1. ^{1}H NMR of complex $\mathbf{1(BF_4)_2}$ in CD_3CN

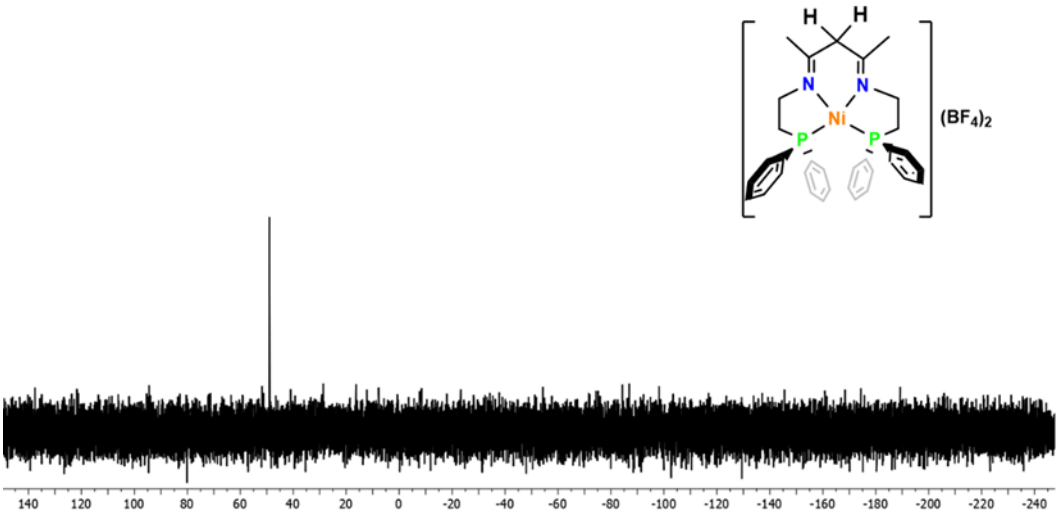

Figure S2. $^{31}P\{H\}$ NMR of complex $\mathbf{1(BF_4)_2}$ in CD_3CN

Chapter 4.

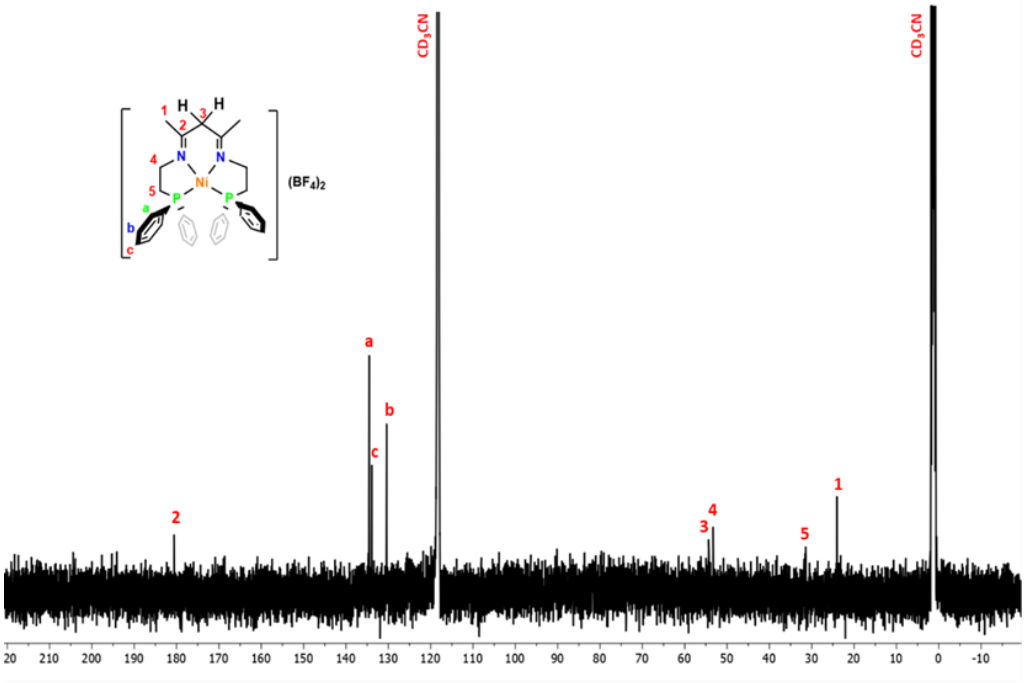

Figure S3. ^{13}C NMR of complex **1(BF$_4$)$_2$** in CD_3CN

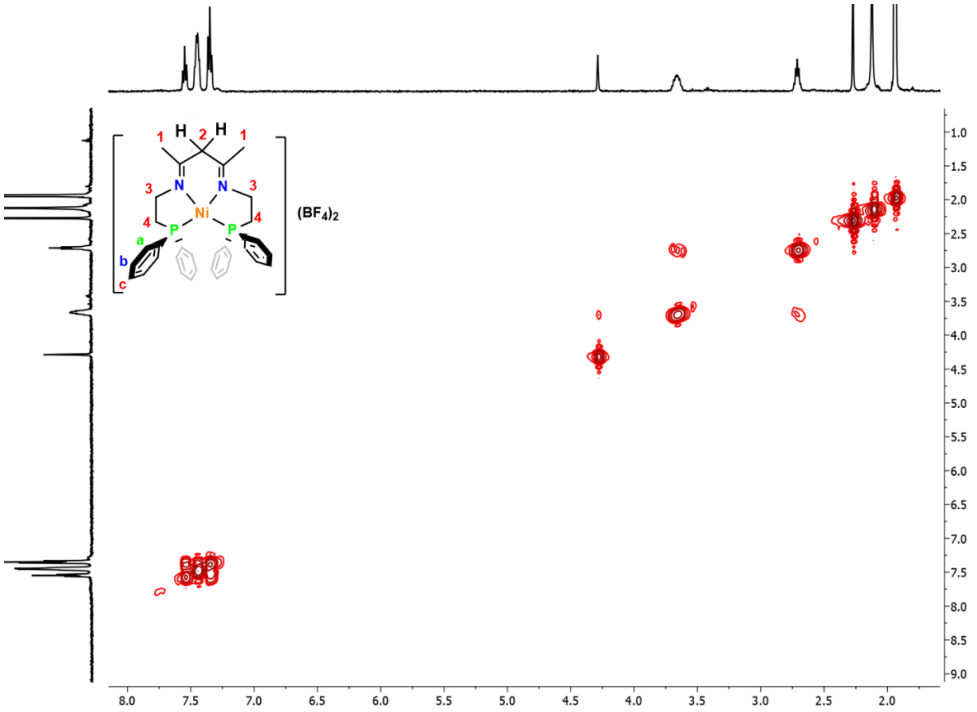

Figure S4. ^{1}H-^{1}H COSY NMR of **1(BF$_4$)$_2$** complex in CD_3CN

Chapter 4.

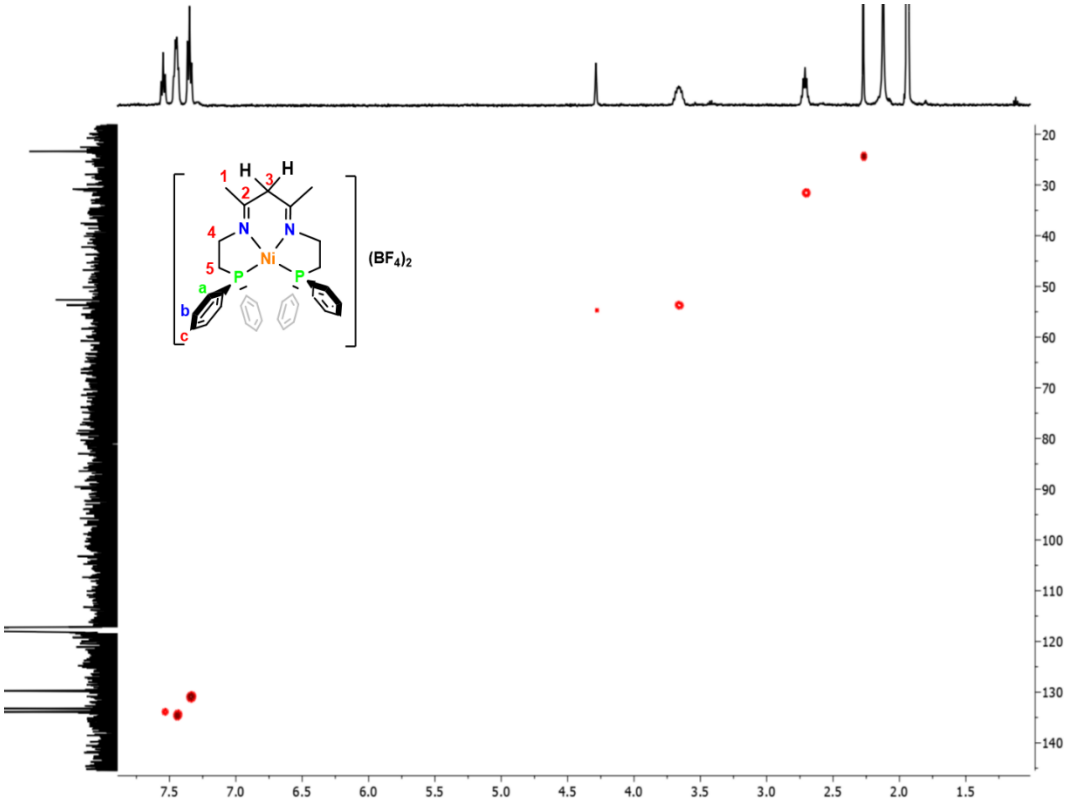

Figure S5. HSQC NMR of **1(BF$_4$)$_2$** complex in CD_3CN

Chapter 4.

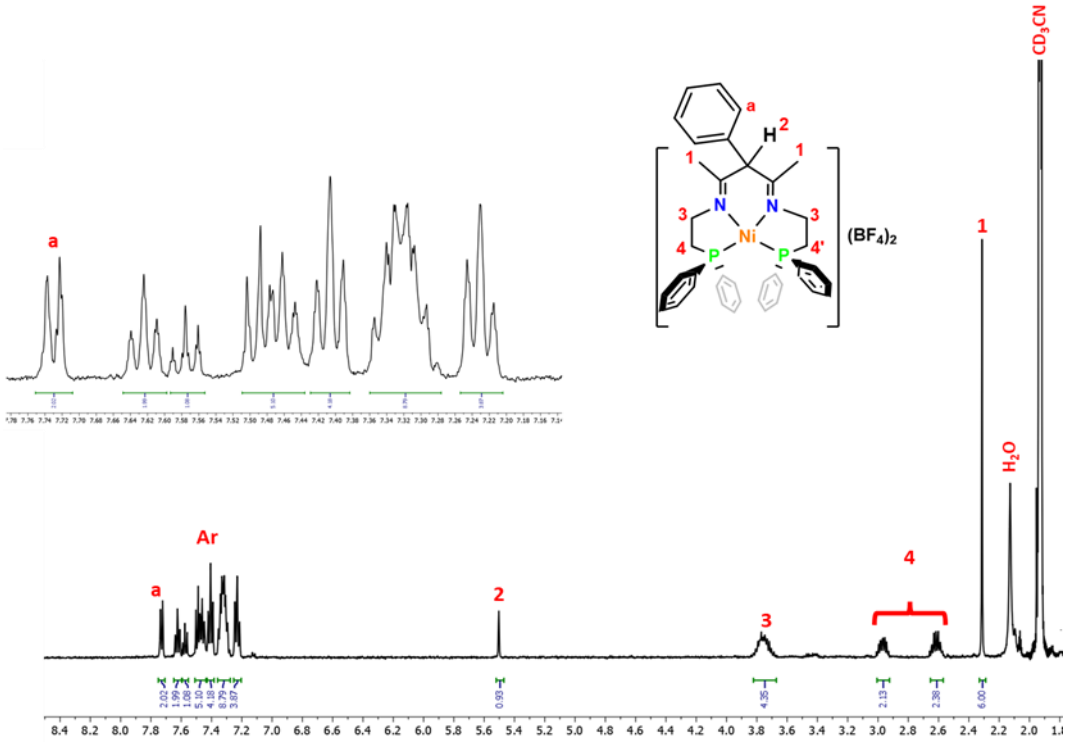

Figure S6. ^{1}H-NMR of complex **2(BF$_4$)$_2$** in CD_3CN

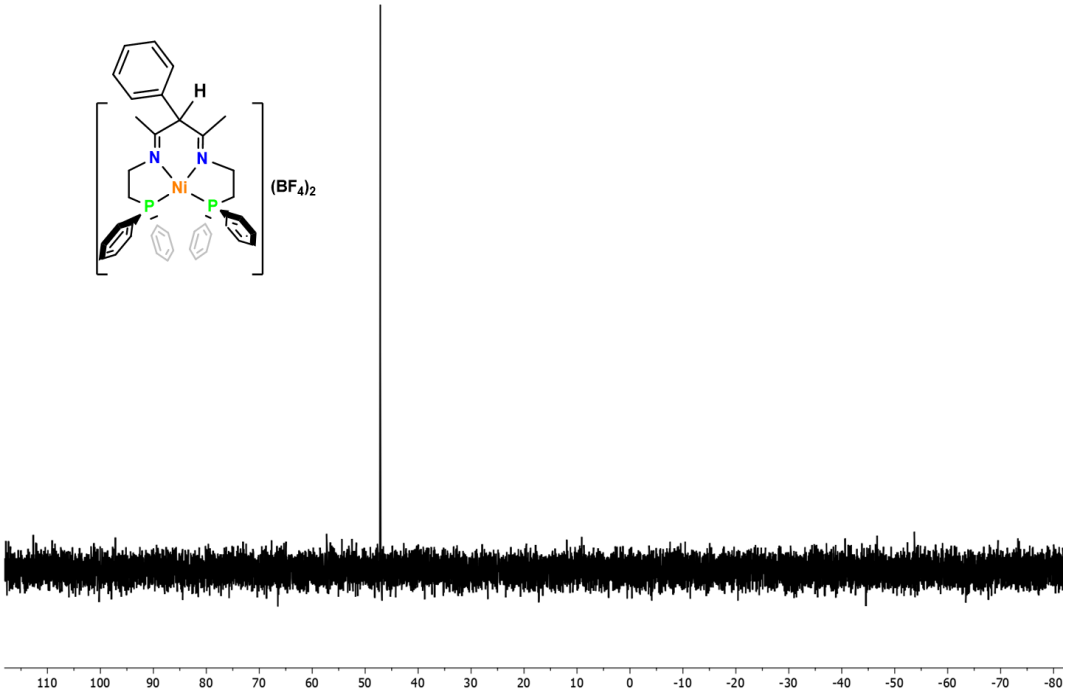

Figure S7. ^{31}P NMR of complex **2(BF$_4$)$_2$** in CD_3CN

Chapter 4.

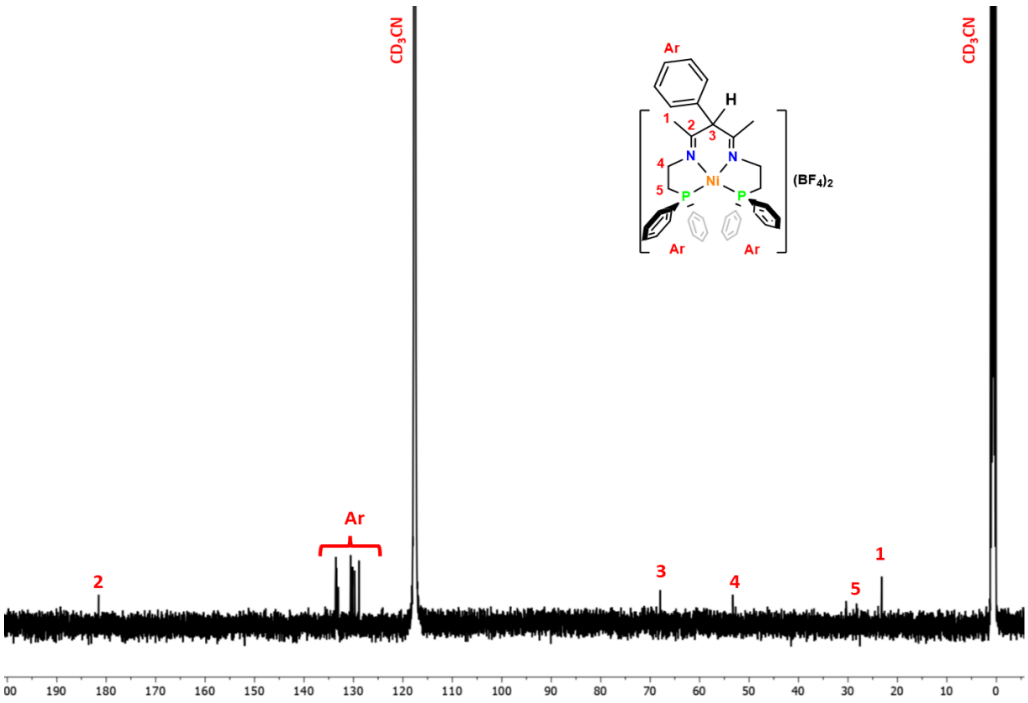

Figure S8. ^{13}C NMR of complex **2(BF4)2** in CD_3CN

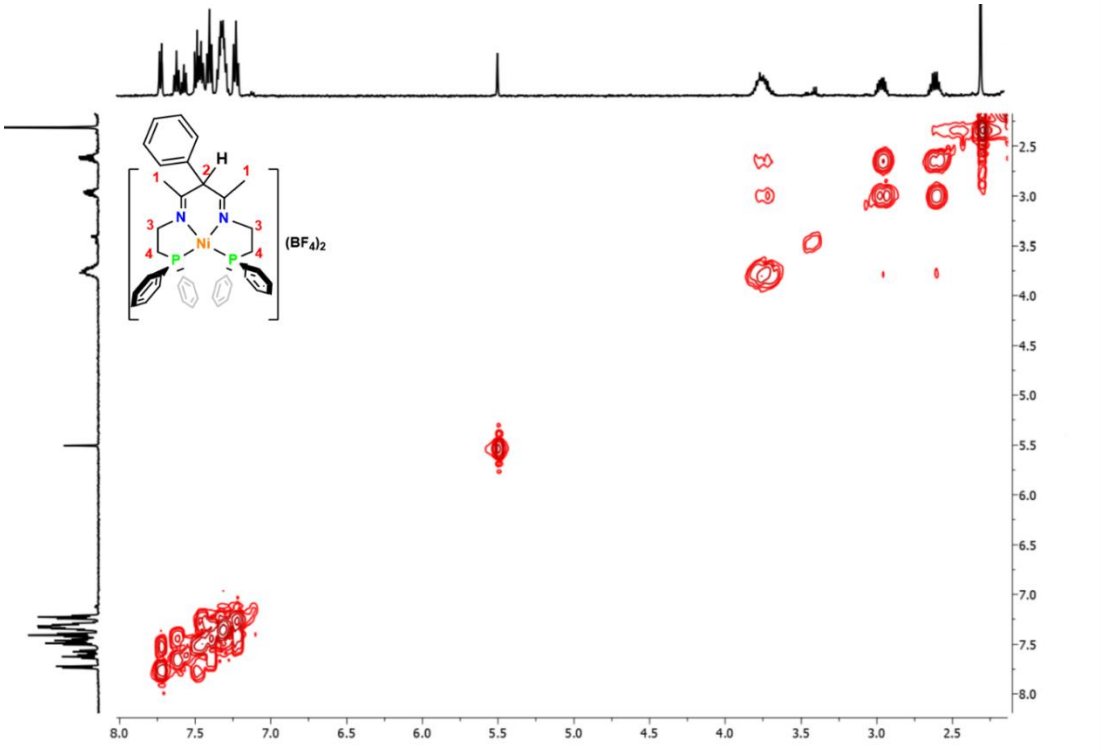

Figure S9. ^{1}H-^{1}H COSY NMR of **2(BF4)2** in CD_3CN

Chapter 4.

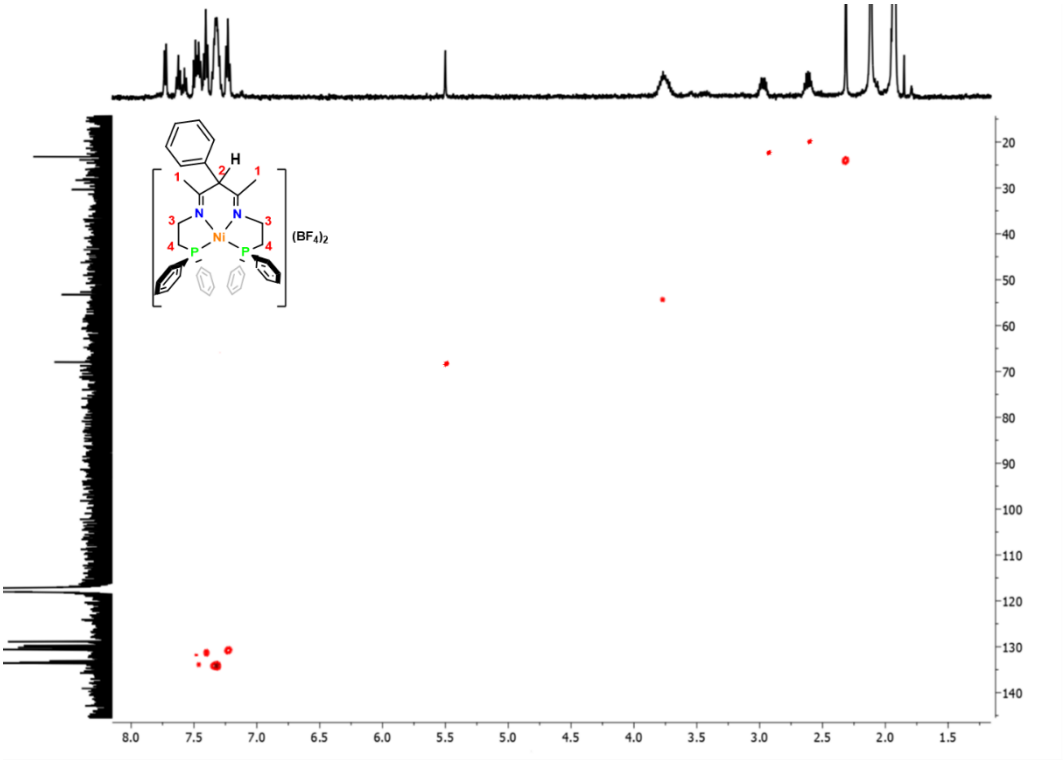

Figure S10. HSQC NMR of **1(BF$_4$)$_2$** complex in **(CD$_3$CN)**

Chapter 4.

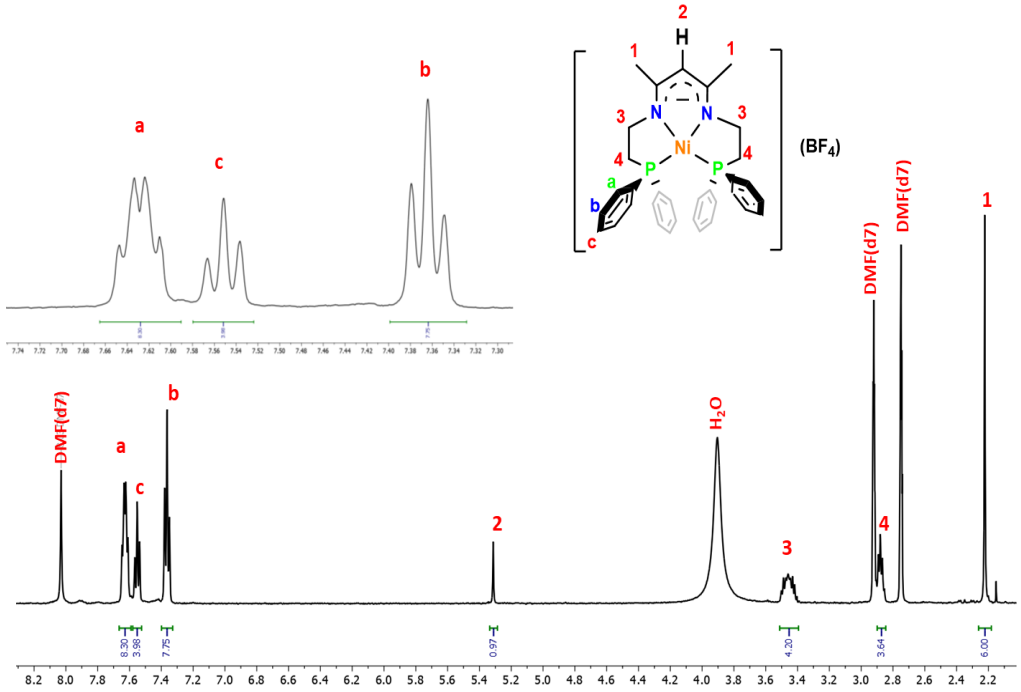

Figure S11. ^{1}H-NMR of complex **1(BF$_4$)$_2$** in **DMF(d$_7$)**

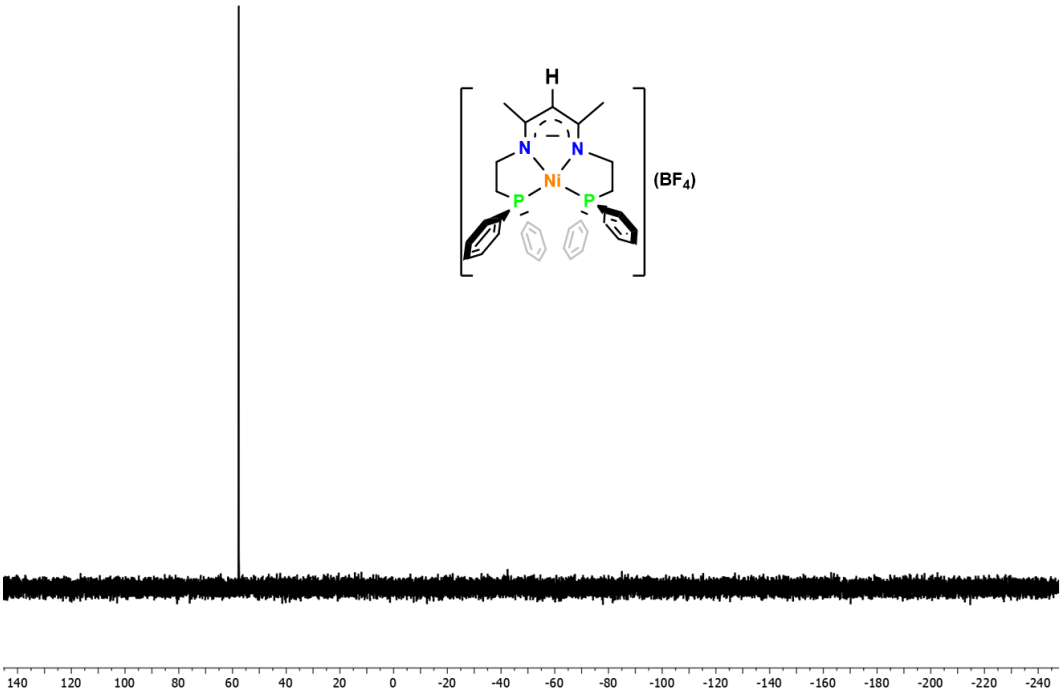

Figure S12. ^{31}P NMR complex **1(BF$_4$)$_2$** in **DMF (d$_7$)**

Chapter 4.

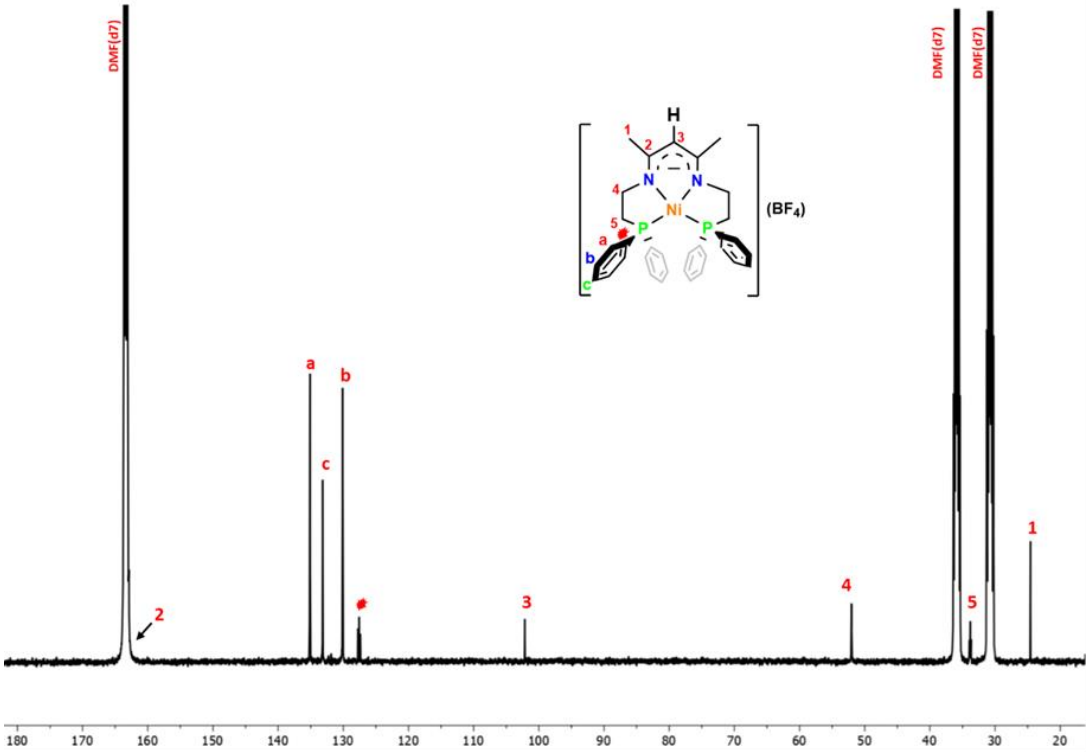

Figure S13. ^{13}C NMR of complex **1(BF$_4$)$_2$** in **DMF (d$_7$)**

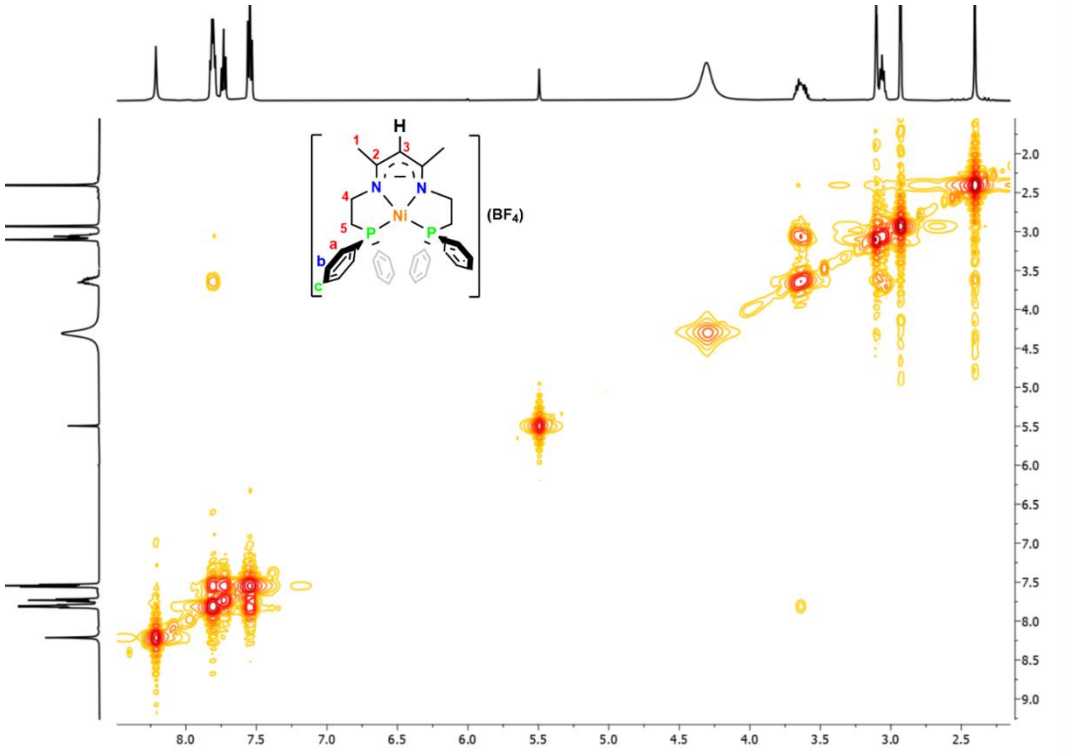

Figure S14. ^{1}H-^{1}H COSY NMR of **1(BF$_4$)$_2$** complex in **DMF (d$_7$)**

Chapter 4.

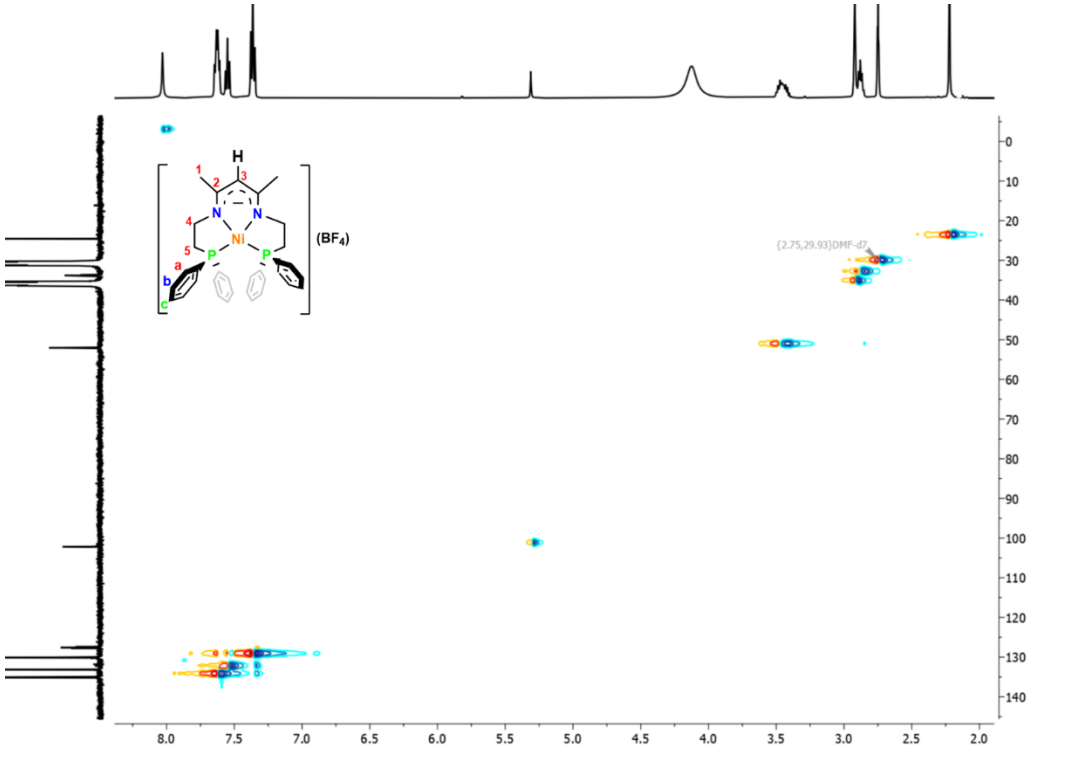

Figure S15- HSQC NMR of **1(BF$_4$)$_2$** complex in **DMF (d$_7$)**

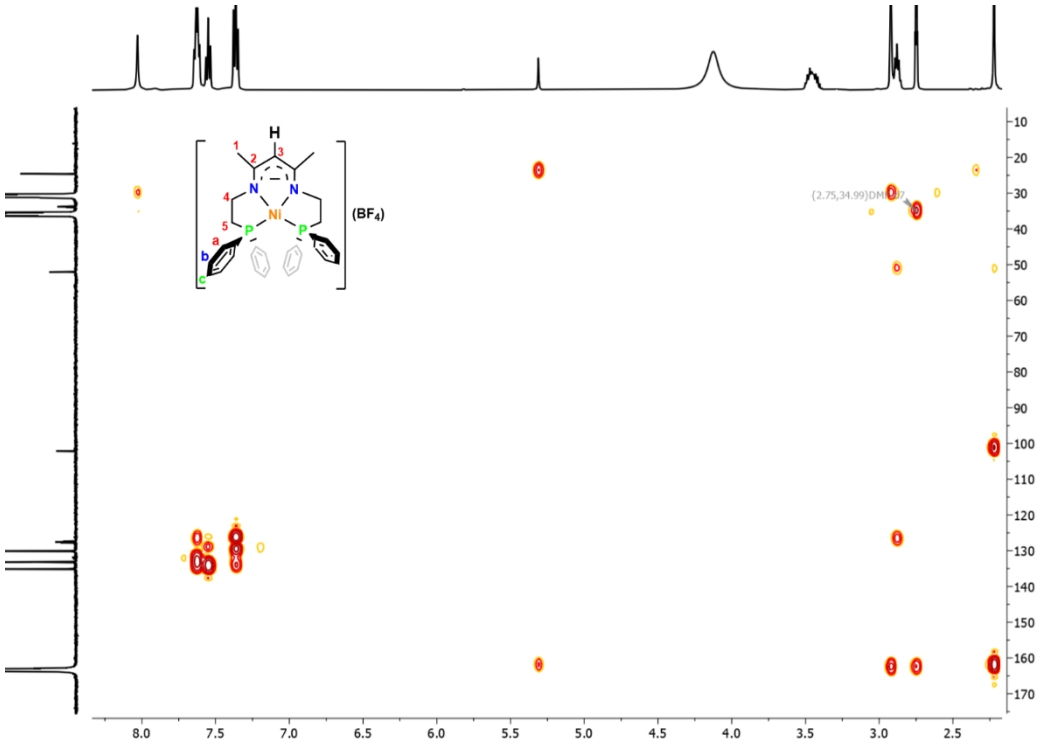

Figure S16- HMBC NMR of **1(BF$_4$)$_2$** complex in **DMF (d$_7$)**

Chapter 4.

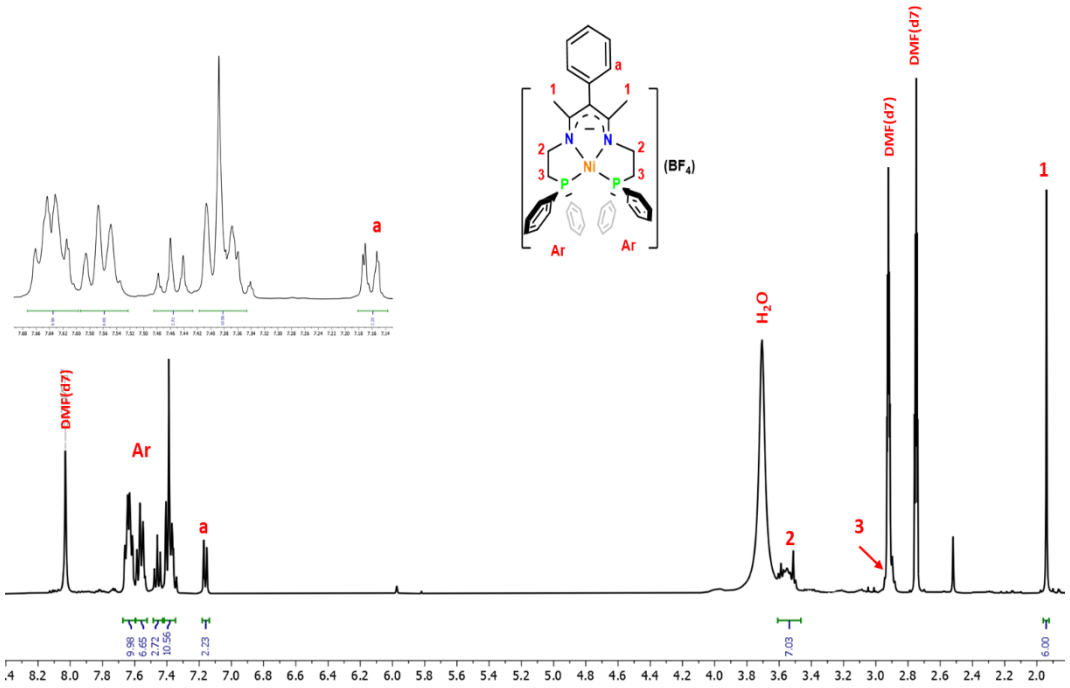

Figure S17-^{1}H-NMR of complex **2(BF$_4$)$_2$** in **DMF (d$_7$)**

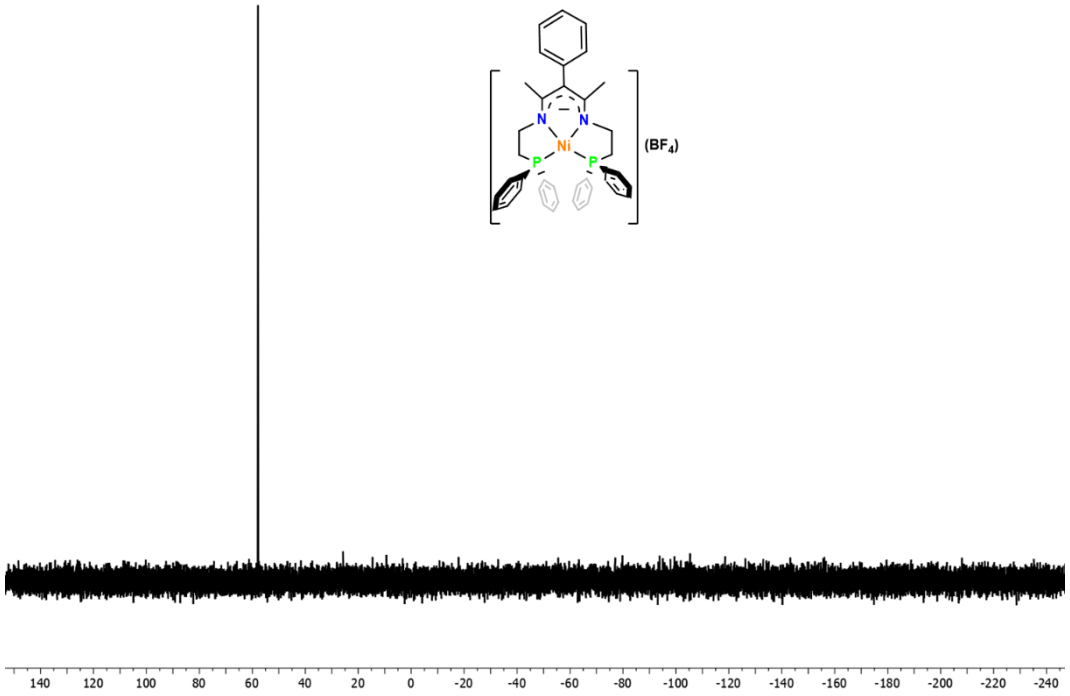

Figure S18-^{31}P NMR of complex **2(BF$_4$)$_2$** in **DMF (d$_7$)**

Chapter 4.

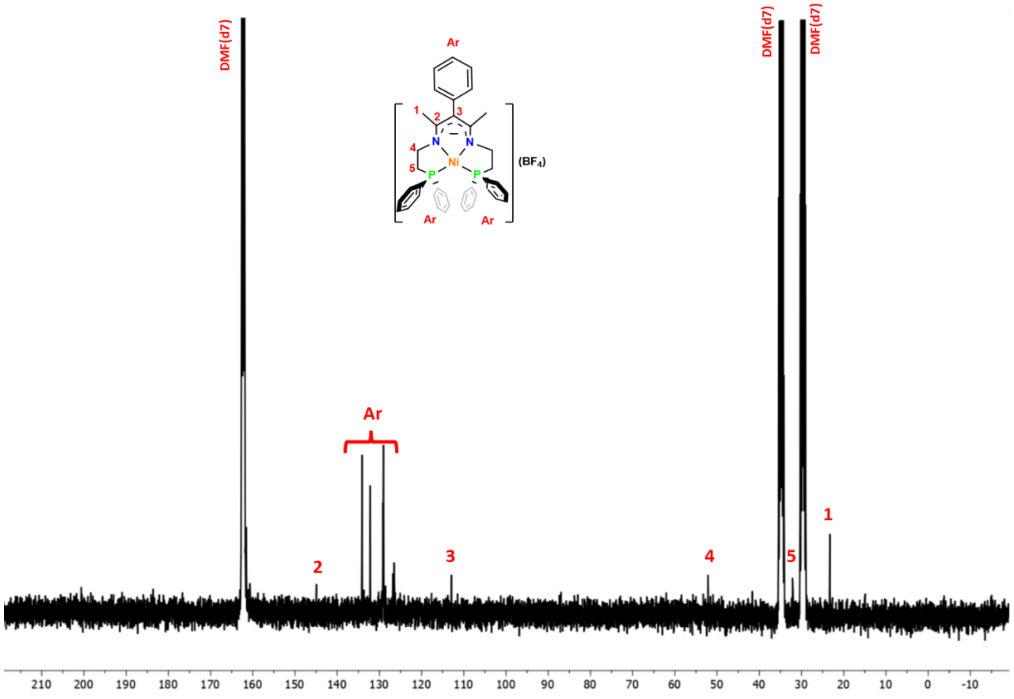

Figure S19-^{13}C NMR of complex **2(BF$_4$)$_2$** in **DMF (d$_7$)**

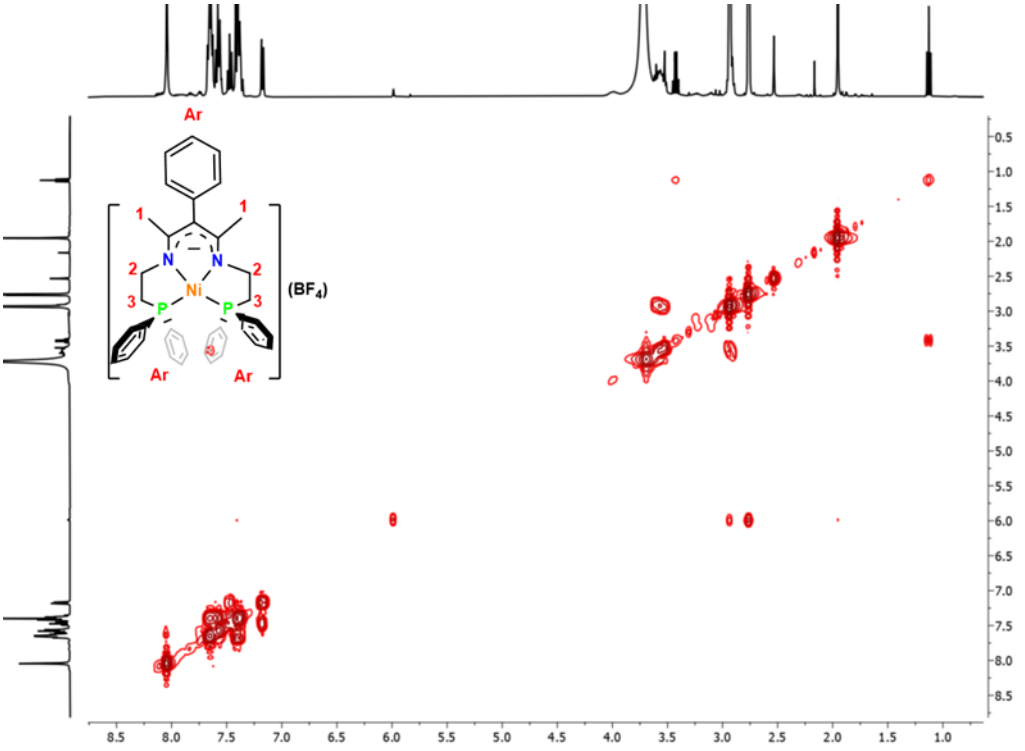

Figure S20-^{1}H-^{1}H COSY NMR of **2(BF$_4$)$_2$** in **DMF (d$_7$)**

Chapter 4.

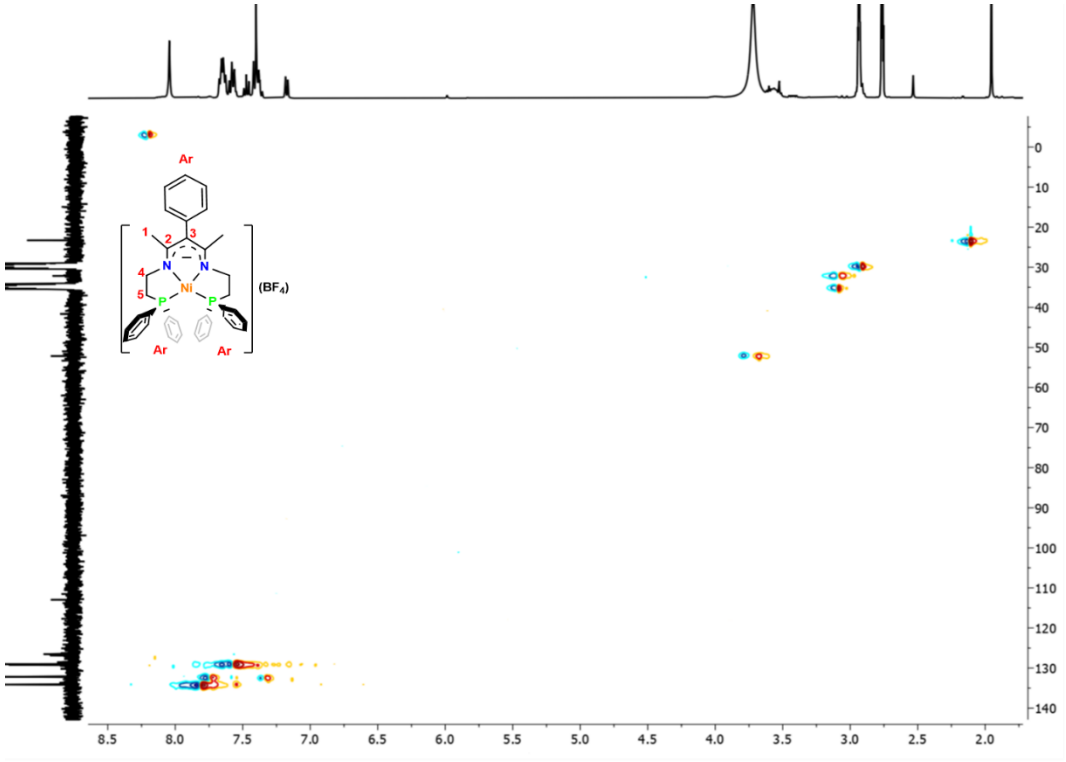

Figure S21- HSQC NMR of complex **2(BF$_4$)$_2$** in **DMF (d$_7$)**

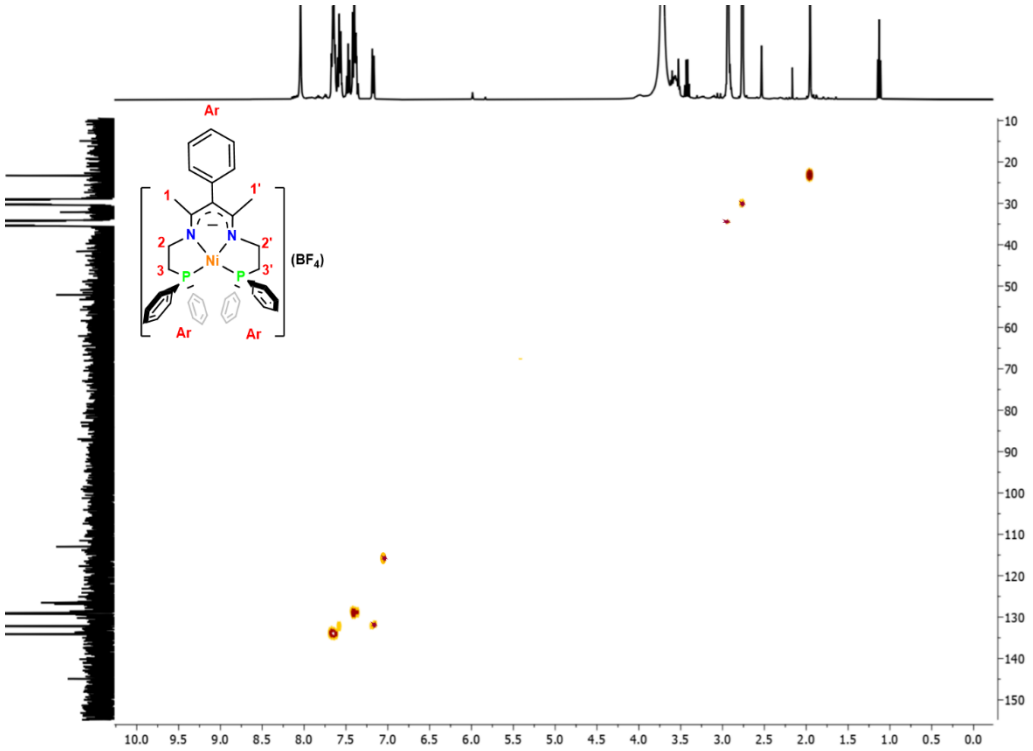

Figure S22- HMBC NMR of complex **2(BF$_4$)$_2$** in **DMF (d$_7$)**

Chapter 4.

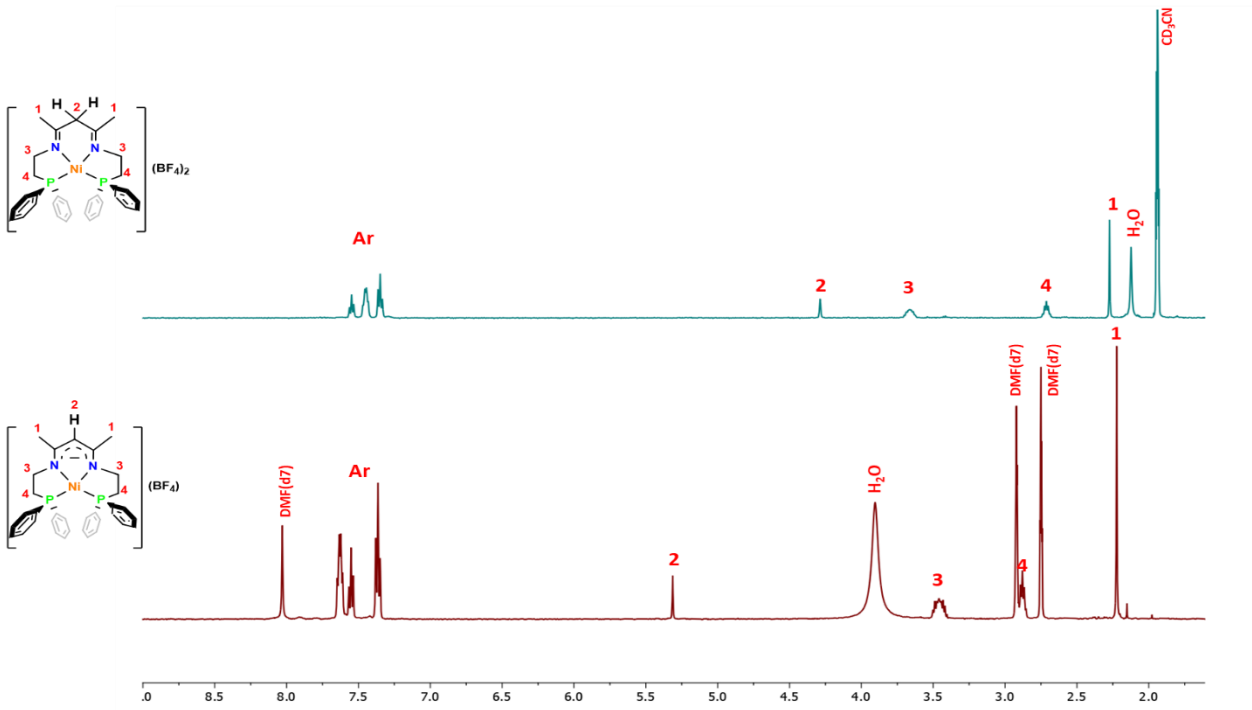

Figure S23- Comparison ^{1}H NMR spectra of Complex **1(BF$_4$)$_2$** in CD_3CN (**top**) and DMF (d_7) (**bottom**)

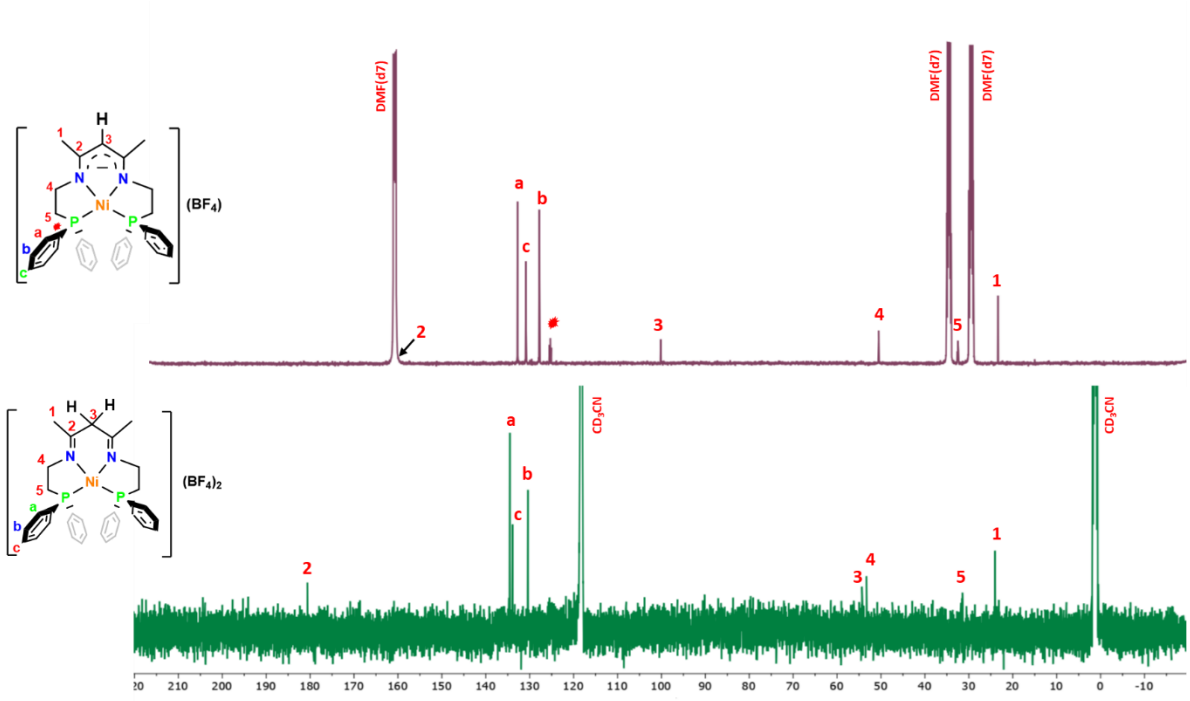

Figure S24- Comparison ^{13}C NMR spectra of Complex **1(BF$_4$)$_2$** in CD_3CN (**Bottom**) and DMF (d_7) (**top**)

Chapter 4.

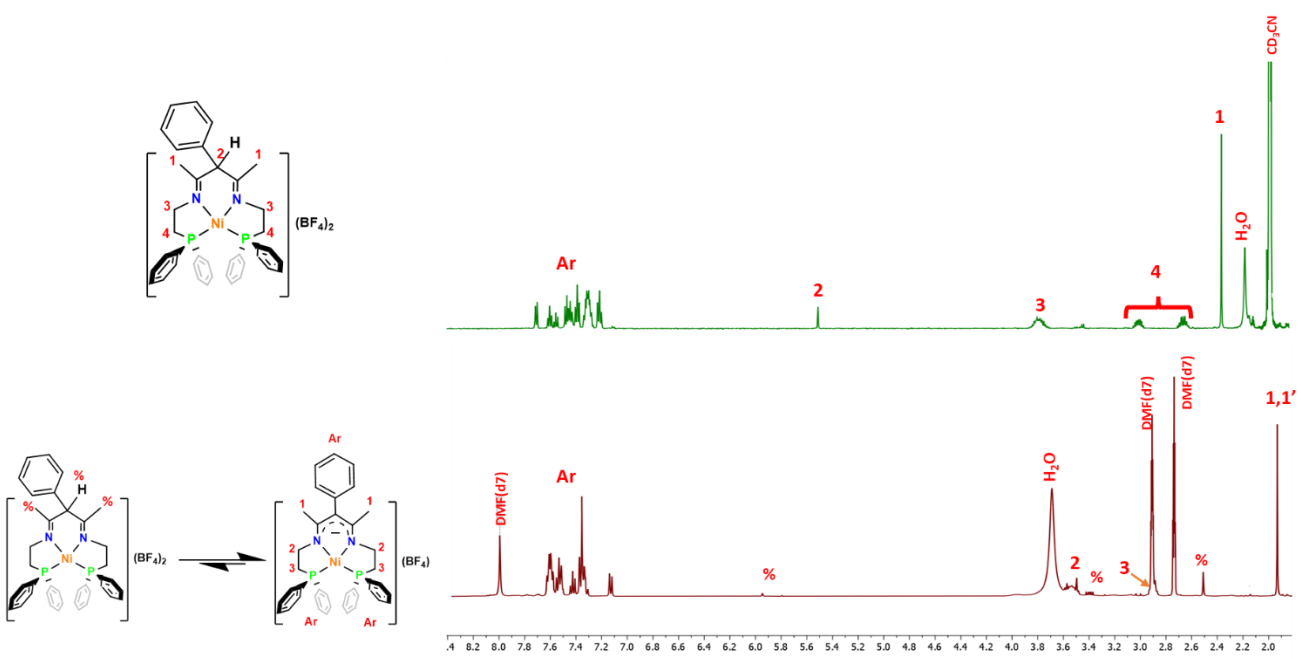

Figure S25- Comparison ^{1}H NMR spectra of Complex **2(BF$_4$)$_2$** in CD_3CN (**top**) and DMF (d_7) (**bottom**)

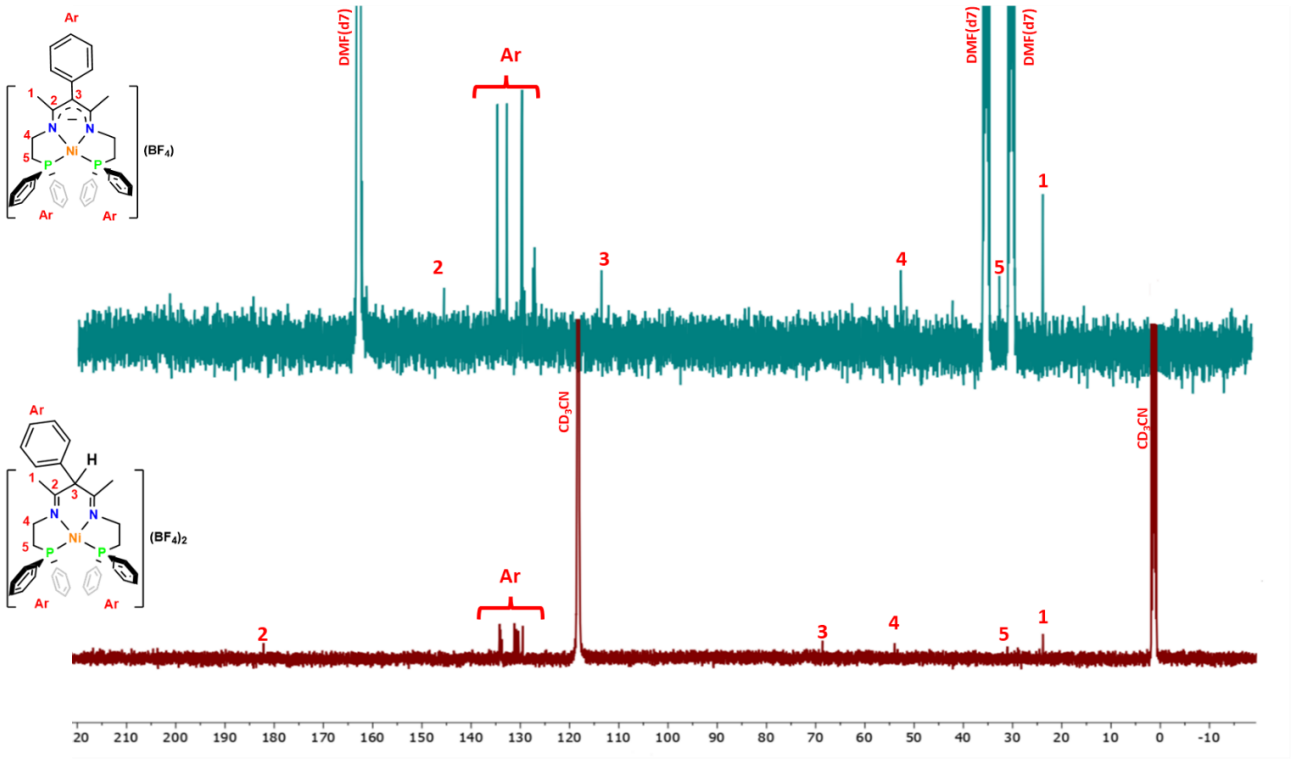

Figure S26- Comparison ^{13}C NMR spectra of Complex **2(BF$_4$)$_2$** in CD_3CN (**bottom**) and DMF (d_7) (**top**)

Chapter 4.

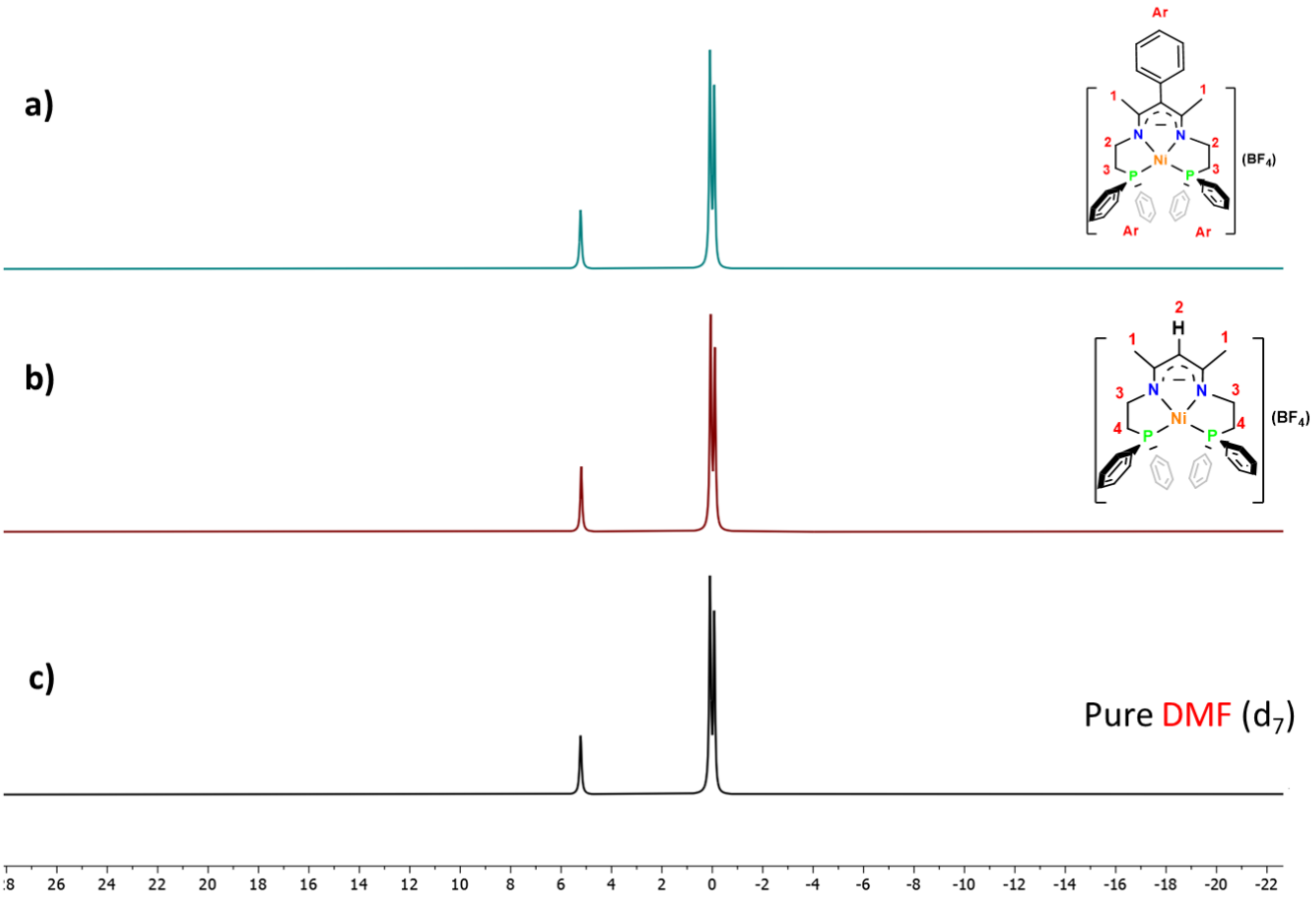

Figure S27- ^{2}D NMR of **2(BF$_4$)$_2$ (a), 1(BF$_4$)$_2$ (b)** in DMF (d$_7$). (**c**) ^{2}D NMR of pure DMF (d$_7$). Number of Scans=128 for each sample

Chapter 4.

4- Electrochemistry and Spectroelectrochemistry of $1(BF_4)_2$ and $2(BF_4)_2$

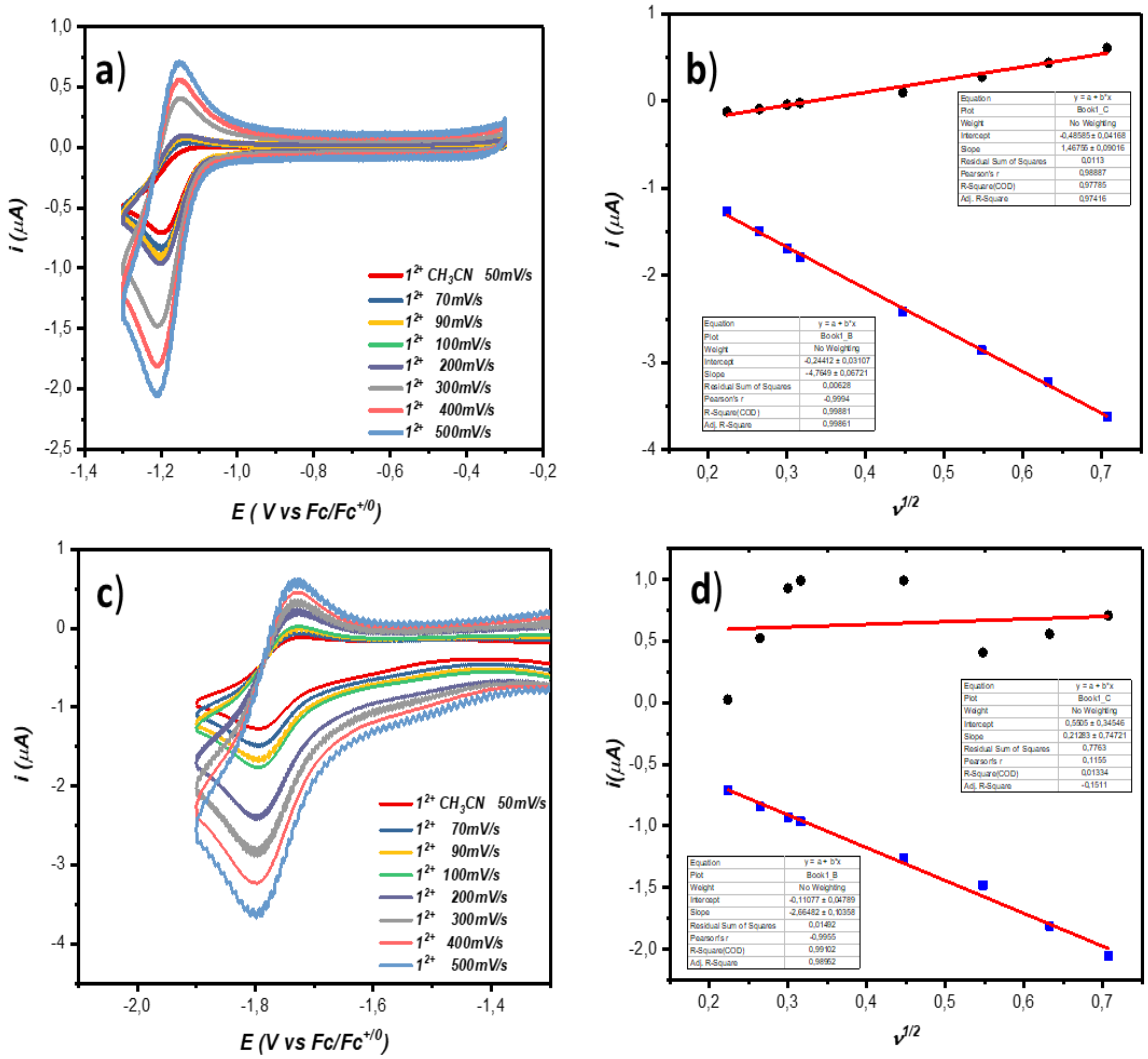

Figure S28. Cyclic voltammograms of 0.5 mM ($\mathbf{1}^{2+}$) on first (**a**) and second (**b**) peak position in acetonitrile (**c,d**) Plots of (i vs $v^{1/2}$) for reduction and oxidation couples in presence of 0.1M $TBAPF_6$ as supporting electrolyte, **WE**: GC(1mm), **CE**: Pt, **REF** electrode: 0.01M $Ag/AgNO_3$

Chapter 4.

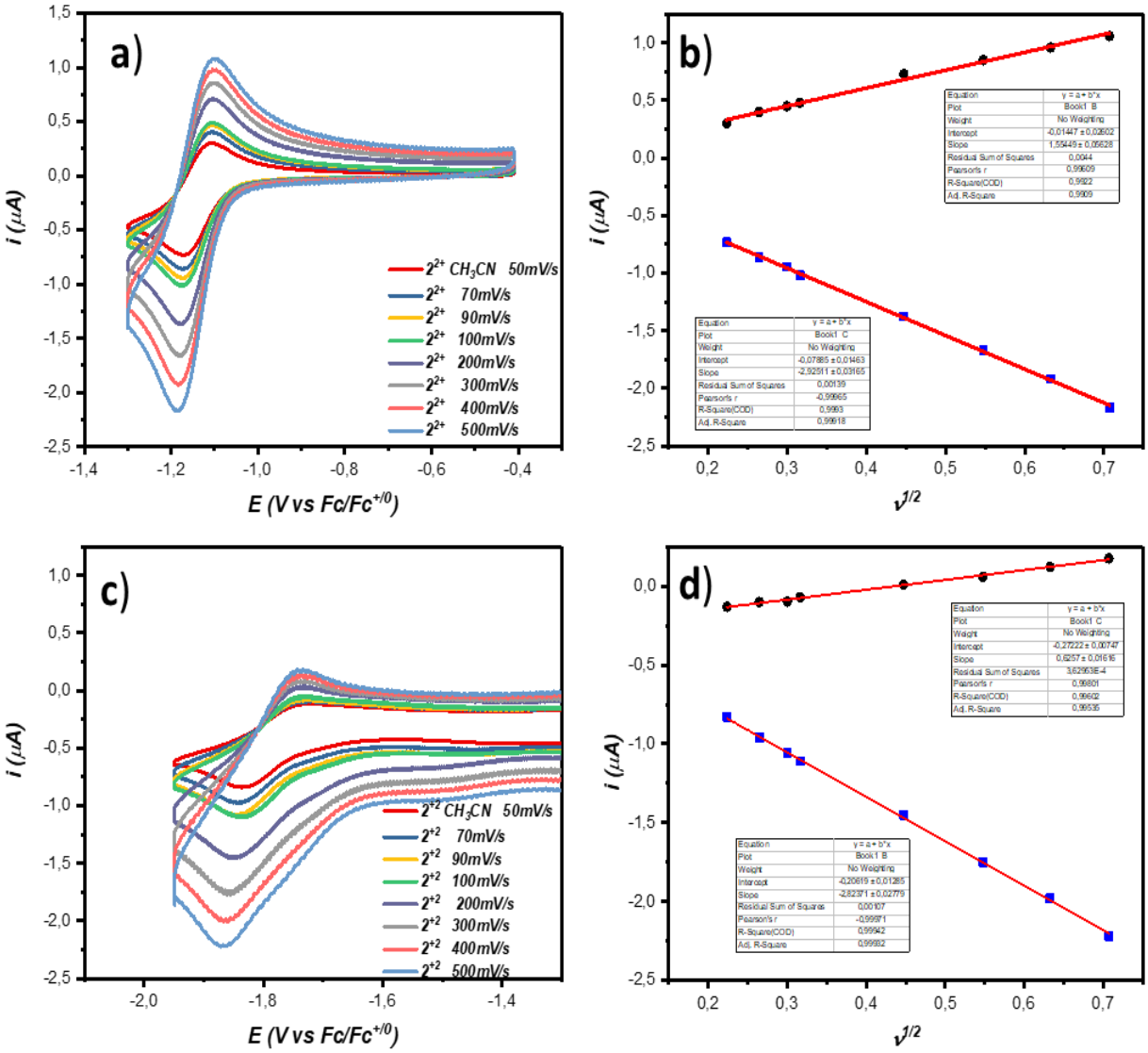

Figure S29- Cyclic voltammograms of 0.5 mM (2^{2+}) on first (**a**) and second peak position (**b**) in acetonitrile. (**c,d**) Plots of (i vs $v^{1/2}$) for reduction and oxidation couples in prescence of 0.1M $TBAPF_6$ as supporting electrolyte, **WE**: GC (1mm), **CE**: Pt, **REF** electrode: 0.01M $Ag/AgNO_3$

Chapter 4.

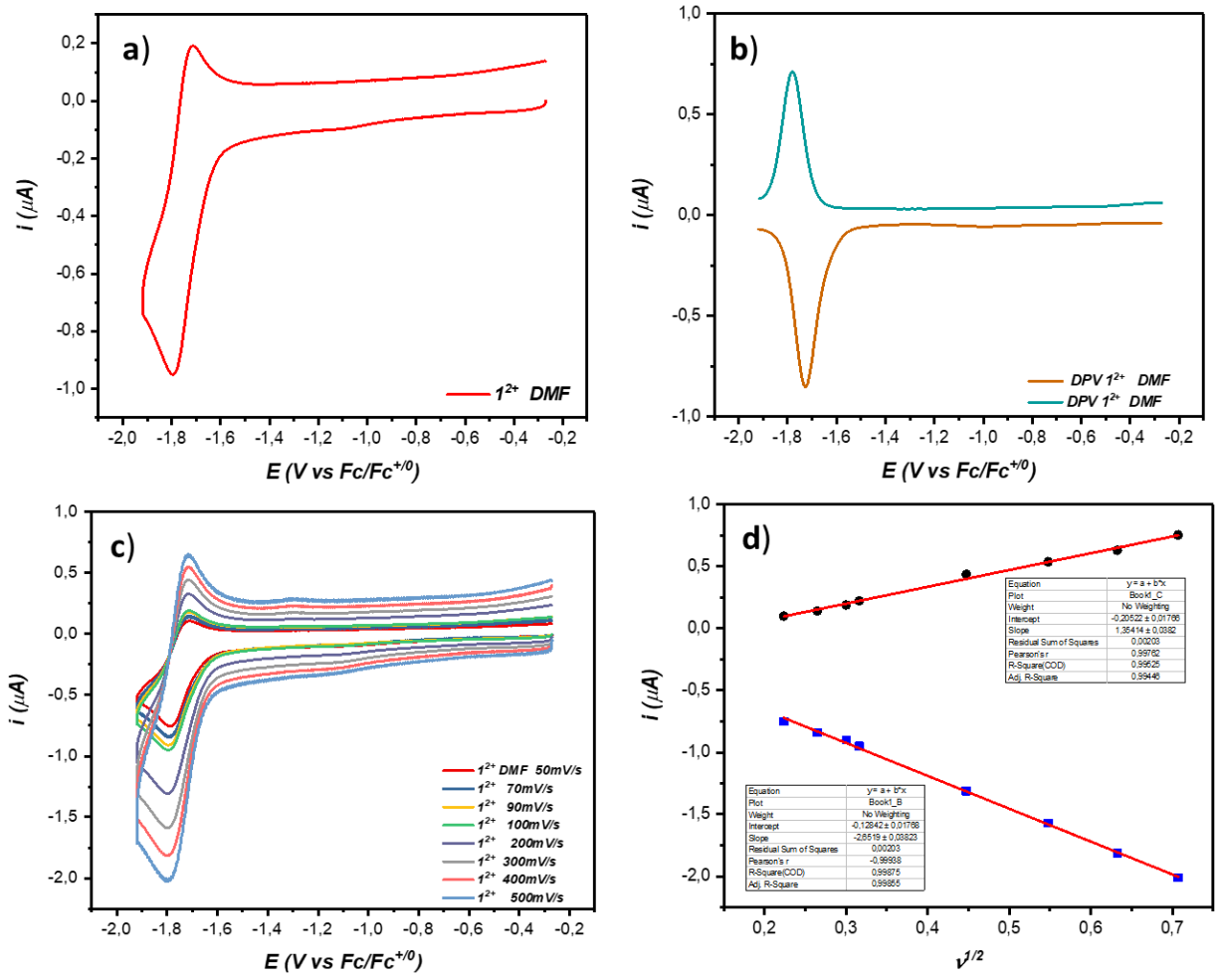

Figure S30. (**a**) cyclic voltammogram of (**1**$^{2+}$) in DMF Scan rate 100mV/s. (**b**) DPV of (**1**$^{2+}$) amplitude 50mV/s. (**c**) cyclic voltammogram of (**1**$^{2+}$) in DMF with different Scan rates. (**d**) Plot of reduction and oxidation peak currents versus square root of Scan rates for (**1**$^{2+}$) in DMF

Chapter 4.

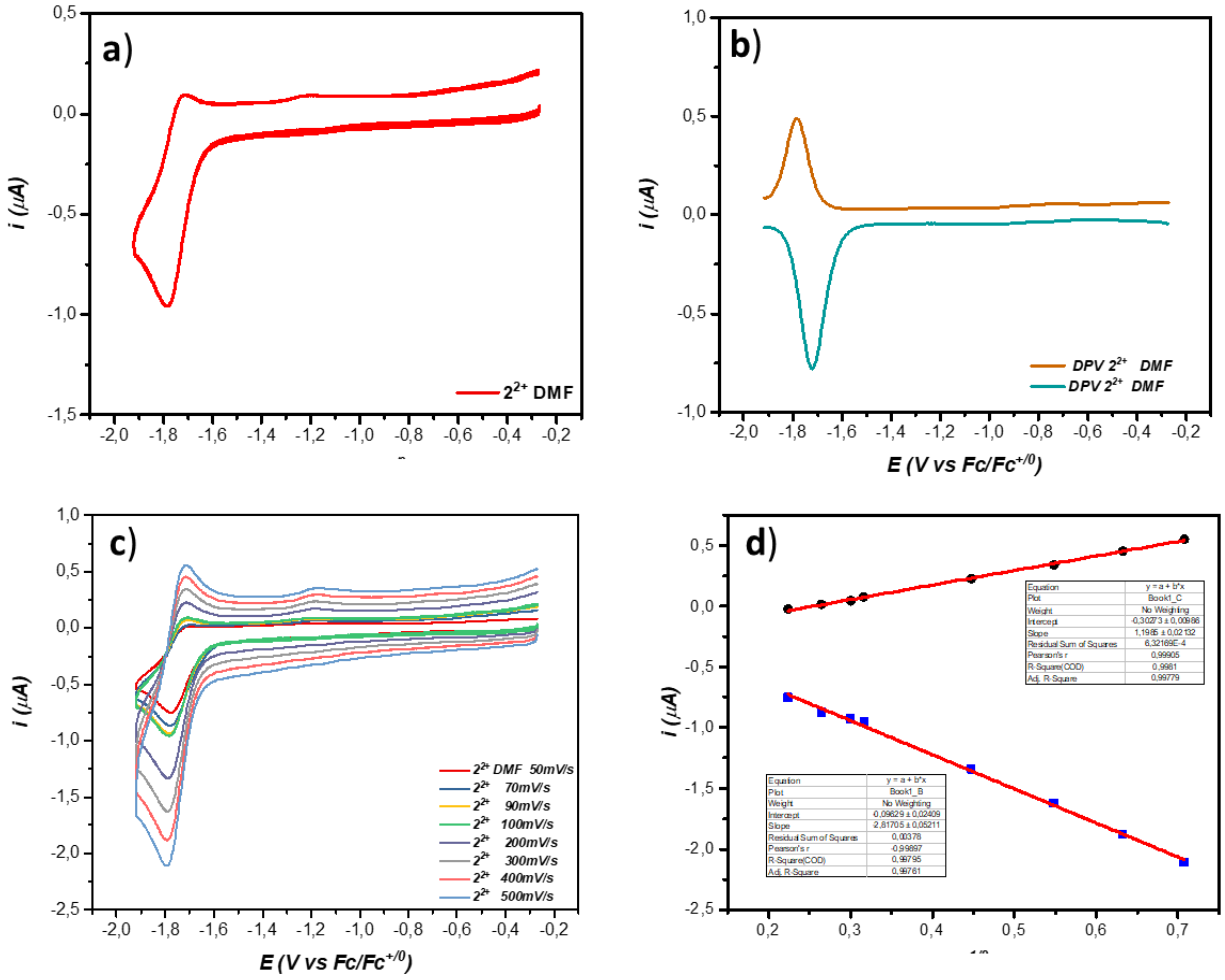

Figure S31. (**a**) cyclic voltammogram of (**2**$^{2+}$) in DMF Scan rate 100mV/s. (**b**) DPV of (**2**$^{2+}$) amplitude 50mV/s. (**c**) cyclic voltammograms of (**2**$^{2+}$) in DMF with different Scan rates. (**d**) Plots of reduction and oxidation peak currents versus square root of Scan rates (**2**$^{2+}$) in DMF

Chapter 4.

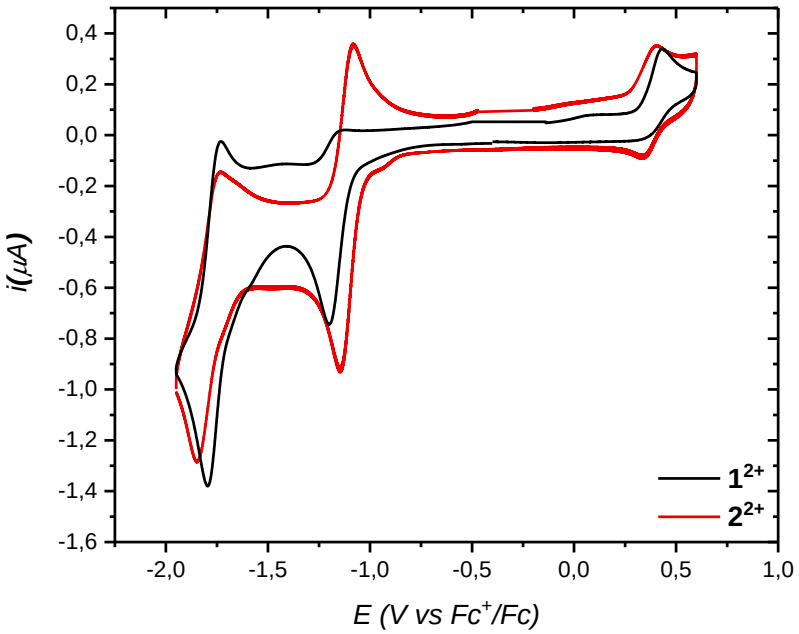

Figure S32. Cyclic voltammograms of 0.5 mM ($\mathbf{2}^{2+}$ -(red)) and ($\mathbf{1}^{2+}$ -(Black)) in acetonitrile in prescence of 0.1M $TBAPF_6$ as supporting electrolyte, **WE**: GC (1mm), **CE**: Pt, **REF** electrode: 0.01M $Ag/AgNO_3$

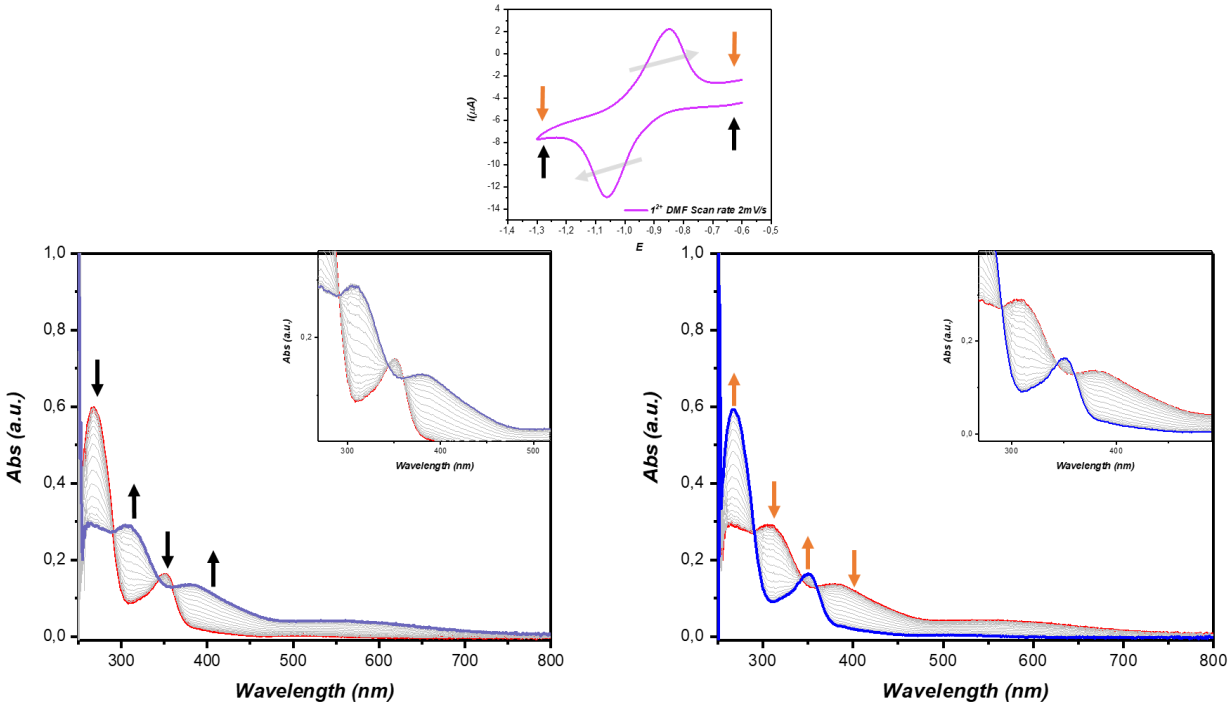

Figure S33. Cyclic voltammetry experiment in the OTTLE cell (WE = Platinum mesh; CE = Platinum wire; RE: Silver pseudo-reference electrode; solvent = dimethylformamide-0.1 M $[Bu_4N]$ PF_6; $[\mathbf{1}^{2+}]$ = 2 mM; scan rate = 2 mV/s. Black, and orange arrows show the starting/ending of the UV-vis spectra acquisition. Grey arrows indicate the polarity of the scan.

Chapter 4.

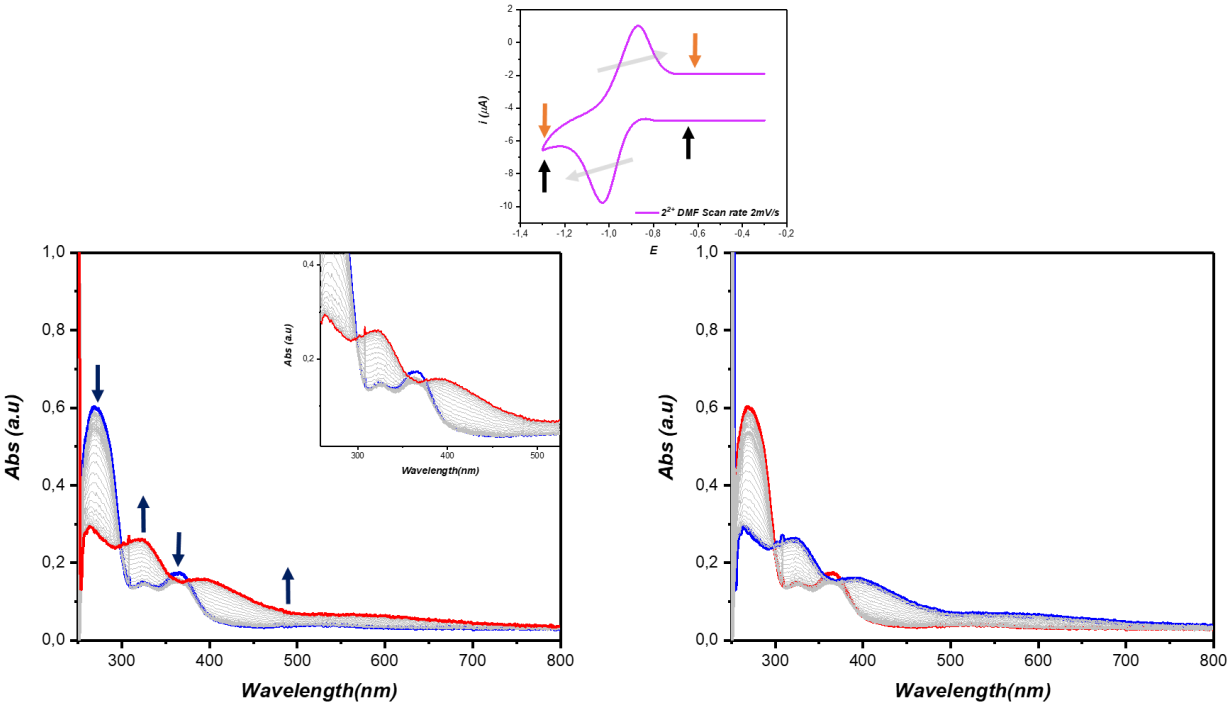

Figure S34- Cyclic voltammetry experiment in the OTTLE cell (WE = Platinum mesh; CE = Platinum wire; RE: Silver pseudo-reference electrode; solvent = dimethylformamide-0.1 M $[Bu_4N]$ PF_6; $[\mathbf{2}^{2+}]$ = 2 mM; scan rate = 2 mV/s. Black, and orange arrows show the starting/ending of the UV-vis spectra acquisition. Grey arrows indicate the polarity of the scan.

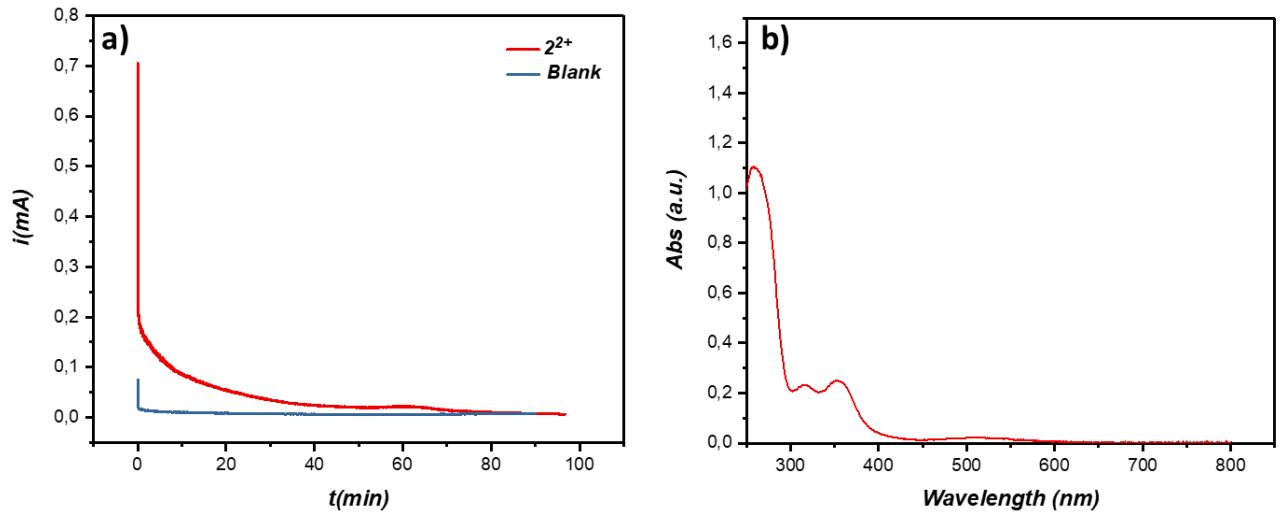

Figure S35- **a)** Bulk electrolysis experiments of a 0.4 mM solution of $\mathbf{2}^{2+}$ in acetonitrile (5ml, 0,1M $TBAPF_6$) at E_{app}= -1.3V vs $Fc/Fc^{+/0}$ in a two compartment cell with of Pt mesh as a counter Electrode, GC rod (S = 3,1 cm^2) as working electrode, and Ag/Ag^+ reference electrode (0.01 $AgNO_3$, 0.1 $TBAPF_6$). **a**) Charge passed through the working electrode during bulk electrolysis after subtraction of the background charge gives (Mols of electron/Mols of initial complex= 1 at -1.3V). **b**) UV-vis spectra of $\mathbf{2}^{2+}$ after the bulk electrolysis experiment in CH_3CN

Chapter 4.

5- UV-Vis Spectroscopy of $1(BF_4)_2$ and $2(BF_4)_2$

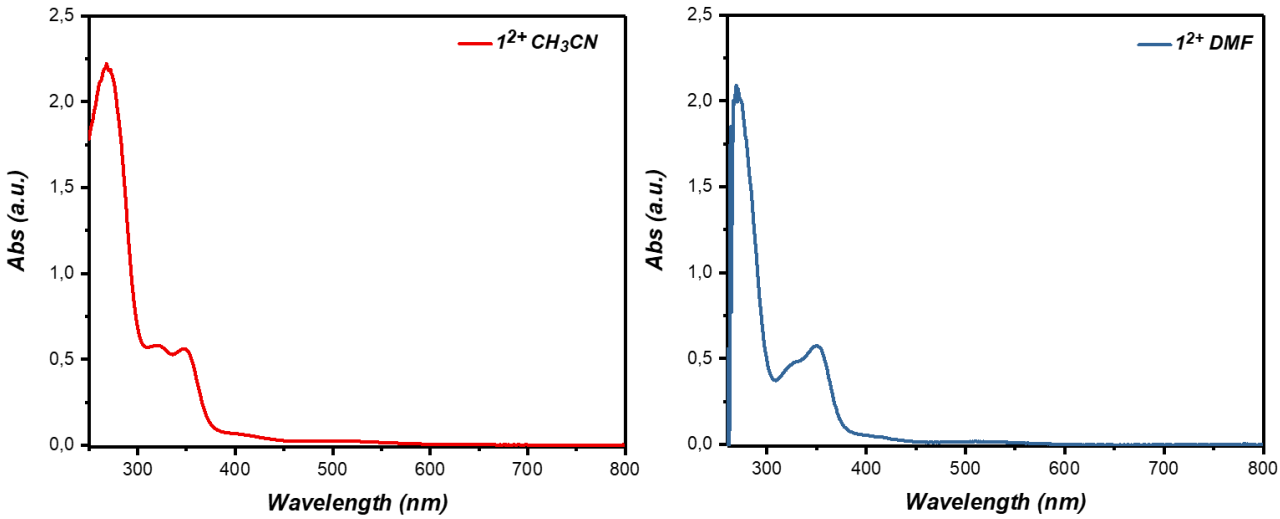

Figure S36- UV-visible spectrum of 0.125mM of $\mathbf{1}^{2+}$ in CH_3CN and DMF. See main manuscript for band position and extinction coefficients.

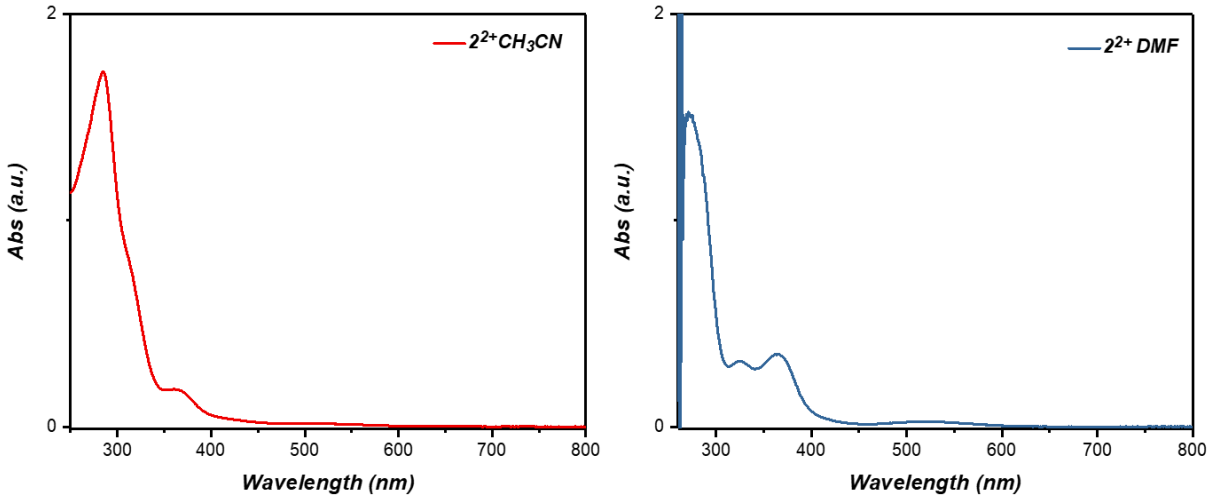

Figure S37- UV visible spectrum of 0.125mM of $\mathbf{2}^{2+}$ in CH_3CN and DMF. See main manuscript for band position and extinction coefficients.

Chapter 4.

6- Electrochemistry and gas detection experiments in the presence of organic acids

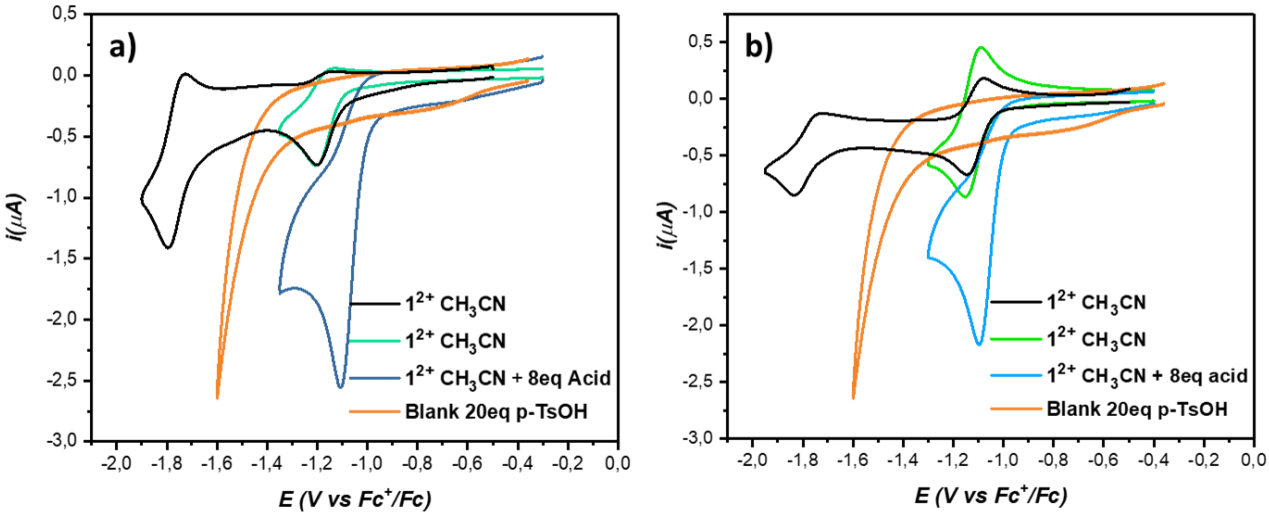

Figure S38-Voltammograms of 0.5 mM $\mathbf{1}^{2+}$ (**a**) and $\mathbf{2}^{2+}$ (**b**) in CH_3CN in absence of proton source (Black and green) and in prescence of 8eq p-TsOH in first reduction peak position (blue). Cyclic voltammogram of the blank in prescence of 20eq p-TsOH indicates proton reduction current on working electrode occurs between first and second reduction peak of the complexes (Orange)

Chapter 4.

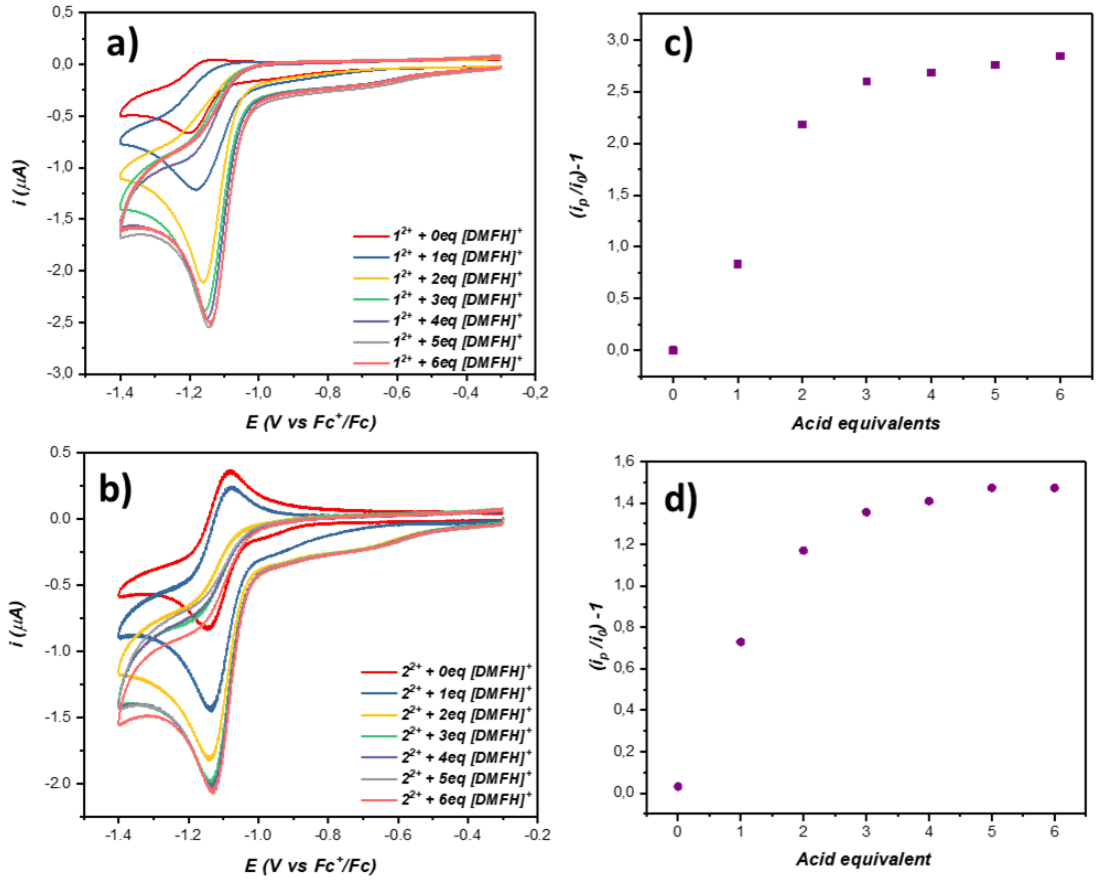

Figure S39. Voltammograms of 0.5 mM $\mathbf{1}^{2+}$ (**a**) and $\mathbf{2}^{2+}$ (**b**) with successive additions of $[[DMFH]^+(CF_3O_3)^-]$ at Scan rate 0.1V/s in the presence of 0.1 M $TBAPF_6$ as supporting electrolyte in CH_3CN solution. (**c**) and (**d**) show the growth of peak intensity (i_p) relative to the peak in the absence of acid (i_0).

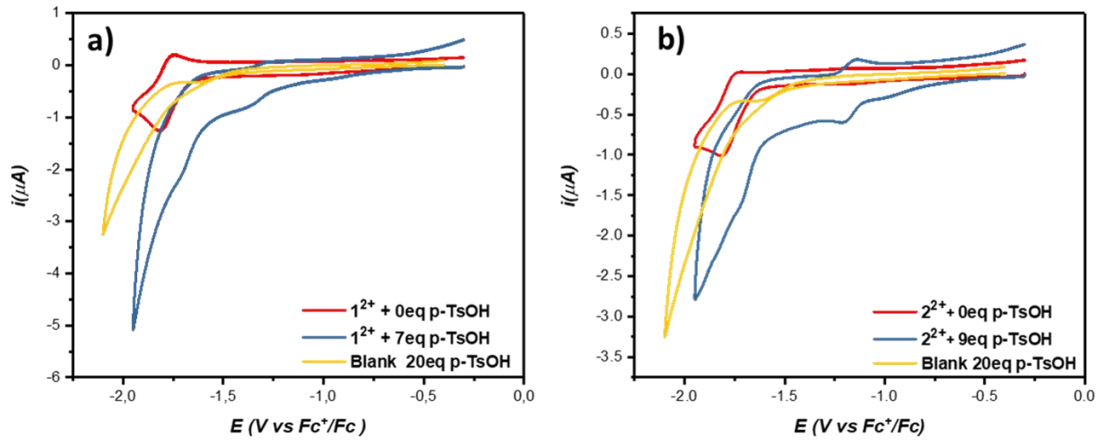

Figure S40- Cyclic Voltammograms of 0.5 mM $\mathbf{1}^{2+}$ (**a**) and $\mathbf{2}^{2+}$ (**b**) in CH_3CN in absence of proton source (red) and in prescence of 7eq p-TsOH and 9eq p-TsOH in DMF (blue). Cyclic voltammogram of the blank in prescence of 20eq p-TsOH in DMF (yellow)

Chapter 4.

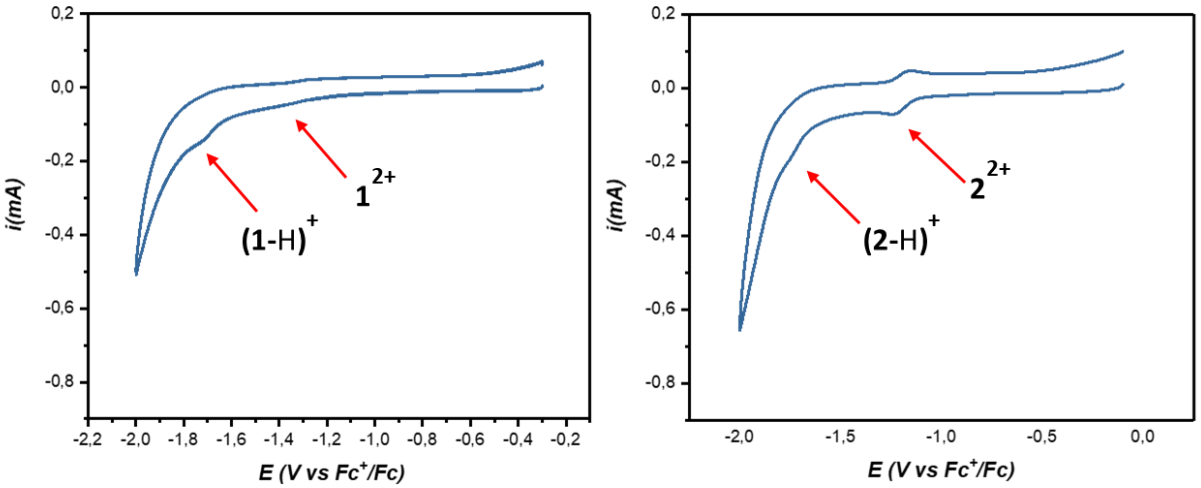

Figure S41- Cyclic Voltammograms of a solution of 0.5 mM solution of $\mathbf{1}^{2+}$ (**a**) and $\mathbf{2}^{2+}$ (**b**) immediately after a BE experiment in at -1.8V vs Fc^+/Fc DMF in the presence of 60 equivalents of p-TsOH showing the presence of the complex and supporting the molecular nature of the catalysis.

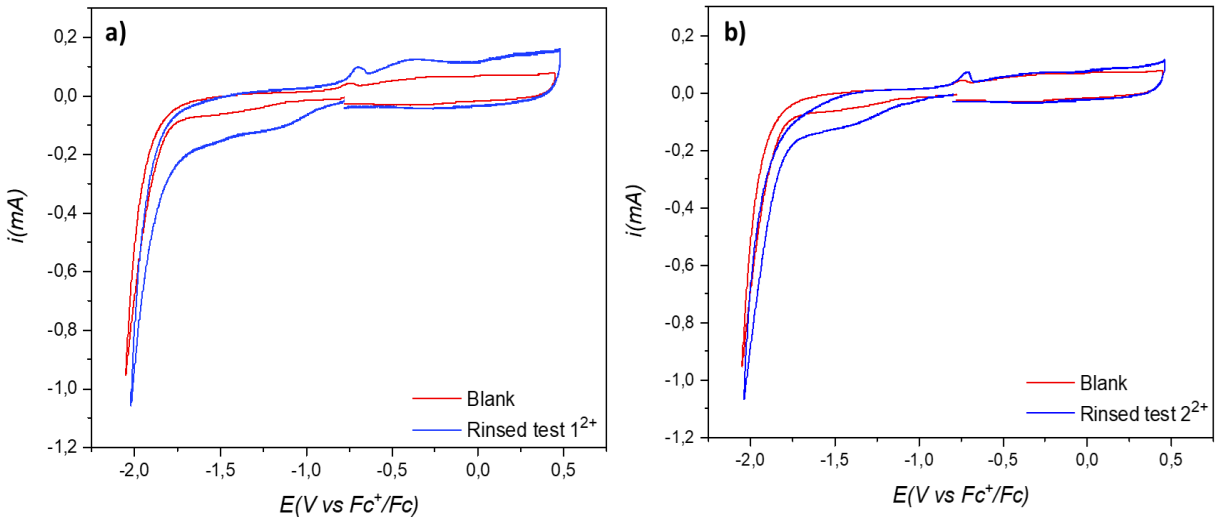

Figure S42- Cyclic Voltammograms of rinsed electrodes after bulk electrolysis with complex $\mathbf{1}^{2+}$ (**a**) and $\mathbf{2}^{2+}$ (**b**) at -1.8V vs Fc^+/Fc in a DMF solution with 60 equivalents of p-TsOH and 0.1 M $TBAPF_6$ as supporting electrolyte

Chapter 4.

6.1- Determination of Faradic efficiency, Turnover Number (TON) and Turnover Frequency (TOF):

The FE and TON are calculated using the following formulas:

$$\boldsymbol{FE}(\%) = \frac{\boldsymbol{n_{H_2\ detected}}}{\boldsymbol{n_{H_2\ theoretical}}} \times \mathbf{100} \qquad \textbf{(eq. 1)}$$

$$\boldsymbol{TON} = \frac{\boldsymbol{n_{H_2\ detected}}}{\boldsymbol{n_{cat}}} \qquad \textbf{(eq. 2)}$$

Where $n_{H2\ detected}$ is the number of mols molecular hydrogen detected by gas chromatography and $n_{H2\ theoretical}$ is the number of theoretical mols of H_2 calculated from the charge that pass through the electrode during bulk electrolysis experiments and n_{cat} is the mols of the catalysts used for molecular hydrogen production.

CP experiments were carried out in a gas-tight two-compartment cell with 6 mL headspace. Complexes were dissolved in 5ml dry acetonitrile containing 0.1M $TBAPF_6$ as supporting electrolyte placed in one compartment with glassy carbon rod ($S=3.14cm^2$ immersed in solution) as WE . reference electrode $Ag/AgNO_3$ (0.01M $Ag/AgNO_3$ in 0.1M $TBAPF_6$ in acetonitrile as supporting electrolyte) A Pt mesh was used as CE in the other compartment. Before any experiment, both compartments were degassed with N_2 for 30 minutes. The experiment was carried under stirring conditions.

Chapter 4.

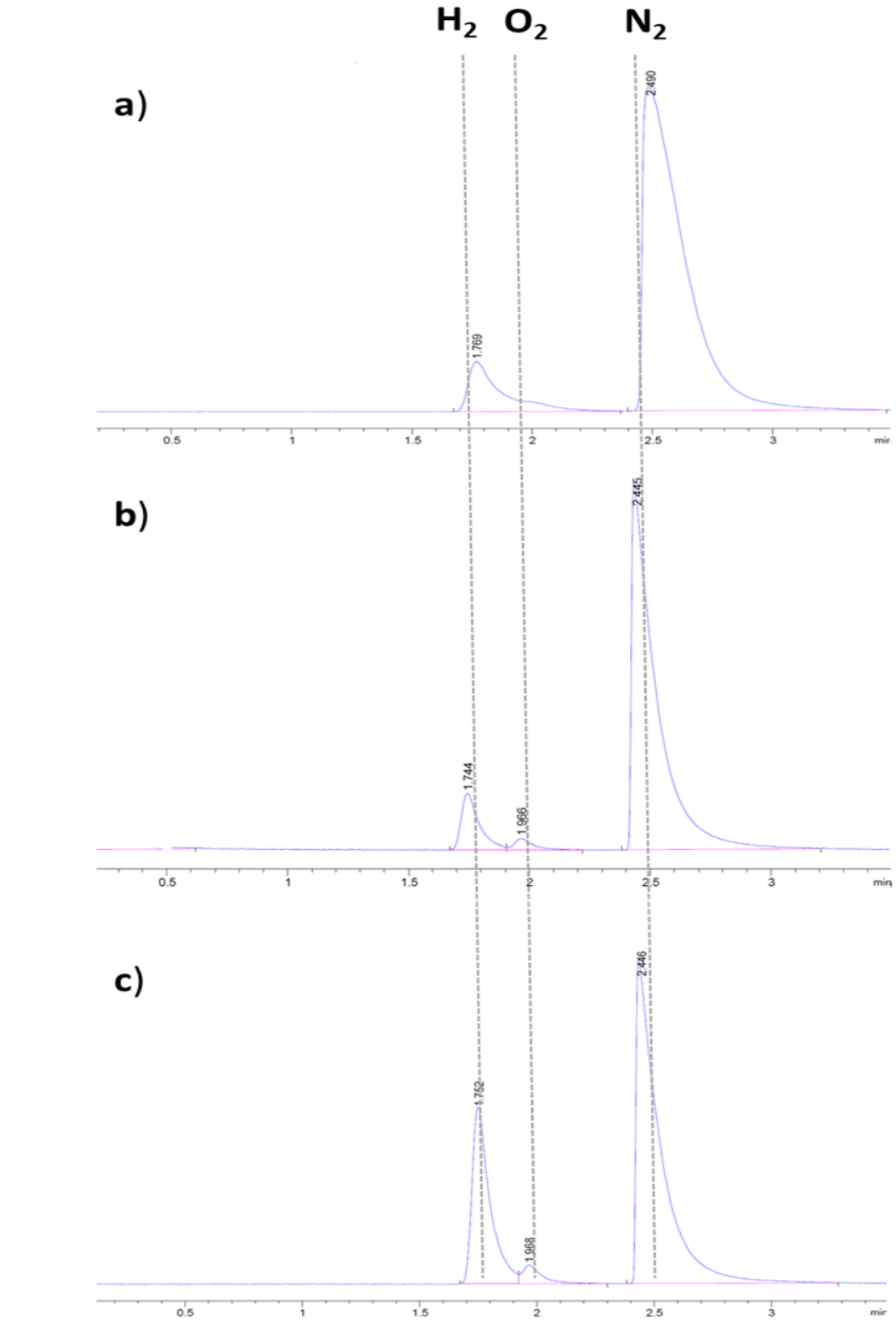

Figure S43- Chromatograms obtained by injection of 50µL of the head space of the cathodic compartment of a bulk electrolysis experiment at -1.8V vs Fc/Fc^+ after 900s, for solutions containing $\mathbf{1}^{2+}$(**a**), $\mathbf{2}^{2+}$(**c**) and blank (**b**). See Figures 9 and 10 of the main manuscript.

Chapter 4.

Calibration slope is required to correlate the peak area of the gas chromatography to the amount of H_2 contained in the headspace.

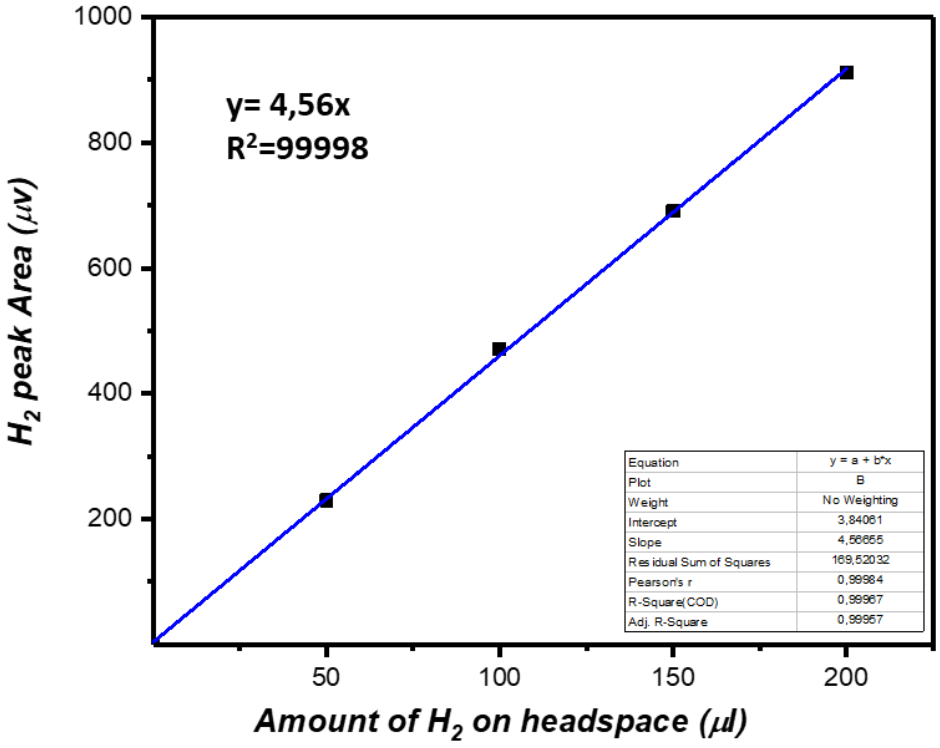

Figure S44- Calibration plot of the gas chromatography.

Table S1- Peak areas and volume of hydrogen calculated from the calibration plot in Figure S42.

Complex	*GC peak area (μV/s*	V_{H2}*(μl)*	V_{H2}*(μl)net*[a]	*Q(C)*	$Q(C)_{net}$
1^{2+}	338.3660	74.20	39	-1.952	0.936
2^{2+}	662.48163	145.28	110.08	-3.489	2.473
Blank	160.52	35.20	-	-1.016	-

[a]Volume of H_2 gas after subtraction of blank. [b]Charge after subtraction of blank.

Chapter 4.

Using the perfect gases equation, we can obtain the number of moles of hydrogen gas produced by the

electrode and measured in the headspace.

$$PV = nRT \qquad \textbf{(eq. 3)}$$

Where P is the pressure of the headspace (1atm), R is the gas constant ($0.082\frac{atm \cdot L}{K \cdot mol}$), and T the temperature (298,15K)

To calculate the theoretical number of moles from the electrical charge transferred to the electrode, where n = 2:

$$2H^+ + 2e^- \rightarrow H_2$$

$$n_{H2\ theoretical} = \frac{C}{F \cdot n} \qquad \textbf{(eq. 4)}$$

Table S2- Hydrogen evolution data for complex $\mathbf{1}^{2+}$, $\mathbf{2}^{2+}$ and blank (see Figures 9b and 10b in the manuscript).

Complex	$n_{(H2)\ detected}$	$n_{(H2),net}$[a]	n_{Cat}	*TON*	$n_{(H2)theoretical}$	$n_{(H2)theoretical,net}$[a]	*FE (%)*
$\mathbf{1}^{2+}$	3.03×10^{-6}	1.59×10^{-6}	2.5×10^{-6}	0.64	1.01×10^{-5}	4.85×10^{-6}	33
$\mathbf{2}^{2+}$	5.94×10^{-6}	4.5×10^{-6}	2.5×10^{-6}	1.80	1.808×10^{-5}	1.28×10^{-5}	35
Blank	1.44×10^{-6}	-	-	-	5.26×10^{-6}	-	27

[a]Mols of hydrogen after subtraction of blank.

Chapter 5

β-diimino and β-diketiminato iron complexes and their interaction with CO_2

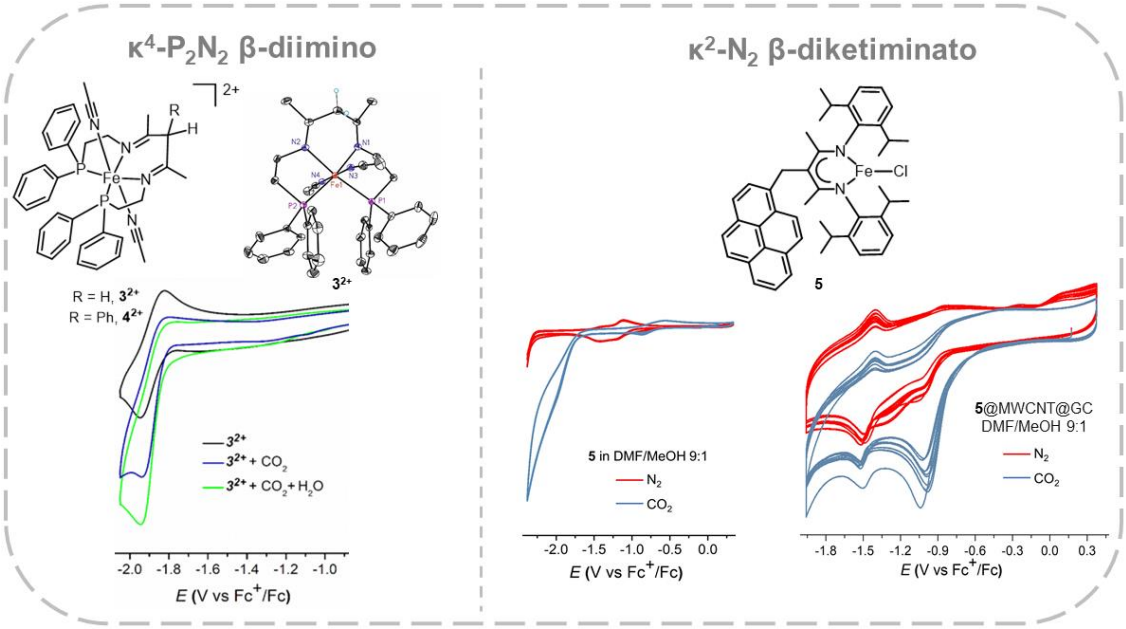

Chapter 5.

1- Introduction

As discussed in Chapters 3 and 4, β-diimino and β-diketiminato ligands are interesting non-innocent ligand backbones with a broad range of applications including the activation of small molecules such as protons, carbon dioxide and nitrogen.[1–3] In particular, iron β-diketiminate complexes have largely been studied by the Holland group reporting a variety of compounds related to these processes (**Figure 1**). The iron hydrido complexes $\mathbf{Fe^{II}\text{-}H_2\text{-}Fe^{II}}$ and $\mathbf{Fe^{II}\text{-}H}$ are the result of the reaction of the parent mononuclear Fe-Cl analogue with an equivalent of $KBEt_3H$ while the N-N bridged complexes $\mathbf{Fe^{I}\text{-}N_2\text{-}Fe^{I}}$ are formed after reaction of the corresponding mononuclear Fe-Cl complex with N_2 in the presence of a reducing agent.[4,5] The iron dicarbonyl complex $\mathbf{Fe^{I}\text{-}(CO)_2}$ and the iron carbonate bridged complexes $\mathbf{Fe^{II}\text{-}CO_3\text{-}Fe^{II}}$ form when $\mathbf{Fe^{I}\text{-}N_2\text{-}Fe^{I}}$ reacts with CO_2.[6] The solid-state structure of $\mathbf{Fe^{II}\text{-}CO_3\text{-}Fe^{II}}$ has two different molecules in the unit cell, one in which the bridging carbonate is coordinated in a μ-η^2:η^2 mode and the other in a μ-η^2:η^1 mode, both depicted in the bottom right of **Figure 1**. The formation of $\mathbf{Fe^{I}\text{-}(CO)_2}$ and $\mathbf{Fe^{II}\text{-}CO_3\text{-}Fe^{II}}$ from $\mathbf{Fe^{I}\text{-}N_2\text{-}Fe^{I}}$ is a clear proof of the capacity of the latter to activate the inert CO_2 molecule, a highly pursued but difficult task.

Although the isolation and characterization of the derivatives shown in **Figure 1** are great advances towards the understanding of processes such as proton, nitrogen or carbon dioxide reductions by iron complexes, they have been prepared from highly air-sensitive compounds with the use of strong reducing agents. No examples based on electrochemical reduction are found in the literature neither in the homogeneous phase nor in the heterogeneous phase, lacking for a great deal of important information. In addition, all these activations and transformations of small molecules (*i.e.* N_2 or CO_2) are stoichiometric reactions with little or no application. Thus, finding new compounds based on β-diketiminato ligands that are catalytic towards proton, nitrogen or carbon dioxide reduction is still a challenge.

Chapter 5.

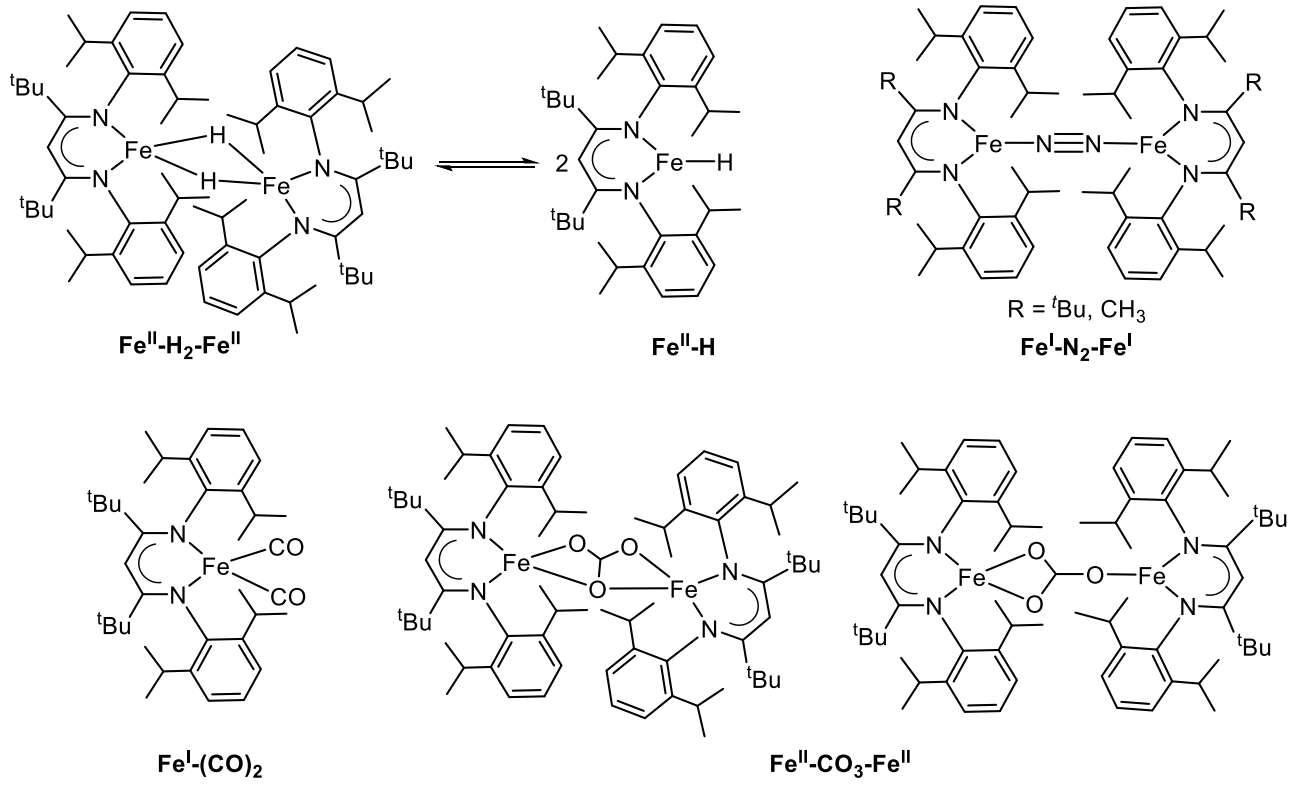

Figure 1. Iron β-diketiminato complexes relevant for the activation of small molecules such as H^+, N_2 or CO_2. [5,6]

In this chapter, ligands **L2**, **L9** (HBDI) and **L10** (PhBDI) prepared in Chapter 3 are used to synthesize β-diimino and β-diketiminato iron complexes. Their interaction with small molecules with emphasis on carbon dioxide is also presented.

2- Results and discussions

2.1- Synthesis and spectroscopic characterisation of complexes 3^{2+} and 4^{2+}

Following the work on nickel complexes of Chapter 4, ligands HBDI (**L9**) and PhBDI (**L10**) were used to prepare iron analogues using iron(II) triflate precursor in acetonitrile solution as indicated in **Scheme 1**. Complex $\mathbf{3}^{2+}$ containing a H in the α-C diamine position was isolated as brown crystals in a 80 % yield. On the other hand, derivative $\mathbf{4}^{2+}$ containing a Ph group was obtained as a brown powder in a lower 23 % yield most likely due to the higher solubility of this complex in the crystallization mixture. Single crystals of $\mathbf{3}^{2+}$ suitable for x-ray diffraction (XRD) analysis were grown by layering Et_2O on top of a saturated solution of the complex in acetonitrile at -30°C. **Figure 2** shows the ORTEP plot of $\mathbf{3}^{2+}$ revealing a symmetrical distorted octahedral geometry with the κ^4-P_2N_2 HDBI ligand occupying the equatorial positions and two

Chapter 5.

acetonitrile ligands occupying the axial positions. The sp^3-hybridized methylene carbon of the α-diimino BDI moiety lies above the equatorial plane as depicted in **Figure S1** in the SI. The two imine C=N bond lengths range from 1.282(1) Å to 1.283(2) Å, and C-N bonds linking the phosphine arms are in the range of 1.476(3) Å-1.478(4) Å. All these features are fully consistent with localized C=N bonds for a β-diimine ligand analogous to those observed for the nickel complexes $\mathbf{1}^{2+}$ and $\mathbf{2}^{2+}$ in Chapter 4. The Fe-N distances are 2.020(2) Å and 2.017(3) Å.

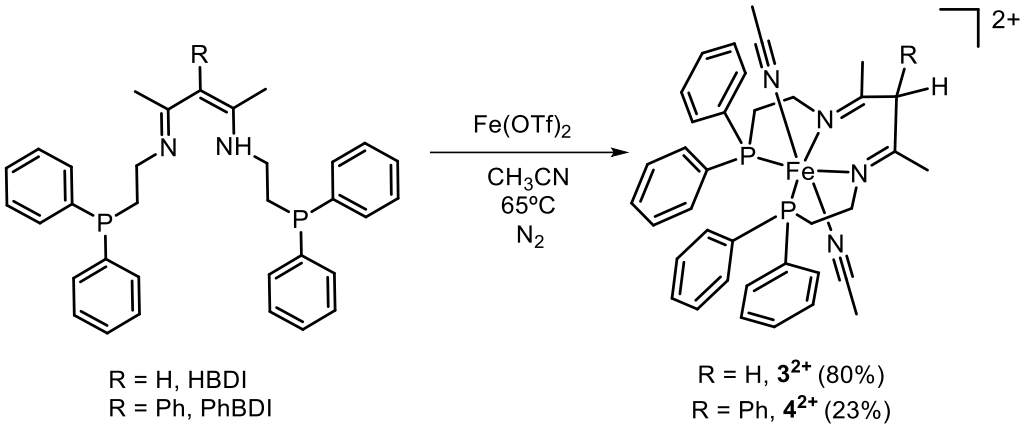

Scheme 1. Synthesis of complexes $\mathbf{3}^{2+}$ and $\mathbf{4}^{2+}$.

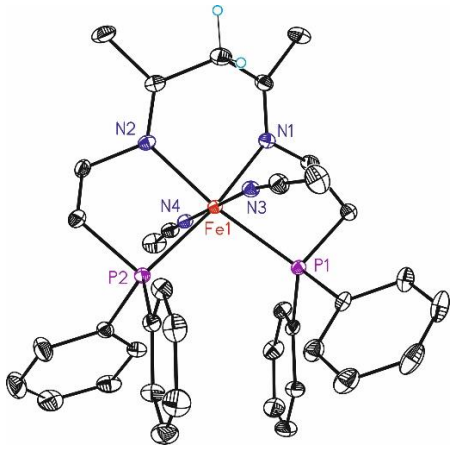

Figure 2. ORTEP representation of $\mathbf{3}^{2+}$ at 50% probability level (counterions and hydrogens are omitted for clarity except for α-carbon hydrogens). **Color code**: **C**, Dark gray; **N**, Blue; **Fe**, red; **P**, purple.

Complexes $\mathbf{3}^{2+}$ and $\mathbf{4}^{2+}$ are Fe(II) d^6 low spin diamagnetic compounds. They were characterized by ^{1}H and ^{31}P NMR in deuterated acetonitrile solution (**Figure 3** and **Figures S2-S7** in the SI). Both complexes show a symmetric structure in solution, as evidenced by a single set of resonance for each methylene group as well as the appearance of a unique

Chapter 5.

resonance in the ^{31}P NMR spectra with chemical shifts of 60.8 and 57.0 for $\mathbf{3}^{2+}$ and $\mathbf{4}^{2+}$ respectively. The characteristic protons in the α diamine position appear at 4.02 ppm integrating 2H for $\mathbf{3}^{2+}$ and at 5.37 ppm integrating 1H for $\mathbf{4}^{2+}$. This significant shift is due to the electronic effect of the phenyl ring directly attached to the same α-C diamine becoming a benzylic position and was also observed for the related nickel complexes $\mathbf{1}^{2+}$ and $\mathbf{2}^{2+}$ in Chapter 4 (4.29 ppm and 5.50 ppm, respectively). This electronic effect is also manifested in the methyl of the BDI group, appearing at 2.5 ppm and 2.27 ppm for $\mathbf{3}^{2+}$ and $\mathbf{4}^{2+}$ respectively and accounting for a 0.23 ppm shift. Importantly, this results together with the XRD structure of $\mathbf{3}^{2+}$ confirm that both complexes are isolated in the β-diimino BDI form of the ligand as opposed to the β-diketiminato BKI form, which is expected considering the lack of a base in the reaction conditions.

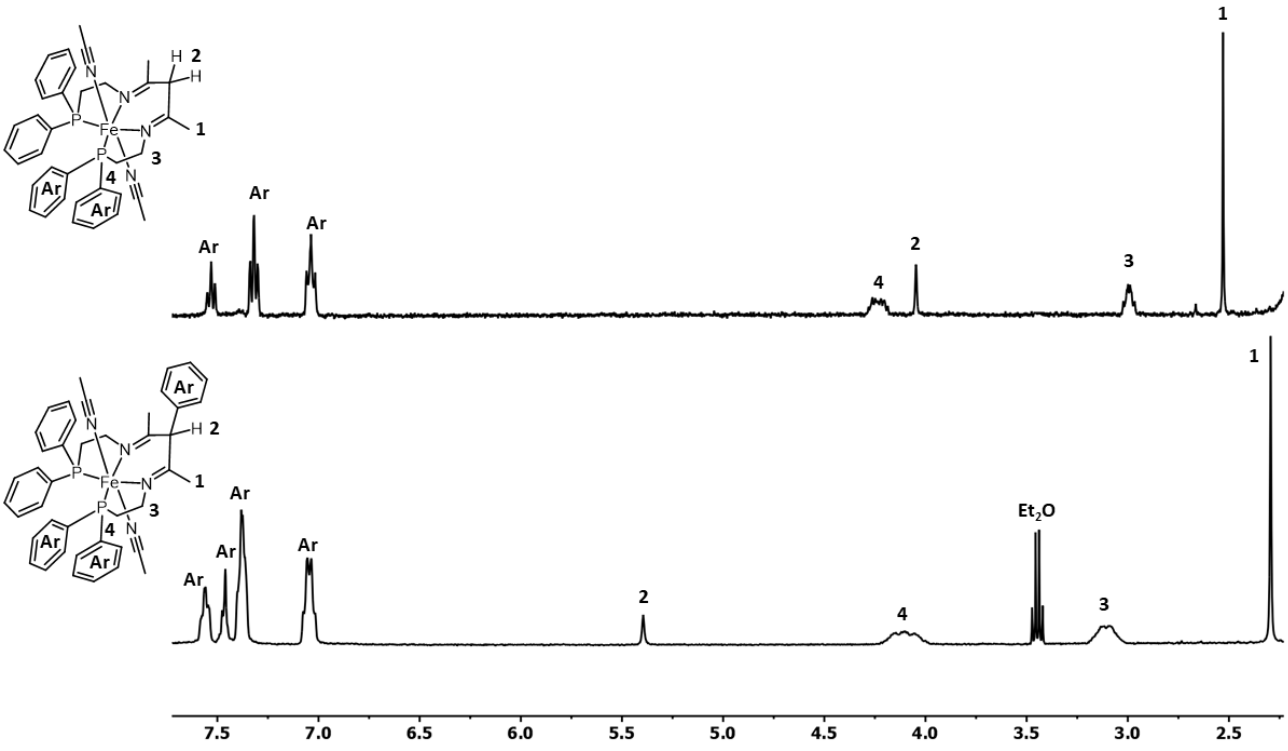

Figure 3. ^{1}H NMR spectra of $\mathbf{3}^{2+}$ (top) and $\mathbf{4}^{2+}$ (bottom) (400 MHz, CD_3CN).

Chapter 5.

2.2- Electrochemical characterisation of 3^{2+} and 4^{2+} in the absence and in the presence of CO_2

The redox properties of complexes $\mathbf{3}^{2+}$ and $\mathbf{4}^{2+}$ were investigated by cyclic voltammetry (CV) in anhydrous acetonitrile containing 0.1M [(*n*-Bu)$_4$ N](PF$_6$) (TBAPF$_6$) as supporting electrolyte in a three electrode one-compartment cell consisting of a glassy carbon working electrode, Pt as counter electrode and Ag/AgNO$_3$ solution in acetonitrile (0.01 M Ag/AgNO$_3$, 0.1 M TBAPF$_6$) as reference electrode, under nitrogen atmosphere. Ferrocene was used as the internal reference, which was added at the end of each experiment.

Cyclic voltammetry of complex $\mathbf{3}^{2+}$ shows a quasi-reversible redox event at $E_{1/2}$ = -1.88V vs $Fc^{+/0}$ (ΔE = 100 mV) which represents cathodic shifts of 710 mV and 120 mV as compared to the first and second redox couples observed for its analogous Ni complex $\mathbf{1}^{2+}$ in Chapter 4, respectively (**Figure 4a** and **Table 1**). On the other hand, complex $\mathbf{4}^{2+}$ shows an irreversible peak at E_c = -1.85 V vs $Fc^{+/0}$ irrespective of the scan rate (**Figure 4b**). This behaviour sharply contrasts with its homolog Ni complex $\mathbf{2}^{2+}$ in Chapter 4, which shows two reversible events at $E_{1/2}$ = -1.11 V and $E_{1/2}$ = -1.78 V (Table 1). Thus, the redox events observed for $\mathbf{3}^{2+}$ and $\mathbf{4}^{2+}$ in **Figure 4** are tentatively assigned to the formal Fe $^{II/I}$ redox couple, presumably involving a significant change in geometry which is not favored by the phenyl ligand PhBDI in $\mathbf{4}^{2+}$ leading to an irreversible process.

Chapter 5.

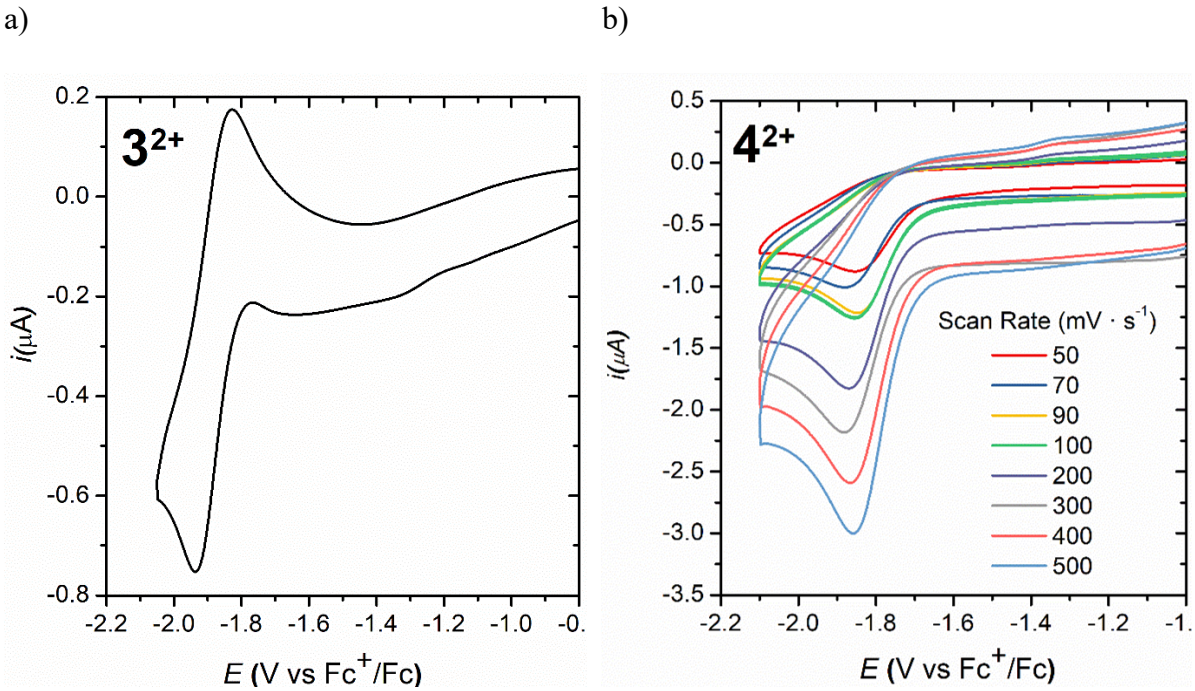

Figure 4. Cyclic voltammetry experiments of a 0.5 mM solution of $\mathbf{3}^{2+}$ (υ = 100 mV/s) (a) and $\mathbf{4}^{2+}$ (b) in acetonitrile.

Table 1*: Comparison of redox potentials of Ni (Chapter 4) and Fe (Chapter 5) complexes* $\mathbf{1}^{2+}$-$\mathbf{4}^{2+}$ *in* CH_3CN*. All potentials are reported in V versus* $Fc^{+/0}$.

Ligand	Metal Center	Complex	$E^1_{1/2}$	ΔE^1(mV)	$E^2_{1/2}$	ΔE^2(mV)
HBDI	Ni	$\mathbf{1}^{2+}$	-1.17	60	-1.76	66
	Fe	$\mathbf{3}^{2+}$	-	-	-1.88	100
PhBDI	Ni	$\mathbf{2}^{2+}$	-1.11	60[a]	-1.78	90
	Fe	$\mathbf{4}^{2+}$	-	-	-1.85[b]	irr

[a]Peak separation potential at high Scan rates (υ = 0.3 V/s).[b] irreversible reduction peak (E_c at υ = 0.1 V/s).

In the presence of carbon dioxide, the reduction wave of $\mathbf{3}^{2+}$ becomes irreversible and significantly increases in intensity indicating that the reduced complex $\mathbf{3}^{+}$ interacts with CO_2 (**Figure 5a**). Addition of water to the CO_2 saturated solution of $\mathbf{3}^{2+}$ induces a further increase

Chapter 5.

in intensity of the reduction wave (compare blue and green traces) suggesting a different kind of reactivity under these conditions.

In the case of the phenyl derivative $\mathbf{4}^{2+}$ (**Figure 5b**), addition of CO_2 to the solution of the complex slightly changes the shape of the irreversible redox wave but does not significantly increase its intensity (compare blue and red traces). In contrast, addition of water to the CO_2 saturated solution of $\mathbf{4}^{2+}$ induces a shift on the onset potential and a significant increase in intensity (compare green and blue traces).

A bulk electrolysis experiment of a solution of $\mathbf{3}^{2+}$ in a CO_2 saturated solution containing 4% v/v of water at an applied potential of E_{app} = -2 V vs Fc^+/Fc was performed in order to assess if the complex was active in the carbon dioxide reduction reaction. After two hours, the headspace of the cathodic compartment of the electrochemical cell was analyzed by gas chromatography coupled to a thermal conductivity detector (GC-TCD) but no reduction product such as carbon monoxide or hydrogen gases could be detected. These preliminary results suggest that $\mathbf{3}^{2+}$ is not active in the reduction of carbon dioxide, instead the increase in intensity of the redox wave observed in **Figure 5a** is attributed to decomposition pathways that are consequence of the reaction of reduced compound $\mathbf{3}^{+}$ with CO_2.

Chapter 5.

a) b)

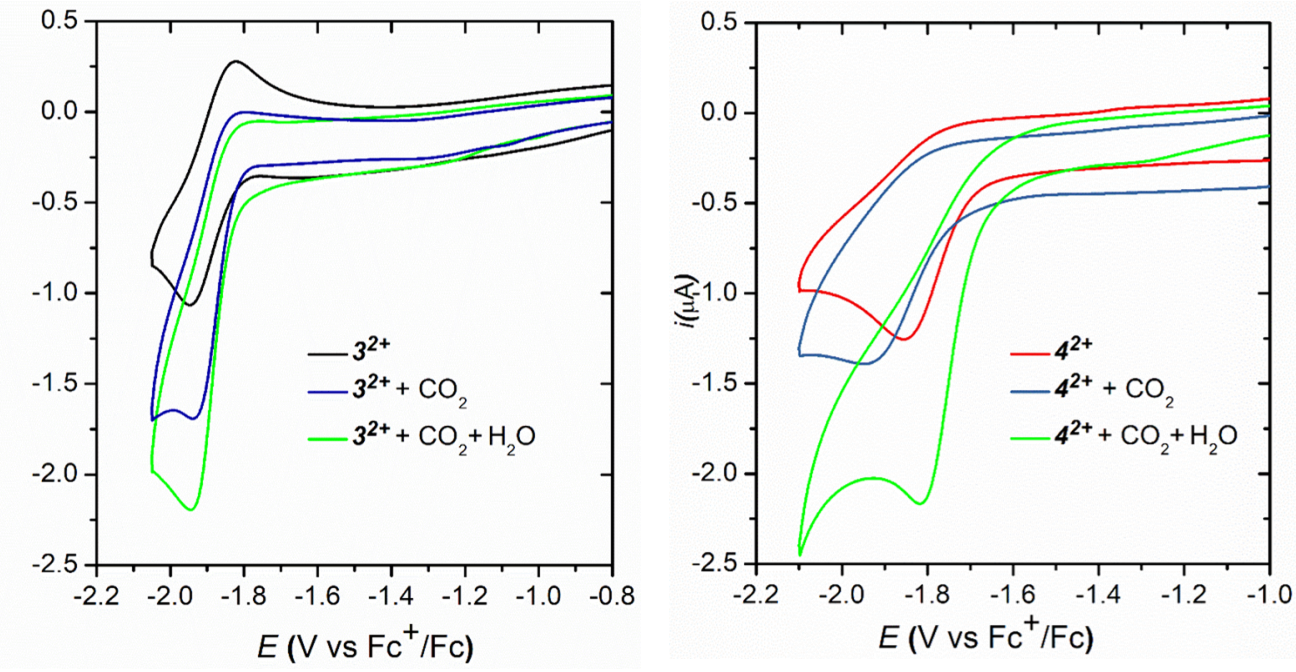

Figure 5. Cyclic voltammetry of a 0.5 mM solution of $\mathbf{3}^{2+}$ (a) and $\mathbf{4}^{2+}$ (b) in a saturated acetonitrile solution with carbon dioxide in the absence (blue) and in the presence carbon dioxide and 4 % v/v of water (green) (υ = 100 mV/s).

2.3- Synthesis and spectroscopic characterisation of complex 5

The β-diketiminato complex **5** in **Scheme 2** containing a dangling pyrene group in the α-carbon intradiimine position was prepared via two steps one-pot procedure.[7] First, the mixture of tautomers of **L2** (see Chapter 3) were treated with 1 equivalent of *n*-BuLi to get a putative intermediate lithiated compound. To the resulting yellow/orange solution, $FeCl_2(THF)_{1.5}$ was added producing a sudden change of colour to bright red. After stirring the solution for 24 h at 60ºC, the solvent was partially evaporated, and hexane added to produce a red precipitate, which is highly air and moisture sensitive. Full characterization of the resulting iron complex was hindered by its paramagnetic nature as well as its low solubility in most organic solvents. Thus, single crystals suitable for XRD analysis could not be obtained and its structure could not be unequivocally ascertained. However, based on previous literature,[8] we propose a neutral three coordinated Fe(II) complex with the BDK ligand coordinating in a bidentate fashion and a chlorido ligand completing the coordination sphere of the metal center (**Scheme 5** and **Figure 6**) although we do not rule out the possibility of having a charged complex with a solvent

Chapter 5.

molecule (THF) coordinated and a chloride counter-anion. Such a low coordination number is favoured by the bulky substituents of the BDK backbone and it has been previously observed not only for Fe but also for Co and Ni related complexes (**Figure 6**).[9] In particular, the *tert*-butyl substituents of the BDK of the reported complexes in **Figure 5** play a key role in forcing the 2,6-diisopropylphenyl group to get closer to the metal center limiting the space available for the coordination of more ligands. This is evident from the C-N-C of the BDK ligand which are much higher when a *tert*-butyl is present as opposed to methyl substituted analogues (see Fe complex in **Figure 6**, angle indicated in red measures 128.4(2)°) while the same angles of methyl substituted analogues measure 118.6–120.3°).[8] Compound **5** reported here do not hold the *tert*-butyl groups but the pyrene bulky substituent in the α-diimine position is believed to exert a similar repulsion effect, since it can fold and get close to the Fe center in the apical position.

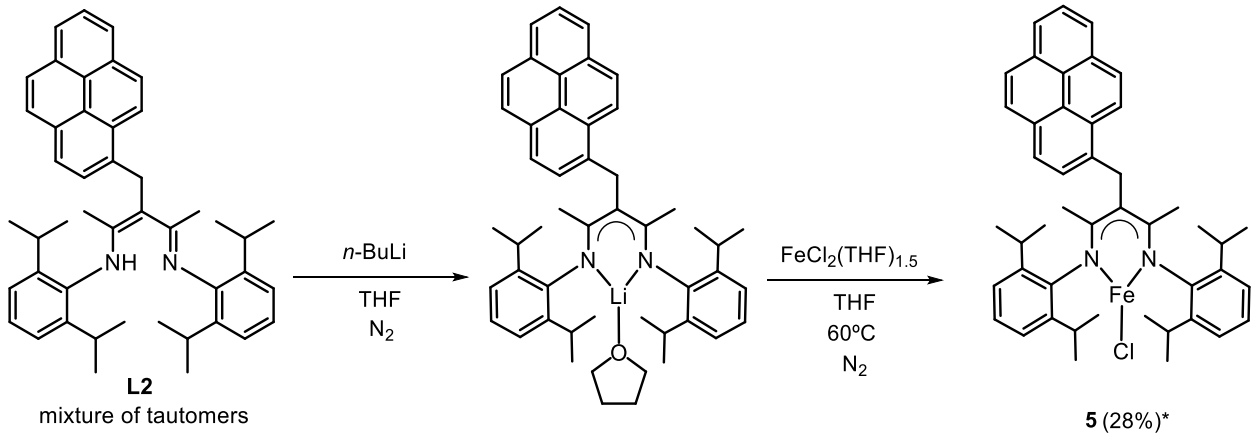

Scheme 2. Synthesis of complex **5**. *Indicates approximate yield since structure has not conclusively been determined.

Chapter 5.

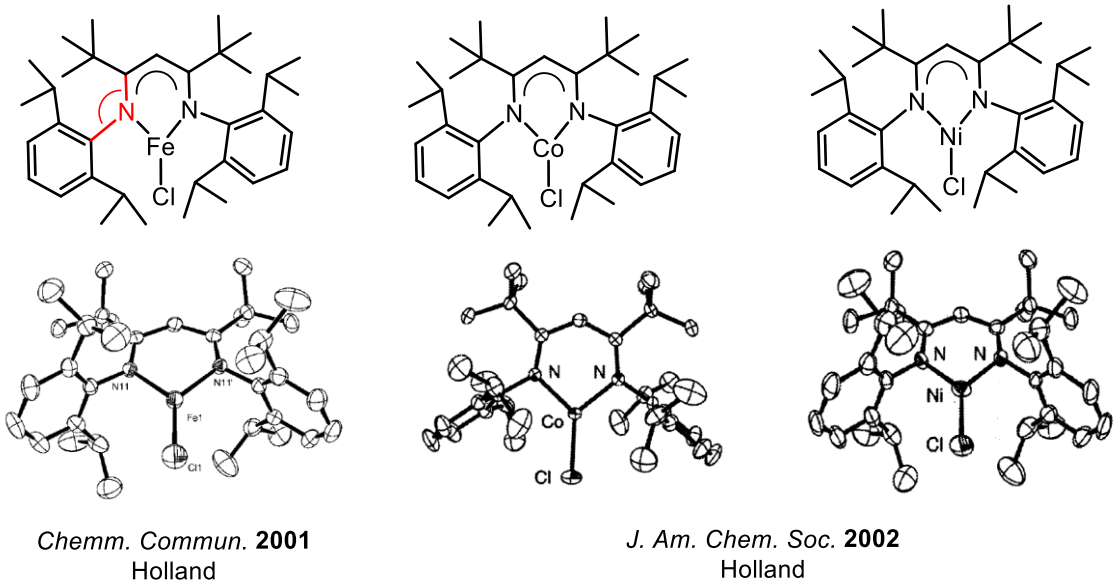

Chemm. Commun. **2001**
Holland

J. Am. Chem. Soc. **2002**
Holland

Figure 6. Three coordinated BDK chlorido complexes reported in the literature. XRD structures are taken from the cited references to show the coordination sphere around the metal centers.[8,9]

2.4- Electrochemical characterization of 5 under homogeneous conditions in the absence and in the presence of CO_2

Cyclic voltammetry of complex **5** in anhydrous DMF containing 0.1M [(*n*-Bu)$_4$ N](PF$_6$) (TBAPF$_6$) as supporting electrolyte under nitrogen atmosphere shows two very close quasi-reversible redox processes at $E_{1/2}$ = -1.18 V vs $Fc^{+/0}$ and $E_{1/2}$ = -1.42 V vs $Fc^{+/0}$, which are tentatively assigned to two consecutive one-electron reduction processes to produce a formal Fe(0) species (**Figure 7**). However, it is known that three coordinated BDK-chlorido Fe complexes can easily be converted to dimeric species upon reduction, where the two iron centers are bridged by a N-N ligand (**Figure 8**),[4] thus we do not rule out that such process takes place in the cyclic voltammetry time scale.

Chapter 5.

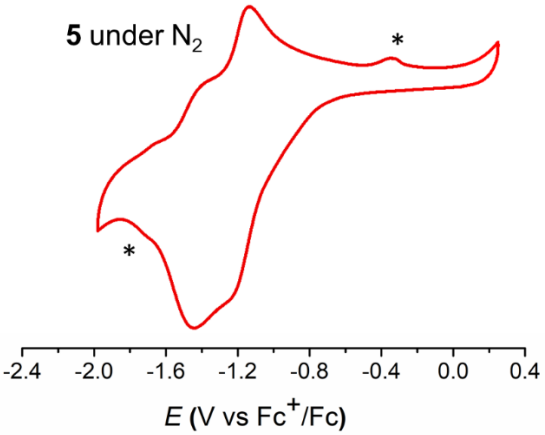

Figure 7. Cyclic voltammetry of a solution of **5** in DMF under nitrogen atmosphere.*Indicates additional peaks that have not been assigned (υ = 100 mV/s).

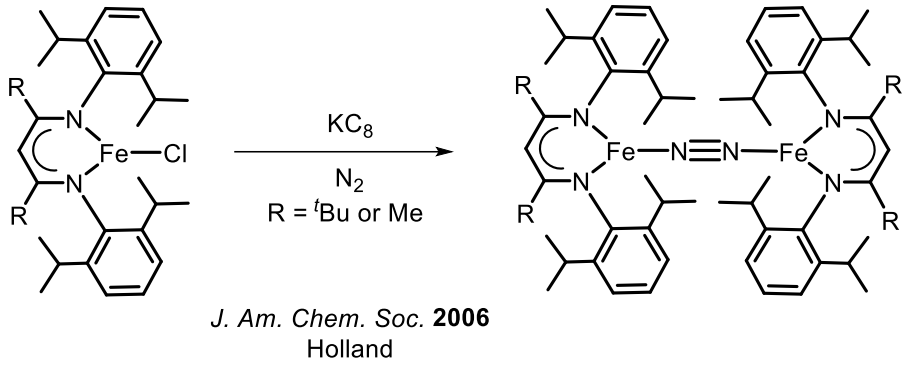

Figure 8. Formation of dimeric species after reduction of BDK chlorido Fe complexes.[4]

In sharp contrast, when the cyclic voltammetry experiment of a solution of **5** is done under a saturated CO_2 atmosphere, a completely different redox profile is observed (**Figure 9**). A single quasi-reversible reduction wave is observed at $E_{1/2}$ = -0.88 V vs $Fc^{+/0}$ which accounts for a 300 mV anodic shift as compared to the first redox event observed when the experiment was done under N_2 atmosphere (**Figure 7**) indicating that **5** reacts with CO_2, generating a new species (**5-CO2**, **Scheme 4**, top). The anodic shift observed in the CV experiment is consistent with the substitution of a negatively charged ligand (chlorido) for a putative neutral ligand (derived from carbon dioxide), although the formation of dimeric species are not ruled out and more

Chapter 5.

experiments devoted to the characterization of the initial and final species should be carried out. Surprisingly, the UV-Vis spectra of **5** under N_2 and CO_2 are virtually the same, showing four clear absorption bands below 400 nm (λ_{max} = 315 nm, 327 nm, 348 nm) and a broad shoulder expanding from 400 nm to 650 nm (Figure S8 in the SI).

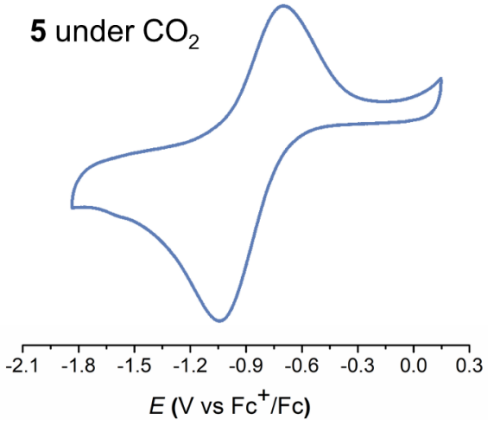

Figure 9: Cyclic voltammetry of a solution of **5** in DMF saturated with CO_2.

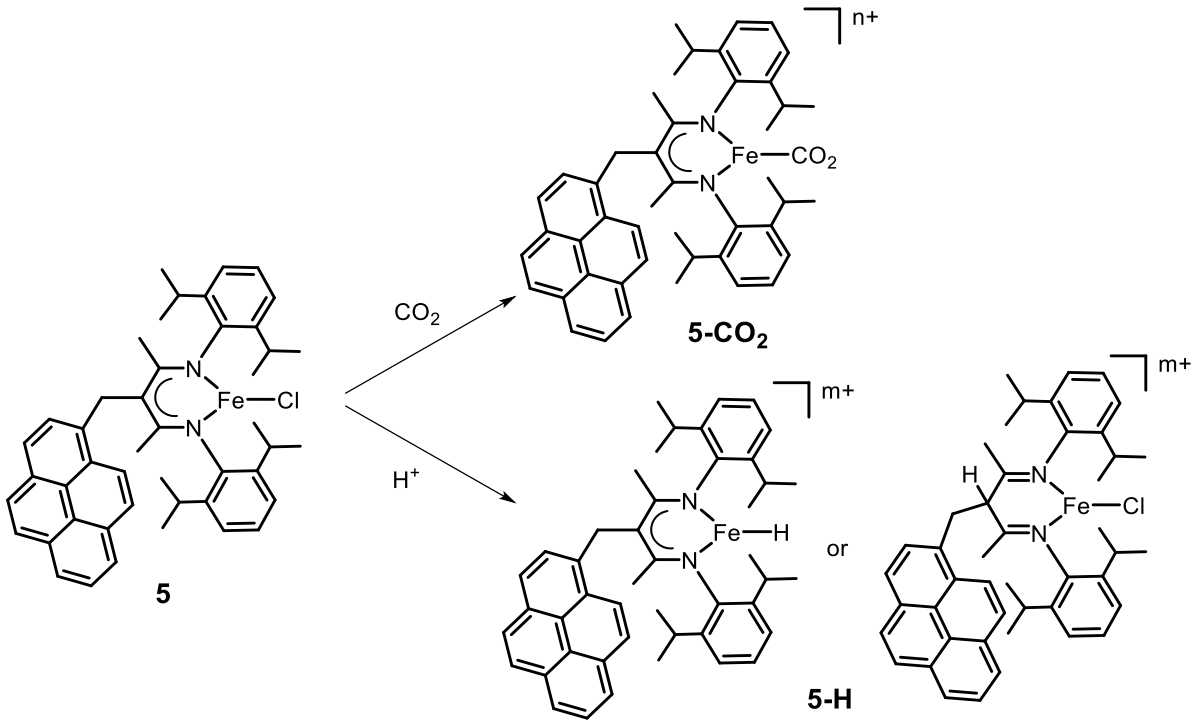

Scheme 3. Reaction of **5** with CO_2 and H^+, leading to putative complexes **5-CO₂** and **5-H**.

Chapter 5.

When a proton source is added to the DMF solution of **5** saturated with CO_2 a progressive anodic shift of the redox wave is observed from $E_{1/2}$ = -0.88 V vs $Fc^{+/0}$ at 0% of MeOH to $E_{1/2}$ = -0.65 V vs $Fc^{+/0}$ at 10% of MeOH or higher concentrations. Additionally, a significant gradual increase in intensity is observed at E_{onset} = -1.58 V vs $Fc^{+/0}$ suggesting a catalytic process in which MeOH is involved (**Figure 10**). A comparison of broad range CVs in DMF/MeOH in the absence and in the presence of CO_2, indicate that only **5-CO₂** is responsible for the increased current below -1.58 V (**Figure 11**).

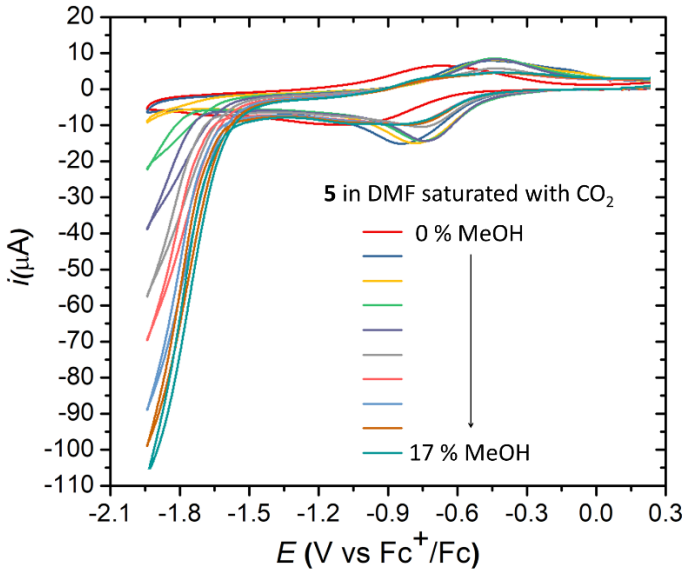

Figure 10: Cyclic voltammetry of a *ca.* 1 mM solution of **5** in DMF saturated with CO_2 after successive additions of MeOH (in % v/v MeOH = 0, 2, 4, 6, 9, 10, 12, 13, 15, 17) (υ = 100 mV/s).

In order to investigate the origin of the catalytic current, a bulk electrolysis experiment of a *ca.* 0.5 mM solution of **5** was carried out at an applied potential E_{app} = -1.9 V vs $Fc^{+/0}$ for four hours. During this time bubbles were formed at the surface of the working electrode while a fairly stable current of *ca. i* = -1.2 mA was measured (**Figure S9**). A sample of the headspace of the cathodic compartment was injected to a GC-TCD and a large amount of H_2 was detected (**Figure S10**). This first preliminary analysis revealed the absence of CO in the headspace. However, further experiments are required to fully rule out the presence of other gaseous products and products from the liquid phase. Importantly, a CV was performed after the

Chapter 5.

electrolysis, and it showed the presence of the complex (**Figure S9**).

The results discussed above are clear evidence of the capacity of **5-CO₂** to reduce protons to give hydrogen gas. The ability of **5** to perform such transformation was also assessed in the absence of CO_2 but using a stronger acid than MeOH. With this purpose, 2,6-lutidinium triflate, LutH(OTf), was added to a solution of **5**. The cyclic voltammetry experiment under nitrogen atmosphere reveals an anodic shift of the first reduction event from $E_{1/2}$ = -1.18 V vs $Fc^{+/0}$ (see **Figure 7**) to $E_{1/2}$ = -0.20 V vs $Fc^{+/0}$ (blue trace in **Figure 12**). A UV-Vis spectrum of **5** in the presence of LutH(OTf) was also carried out showing an increased in intensity of the characteristic bands of **5** below λ = 375 nm, together with the appearance of a significant shoulder in the range of λ = 375-400 nm (**Figure S8**). In addition, a loss in intensity of the broad absorption at λ = 400-650 nm characteristic of **5** is also observed. These results indicate that **5** reacts with protons to give a new compound that is tentatively assigned to the hydride or β-diimino species **5-H** in **Scheme 3** but hydrido-bridged dimeric species are also plausible candidates. Thus, further experiments are necessary to prove the real structure of the derivative compound formed after reaction of **5** with protons. Besides the reduction wave at $E_{1/2}$ = -0.22 V vs $Fc^{+/0}$, the CV of **5** in the presence of $LutH^+$ shows an intense peak at E_{onset} = -1.58 V vs $Fc^{+/0}$ most likely due to the reduction of protons to give hydrogen. However, a blank experiment in the absence of complex, gave a similar electrochemical profile and thus, this process was not further studied.

Finally, an analogous experiment done under argon atmosphere was carried out in order to assess the possibility of performing the electrochemical nitrogen reduction reaction, a process that has been widely studied by the Holland group with related Fe BDK complexes (**Figure 1**).[1] As shown in **Figure 12**, no significant difference of the CVs is observed between the experiment done under nitrogen (blue trace) or under argon (red trace), ruling out this possibility.

Chapter 5.

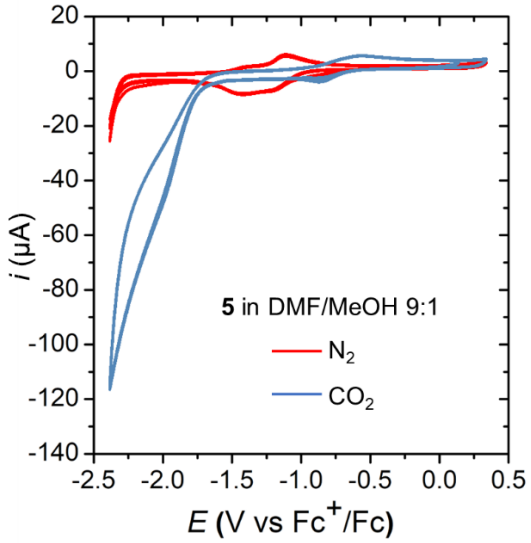

Figure 11: Cyclic voltammetry of a *ca.* 0.5 mM solution of **5** in DMF/MeOH 9:1under N_2 gas (red) or CO_2 (blue) (υ = 100 mV/s).

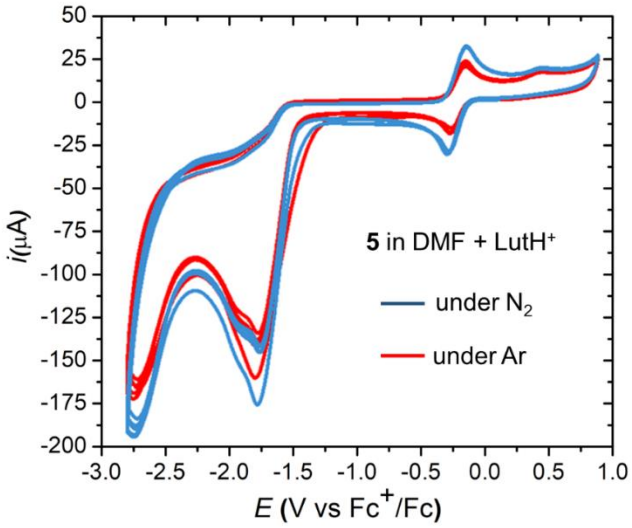

Figure 12. Cyclic voltammetry of **5** in DMF containing *ca.* 10 equiv. of [LutH]OTf under N_2 (blue) and under Are (red) (υ = 100 mV/s).

2.5- Electrochemical characterization of 5 under heterogeneous conditions

The presence of the pyrene group in **5** allows to anchor the complex onto 2D π-extended materials, a strategy that has been successful for several molecular complexes in the field of artificial photosynthesis including water oxidation, proton reduction and carbon dioxide

Chapter 5.

reduction catalysts.[10-12]

In order to prepare an electrode modified with **5**, multiwalled carbon nanotubes (MWCNT) were suspended in a solution of the complex in DMF under inert atmosphere (**Figure 13**). After sonication, the mixture was stirred overnight. The modified material, namely **5**@MWCNT, was filtered and washed with DMF to remove unreacted complex. UV-Vis spectra of the solution of **5** before and after deposition show that *ca.* 65% of the complex has been successfully attached to the MWCNT (**Figure 13**, right). The hybrid material **5**@MWCNT was resuspended in DMF and drop-casted onto a glassy carbon disk to produce the **5**@MWCNT@GC, that was used as working electrode in cyclic voltammetry experiments.

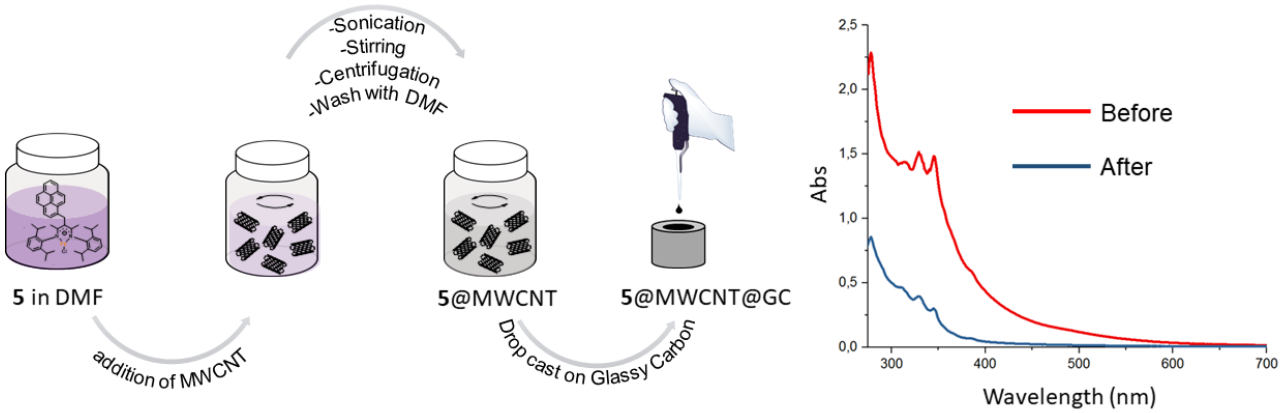

Figure 13. Left) Schematic representation of the preparation of **5**@MWCNT@GC electrode. Right) UV-Vis spectra of a solution of 5 before (red) and after (blue) deposition on MWCNT.

Figure 14 shows the cyclic voltammetry experiments measured using **5**@MWCNT@GC as working electrode in DMF/CH_3OH (9:1). When the experiment is done under nitrogen atmosphere (red trace), and after performing several cycles, two redox processes are clearly identified at E_c = -1.0 V vs $Fc^{+/0}$ and $E_{1/2}$ = -1.48 V vs $Fc^{+/0}$, which are slightly anodically shifted compared to those observed under homogeneous conditions at $E_{1/2}$ = -1.18 V vs $Fc^{+/0}$ and $E_{1/2}$ = -1.42 V vs $Fc^{+/0}$ (**Figure 7**). In addition, the first reduction is irreversible for the heterogeneous complex while it is quasi-reversible for the homogeneous analog. After 20 cycles, carbon dioxide was bubbled to saturate the solution and 20 additional CV cycles were run (**Figure 14**, blue trace). A significant increase in the current is observed at E_{onset} = -0.6 V vs $Fc^{+/0}$ with a E_p = -1.0 V vs $Fc^{+/0}$, matching that of the first reduction observed under nitrogen

while the second wave remains reversible. These results are consistent with (i) the conversion of the initial chlorido complex **Fe-Cl** to the **Fe-CO2** substituted product as suggested in **Scheme 3** for the homogeneous complex or (ii) a catalytic current induced by the **Fe-CO2** complex in the presence of a proton source consistent with the results shown in **Figure 11** but with a E_{onset} anodically shifted by 980 mV (E_{onset} = -1.58 V vs $Fc^{+/0}$ for the homogeneous complex). Further analyses are necessary to conclusively assign the redox process observed in the CV of **5**@MWCNT@GC in the absence and in the presence of CO_2.

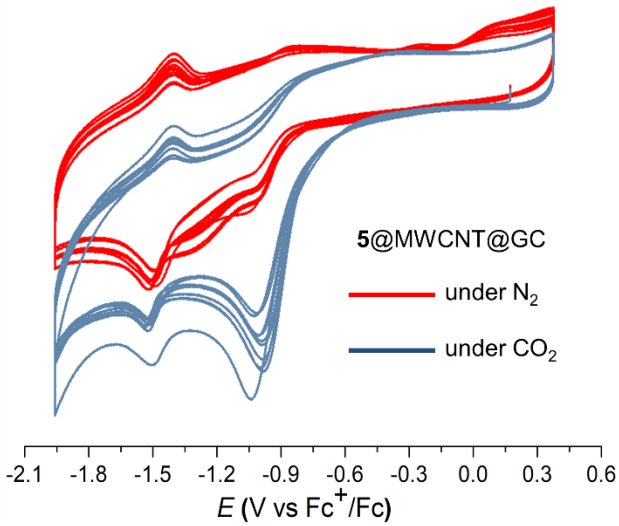

Figure 14. Consecutive cyclic voltammetry scans using **5**@MWCNT@GC as working electrode in DMF/CH_3OH (9:1) under N_2 (red, 1 to 20 cycles) and CO_2 (blue, 21 to 40 cycles).

3- Conclusion

Three iron complexes containing β-diimino (**3**$^{2+}$ and **4**$^{2+}$) and β-diketiminato (**5**) ligands have been prepared. Compounds **3**$^{2+}$ and **4**$^{2+}$ are Fe(II) low spin diamagnetic compounds that have been characterized by NMR spectroscopy. Compound **3**$^{2+}$ has also been characterized by XRD, confirming an octahedral geometry with two acetonitrile ligands in trans disposition. The diamagnetic nature of these complexes is not trivial and is presumably favoured by the four nitrogen donors of the imino and acetonitrilo ligands. Preliminary electrochemical experiments with **3**$^{2+}$ and **4**$^{2+}$ show that they are not stable under electrochemical carbon dioxide reduction conditions. However, their β-diketiminato derivatives could be easily

Chapter 5.

prepared by deprotonation (see Chapter 4), offering new possibilities in the CO_2 and proton reduction reactions.

On the other hand, complex **5**, bearing a dangling pyrene group in the α-diimino position has been prepared and characterized by UV-Vis and electrochemical techniques. It is a very air-sensitive paramagnetic compound, whose structure has not conclusively been confirmed. However, based on related literature, a mononuclear three coordinated Fe-chlorido complex holding a β-diketiminato ligand is proposed (**Fe-Cl**). Complex **Fe-Cl** reacts with carbon dioxide to give a new complex **Fe-CO₂** as demonstrated by cyclic voltammetry. Similarly, when **Fe-Cl** is treated with a strong acid source, it evolves to a different compound, presumably a mononuclear iron-hydrido compound or β-diimino derivative, labelled as **Fe-H**, although dimeric structures are not ruled out. In addition, **5** shows a high catalytic current in the presence of both CO_2 and a proton source (MeOH) suggesting a putative CO_2 reduction process. However, preliminary studies have only proven the generation of H_2 gas. Regardless of the nature of the catalytic current (H^+ and/or CO_2 reduction), this is the first example of a fully electrochemically characterized iron β-diketiminato complex that is electrocatalytically active. Finally, compound **5** has been grafted to multiwalled carbon nanotubes (MWCNT) to afford the hybrid **5**@MWCNT. Electrochemical analysis of the material is consistent with the presence of the complex. If confirmed, **5**@MWCNT would be the first example of iron β-diketiminato complex attached to electrodes with promising results in the carbon dioxide electroreduction.

All complexes described in this chapter $\mathbf{3}^{2+}$, $\mathbf{4}^{2+}$ and **5** have shown affinity towards CO_2, however, further characterization is required to not only detect the reaction/catalysis products but also to fully characterize intermediate species involved in the interaction/catalytic process.

Chapter 5.

4- Experimental Section

4.1- Synthesis of complex 3(OTf)$_2$

In a round bottom flask equipped with a reflux condenser, Iron (II) trifluoromethanesulfonate (62 mg, 0.18 mmol) was dissolved in 30 mL of anhydrous and degassed acetonitrile under nitrogen. A transparent yellowish solution of (2, 4)-N-(2-(diphenylphosphaneyl) ethyl (diphenylphosphaneyl) ethyl) imino) pent-2-en-2-amine dissolved (**L9**, 100 mg, 0.18 mmol) in 15 mL DCM was transferred the former solution via cannula. Upon addition of the ligand solution, the color of the reaction changed from yellow to dark red. The reaction mixture was stirred at 65 ℃ under Nitrogen overnight. The volatiles were removed under reduced pressure leaving a red oily compound, which was dissolved in the minimum amount of acetonitrile and layered with Et_2O, causing the mixture to become cloudy. After keeping the mixture at -30℃, brown crystals appeared, which were filtered and washed with Et_2O (50 mg, 0.14 mmol, 80%). Some of the crystals that formed were suitable for single crystal XRD analysis.**^{1}H NMR (400 MHz, CD_3CN)** δ 7.50 (t, J = 7.6 Hz, 4H), 7.33 – 7.25 (m, 7H), 7.05 – 6.97 (m, 9H), 4.21 (s, 4H), 4.02 (s, 2H), 2.96 (d, J = 5.5 Hz, 4H), 2.50 (s, 6H). **^{31}P NMR (162 MHz, CD_3CN)** δ 60.80. **Anal. Calcd $C_{39}H_{42}F_6FeN_4O_6P_2S_2$ (3(OTf)$_2$):** C, 48.86; H, 4.42; N, 5.84; S, 6.69. **Found**: C, 48.89; H, 4.49; N, 5.47, S, 6.32. **ESI(+)-Mass** Calcd for: $[M\text{-}CH_3CN\text{-}SO_3CF_3]^+$: 768.15, Found: 768.1.

4.2- Synthesis of complex 4(OTf)$_2$

In a round bottom flask equipped with a reflux condenser, Iron (II) trifluoromethanesulfonate (60 mg, 0.17 mmol) was dissolved in a 30 mL anhydrous and degassed acetonitrile under nitrogen A transparent yellowish solution of (2, 4)-N-(2-(diphenylphosphaneyl) ethyl)-4-((2-(diphenylphosphaneyl) ethyl) imino)-3-phenylpent-2-en-2-amine (**L10**, 100 mg, 0.17 mmol) dissolved in 15 mL DCM was transferred the former solution via cannula. Upon addition of the ligand solution, the color of the reaction changed from yellow to dark red. The reaction mixture was stirred at 65 ℃ under Nitrogen overnight. The volatiles were removed under reduced pressure leaving a red oily compound, which was dissolved in the minimum amount of acetonitrile and layered with Et_2O. The mixture became

cloudy, and a brown powder gradually formed. The solid was filtered and washed with Et_2O (40 mg, 0.038 mmol, 23 %). **^{1}H NMR (400 MHz, CD_3CN)** δ 7.52 (d, J = 7.9 Hz, 4H), 7.44 (d, J = 6.5 Hz, 3H), 7.38 – 7.32 (m, 10H), 7.02 (d, J = 7.8 Hz, 8H), 5.37 (s, 1H), 4.18 – 3.95 (m, 4H), 3.08 (s, 4H), 2.27 (s, 6H). **^{31}P NMR (162 MHz, CD_3CN)** δ 57.00. **Anal. Calcd** for $C_{45}H_{48}F_6FeN_4O_7P_2S_2$ ($4(OTf)_2 + H_2O$): C, 51.34; H, 4.60; N, 5.32; S, 6.09; **Found**: C, 51.44; H, 4.26; N, 5.30; S, 6.19. **ESI(+)-Mass** Calcd for $[M\text{--}2SO_3CF_3]^+$: m/z = 736.25; Found: m/z = 736.1. Calcd for $[M\text{-}2CH_3CN\text{-}2SO_3CF_3]^{2+}$ m/z = 327.10; Found: m/z = 327.1.

4.3- Synthesis of complex 5

Under dry and oxygen free conditions, the β-diimino compound **L2** (633 mg, 1 mmol) was dissolved in THF (10 mL). *n*-BuLi in hexanes (0.8 mL of 2.5M solution, 2 mmol) was added into the THF solution under -78 ºC and the reaction mixture left to stir for 12 h during while gradually warming up to room temperature. The color of the solution changed from yellow to red and then to orange yellow, indicative of the formation of the lithiated intermediate Li(**L2**-H). $FeCl_2(THF)_{1.5}$ (236 mg, 1 mmol) [13] was dissolved in THF and added dropwise to the solution containing the lithiated compound. The solution immediately changed into red color. The mixture was stirred at 60 ºC and the color deepened as the reaction proceeded. After 24h, the solvent was vacuum evaporated leaving a minimum amount of soluble solution. Dry hexane was added affording a red precipitate, which was filtered inside the glovebox and dried under vacuum (205 mg, *ca.* 28%, based on the structure shown in **Scheme 2**). The compound was analyzed by cyclic voltammetry.

4.4- Preparation of 5@MWCNT@GC

To a solution of complex **5** in DMF (5 mg in 15 mL), 5mg of multiwalled carbon nanotubes (MWCNT) were added and the mixture sonicated for 30 minutes under nitrogen. The resulting slurry was stirred for 24 h inside the glovebox. A UV-Vis analysis of the resulting solution indicated that adsorption of the complex was success leaving 35 % of the initial complex in solution (Figure 13 in the manuscript). The modified MWCNT were filtered and washed with

DMF to remove the non-adsorbed complex and re-dispersed in DMF, followed by sonication. This new hybrid material (**5**@MWCNT) was drop casted onto a glassy carbon disk electrode (GC, S = 0.07 cm^2, 4 x 10µL DMF solution). Each drop was placed after the previous drop was completely dried. The resulting electrode (**5**@MWCNT@GC) was then ready for electrochemical measurements.

5- References:

(1) Rodriguez, M. M.; Bill, E.; Brennessel, W. W.; Holland, P. L. N_2 Reduction and Hydrogenation to Ammonia by a Molecular Iron-Potassium Complex. *Science (80-.).* **2011**, *334* (6057), 780–783. https://doi.org/10.1126/science.1211906.

(2) Duan, P.; Schulz, R. A.; Römer, A.; Van Kuiken, B. E.; Dechert, S.; Demeshko, S.; Cutsail, G. E.; DeBeer, S.; Mata, R. A.; Meyer, F. Ligand Protonation Triggers H 2 Release from a Dinickel Dihydride Complex to Give a Doubly "T"-Shaped Dinickel(I) Metallodiradical . *Angew. Chemie* **2021**, *133* (4), 1919–1924. https://doi.org/10.1002/ange.202011494.

(3) Roy, L.; Al-Afyouni, M. H.; Derosha, D. E.; Mondal, B.; Dimucci, I. M.; Lancaster, K. M.; Shearer, J.; Bill, E.; Brennessel, W. W.; Neese, F.; Ye, S.; Holland, P. L. Reduction of CO2 by a Masked Two-Coordinate Cobalt(i) Complex and Characterization of a Proposed Oxodicobalt(Ii) Intermediate. *Chem. Sci.* **2019**, *10* (3), 918–929. https://doi.org/10.1039/c8sc02599a.

(4) Rose, M. J.; Mascharak, P. K. Studies of Low-Coordinate Iron Dinitrogen Complexes. *Chemtracts* **2005**, *18* (8), 471–472.

(5) Smith, J. M.; Lachicotte, R. J.; Holland, P. L. N=N Bond Cleavage by a Low-Coordinate Iron(II) Hydride Complex. *J. Am. Chem. Soc.* **2003**, *125* (51), 15752–15753. https://doi.org/10.1021/ja038152s.

(6) Sadique, A. R.; Brennessel, W. W.; Holland, P. L. Reduction of CO_2 to CO Using Low-Coordinate Iron: Formation of a Four-Coordinate Iron Dicarbonyl Complex and a

Chapter 5.

Bridging Carbonate Complex. *Inorg. Chem.* **2008**, *47* (3), 784–786. https://doi.org/10.1021/ic701914m.

(7) Vela, J.; Vaddadi, S.; Cundari, T. R.; Smith, J. M.; Gregory, E. A.; Lachicotte, R. J.; Flaschenriem, C. J.; Holland, P. L. Reversible Beta-Hydrogen Elimination of Three-Coordinate Iron(II) Alkyl Complexes: Mechanistic and Thermodynamic Studies. *Organometallics* **2004**, *23* (22), 5226–5239. https://doi.org/10.1021/om049415+.

(8) Smith, J. M.; Lachicotte, R. J.; Holland, P. L. Tuning Metal Coordination Number by Ancillary Ligand Steric Effects: Synthesis of a Three-Coordinate Iron(II) Complex. *Chem. Commun.* **2001**, *1* (17), 1542–1543. https://doi.org/10.1039/b103635c.

(9) Holland, P. L.; Cundari, T. R.; Perez, L. L.; Eckert, N. A.; Lachicotte, R. J. Electronically Unsaturated Three-Coordinate Chloride and Methyl Complexes of Iron, Cobalt, and Nickel. *J. Am. Chem. Soc.* **2002**, *124* (48), 14416–14424. https://doi.org/10.1021/ja025583m.

(10) Wang, J. W.; Gil-Sepulcre, M.; Huang, H. H.; Solano, E.; Mu, Y. F.; Llobet, A.; Ouyang, G. CH-π Interaction Boosts Photocatalytic CO_2 Reduction Activity of a Molecular Cobalt Catalyst Anchored on Carbon Nitride. *Cell Reports Phys. Sci.* **2021**, *2* (12), 100681. https://doi.org/10.1016/j.xcrp.2021.100681.

(11) Nie, C.; Liu, C.; Gong, L.; Wang, M. Boosting the Performance of a Silicon Photocathode for Photoelectrochemical Hydrogen Production by Immobilization of a Cobalt Tetraazamacrocyclic Catalyst. *J. Mater. Chem. A* **2021**, *9* (1), 234–238. https://doi.org/10.1039/d0ta09942b.

(12) Matheu, R.; Ertem, M. Z.; Gimbert-Suriñach, C.; Benet-Buchholz, J.; Sala, X.; Llobet, A. Hydrogen Bonding Rescues Overpotential in Seven-Coordinated Ru Water Oxidation Catalysts. *ACS Catal.* **2017**, *7* (10), 6525–6532. https://doi.org/10.1021/acscatal.7b01860.

(13) Holland, P. L. Electronic Structure and Reactivity of Three-Coordinate Iron Complexes. *Acc. Chem. Res.* **2008**, *41* (8), 905–914. https://doi.org/10.1021/ar700267b.

Chapter 5.

Supporting information

Table of contents

Chapter 5.

1- X-ray Diffraction analysis

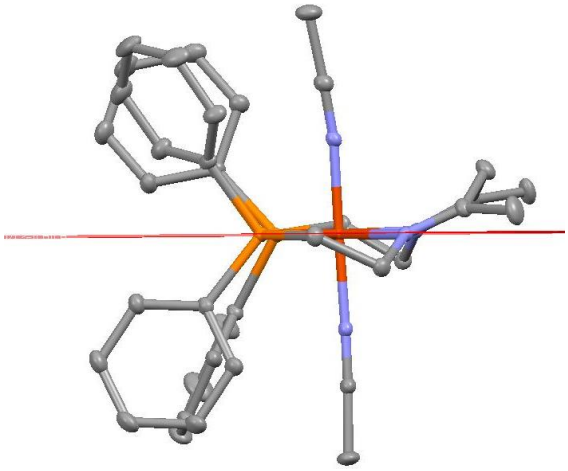

Figure S1. ORTEP representation of $\mathbf{3}^{2+}$ at 50% probability level (counterions and hydrogens are omitted for clarity). **Color code**: **C**, Dark gray; **N**, Blue; **Fe**, red; **P**, orange. Red line depicts the plane formed by the Fe1-P1-P2 atoms (see Figure 1 in main manuscript).

Chapter 5.

2- NMR spectroscopy

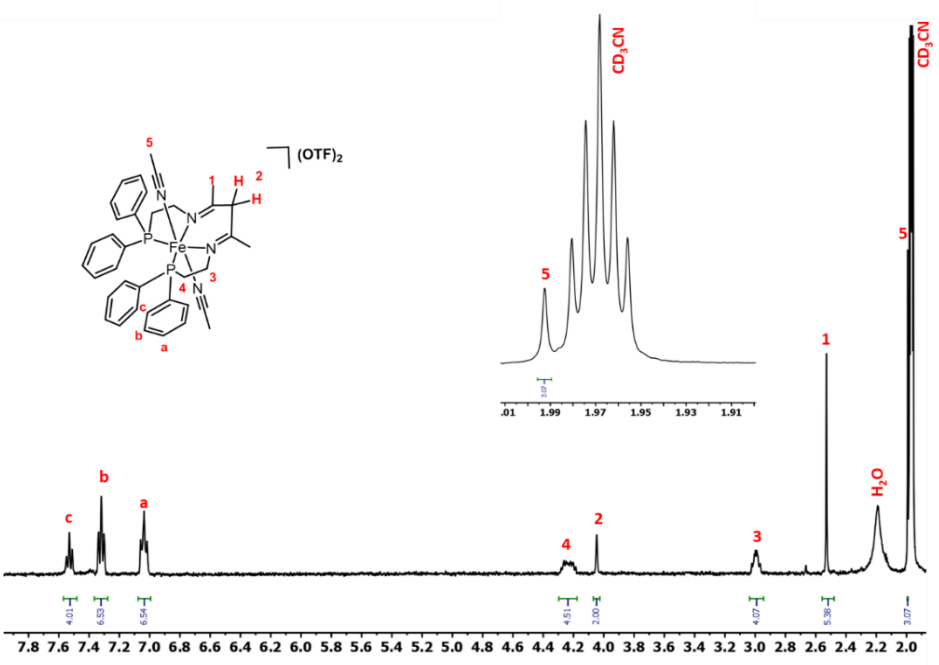

Figure S2. ^{1}H NMR of complex **3(OTF)$_2$** (400 MHz, CD_3CN)

Chapter 5.

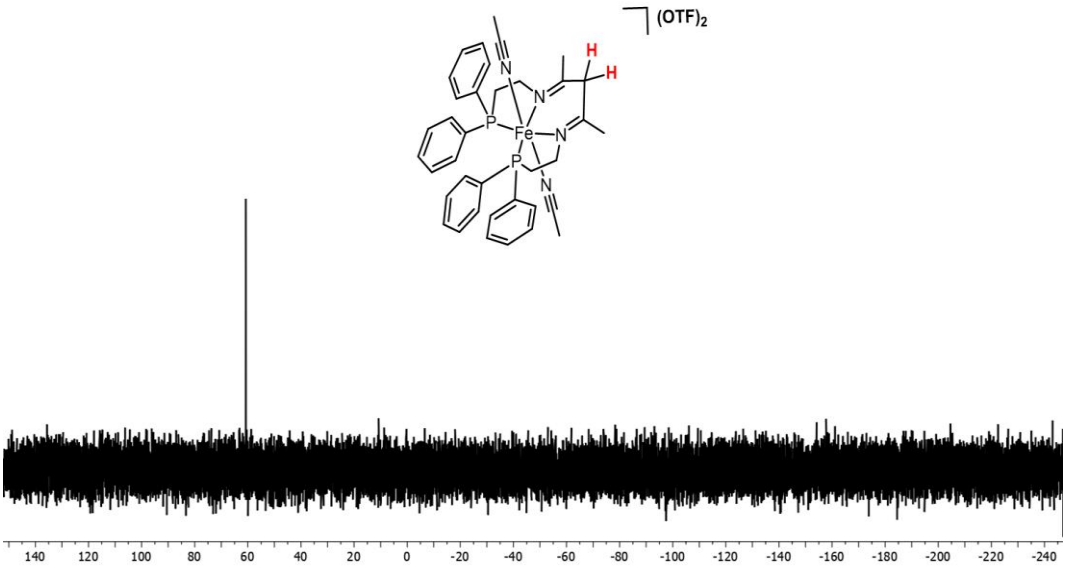

Figure S3. ^{31}P NMR of complex **3(OTF)$_2$** (162 MHz, CD_3CN)

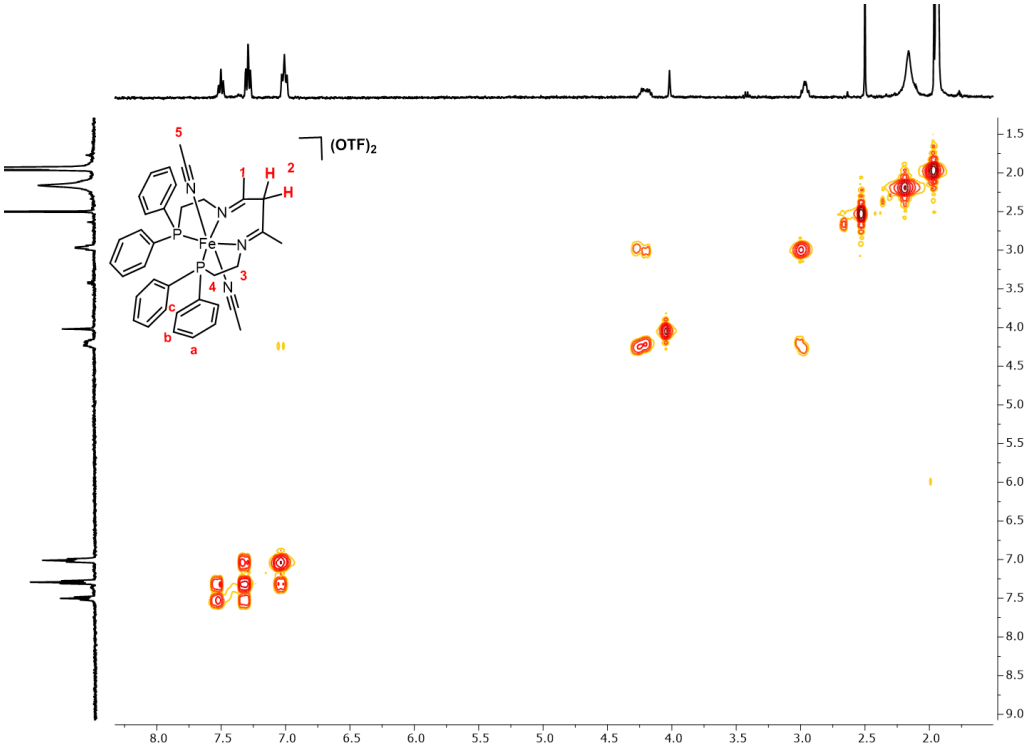

Figure S4. ^{1}H-^{1}H COSY NMR of **3(OTF)$_2$** (400 MHz, CD_3CN)

Chapter 5.

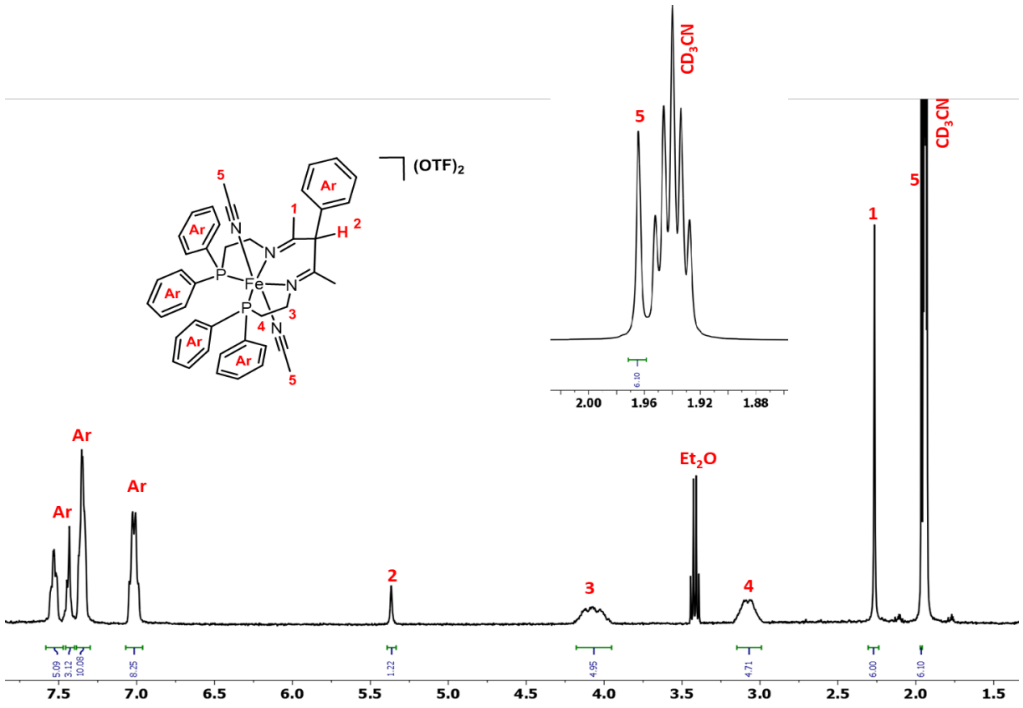

Figure S5. ^{1}H NMR of complex **4(OTf)$_2$** (400 MHz, CD_3CN)

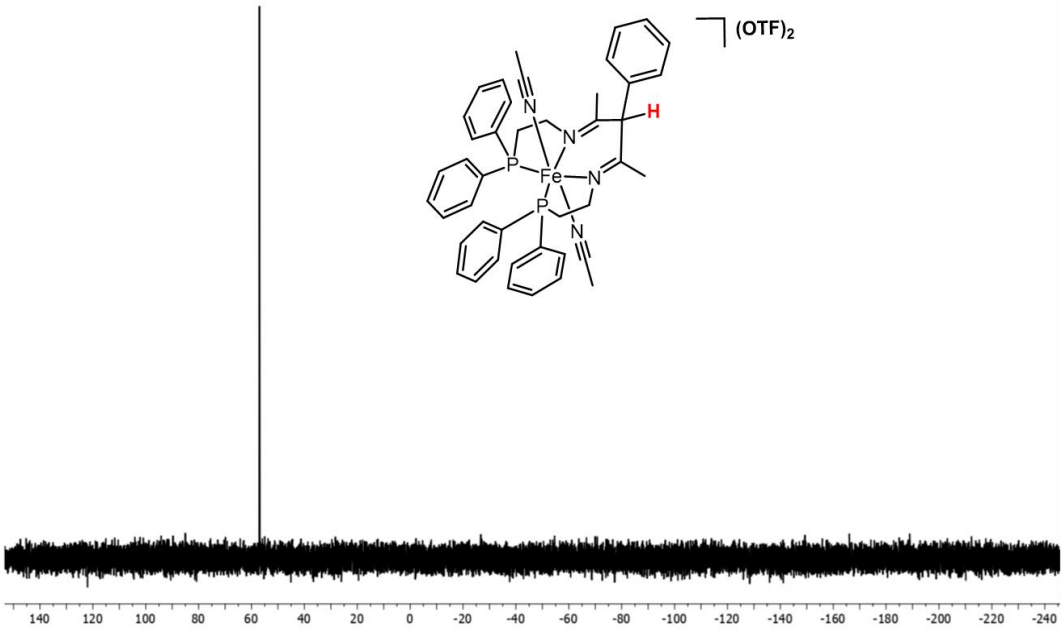

Figure S6. ^{31}P NMR of complex **4(OTf)$_2$** (162 MHz, CD_3CN)

Chapter 5.

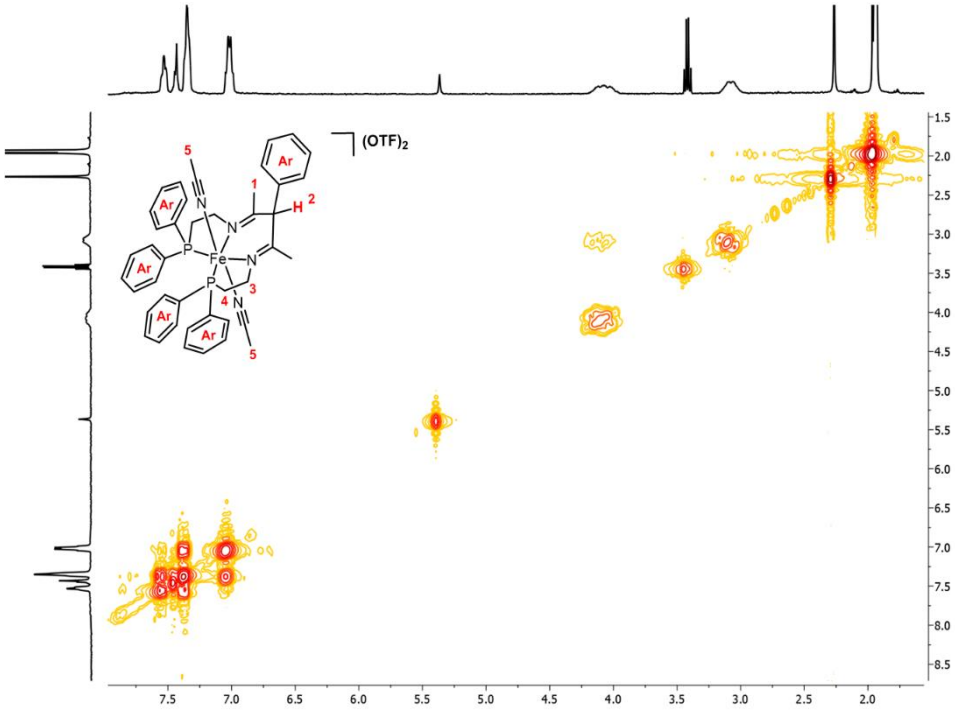

Figure S7. ^{1}H-^{1}H COSY NMR of complex **4(OTF)$_2$** (400 MHz, CD_3CN)

Chapter 5.

3- UV-Vis spectroscopy of complex 5

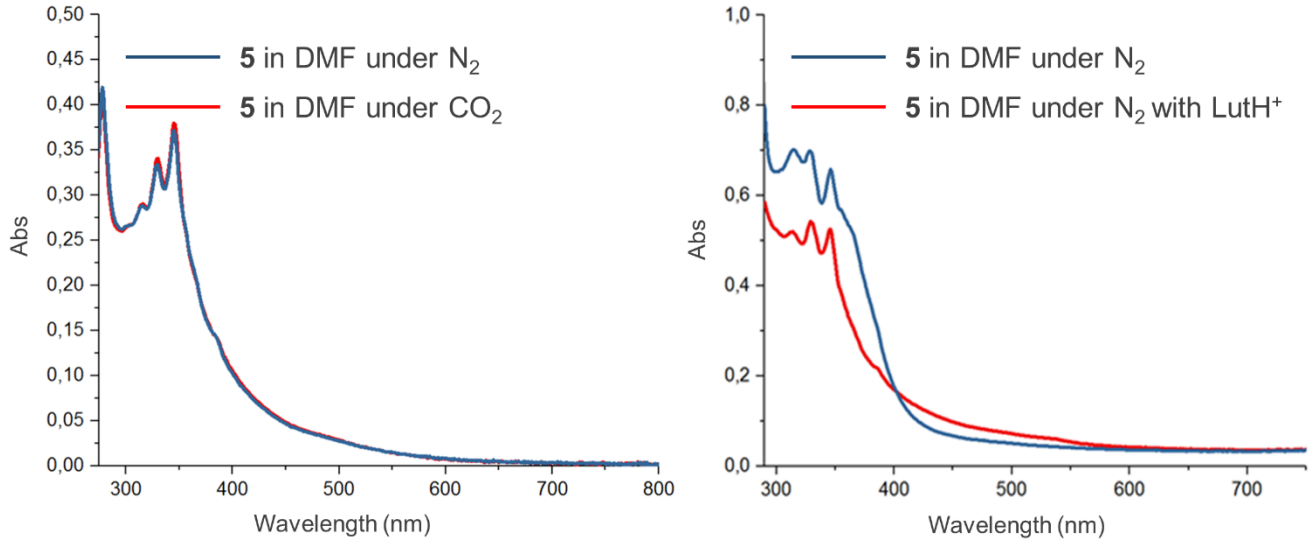

Figure S8. UV-Vis spectra of **5** in (a) DMF under nitrogen (red) or DMF under CO_2 (blue) and (right) in DMF under nitrogen in the absence (blue) and in the presence (red) of lutidinium triflate as proton source).

4- Electrochemical analysis of complex 5

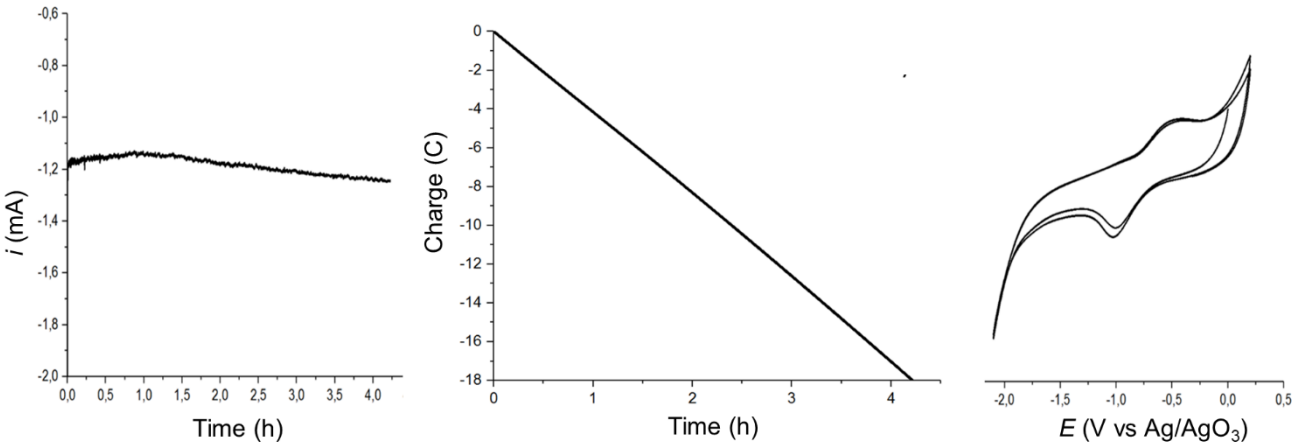

Figure S9. Left and Middle) Bulk electrolysis experiment at E_{app} = -1.9 V vs $Fc^{+/0}$ of a 5 mM solution of **5** in DMF/CH_3OH (9:1). Right) CV after the bulk electrolysis experiment showing the presence of the complex.

Chapter 6

Nickle complexes with N_4 type ligands for CO_2 reduction reaction

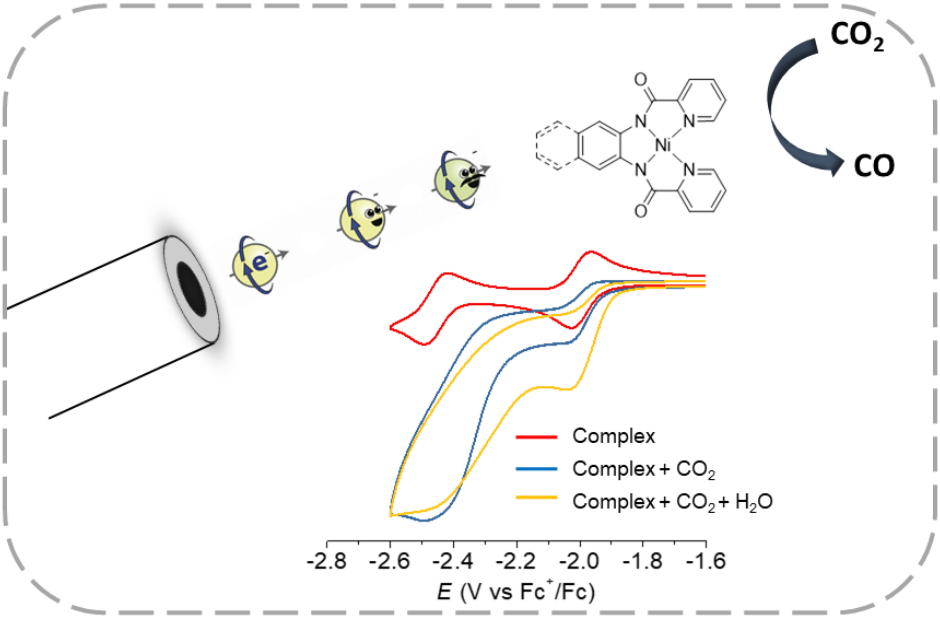

Chapter 6.

1- Introduction

In the field of molecular carbon dioxide reduction (CO_2RR) catalysis, the most prominent achievements of the last decade are based on Iron and Cobalt complexes.[1] They have shown excellent performance in terms of activity,[2] and reaction selectivity[3] (see Chapter 1). On the other hand, Nickel complexes have received less attention, yet one of the first highly selective molecular catalyst for the conversion of CO_2 to CO was the macrocyclic Ni(II) complex $[Ni(cyclam)]^{2+}$ in the top left of **Figure 1**.[4]

Related tetraazomacrocyclic ligands have also led to active Nickel catalysts, such as $[Ni(mac\text{-}N_4)]^{2+}$ and $[Ni(CR)]^{2+}$ in **Figure 1** (top).[8] The latter is characterized by holding a bis(imino)pyridyl ligand (CR) which is redox active and is involved in the reduction chemistry of the complex. Phtalocyanine (Pc) Ni complexes are also early examples of molecular CO_2RR catalysts characterized by the redox non-innocent nature of the ligand, which has a highly conjugated structure.[9,10] In fact, the capacity of ligands to accept reductive equivalents in Nickel complexes have been proposed to be key in the selectivity of the CO_2RR reaction over the hydrogen evolution reaction (HER). This has been related to the easy formation of Ni-hydride species when the metal is reduced as key precursors to H_2 evolution.[11,12] In contrast, when the reduction takes place at the ligand, Ni-CO_2 intermediate derivatives are favoured and lead to higher selectivity towards CO_2 reduction products such as CO,[12] formate[13] or even CH_4[11,5]. An illustrative example is provided by complexes holding tetradentate ligands based on bis(pyridine)/bis(carbene) scaffolds (**Figure 1**, bottom).[14] There are striking differences between the selectivity of the catalyst containing an open-kelate ligand ($[Ni(o\text{-}N_2C_2\text{-}\mathbf{2})]^{2+}$) in comparison to their macrocyclic analogues ($[Ni(mac\text{-}N_2C_2\text{-}\mathbf{1})]^{2+}$ and $[Ni(mac\text{-}N_2C_2\text{-}\mathbf{2})]^{2+}$). For the former, the $CO:H_2$ selectivity is 5:85, significantly lower than that obtained for $[Ni(mac\text{-}N_2C_2\text{-}\mathbf{1})]^{2+}$ (56:43) and even more when compared to the more rigid and planar $Ni(mac\text{-}N_2C_2\text{-}\mathbf{2})]^{2+}$ (89:11). It is important to remark that even if the Ni-hydride intermediate is mostly associated with the HER, it has also been proposed as key in some CO_2 reduction catalytic cycles by Ni catalysts.[12,14] All these results are clear evidence of the important role the ligand plays in the CO_2RR catalysis. However, there is still a lack of mechanistic information on CO_2RR catalysis by Ni complexes and a conclusive proof of the ligand involvement in the catalytic process is still missing.

One of the common features of the selected Ni catalysts in **Figure 1** is that they all have N-

donor atoms in their ligand structure, which are combined with other type of ligands such as those containing sulfur donors (NiFeCp and $[Ni(bpet)]^{2+}$ in **Figure 1**, middle),[5,15] with the aim of mimicking the CO dehydrogenase enzyme cofactor [NiFe] CODH, responsible of the conversion of CO_2 to CO in living organisms (see Chapter 1).[16] Another strategy has been to combine pyridine donor groups with carbenes, leading to great catalytic activity and selectivity as discussed above.[5,7,12,13,15]

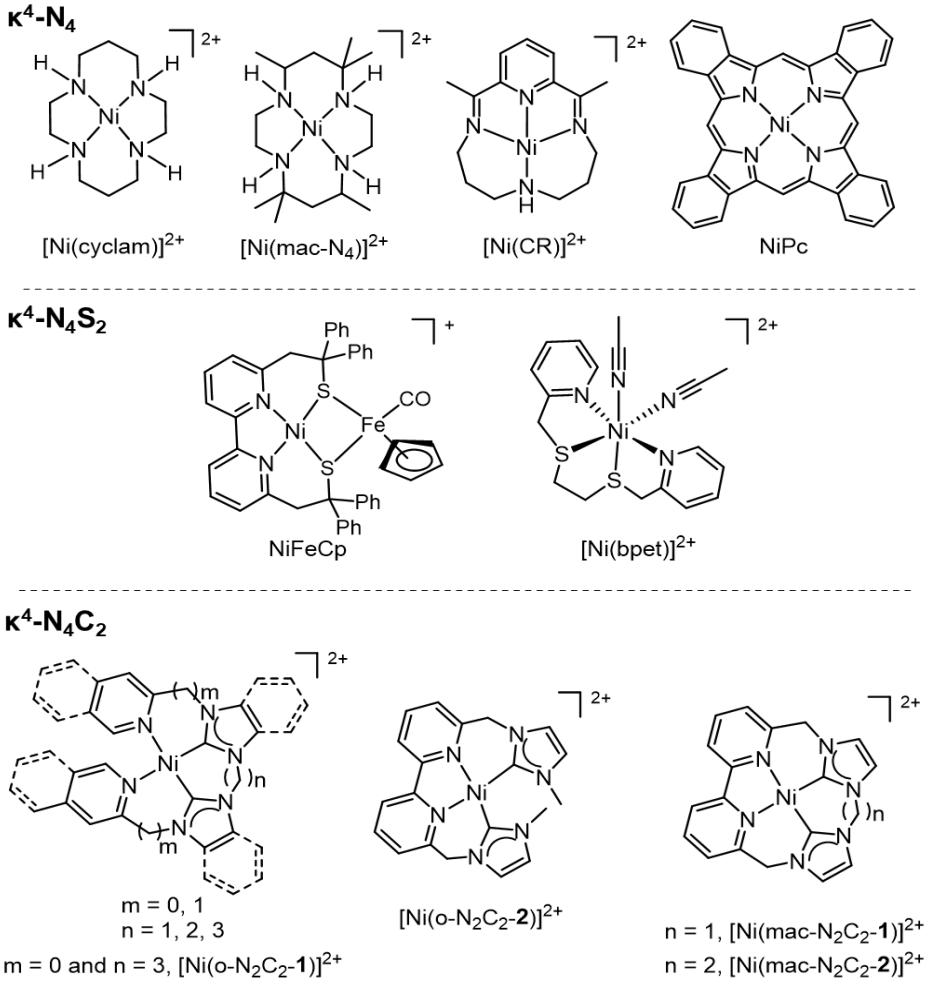

Figure 1. Reported nickel complexes stabilized with N-donor ligands that have shown to trigger CO_2 reduction reactions.[5–7]

In this chapter, two Nickel complexes containing potentially redox active dipicolinamide scaffolds with different π-extended structures and holding pyridine groups are described (**Scheme 1**). They are danionin κ^2-N_4 ligands, a characteristic that they share with Pc analogues (**Figure 1**, top right). They have been designed with the aim of getting high activity/selectivity

as well as more insights into the ligand role in CO_2RR catalysis.

2- Results and discussions

2.1- Synthesis and characterisations of complexes 6 and 7

The synthesis of Ni(II) complexes **6** and **7** in **Scheme 1** follows a two-step methodology from commercially available benzene-1,2-diamine and naphthalene-1,2-diamine, respectively. In the first step, ligand precursors *N*,*N*'-(1,2-phenylene)dipicolinamide ($PDPAH_2$, **L12**) and *N*,*N*'-(naphthalene-2,3-diyl)dipicolinamide (NDPAH2 (**L13**)) were prepared following an adapted reported procedure, which consists of the double condensation reaction of the diamine precursors with two equivalents of picolinamide in the presence of triphenylphosphate.[5,17–19] In the second step, **L12** or **L13** were reacted with $Ni(OAc)_2$, affording complexes **6** and **7**, respectively, in quantitative yields assuming a chemical composition based on the neutral structure indicated in **Scheme 1**.

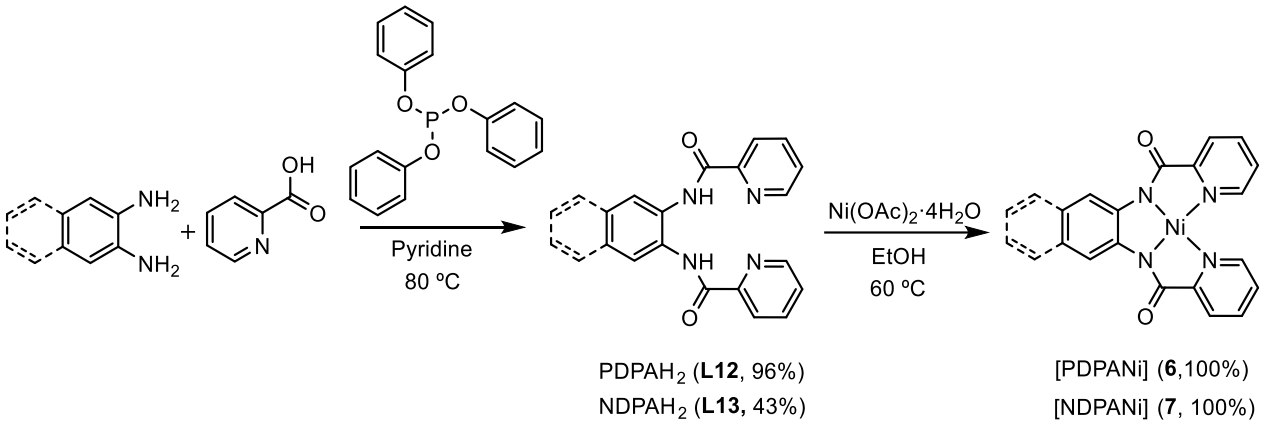

Scheme 1- Synthesis of complexes **6** and **7**.

Based on previous literature, we propose that complexes **6** and **7** are square planar Ni(II) d^8 diamagnetic compounds with **L12** and **L13** acting as a dianionic κ^4-N_4 ligand after deprotonation by the acetate of the $Ni(OAc)_2$ precursor.[19,20] This is supported by the ^{1}H NMR spectra which shows uniquely the typical signals of deprotonated **L12** and **L13** (**Figure 2** and **Figures S1-S10** in the Supporting Information).

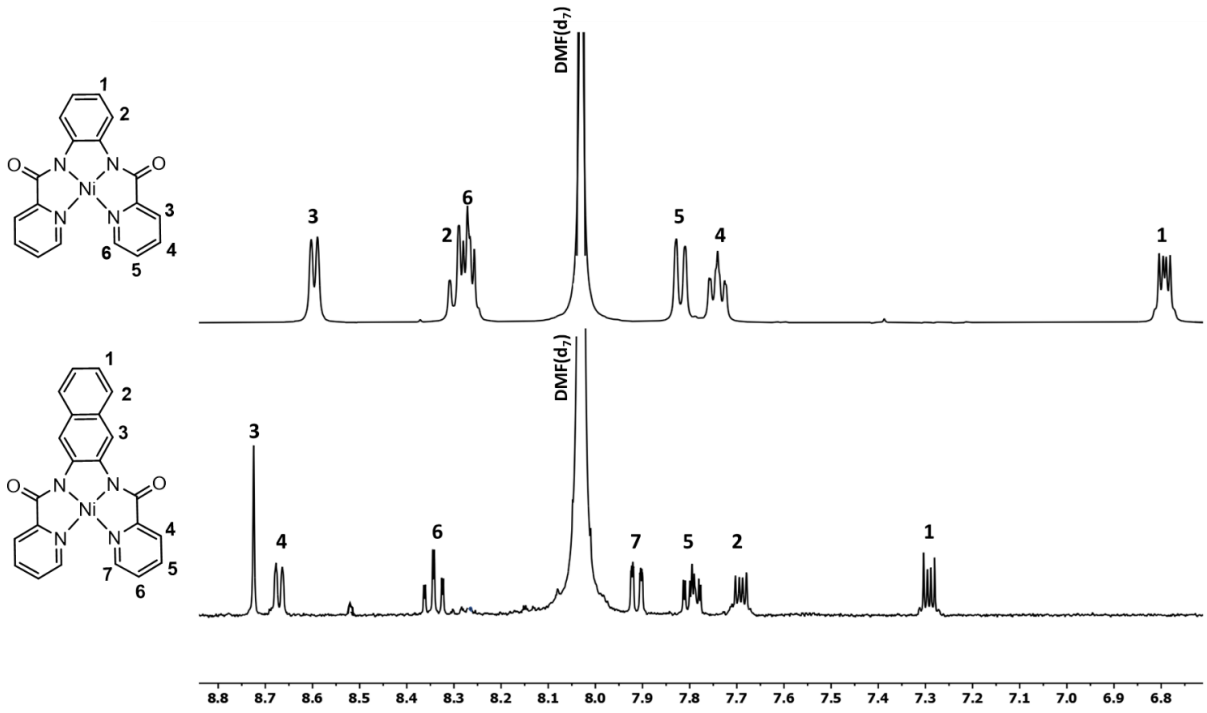

Figure 2- ^{1}H NMR spectra of complexes **6** (**top**) and **7** (**bottom**) in DMF-d_7.

2.2- Electrochemical characterization of 6 and 7

The redox properties of complexes **6** and **7** were investigated by cyclic voltammetry (CV) in *N,N*-Dimethylformamide (DMF) containing 0.1 M [(n-Bu) $_4$ N](PF$_6$) (TBAPF$_6$) as supporting electrolyte in a one compartment cell consisting of glassy carbon electrode as working electrode, Pt as counter electrode, (0.01 M Ag/AgNO$_3$, 0.1 M TBAPF$_6$) as reference electrode and ferrocene as the internal reference which was added at the end of each experiment.

Cyclic voltammetry of a 0.5 mM solution of **6** shows two one-electron reversible waves at $E_{1/2}$ = -1.99 V vs Fc/Fc$^{+/0}$ (ΔE = 60 mV) and $E_{1/2}$ = -2.45 V vs Fc/Fc$^{+/0}$ (ΔE = 60mV) (**Figure 3** and **Table 1**). Complex **7** is less soluble than **6** in DMF and the cyclic voltammetry was performed for a saturated solution with unknown concentration. Analogously to compound **6**, the cyclic voltammetry of **7** shows a reversible one electron redox peak at $E_{1/2}$ = -1.95 V vs Fc/Fc$^{+/0}$ (ΔE = 61mV) and a one-electron quasi-reversible redox event at $E_{1/2}$ = -2.41 V vs Fc/Fc$^{+/0}$ (ΔE = 80mV) (**Figure 3** and **Table 1**). These values account for 40 mV for both redox

events as compared to **6**. Considering the redox non-innocent nature of the ligands and the higher charge delocalization of the naphthalene ring in **L13** as compared to the phenyl ring in **L12**, a first ligand-based reduction process would be plausible and consistent with the easier reduction of the former, also suggested in the literature for related Ni complexes.[18] However, further analyses including density functional theory calculations (DFT) are required to conclusively attribute the two reductions observed for **6** and **7** to metal or ligand-based processes.

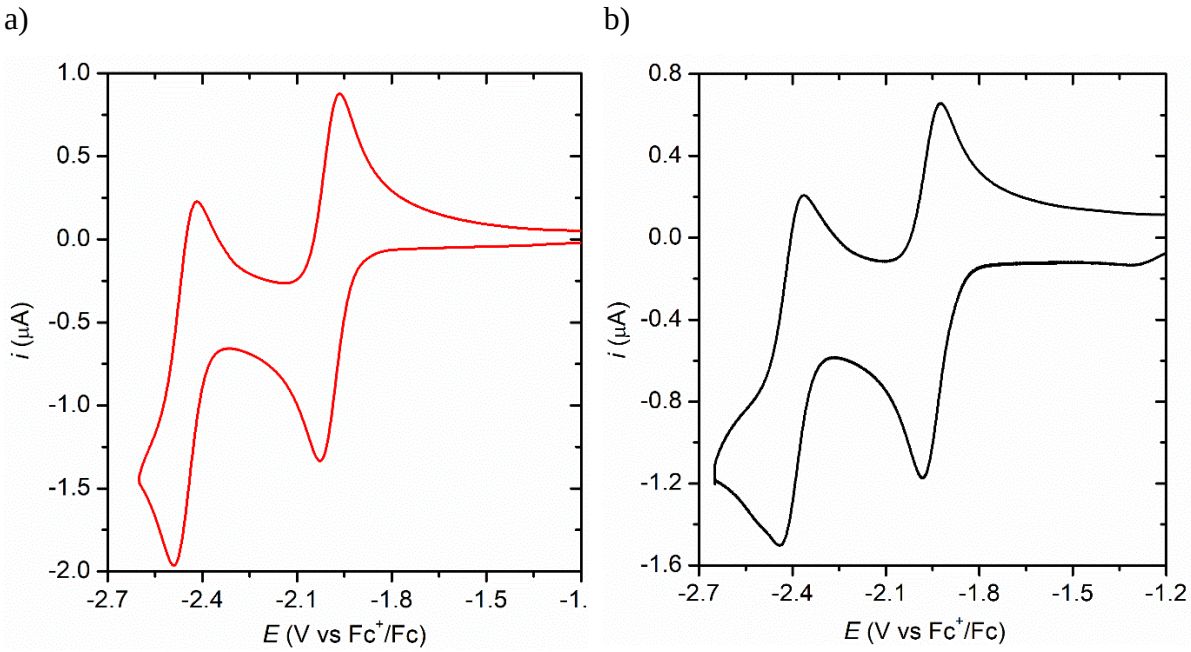

Figure 3- a) Cyclic voltammetry experiments of a 0.5 mM solution of **6 (left)** and **7 (right)** in DMF and scan rate of 100 mV/s.

Table 2*- Redox potentials data for complexes **6** and **7** in DMF. All potentials reported in V versus ferrocene.*

Complex	E^1_{pa}	E^1_{pc}	$E^1_{1/2}$	ΔE^1 (mV)	E^2_{pa}	E^2_{pc}	$E^2_{1/2}$	ΔE^2 (mV)
6	-1.96	-2.02	-1.99	60	-2.48	-2.42	-2.45	60
7	-1.92	-1.98	-1.95	61	-2.45	-2.37	-2.41	80

2.3- CO_2 reduction catalysis

When cyclic voltammetry experiments of complexes **6** and **7** were performed in a CO_2 saturated DMF solution, the first reduction event for both complexes became irreversible (compare red and blue traces in **Figure 4a** and black and blue traces in **Figure 4b**). In addition, a significant increase in the current intensity is observed at $E_{p,c}$ = -2.46 V vs $Fc^{+/0}$ and $E_{p,c}$ = -2.36 V vs $Fc^{+/0}$ for **6** and **7**, respectively, which represent 40-50 mV anodic shifts as compared to the cathodic peak of the second reduction event of the complexes in the absence of CO_2. These results are a clear indication of the interaction of the reduced complexes **6** and **7** with CO_2 and point to an electrocatalytic response at the second reduction wave.

If the same experiment is done in the presence of 4% H_2O as proton source, the current of the first reduction at $E_{p,c}$ = -2.03 V vs $Fc^{+/0}$ for **6** and $E_{p,c}$ = -1.95 V vs $Fc^{+/0}$ for **7** increases suggesting that a catalytic process is also taking place at this potential (compare yellow and blue traces in **Figure 4**). In contrast, the intensity in the second catalytic process seems to decrease in the presence of protons.

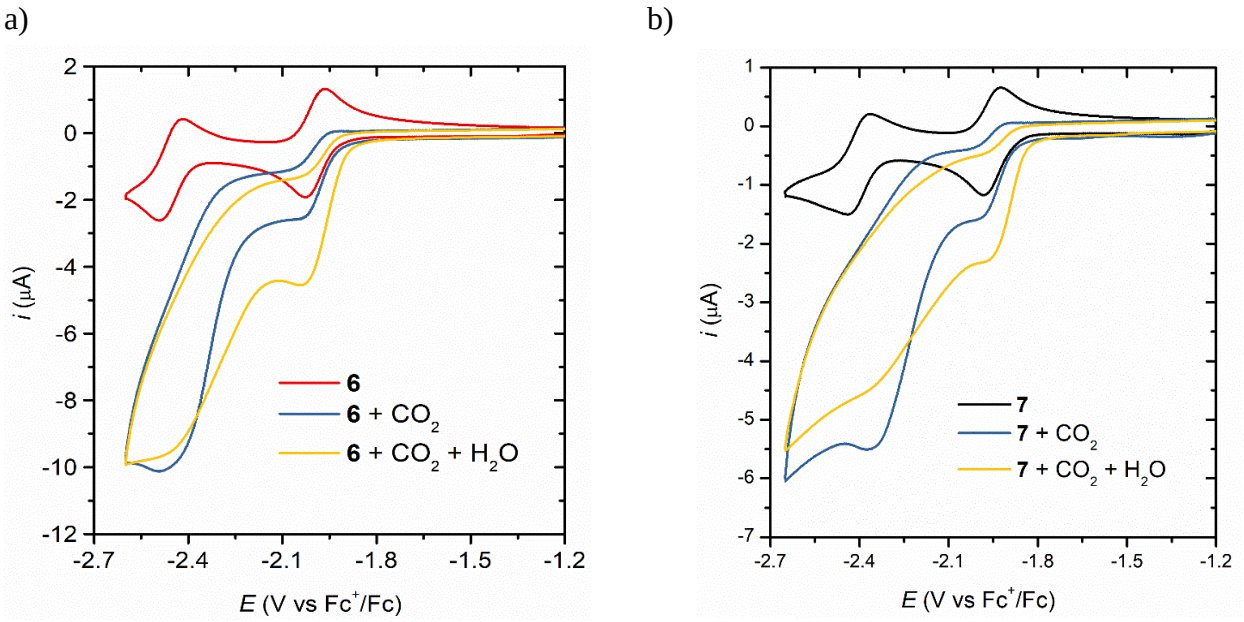

Figure 4- Cyclic voltammogram of a solution of **6** (**a**) and **7** (**b**) in DMF in the absence and in the presence of a CO_2 and water as proton source.

An analogous phenomenon is observed when trifluoroethanol (TFE) is used as proton source

(**Figure 5**). These results indicate that the potential catalytic processes are not dependent of the acidic strength of the proton source. Control experiments in the presence of TFE and in the absence of CO_2 were performed to assess the competing HER reaction. Indeed, as shown in **Figures S11** of the SI, a significant catalytic wave is observed at $E_{p,c}$ = -2.4 V vs $Fc^{+/0}$ suggesting that HER will compete with a putative CO_2RR.

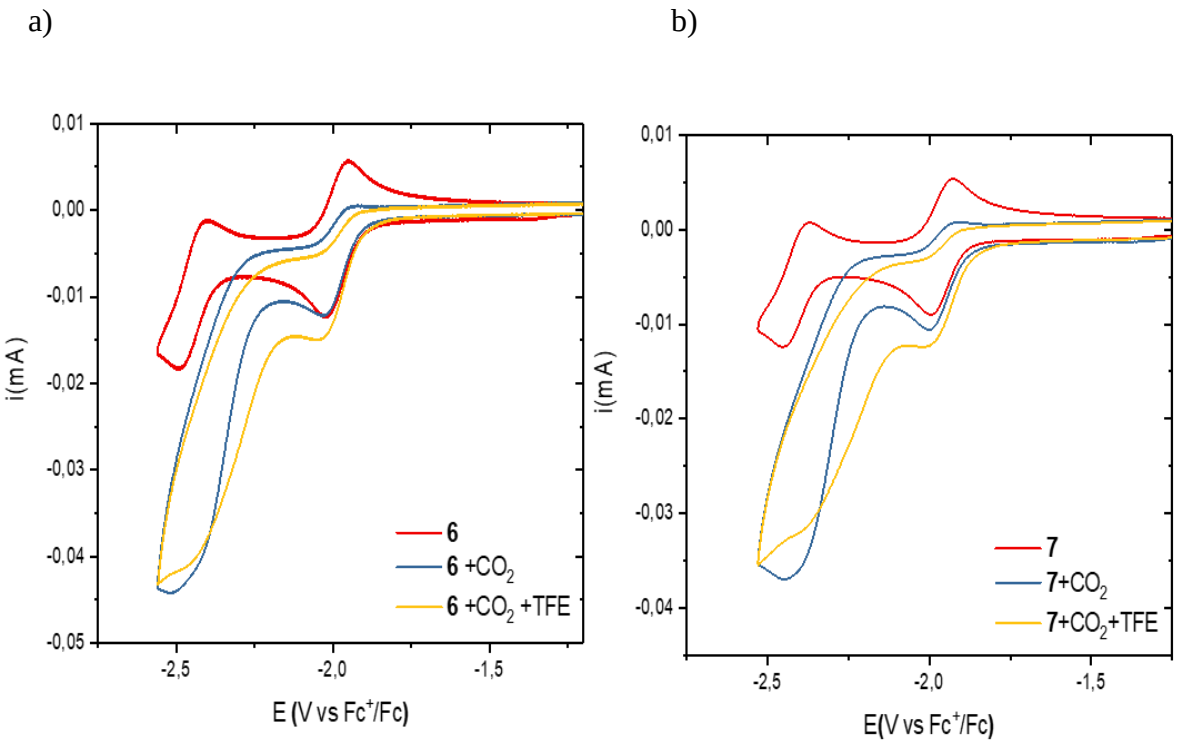

Figure 5- Cyclic voltammogram of a solution of **6** (**a**) and **7** (**b**) in DMF in the absence and in the presence of a CO_2 and trifluoroethanol as proton source.

To ascertain the possible CO_2 reduction ability of the complexes, a preliminary bulk electrolysis experiment of a DMF solution of **6** saturated with CO_2 and containing 4% H_2O was performed at E_{app} = -2V vs $Fc^{+/0}$. The current vs time profile decays slowly over time presumably due to the consumption of the CO_2 substrate (**Figure 6**). Analysis of the headspace of the cathodic compartment revealed the presence of a small amount of carbon monoxide, resulting from the two-electron reduction of CO_2 by the nickel complex. On the other hand, a high amount of hydrogen gas was detected confirming poor selectivity of **6** to perform CO_2RR over HER (**Figure S11** in the SI). However, these preliminary results are highly remarkable since electrocatalytic CO2RR and HER are known to compete at such low applied potentials. The origin of the low selectivity of the complex **6** towards CO_2 reduction might be attributed

to the formation of a low-valent metal centre triggering the formation of a Ni-hydride intermediate that would favour HER, although further analysis including DFT calculations are necessary to get more insights into the catalytic processes.

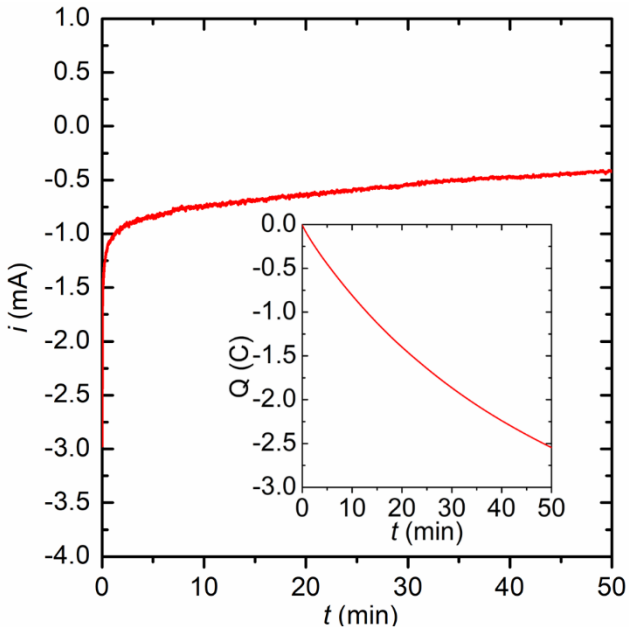

Figure 6. Bulk electrolysis experiment of a DMF solution of **6** saturated with CO_2 and containing 4% H2O, performed at E_{app}= -2V vs $Fc^{+/0}$. The experiment was done in a two-compartment cell consisting of a Pt mesh as a counter electrode, GC rod (S = 3,14 cm^2) as working electrode, and Ag/Ag^+ (0,01 M $Ag/AgNO_3$,0,1 $MTBAPF_6$) as reference electrode.

A CV experiment performed after the bulk electrolysis showed the same redox profile of the complex, with no new additional peak, pointing to the molecular nature of catalysis (**SI Figure S1)**. However, a loss of intensity compared to the CV recorded before the bulk electrolysis is observed and can be attributed to the decreased concentration of CO_2/proton source in the solution due to their consumption in the catalytic process. Further quantitative analysis, including blank experiments, rinse tests together with further spectroscopic characterization after bulk electrolysis are necessary to conclusively attribute this process to a molecular CO_2 reduction process.

3- Conclusions

A straightforward, high yield synthetic route towards Ni(II) complexes containing tetradentate dipicolinamido ligands have been described. The novel two Ni complexes differ on the degree of conjugation of the ligand, which has been found to have an influence on their redox properties; complex **6** contains the ligand *N*,*N*′-(1,2-phenylene)dipicolinamido while

complex **7** has *N*,*N'*-(naphthalene-2,3-diyl)dipicolinamido. Cyclic voltammetry experiments show analogous redox profile for both complexes with two reversible waves at $E_{1/2}$ = -1.99 V (**6**) and $E_{1/2}$ = -1.95 V (**7**) vs $Fc/Fc^{+/0}$ and a reversible or quasi-reversible wave at $E_{1/2}$ = -2.45 V and $E_{1/2}$ = -2.41 V vs $Fc/Fc^{+/0}$ for **6** and **7**, respectively. Both complexes have shown promising results as potential CO_2 reduction catalysts to form CO, as demonstrated by the catalytic wave observed in the presence of CO_2 and water at $E_{p,c}$ = -2.03 V vs $Fc^{+/0}$ for **6** and $E_{p,c}$ = -1.95 V vs $Fc^{+/0}$ for **7** and also by a bulk electrolysis experiment of **6** at E_{app} = -2.00 vs $Fc^{+/0}$ that produces hydrogen and CO. the low selectivity of the complexes attributed to more favourable production of Ni^{III}-H intermediate compare to Ni^{III}-COOH from one electron reduction of metal center which favours the hydrogen production. Further experiments are required to get a quantitative analysis of the catalytic process, and the full spectroscopic characterization of the complexes before and after catalysis to ascertain the real molecular nature of the process. The preliminary results shown in this chapter are a valuable starting point towards a new family of Ni complexes active for the CO_2RR. Further efforts should focus on enhancing the ligand ability to store electrons thus precluding the formation of the Ni-hydride intermediate and potentially increasing the selectivity of the electroreduction to CO rather than H_2.

Chapter 6.

4- Experimental section

4.1- Synthesis of *N, N'*-(1, 2-phenylene)dipicolinamide, L12

The synthesis of the ligand **L12** was performed based on reported procedures.[17,21–23] 2-pyridinecarboxylic acid (1.23 g, 10 mmol) and 1,2 diaminobenzene (0.54 g, 5 mmol) were added to 10 mL of stirring pyridine. Then, triphenylphosphite (2.6 mL, 10 mmol) was added to the solution and the reaction mixture heated up to 80℃ for 4 h. After cooling down to room temperature, the solution was left standing overnight. A pale brown crystalline solid formed, which was filtered, washed with methanol leaving long white needles. (305 mg, 4.8 mmol, 96%). ^{1}H NMR (400 MHz, $CDCl_3$) δ 10.29 (s, 2H), 8.58 (ddd, *J* = 4.8, 1.7, 0.9 Hz, 2H), 8.34 (dt, *J* = 7.8, 1.1 Hz, 2H), 7.96 – 7.91 (m, 2H), 7.91 – 7.88 (m, 2H), 7.48 (ddd, *J* = 7.6, 4.8, 1.2 Hz, 2H), 7.33 (dd, *J* = 6.1, 3.5 Hz, 2H). ^{13}C NMR (101 MHz, $CDCl_3$) δ 149.70, 148.14, 137.59, 126.50, 126.22, 124.73, 122.64.

4.2- Synthesis of *N,N'*-(naphthalene-2,3-diyl)dipicolinamide, L13

2-pyridinecarboxylic acid (1.23 g, 10 mmol) and 2, 3-diaminonaphtalene (0.79 g, 5 mmol) were added to 10 mL of stirring pyridine. Then, triphenylphosphite (2.6 mL, 10 mmol) was added to the solution and the reaction mixture heated up to 80℃ for 4 h. After cooling down to room temperature, the solution was left standing overnight. A dark brown crystalline solid resulted, which was filtered, washed with methanol leaving long brown needles (800 mg, 2.17 mmol, 4 3%).**^{1}H NMR (400 MHz, $CDCl_3$)** δ 10.52 (s, 2H), 8.60 (s, 2H), 8.51 (s, 2H), 8.40 (d, *J* = 7.4 Hz, 2H), 7.87 (dd, *J* = 6.2, 3.3 Hz, 2H), 7.55 (s, 2H), 7.49 (dd, *J* = 6.2, 3.2 Hz, 2H).**^{13}C NMR (101 MHz, $CDCl_3$)** δ 206.94, 162.79, 149.45, 147.64, 138.25, 131.56, 128.76, 127.60, 126.70, 126.06, 122.99, 122.29.

4.3- Synthesis of complex 6

In a round-bottom flask equipped with are flux condenser, Nickel(II) acetate tetrahydrate (100 mg, 0.31 mmol) was dissolved in 30 mL of hot ethanol under nitrogen atmosphere. Then, *N, N'*-(1, 2-phenylene)dipicolinamide (78 mg, 0.31 mmol) was dissolved in the minimum

amount of DCM and added to metal salt solution under nitrogen. Upon adding the ligand solution to the metal solution, the color of the reaction turned red and gradually the solution became cloudy. The reaction mixture was stirred overnight under nitrogen at 60℃. The resulting orange precipite was filtered, washed with ethanol, and used for further investigation (117 mg, 0.31mmol, quantitative). **^{1}H NMR (400 MHz, DMF)** δ 8.72 (s, 2H), 8.70 – 8.65 (m, 2H), 8.34 (td, *J* = 7.6, 1.3 Hz, 2H), 7.91 (ddd, *J* = 7.7, 1.7, 0.6 Hz, 2H), 7.82 – 7.77 (m, 2H), 7.70 (dt, *J* = 6.1, 3.4 Hz, 2H), 7.29 (dd, *J* = 6.2, 3.2 Hz, 2H).

4.4- Synthesis of complex 7

In a round-bottom flask equipped with a reflux condenser, Nickel(II) acetate tetrahydrate (34 mg, 0.14 mmol) was dissolved in 30 mL of hot ethanol under nitrogen atmosphere. Then *N, N'*-(naphthalene-2,3-diyl)dipicolinamide, (78 mg, 0.14 mmol) was dissolved in the minimum amount of DCM and added to the metal salt solution under nitrogen. Addition of the ligand solution to the metal solution caused the color of the reaction to turn red and immediately the solution became cloudy. The reaction mixture was stirred overnight under nitrogen at 60℃. The resulting brown precipitate was filtered, washed with ethanol, and used for further investigation (57 mg, 0.14 mmol, quantitative). **^{1}H NMR (400 MHz, DMF)** δ 8.72 (s, 2H), 8.70 – 8.65 (m, 2H), 8.34 (td, J = 7.6, 1.3 Hz, 2H), 7.91 (ddd, J = 7.7, 1.7, 0.6 Hz, 2H), 7.82 – 7.77 (m, 2H), 7.70 (dt, J = 6.1, 3.4 Hz, 2H), 7.29 (dd, J = 6.2, 3.2 Hz, 2H).

5- References

(1) Francke, R.; Schille, B.; Roemelt, M. Homogeneously Catalyzed Electroreduction of Carbon Dioxide - Methods, Mechanisms, and Catalysts. *Chem. Rev.* **2018**, *118* (9), 4631–4701. https://doi.org/10.1021/acs.chemrev.7b00459.

(2) Costentin, C.; Robert, M.; Savéant, J. M.; Tatin, A. Efficient and Selective Molecular Catalyst for the CO_2-to-CO Electrochemical Conversion in Water. *Proc. Natl. Acad. Sci. U. S. A.* **2015**, *112* (22), 6882–6886. https://doi.org/10.1073/pnas.1507063112.

(3) Talanquer, V.; Oxtoby, D.; Islam, M. F.; Zhang, J.; Collings, P. J.; Yodh, A. G.; Gleiter, H.; Perepezko, J.; Terrones, M.; Dwyer, J. R.; Jordan, R. E.; Miller, R. J.; Enomoto, M.; Lee, J. K.; Group, F.; Lekkerkerker, H. N.; Grier, D. G.; Weeks, E. R.; Schofield, A.; Pusey, P. N.; Weitz, D. A.; Blair, D. W.; Levine, A. J.; Guyer, R. A.; Dinsmore, A. D.; Alsayed, A. M.; Yodh, A. G.; Han, Y.; Megen, W. Van; Grier, D. G.; Dobry, A.; Diep, H. T.; Burakovsky, L.; Preston, D. L.; Silbar, R. R.; Grimvall, G.; Li, M.; Bongiorno, A.; Ostwald, W.; Li, M.; Denton, A. R.; Ashcroft, N. W.; Auer, S.; Frenkel, D.; Davidchack, R. L.; Moroni, D.; Bolhuis, P. G.; Lu, K.; Li, Y.; Jin, Z. H.; Gumbsch, P.; Lu, K. Molecular Fe Catalyst. *Science (80-.).* **2012**, *338* (October), 90–94.

(4) BELEY, M.; COLLIN, J.-P.; RUPPERT, R.; SAUVAGE, J.-P. ChemInform Abstract: Electrocatalytic Reduction of CO_2 by Ni [Cyclam]$^{2+}$ in Water: Study of the Factors Affecting the Efficiency and the Selectivity of the Process. *ChemInform* **1987**, *18* (14), 7461–7467. https://doi.org/10.1002/chin.198714076.

(5) Ahmed, M. E.; Adam, S.; Saha, D.; Fize, J.; Artero, V.; Dey, A.; Duboc, C. Repurposing a Bio-Inspired NiFe Hydrogenase Model for CO_2 Reduction with Selective Production of Methane as the Unique C-Based Product. *ACS Energy Lett.* **2020**, *5* (12), 3837–3842. https://doi.org/10.1021/acsenergylett.0c02002.

(6) Collin, J. P.; Sauvage, J. P. Electrochemical Reduction of Carbon Dioxide Mediated by Molecular Catalysts. *Coord. Chem. Rev.* **1989**, *93* (2), 245–268. https://doi.org/10.1016/0010-8545(89)80018-9.

(7) Thoi, V. S.; Kornienko, N.; Margarit, C. G.; Yang, P.; Chang, C. J. Visible-Light

Photoredox Catalysis: Selective Reduction of Carbon Dioxide to Carbon Monoxide by a Nickel N-Heterocyclic Carbene-Isoquinoline Complex. *J. Am. Chem. Soc.* **2013**, *135* (38), 14413–14424. https://doi.org/10.1021/ja4074003.

(8) Carolina, N.; Efros, L. L.; Thorp, H. H.; Brudvig, G. W.; Crabtree, R. H. Gm 29225. **1992**, 1722–1724.

(9) Meshitsuka, S.; Ichikawa, M.; Tamaru, K. Metal Phthalocyanines in the Reduction of Carbon Dioxide. *J.C.S. Chem. Comm.* **1974**, No. 158, 158–159.

(10) Furuya, N.; Koide, S. Electroreduction of Carbon Dioxide by Metal Phthalocyanines. *Electrochim. Acta* **1991**, *36* (8), 1309–1313. https://doi.org/10.1016/0013-4686(91)80010-6.

(11) Shirley, H.; Su, X.; Sanjanwala, H.; Talukdar, K.; Jurss, J. W.; Delcamp, J. H. Durable Solar-Powered Systems with Ni-Catalysts for Conversion of CO_2 or CO to CH_4. *J. Am. Chem. Soc.* **2019**, *141* (16), 6617–6622. https://doi.org/10.1021/jacs.9b00937.

(12) Su, X.; McCardle, K. M.; Panetier, J. A.; Jurss, J. W. Electrocatalytic CO_2 Reduction with Nickel Complexes Supported by Tunable Bipyridyl-N-Heterocyclic Carbene Donors: Understanding Redox-Active Macrocycles. *Chem. Commun.* **2018**, *54* (27), 3351–3354. https://doi.org/10.1039/c8cc00266e.

(13) Sheng, M.; Jiang, N.; Gustafson, S.; You, B.; Ess, D. H.; Sun, Y. A Nickel Complex with a Biscarbene Pincer-Type Ligand Shows High Electrocatalytic Reduction of CO_2 over H_2O. *Dalt. Trans.* **2015**, *44* (37), 16247–16250. https://doi.org/10.1039/c5dt02916c.

(14) Fogeron, T.; Todorova, T. K.; Porcher, J. P.; Gomez-Mingot, M.; Chamoreau, L. M.; Mellot-Draznieks, C.; Li, Y.; Fontecave, M. A Bioinspired Nickel(Bis-Dithiolene) Complex as a Homogeneous Catalyst for Carbon Dioxide Electroreduction. *ACS Catal.* **2018**, *8* (3), 2030–2038. https://doi.org/10.1021/acscatal.7b03383.

(15) Hong, D.; Tsukakoshi, Y.; Kotani, H.; Ishizuka, T.; Kojima, T. Visible-Light-Driven Photocatalytic CO_2 Reduction by a Ni(II) Complex Bearing a Bioinspired Tetradentate Ligand for Selective CO Production. *J. Am. Chem. Soc.* **2017**, *139* (19), 6538–6541.

https://doi.org/10.1021/jacs.7b01956.

(16) Appel, A. M.; Bercaw, J. E.; Bocarsly, A. B.; Dobbek, H.; Dubois, D. L.; Dupuis, M.; Ferry, J. G.; Fujita, E.; Hille, R.; Kenis, P. J. A.; Kerfeld, C. A.; Morris, R. H.; Peden, C. H. F.; Portis, A. R.; Ragsdale, S. W.; Rauchfuss, T. B.; Reek, J. N. H.; Seefeldt, L. C.; Thauer, R. K.; Waldrop, G. L. Frontiers, Opportunities, and Challenges in Biochemical and Chemical Catalysis of CO_2 Fixation. *Chem. Rev.* **2013**, *113* (8), 6621–6658. https://doi.org/10.1021/cr300463y.

(17) Kärkäs, M. D.; Åkermark, T.; Chen, H.; Sun, J.; Åkermark, B. A Tailor-Made Molecular Ruthenium Catalyst for the Oxidation of Water and Its Deactivation through Poisoning by Carbon Monoxide. *Angew. Chemie - Int. Ed.* **2013**, *52* (15), 4189–4193. https://doi.org/10.1002/anie.201210226.

(18) Weeks, C. L.; Turner, P.; Fenton, R. R.; Lay, P. A. Nickel(II) Complexes with Amide Ligands: Oxidative Dehydrogenation of the Amines in a Tetradentate Diamide-Diamine Ligand. *J. Chem. Soc. Dalt. Trans.* **2002**, No. 6, 931–940. https://doi.org/10.1039/b107378h.

(19) Mukherjee, T.; Sen, B.; Zangrando, E.; Hundal, G.; Chattopadhyay, B.; Chattopadhyay, P. Palladium(II) and Platinum(II) Complexes of Deprotonated N,N′-Bis(2-p-Yridinecarboxamide)-1, 2-Benzene: Synthesis, Structural Characterization and Binding Interactions with DNA and BSA. *Inorganica Chim. Acta* **2013**, *406*, 176–183. https://doi.org/10.1016/j.ica.2013.04.033.

(20) Wilson, R. K.; Brooker, S. Oxidative Dehydrogenation of a New Tetra-Amine N4-Donor Macrocycle Tunes the Nickel(II) Spin State from High Spin to Low Spin. *Dalt. Trans.* **2013**, *42* (34), 12075–12078. https://doi.org/10.1039/c3dt51776d.

(21) Adolph, M.; Zevaco, T. A.; Altesleben, C.; Walter, O.; Dinjus, E. New Cobalt, Iron and Chromium Catalysts Based on Easy-to-Handle N4-Chelating Ligands for the Coupling Reaction of Epoxides with CO_2. *Dalt. Trans.* **2014**, *43* (8), 3285–3296. https://doi.org/10.1039/c3dt53084a.

(22) Afshar, R. K.; Eroy-Reveles, A. A.; Olmstead, M. M.; Mascharak, P. K. Stoichiometric

and Catalytic Secondary O-Atom Transfer by Fe(III)-NO_2 Complexes Derived from a Planar Tetradentate Non-Heme Ligand: Reminiscence of Heme Chemistry. *Inorg. Chem.* **2006**, *45* (25), 10347–10354. https://doi.org/10.1021/ic0614115.

(23) Baydoun, H.; Mazumder, S.; Schlegel, H. B.; Verani, C. N. Deactivation of a Cobalt Catalyst for Water Reduction through Valence Tautomerism. *Chem. - A Eur. J.* **2017**, *23* (39), 9266–9271. https://doi.org/10.1002/chem.201701783.

Chapter 6.

Supporting information

Table of content

Chapter 6.

1- NMR spectroscopy

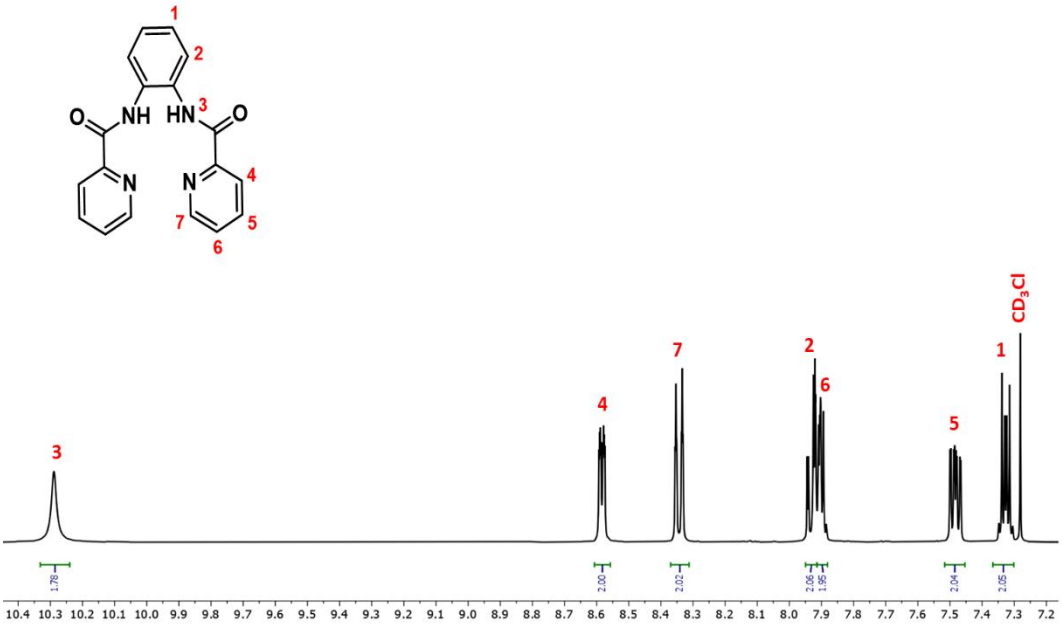

Figure S1. ^{1}H NMR of **L$_{12}$** (400 MHz, $CDCl_3$).

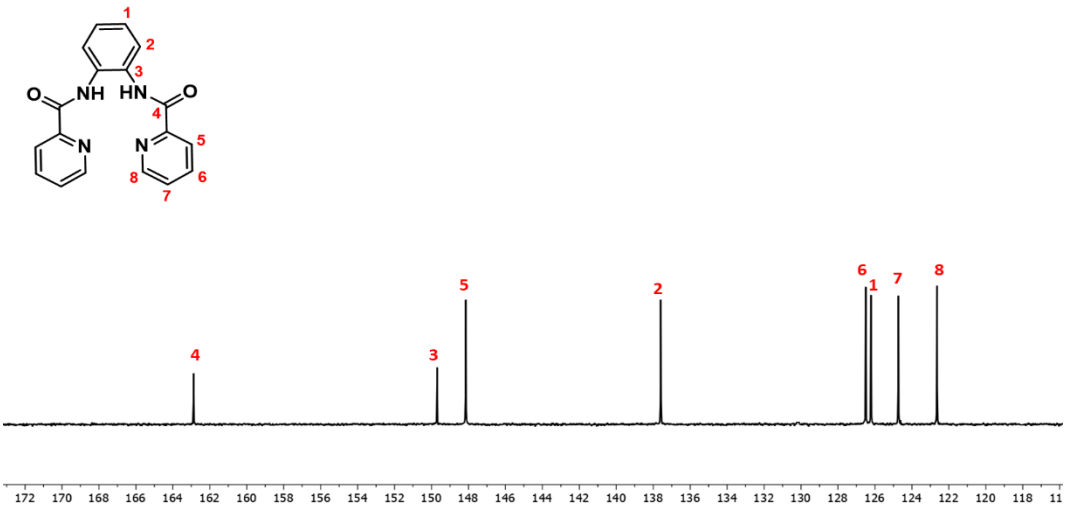

Figure S2. ^{13}C NMR of **L$_{12}$** (101 MHz, $CDCl_3$).

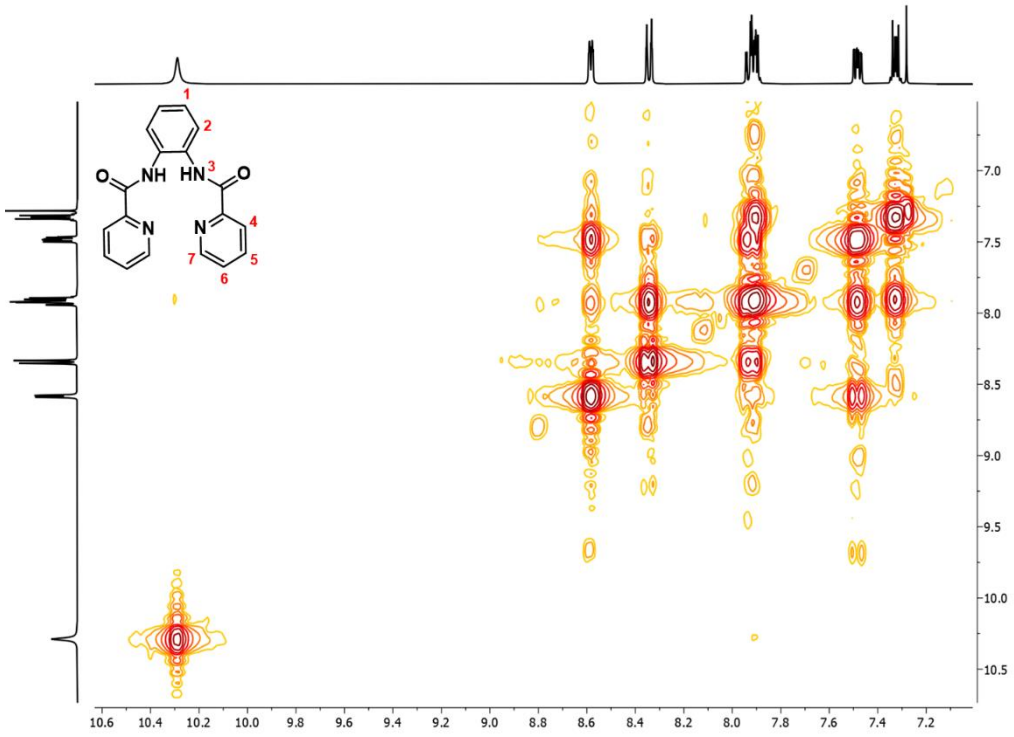

Figure S3. ^{1}H-^{1}H COSY NMR of **L_{12}** (400 MHz, $CDCl_3$).

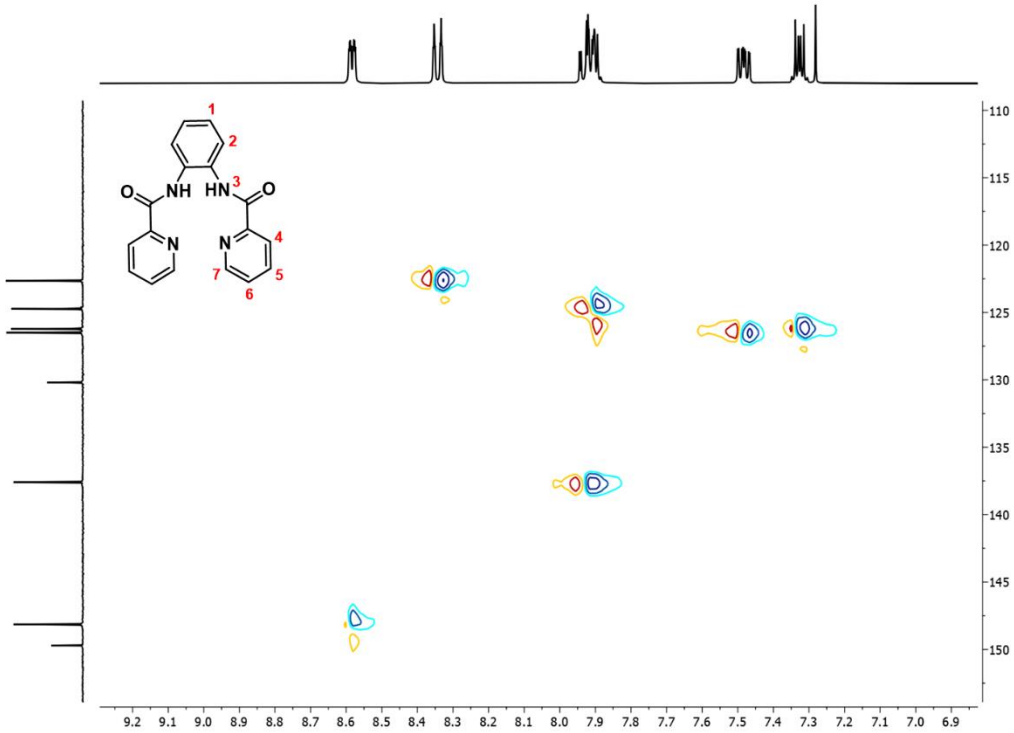

Figure S4. ^{1}H- ^{13}C HSQC NMR of **L_{12}** (400 MHz, $CDCl_3$).

Chapter 6.

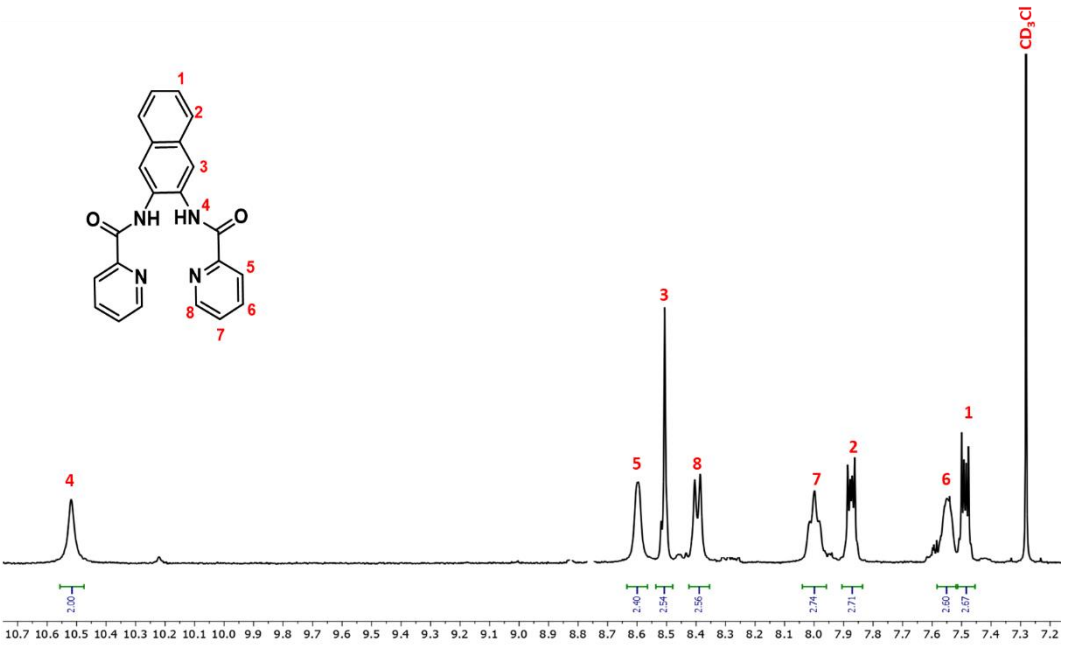

Figure S5. ^{1}H NMR of **L$_{13}$** (400 MHz, $CDCl_3$).

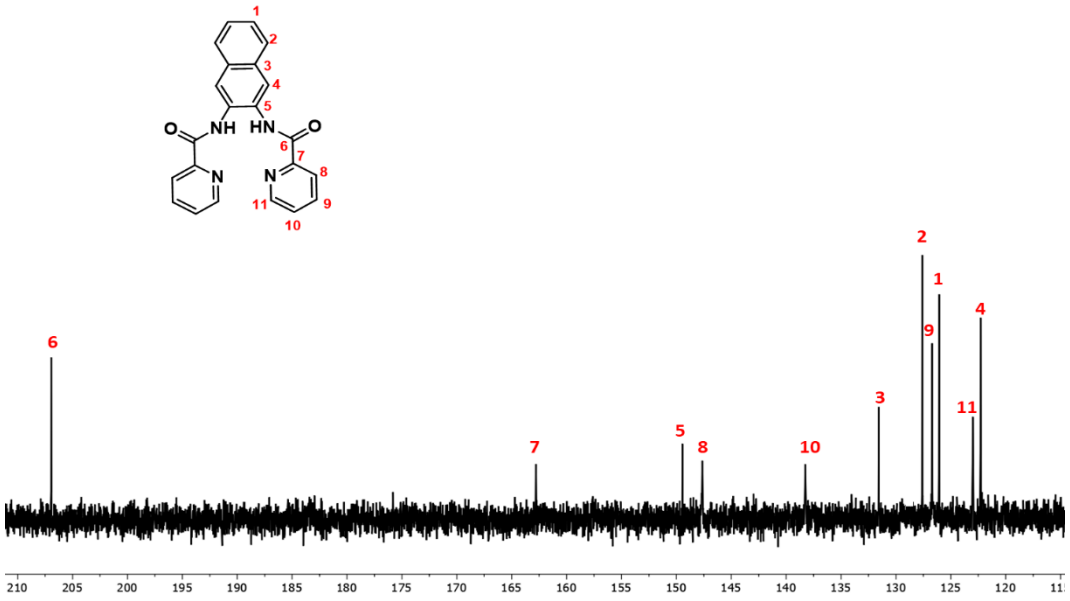

Figure S6. ^{13}C NMR of **L$_{13}$** (101 MHz, $CDCl_3$).

Chapter 6.

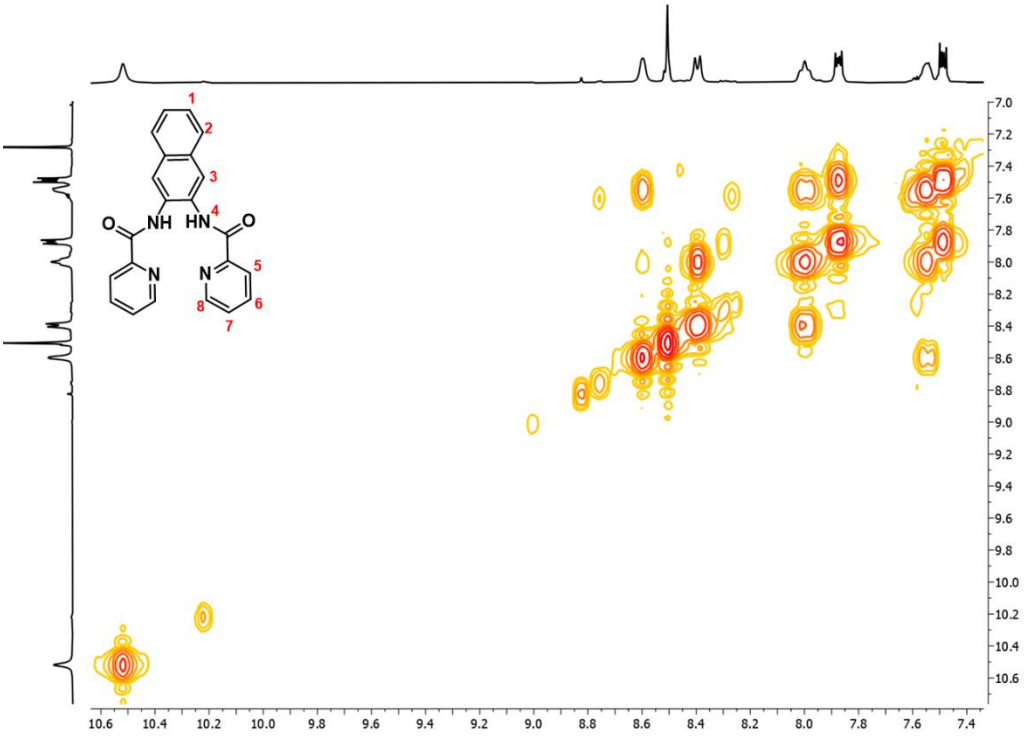

Figure S7. ^{1}H-^{1}H COSY NMR of **L$_{13}$** (400 MHz, $CDCl_3$).

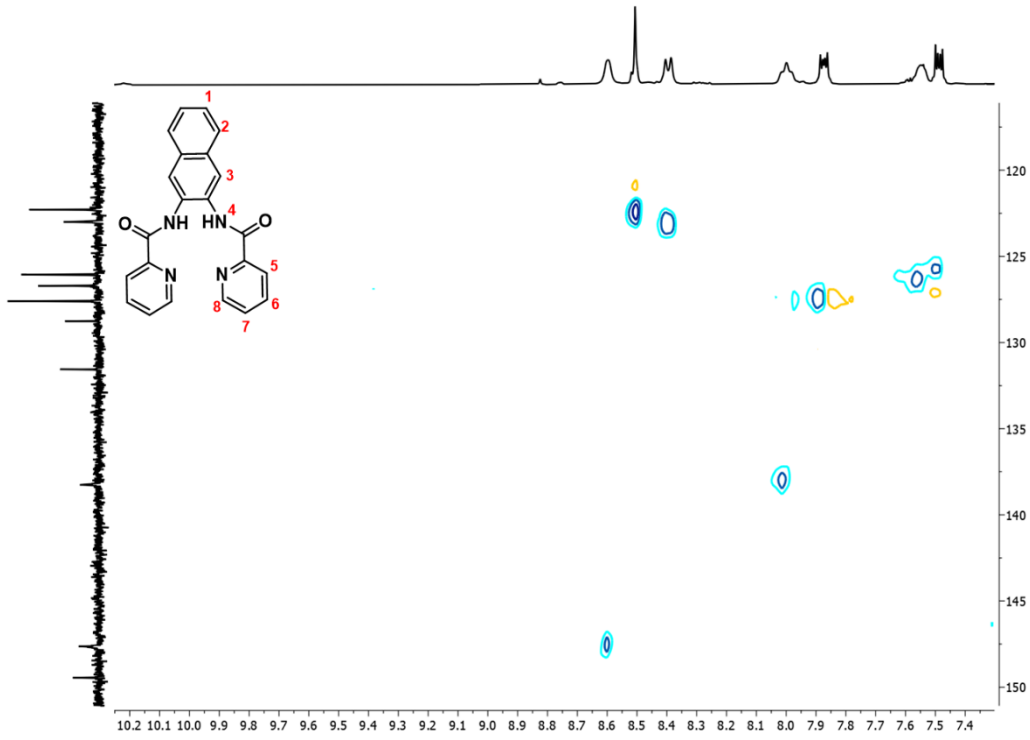

Figure S8. ^{1}H- ^{13}C HSQC NMR of **L$_{13}$** (400 MHz, $CDCl_3$).

Chapter 6.

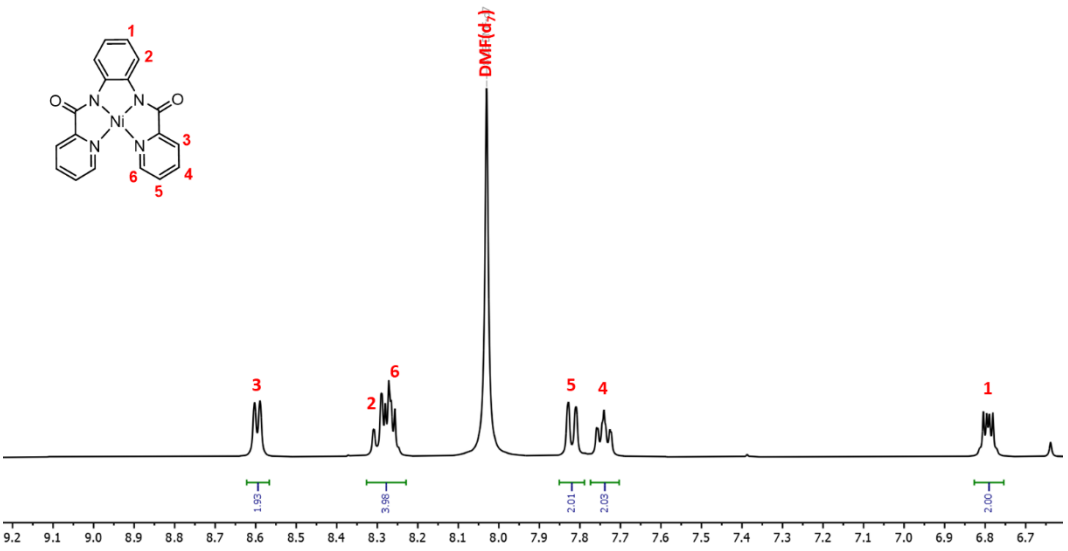

Figure S9-^{1}H NMR of complex **6** (400 MHz, DMF-d_7).

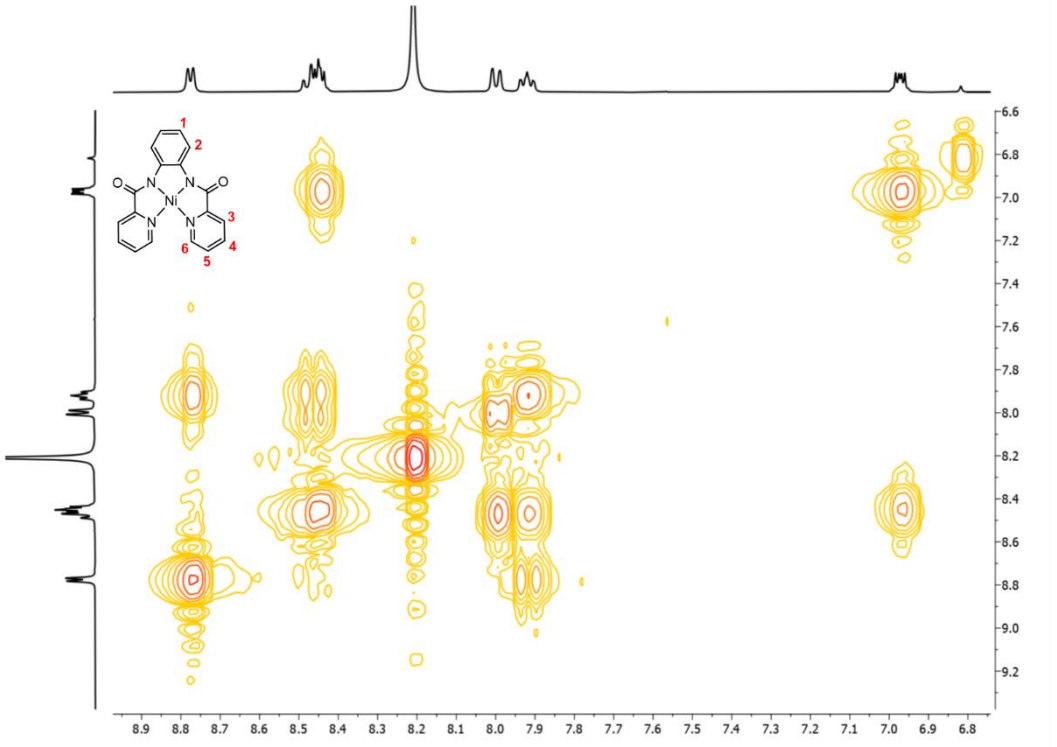

Figure S10-^{1}H-^{1}H COSY NMR of complex **6** (400 MHz, DMF-d_7).

Chapter 6.

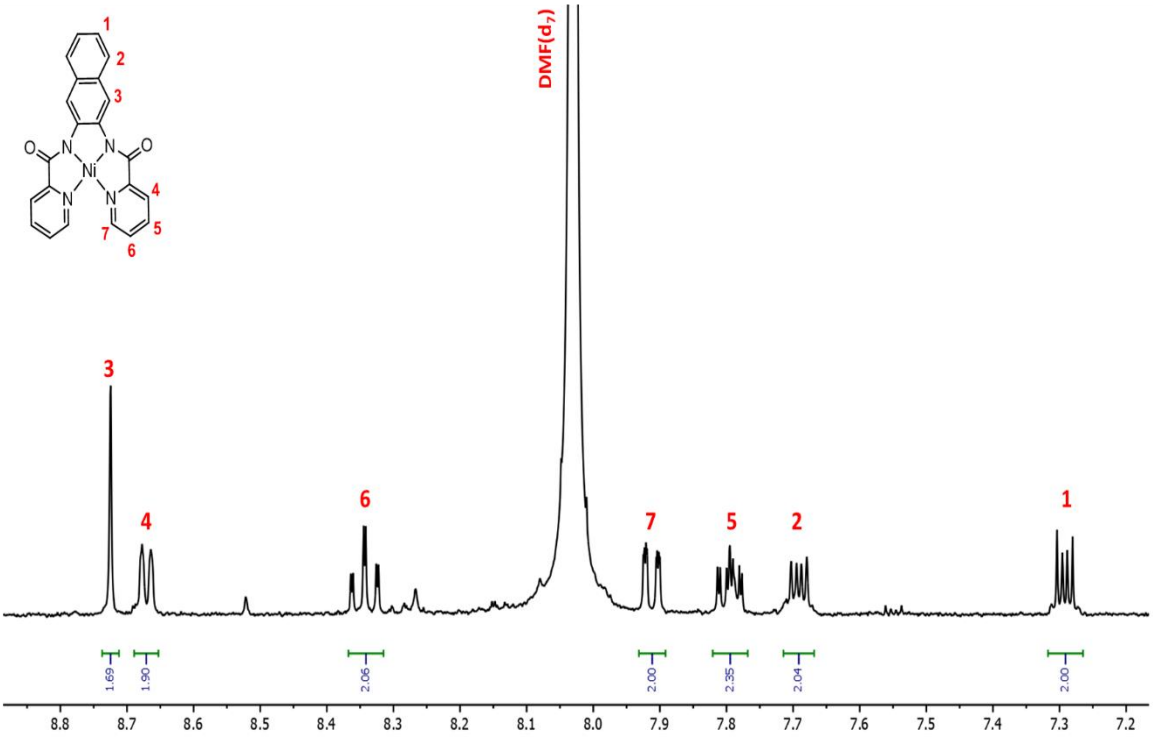

Figure S11-^{1}H NMR of complex **7** (400 MHz, DMF-d_7).

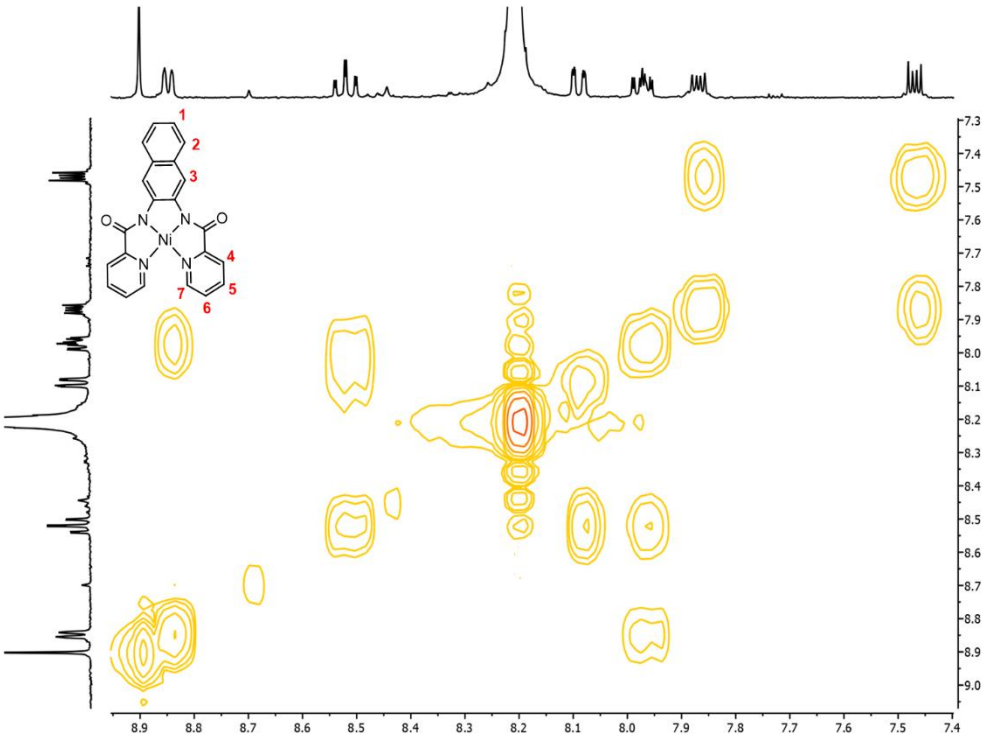

Figure S12-^{1}H-^{1}H COSY NMR of complex **7** (400 MHz, DMF-d_7).

Chapter 6.

2- Electrochemistry and Gas Detection Experiments in the presence of proton source

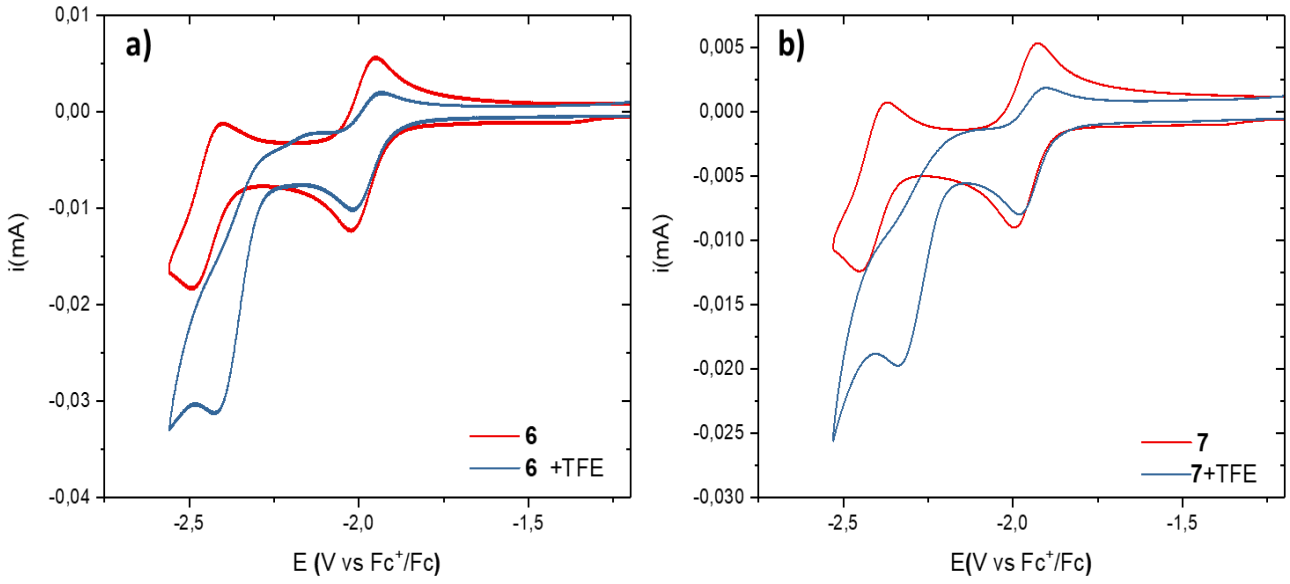

Figure S13. Cyclic voltammetry of 0.5mM solution of **6**(a) and **7**(b) in prescence of trifluoroethanol as proton source in DMF Scan rate 100mv/s

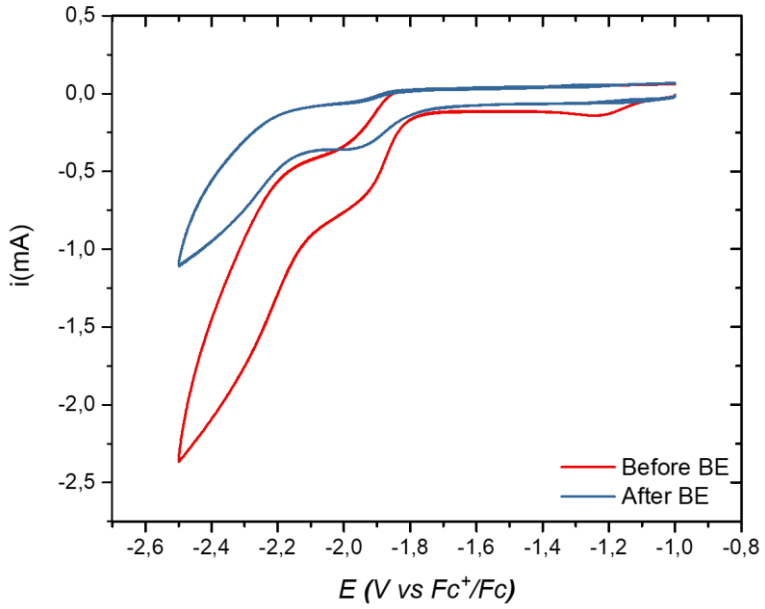

Figure S14. CV performed before and after bulk electrolysis at cell before and after CPE at E_{app}= -2V vs $Fc/Fc^{+/0}$ on DMF for **(6)** at two compartment cell consist of Pt mesh as a counter Electrode, GC rod ($S=3,14cm^2$) as working electrode, and Ag wire (in solution of the $0,01Ag/AgNO_3$,0,1$TBAPF_6$) as reference Electrode.

Chapter 6.

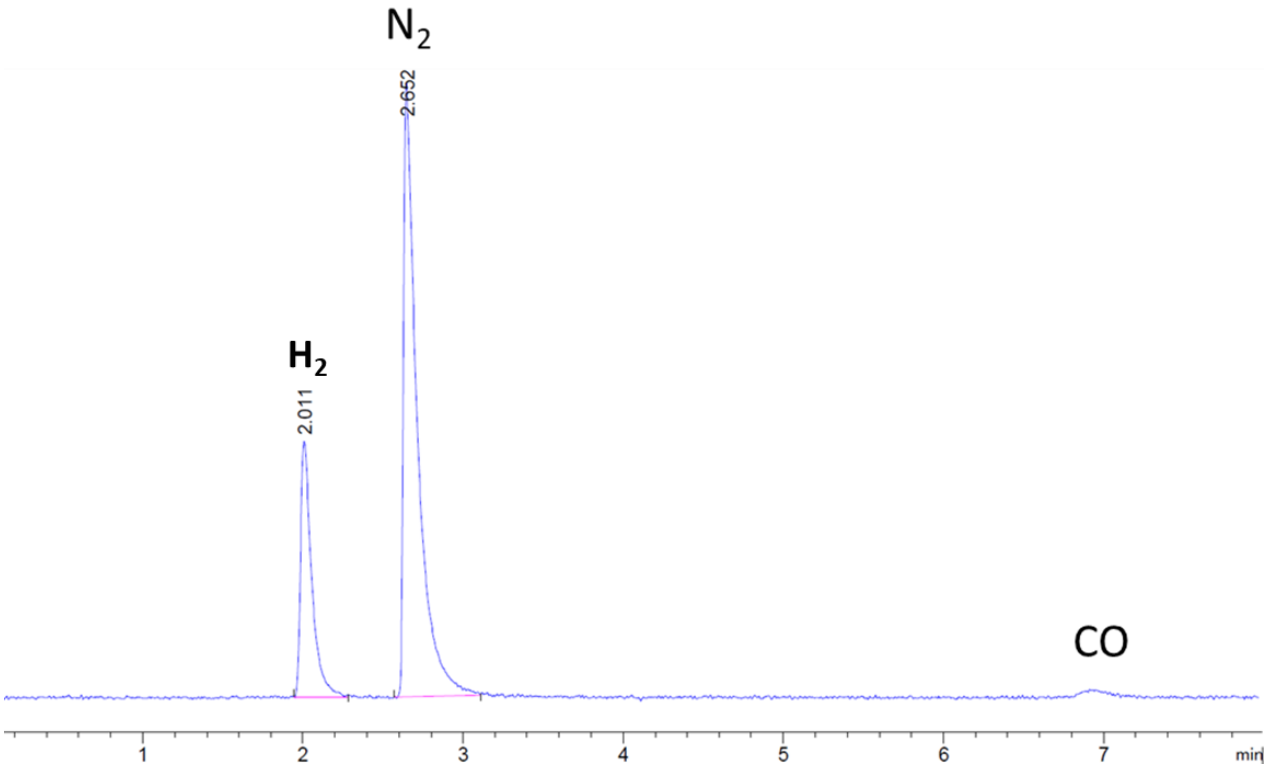

Figure S15- Chromatograms obtained by injection of 50µL of headspace after bulk electrolysis of a DMF solution of **6** saturated with CO_2 and containing 4% H_2O, at E_{app} = -2V vs Fc^+/Fc for 900s **6**.

Chapter 7

General conclusions

Chapter 7. General Conclusions

• Chapter 3.

❖ Two methods have been used for the synthesis of β-diimine derivatives. The first one is only valid for symmetrical compounds and is based on the already known one-pot acid-catalyzed bis(condensation) reaction of a β-diketone and two equivalents of an amine. On the other hand, a two-step sequential synthesis has been described for the first time and it is useful for both symmetrical and non-symmetrical β-diimine molecules. It consists of a first condensation of the β-diketone and one equivalent of one amine in the presence of catalytic amount of acid. After isolation of the monoimine intermediate, this is submitted to a second condensation reaction using dimethylsulphate as activating agent.

❖ Overall, nine β-diimine compounds have been prepared with different substituents at different positions. In particular, the imine nitrogen atoms have been modified to obtain a series of κ^3-PN_2 or κ^3-PNO asymmetric ligands and κ^2-N_2 or κ^4-P_2N_2 symmetric ligands. In addition, the α-intradiimino carbon has been successfully derivatized with phenyl or pyren-1-ylmethyl groups.

All the ligands have been tested in complexation reactions using iron, nickel, and cobalt precursors. However only a few of them resulted in useful metal complexes that have been used as HER or CO_2RR catalysts as described in Chapters 4, 5 and 6 of this thesis.

❖ Chapter 4.

❖ The synthesis, spectroscopic and electrochemical characterisation of two novel nickel complexes containing a κ^4-P_2N_2 ligand have been described ($\mathbf{1}^{2+}$ and $\mathbf{2}^{2+}$).

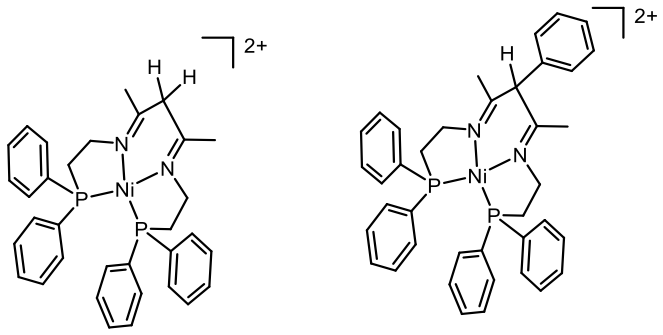

$\mathbf{1}^{2+}$ $\mathbf{2}^{2+}$

- Complexes $\mathbf{1}^{2+}$ and $\mathbf{2}^{2+}$ have a β-diimino (BDI) ligand that has been found to interconvert to the β-diketiminato (BDK) upon reduction and hydrogen atom loss, affording derivatives $(1\text{-H})^{+}$ and $(\mathbf{2}\text{-H})^{+}$.

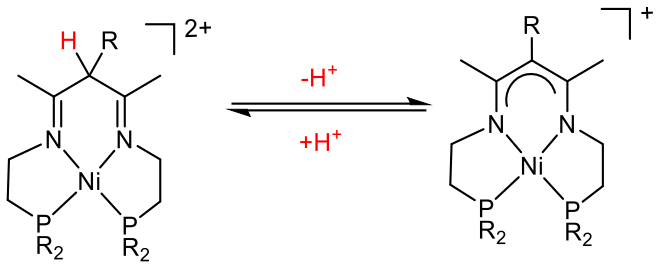

- Two possible pathways are proposed for this transformation, both starting from a metal-based reduction of the initial Ni(II) in $\mathbf{1}^{2+}$ and $\mathbf{2}^{2+}$ to form a formal Ni(I) species that rapidly evolves to a Ni(III)-hydride derivative. At this point, the formed intermediate species can be involved either in hydrogen evolution through bimolecular reductive elimination or in metal hydride induced hydrogen atom transfer (HAT) reaction to the acetonitrile solvent.

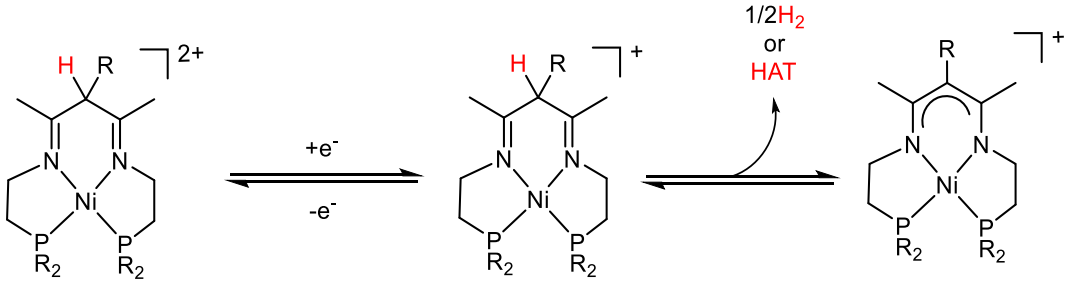

- Hydrogen gas detection experiments in the presence of acid sources rule out a HER in the first reduction wave of $\mathbf{1}^{2+}$ and $\mathbf{2}^{2+}$ presumably due to decomposition of the BDI ligand that can be reduced to a diamine. In contrast, hydrogen evolution is demonstrated in the second

reduction wave where the decomposition route is partially overcome by further reduction of catalytic intermediates. Bulk electrolysis experiments show the greater stability of complex $\mathbf{2}^{2+}$ containing a phenyl group in the intradiimino position as compared to $\mathbf{1}^{2+}$ having a Hydrogen atom at the same position.

❖ This work is a new example demonstrating the non-innocent nature of the BDI-BDK ligands, a powerful tool in multielectron-multiproton transformations.

- **Chapter 5.**

❖ Two iron complexes containing β-diimino ligands have been prepared ($\mathbf{3}^{2+}$ and $\mathbf{4}^{2+}$) and characterized by ^{1}H NMR, cyclic voltammetry and single crystal x-ray diffraction (only $\mathbf{3}^{2+}$) techniques.

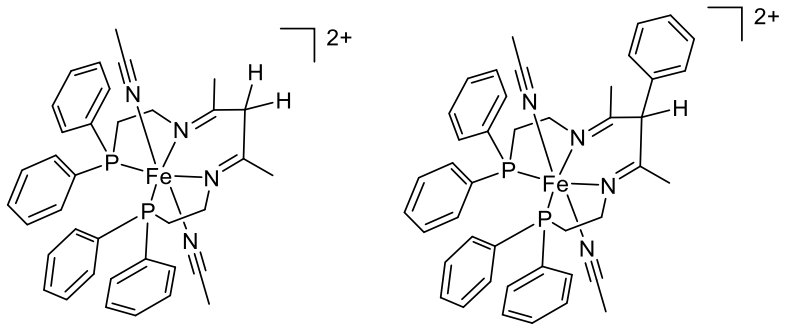

$\mathbf{3}^{2+}$ $\mathbf{4}^{2+}$

❖ Compounds $\mathbf{3}^{2+}$ and $\mathbf{4}^{2+}$ are Fe(II) low spin diamagnetic compounds with an octahedral geometry with the β-diimino ligand occupying the equatorial position and two acetonitrile ligands in the axial positions.

❖ Although $\mathbf{3}^{2+}$ and $\mathbf{4}^{2+}$ show interaction with CO_2 upon reduction, they do not perform CO_2RR and the formed derivative species decomposes.

Chapter 7. General Conclusions

❖ A β-diketiminato Iron complex (**5**) bearing a dangling pyrene group in the α-diimino position has been prepared and characterized by UV-Vis and electrochemical techniques. It is a very air-sensitive paramagnetic compound. Although its structure has not fully been ascertain, a mononuclear three coordinated Fe-chlorido complex holding is proposed (**Fe-Cl**).

❖ Complex **5** reacts with carbon dioxide to give a new complex as demonstrated by cyclic voltammetry. Similarly, when **5** is treated with a strong acid source, it evolves to a different compound, presumably a mononuclear iron-hydrido compound or β-diimino derivative.

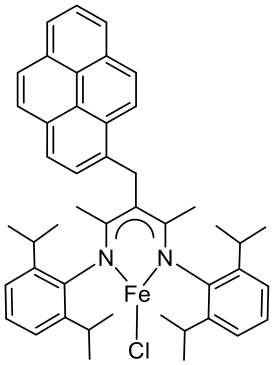

5

❖ Complex **5** shows a high catalytic current in the presence of both CO_2 and a proton source (MeOH) suggesting a putative CO_2 reduction process. However, preliminary studies have only proven the generation of H_2 gas.

❖ Complex **5** has been used to functionalize multiwalled carbon nanotubes (MWCNT) via π,π-stacking interactions (**5**@MWCNT). Preliminary cyclic voltammetry experiments using a working electrode of glassy carbon (GC) drop cast with **5**@MWCNT show analogous

behavior to that of the homogenous complex **5** suggesting successful attachment. This would be the first example of a heterogenized β-diketiminate complex.

- **Chapter 6**

❖ A straightforward route towards Ni(II) neutral complexes **6** and **7** containing tetradentate dipicolinamido ligands have been described. The novel two Ni complexes differ on the degree of conjugation of the ligand, which has been found to have an influence on their redox properties

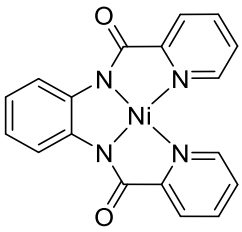

6

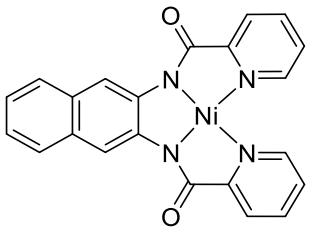

7

❖ Cyclic voltammetry experiments show analogous redox profile for both complexes with two reversible and a quasi-reversible wave, tentatively attributed to metal based/ligand based reductions.

❖ Both complexes have shown promising results as potential CO_2 reduction catalysts to form CO and H_2, as demonstrated by the catalytic wave observed in the cyclic voltammetry experiments done in the presence of CO_2 and water/TFE.

UNIVERSITAT ROVIRA I VIRGILI
NICKEL AND IRON COMPLEXES FOR ELECTROCHEMICAL REDUCTION OF PROTONS AND CARBON DIOXIDE
Navid Jameei Moghaddam

UNIVERSITAT ROVIRA I VIRGILI
NICKEL AND IRON COMPLEXES FOR ELECTROCHEMICAL REDUCTION OF PROTONS AND CARBON DIOXIDE
Navid Jameei Moghaddam

UNIVERSITAT
ROVIRA i VIRGILI